Dissertation

SUBMITTED TO THE

Combined Faculties of the Natural Sciences and Mathematics
of the Ruperto-Carola-University of Heidelberg, Germany

FOR THE DEGREE OF

Doctor of Natural Sciences

Put forward by

Martin Gärttner

born in Ludwigsburg, Germany

Oral examination: December 17th, 2013

Many-Body Effects in Rydberg Gases

Coherent Dynamics of Strongly Interacting Two-Level Atoms and
Nonlinear Optical Response of a Rydberg Gas in EIT Configuration

Referees:

Priv. Doz. Dr. Jörg Evers
Prof. Dr. Andreas Komnik

Vielteilcheneffekte in Rydberg-Gasen: Kohärente Dynamik stark wechselwirkender Zwei-Niveau-Atome und nichtlineare optische Antwort eines Rydberg-Gases in EIT Konfiguration – Gegenstand dieser Arbeit ist die theoretische Untersuchung von Ensembles von Atomen, die durch kohärente Laseranregung in einen Rydbergzustand gebracht werden. Rydbergatome wechselwirken über weite Entfernungen miteinander, was zu stark korrelierter Vielteilchendynamik führt, für deren Modellierung anspruchsvolle numerische Techniken notwendig sind. Im ersten Teil der Arbeit werden effektive Zwei-Niveau-Atome bestehend aus Grundzustand und Rydbergzustand untersucht. Bei resonanter Laseranregung wird ein verändertes Skalierungsverhalten der Anregungszahl beobachtet, welches auf Effekte endlicher Systemgröße und die Grobkörnigkeit des Mediums aufgrund der endlichen Atomdichte zurückzuführen ist. Bei nicht-resonanter Anregung bilden sich geordnete Strukturen aus einem anfänglich homogenen Gas, die sich in ausgeprägten Peaks in den räumlichen Korrelationen und modifizierter Anregungs-Statistik widerspiegeln. Im zweiten Teil wird ein schnell zerfallendes mittleres Niveau hinzugenommen. Dadurch erhält man das Phänomen der elektromagnetisch induzierten Transparenz (EIT). Durch die starken Wechselwirkungen zwischen den Rydbergatomen wird dieser Effekt jedoch unterdrückt, was zu einer optischen Nichtlinearität führt. Es wird ein Modell entwickelt, mit dem sich die Eigenschaften einer Wolke von Rydbergatomen in EIT Konfiguration vorhersagen lassen. In beiden Teilen werden die Vorhersagen der Modelle mit experimentellen Beobachtungen verglichen.

Many-Body Effects in Rydberg Gases: Coherent Dynamics of Strongly Interacting Two-Level Atoms and Nonlinear Optical Response of a Rydberg Gas in EIT Configuration – Subject of this thesis is the theoretical investigation of ensembles of atoms that are coherently laser-excited to a Rydberg state. Rydberg excited atoms interact with each other over large distances, which leads to strongly correlated many-body dynamics, demanding powerful numerical tools for their modeling. The first part of the thesis deals with effective two-level atoms consisting of a ground and a Rydberg state only. For resonant laser excitation a modified scaling behavior of the excitation number is observed, which is caused by effects of finite system size and coarse graining of the medium due to the finite atomic density. For off-resonant excitation, ordered structures arise out of an initially homogeneous gas, which are reflected in strongly peaked spatial correlations and modified excitation statistics. In the second part a fast decaying intermediate level is additionally taken into account. In this situation the phenomenon of electromagnetically induced transparency (EIT) is encountered. This effect is suppressed in the presence of strong interactions between the Rydberg atoms leading to an optical nonlinearity. A model predicting the properties of a cloud of Rydberg atoms in EIT configuration is developed. In both parts the models are validated by comparing their predictions to recent experimental observations.

Contents

Chapter 1

Introduction

Rydberg states, highly excited electronic states of atoms, have been studied for more than a century. The term Rydberg atom goes back to Johannes Rydberg (1854-1919), who studied the spectral properties of the light emitted by atoms in the 1880s and discovered a simple formula describing the frequencies of the emitted lines [1]. In twentieth century the properties of Rydberg atoms were studied extensively [2]. However, until the year 2000 these studies were focused on the spectroscopic properties of Rydberg atoms in thermal vapors. Then, the appearance of several seminal articles [3–5] marked a decisive turning point in the development of Rydberg physics. Triggered by the idea to use Rydberg atoms for applications in quantum information science, Rydberg physics evolved into an interdisciplinary field with a broad range of applications in other areas of physics. In the following, a brief outline of these fascinating developments is provided.

During the 1990s powerful techniques for laser cooling and trapping of atoms were developed. With these techniques an unprecedented degree of coherent control over external and internal degrees of freedom of atoms could be achieved. This lead to a number of remarkable discoveries at the heart of quantum mechanics. The most well-known achievement was probably the realization of a Bose-Einstein condensate (BEC) in 1995 [6, 7], a phenomenon already predicted in the early days of quantum mechanics [8–10]. The advances in ultracold physics and coherent control sparked a rapid growth of quantum information science [11, 12]. What certainly heated this field additionally, were breakthroughs in quantum information theory like Shor's factoring algorithm [13] or quantum error correction [14].

These developments set the stage for the idea to combine the long-range interactions of Rydberg atoms with the coherent control of cold atomic gases. In early studies of Rydberg atoms in the "frozen" regime line broadening and deformation was observed as a signature of Rydberg-Rydberg interactions [15, 16]. The key ideas, however, that lead to a real explosion of the field and let it become increasingly interdisciplinary, appeared in the years 2000/2001 [3, 4]. These works contain two aspects that reappear over and over in works on many-body physics with Rydberg atoms and also in this thesis. These concepts are the dipole blockade and collective Rabi oscillations. For two nearby atoms, the dipole-dipole interactions between Rydberg atoms result in an energy shift of the doubly excited state, as illustrated in Fig. 1.1(a). Thus, if those two atoms are laser-excited resonantly from the ground to the Rydberg state, the doubly excited state becomes off-resonant due to the interaction shift and double excitation is inhibited. This was first exploited in Ref. [3] to construct a quantum gate. In an extended atomic sample the interaction shift of states with two nearby excitations leads to a certain exclusion distance R_b. Therefore, two Rydberg excited atoms can never appear at a distance smaller than the blockade radius R_b from each other, as illustrated in Fig. 1.1(b). This phenomenon, leading to an interaction induced suppression of excitation, is what is called the *dipole blockade* [4]. In Fig. 1.1(c) another consequence of the blockade

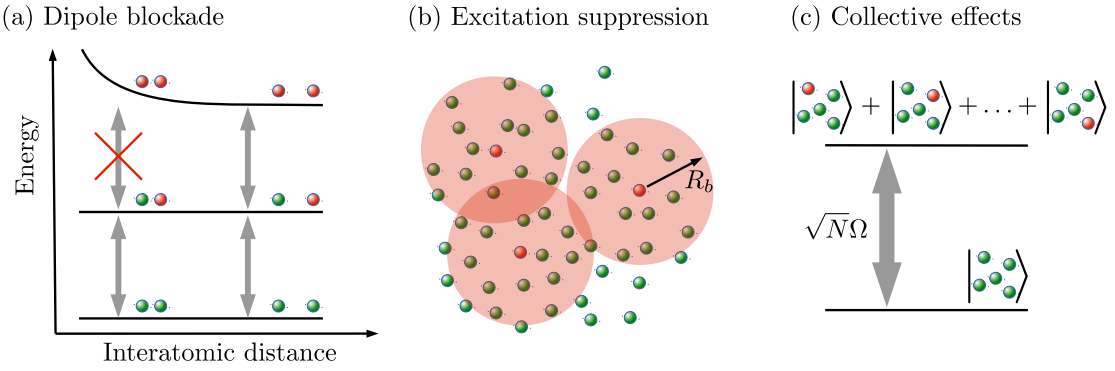

Figure 1.1: (a) The dipole blockade mechanism: Two atoms in the ground state (green spheres) are excited to the Rydberg state (red spheres). If the distance between the atoms is small, the doubly excited state is shifted out of resonance due to the dipole-dipole interactions between Rydberg excited atoms. (b) Due to the blockade effect any Rydberg atom inhibits the excitation of further Rydberg atoms in its vicinity, leading to a suppression of excitation compared to the noninteracting case. (c) In a small sample, in which only one excitation is possible, the atoms act collectively, since it is unknown which atom is excited. Therefore the excitation dynamics is collectively enhanced.

is illustrated. In a perfectly blockaded ensemble only one atom can be excited to a Rydberg state. If the excitation process is perfectly coherent, it is impossible to tell which atom gets Rydberg excited. Thus, quantum mechanically the system will be in a symmetric superposition of all possible singly excited states. This leads to a collective enhancement of the atom-light coupling and hence to an enhanced excitation rate [4, 17, 18].

From the theory point of view, before the year 2000, inter-atomic interactions were mostly treated as point-like in cold atom physics. The Gross-Pitaevskii equation proved to be a powerful tool for describing ensembles of ultracold atoms [19, 20]. Generally, the great majority of tools for describing quantum many-body systems rely on the finite range of spatial correlations [21]. For Rydberg atoms, however, these methods can only be applied in a limited range of parameters due to the long-range interactions which lead to the emergence of strong many-particle correlations. This poses a tremendous theoretical challenge on the simulation of Rydberg gases and their interaction with light. The improvement of the modeling of the many-body dynamics in strongly interacting Rydberg gases and the search for new intriguing many-body effects arising in such systems are the goals of this thesis.

However, before outlining the content of the thesis in detail, the historical overview is continued by briefly mentioning the major experimental and theoretical achievements that have been made in the field of Rydberg physics over the past decade. The motivation for this attempt of a review is to give an impression of how dynamical and interdisciplinary Rydberg physics is, since this is what makes it such a fascinating field of research. During the past few years it has become almost impossible to follow all the developments and new ideas that pop up. These ideas range from applications in quantum information science over quantum optics and BEC physics to solid state and plasma physics. It has to be noted that the view of the "Rydberg world" presented here is naturally biased by the specific research interests of the author and can never claim to be complete. For recent review articles of the topic, the reader is referred to Refs. [22–26].

Multidisciplinary Rydberg research

The early 2000s saw a tremendous boost of experimental activities aiming at the demonstration of the dipole blockade and collective effects in mesoscopic ensembles. Excitation suppression due to interaction effects was first reported in 2004 in Freiburg [27] and Storrs [28] (see also Refs. [29–35]). Collective Rabi oscillations of two [17] and many atoms [18] have recently been observed. For resonant excitation of Rydberg atoms the blockade mechanism leads to a dense packing of blockade spheres, which manifests itself in sub-Poissonian excitation number statistics [36–39]. Off resonance, the Rydberg-Rydberg interactions can lead to distance selective excitation of atom pairs and aggregates [40,41] that result in super-Poissonian excitation statistics, which was recently observed in Pisa [42] and Heidelberg [43]. At the moment, many groups are working on techniques for measuring spatially resolved observables in Rydberg excited ensembles [44–48].

Great effort was put into the study of the atomic properties of Rydberg atoms [49–54] and their interactions [55–63]. Initially the focus had mainly been on alkali atoms, but recently also alkaline earth atoms and Rydberg ions have been under discussion [64–67]. Again in the year 2000, it was realized that the wave function of a Rydberg electron can feature bound states of Rydberg and ground state atoms resulting in extremely weakly bound gigantic molecules [5]. The first observation of such molecules was reported by the Stuttgart group in 2009 [68] and research on this topic is still ongoing [69–75]. Also, the sensitivity of Rydberg atoms to external fields was investigated, which includes ionization by small electric fields [76–80], tuning of interactions by external fields [81–85], surface effects [86–88], and the possibilities of trapping of Rydberg atoms [89–94]. It was found that, due to their large polarizability, Rydberg atoms find applications in electric field sensing [95, 96].

Even more interesting from the author's perspective are the advances in the modeling of many-body dynamics of strongly interacting cold samples in the motionally frozen regime. This is the field, in which the first main part of this thesis (Chap. 3) is located. Here, the driving forces were (and are) the groups in Dresden [97–103], Nottingham [104–109], Auburn [110–113], and Stuttgart [26, 114, 115], but also many others [116–133], as Fig. 1.2 illustrates. The progress in this discipline is discussed in detail in the main part of this thesis. Here, we only highlight some of the findings that lead to connections of Rydberg physics with other fields. As mentioned before, due to the Rydberg blockade, a dense packing of excitations, i.e., a self assembled structure emerges in Rydberg gases [134–138]. A similar effect arises for blue detuned excitation [139–145]. Here, also self assembled crystalline structures can be created [136, 146–148]. By field ionizing the Rydberg atoms in such a structured medium plasmas with a pre-structured charge distribution are accomplished [149–152]. Another idea is, to use the Rydberg blockade to design a deterministic single-ion source [153]. Applying far red detuned laser fields a small admixture of the Rydberg state is added to the atomic ground state. This results in an effective soft core potential of the "Rydberg dressed" atoms [92, 154–156]. Rydberg dressing of BECs results in interesting novel many-body phases such as supersolids [157–168]. A connection to solid state physics arises for many-body simulations in lattice geometries [169,170]. Laser driven lattice gases of Rydberg atoms can be mapped on spin Hamiltonians, well known in solid state physics, but now including nonlocal interactions [106,171–176]. Here, strongly interacting cold atoms offer a rich playground for exploring, for example, the role of quantum correlations and entanglement in spin systems [177], quantum phase transitions [178,179], or entanglement transport. Including dissipation in such models,

Figure 1.2: The map of world-wide Rydberg research. In order to quantify the contributions of the different groups to the field we tried to count the number of publications on this topic. This is of course not exact and does not necessarily quantify the value of these contribution to the field of Rydberg physics.

interesting effects relating to classical thermodynamics [138, 180, 181] and chaotic, bistable systems are encountered [182–188].

A largely unexplored direction is the physics beyond the frozen gas approximation, i.e., taking into account the motional dynamics of the atoms in a strongly interacting gas. On the one hand, this is necessary for the description of many experimental setups [157, 189–194] as will be shown in Secs. 3.8 and 4.3. On the other hand, it also uncovers interesting physics, such as transport phenomena and entanglement between motional and internal degrees of freedom [25, 102, 195–202].

In the realm of quantum information applications, the blockade gate proposal from 2000 [3] was soon followed by more and more involved studies [203–213]. The main driving force in this direction was the group in Wisconsin [22, 214–218]. There, the experimental realization of a CNOT gate with Rydberg atoms was achieved in 2010 [217, 218]. Recent ideas include hybrid systems of Rydberg atoms and BECs [219], entanglement generation in dissipative systems [220, 221], and quantum computation with Rydberg ions [25, 193]. An effort aiming at coherent manipulation of micro cells filled with hot atomic vapor is pursued in Stuttgart [222–225].

Another major part of Rydberg research is dedicated to quantum optics and the interaction of laser light with Rydberg gases [226–244]. This field has probably been pushed most by the group in Durham [24, 216, 245–252]. The phenomenon of electromagnetically induced transparency (EIT) with Rydberg atoms is the main idea which the second part of this thesis (Chap. 4) is based on [38, 43, 253–256]. The strong interactions between the Rydberg atoms can be used to mediate effective interactions between photons [257–260]. On this

basis, a number of groups recently realized single-photon sources using quasi-one-dimensional clouds of Rydberg atoms [243, 247, 261]. Further theoretical ideas reach from single-photon switches [262] over crystalline states of light [263] to photon-photon bound states.

This brief overview shows that as a researcher in Rydberg physics one can probably regard oneself as a generalist among the often highly specialized modern physicists. From the author's point of view, this is the main reason why not only the atoms themselves, but also the scientists studying them, are highly excited.

Outline of this work

What is the objective of this thesis in this diverse Rydberg world? As indicated above, the simulation of strongly interacting quantum many-body systems poses a great challenge due to the emergence of long-range correlations. In this context a powerful toolbox of numerical methods has been developed in our group since the Rydberg project was started about three years ago. This toolbox enabled us to reveal a number of intriguing many-body effects in different parameter regimes and setups. As we are lucky to work very closely with an experimental group in Heidelberg, we had the chance to test our models by comparing their predictions to experimental observations. This requires a modeling that is capable of describing the dynamics of ultracold Rydberg gases under realistic experimental conditions. Depending on those conditions different models may be suited. This is why this thesis is divided into two main parts. The first part deals with coherent dynamics in an ensemble of strongly interacting two-level atoms. The second part treats three-level atoms and the aspect of nonlinear absorption in Rydberg media in the presence of dissipation. The structure of the thesis is detailed in the following.

Chapter 2 summarizes the physical concepts leading to the working equations that are used in later chapters as starting points for the many-body modeling. First, the exceptional properties of Rydberg atoms are described. Then, we derive the interaction potential between two Rydberg atoms in the simplest case of s-states (angular momentum quantum number $l = 0$). Subsequently, an introduction to the interaction of light with a few level atom is given. Also, it is shown how dissipation can be included in the description using the density operator to represent the state of the system. The dynamics of this operator is then governed by a master equation. Finally, the relevant energy, length, and time scales involved in typical experiments are compared.

Chapter 3 is dedicated to the solution of the Schrödinger equation of an ensemble of two-level atoms coherently laser-excited to a Rydberg state. We start with a technical part on the structure of the underlying Hilbert space and Hamiltonian as well as its numerical implementation. Thereafter, an extensive parameter study of the system is provided for resonant excitation laser. Here, effects of finite sample size, atomic density and potential shape are identified. Then, allowing the laser detuning to be nonzero, interesting effects are found especially on the blue detuned side. We observe a broadening and asymmetry of the Rydberg line caused by the presence of resonant excitation of Rydberg aggregates. This asymmetry has recently been observed experimentally in Heidelberg, which is discussed in the last section of Chap. 3.

Chapter 4 deals with three-level atoms that are driven to a Rydberg state by resonant two-step excitation via an intermediate state. The laser which drives the lower transition is very weak. Nevertheless, without Rydberg interaction the laser light would travel through

the medium without being absorbed due to the EIT effect. If, however, strongly interacting Rydberg atoms are present, this effect is rendered ineffective and the medium becomes opaque. After introducing the basics of light propagation in atomic media and EIT, the phenomenology of Rydberg EIT and current state-of-the-art models are reviewed. Then, a rate equation model for the calculation of the steady state of an ensemble of three-level Rydberg atoms in the strongly dissipative regime is introduced. The properties of this model can be understood in terms of a semi-analytical approach explaining the emergence of collective effects. Testing the rate equation model by comparing to exact master equation calculations we find interesting parameter regimes featuring a coherent collective enhancement of Rydberg excitation. Finally, we show how to include the absorption of the laser light in this model and compare our simulation results to experimental observations.

Chapter 5 summarizes the results of the preceding two chapters and gives an outlook on possible directions of future research.

Chapter 2

Basic concepts

This chapter summarizes the basic physical concepts underlying the description of an ensemble of ultracold alkali atoms being laser excited to a Rydberg state. Particular focus is put on the numerous approximations that are made in the derivation of our working equations, some of which will have to be questioned under realistic experimental conditions in Secs. 3.8 and 4.3. We try to keep this introduction as short as possible and focus only on the aspects relevant for the later discussion and rather refer the reader to the literature for further details. Section 2.1 is dedicated to the basic properties of Rydberg atoms [2, 264, 265]. In Sec. 2.2 it is demonstrated how these properties lead to long-range dipole-dipole interactions and that the interaction potential is typically van der Waals like [22, 23, 266–270]. The modeling of the excitation of Rydberg states by laser light is presented in Sec. 2.3. Here, we describe the typical two-step excitation scheme and show how the intermediate level can be adiabatically eliminated [271,272]. Section 2.4 formulates the working equations describing the many-body dynamics in a motionally frozen Rydberg gas.

2.1 Rydberg atoms

The term Rydberg atoms refers to electronic states in which at least one electron is excited to a state with a principal quantum number n that is much larger than the one of the corresponding ground-state level [2]. Our discussion is restricted to alkali atoms, since these are the ones most used in experiments. Note, however, that proposals to use alkaline earth atoms and ions [64, 65] are presently being discussed. The experiments described in detail in Secs. 3.8 and 4.3 exclusively use rubidium, as it has advantageous properties in terms of laser cooling and trapping [273]. For alkali atoms, the electronic structure is particularly simple, due to its similarity to atomic hydrogen. The highly excited valence electron orbits are localized far away from the core which is shielded by the remaining closely bound electrons. Therefore, deviations from the hydrogenic character are only present if the electronic wave function of the Rydberg electron penetrates the closed-shell core and thus experiences the effect of the highly charged nucleus. This is the case for low angular momentum l, as indicated in Fig. 2.1(a). Thus, low angular momentum orbitals become more closely bound with respect to the corresponding hydrogen levels and their binding energy increases, whereas high angular momentum states ($l \gtrsim 3$) are almost perfectly hydrogen-like [see Fig. 2.1(c)]. Rydberg levels can be parametrized modifying the hydrogen levels by introducing the so called *quantum defect* δ_{njl} that depends on the quantum numbers n, j, and l. With this, the binding energy of the Rydberg state reads

$$E_{njl} = -\frac{Ry}{(n-\delta_{njl})^2}\,, \tag{2.1}$$

where $Ry = 13.61\,\mathrm{eV}$ is the *Rydberg constant*.

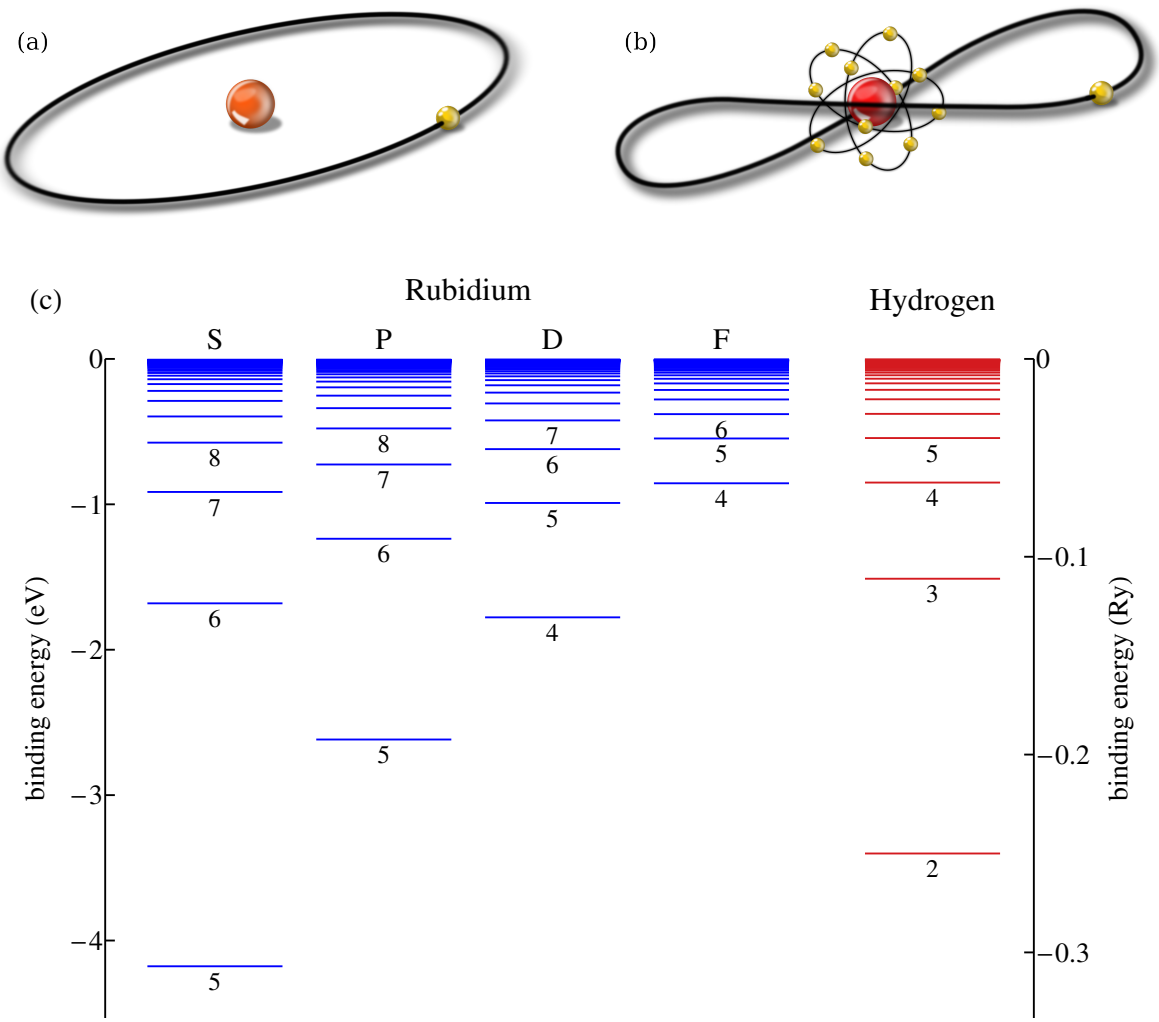

Figure 2.1: Sketch of an alkali atom in a highly excited state with (a) high and (b) low angular momentum. In the former case the Rydberg electron does not resolve the electronic structure of the ionic core. Such states with $m = l = n - 1$ are called circular Rydberg states [274]. Their orbitals coincide with the ones predicted by the Bohr model. In the latter case the electron has a finite probability to be localized inside the finite size ionic core. Thus the shielding of the core becomes nonperfect leading to stronger binding reflected by the quantum defect δ_{njl}. (c) Energy levels of rubidium and hydrogen. The numbers below the lines indicate the principle quantum number n. Already for $l = 3$ (F-states) the quantum defect is small and the levels deviate little from the respective hydrogen levels. For $n \geq 8$ the energies are calculated from Eq. (2.1) where the values of δ_{njl} are taken from [49, 275]. The energies of the small n levels are taken from the NIST ATOMIC SPECTRA DATABASE [276]. Figure adopted from [264] with friendly permission of M. Mayle.

Rydberg atoms have exaggerate properties in many respects [2]. The small binding energy of the Rydberg electron, scaling as n^{-2}, makes Rydberg atoms very fragile objects, as already a small electric field leads to their ionization. Nevertheless, they have extremely long radiative lifetimes due to the fact that the transition dipole matrix elements to the ground state $\mu_{gr} = \langle g | \mu | r \rangle$ scale as $n^{-3/2}$. This leads to lifetimes of $\sim 100\,\mu$s for $n \approx 50$ rendering Rydberg states metastable. This is crucial for applications, e.g., in quantum information [22]. At the same time the size of the transition dipole matrix element between *adjacent* Rydberg states $\mu_{rr'}$

Table 2.1: Properties of Rydberg atoms. The n-dependence is adapted from Ref. [2]. The numerical values are calculated from the quantum defects in [49, 275] and taken from [50].

Property	n-dependence	Value for $55s$ state of ^{87}Rb
Binding energy	n^{-2}	-5 meV
Level spacing between adjacent n states[1]	n^{-3}	46 GHz
Orbital radius[2]	n^2	0.14 μm
Dipole moment $\langle ns\vert\, er\,\vert np\rangle$	n^2	
Polarizability	n^7	
Radiative lifetime τ_0[3]	n^3	191 μs
Black-body lifetime τ_{bb}[4]	n^2	143 μs
Effective lifetime $(1/\tau_0 + 1/\tau_{bb})^{-1}$		82 μs

scales as n^2, which makes Rydberg atoms very easily polarizable and sensitive to electric and microwave fields. The different scalings of μ_{gr} and $\mu_{rr'}$ with n are easy to understand. The spatial overlap with the ground-state wave function decreases with increasing n, while the for example the matrix elements $\langle ns\vert\, r\,\vert np\rangle$ become larger with increasing n as the mean distance to the core $\langle r\rangle$ increases. The large $\mu_{rr'}$ and the small energy splitting $\Delta E_{rr'} \propto n^{-3}$ between adjacent Rydberg levels leads to strong dipole-dipole interactions, which are discussed in the next section. In the Bohr model, the orbital radius of the electron is

$$r = \frac{4\pi\epsilon_0\hbar^2}{e^2 m_e} n^2 = a_0 n^2 \tag{2.2}$$

where a_0 is the Bohr radius. This means that r is of the order of 1 μm for $n \approx 100$. The scaling properties of various quantities with the principal quantum number n are summarized in Tab. 2.1.

2.2 Rydberg-Rydberg interactions

Crucial for almost all applications of Rydberg atoms are the strong dipole-dipole interactions between them. They arise as a result of the large mean separation between the Rydberg electron and ionic core. In a classical picture, this large separation leads to a large dipole moment $\boldsymbol{\mu} = e\mathbf{r}$. Two such dipoles will interact strongly and over large distances [23]. However, in the absence of external fields, there is no preferred orientation of the dipoles. Thus, at least in the limit of interatomic distance $R \gg |\mathbf{r}|$, the resulting interaction will not be a direct dipole-dipole one ($V \propto R^{-3}$) but rather an induced (retarded) one ($V \propto R^{-6}$) [23]. Note that the potential arising from the retarded interaction in principle contains additional terms decreasing with other powers of R. A detailed account of this can be found in Refs. [23, 269] and the references therein. In the following it is shown, how the interaction potential $V(R)$ can be obtained from perturbation theory in the case of a $ns + ns$ manifold.

[1] The numerical value is the spacing between $55s$ and $56s$.
[2] Numerical value calculated as $a_0(n - \delta_{njl})^2$ [2].
[3] Numerical value taken from Ref. [50].
[4] Numerical value calculated according to Eq. (14) in Ref. [50] with $T = 300$ K.

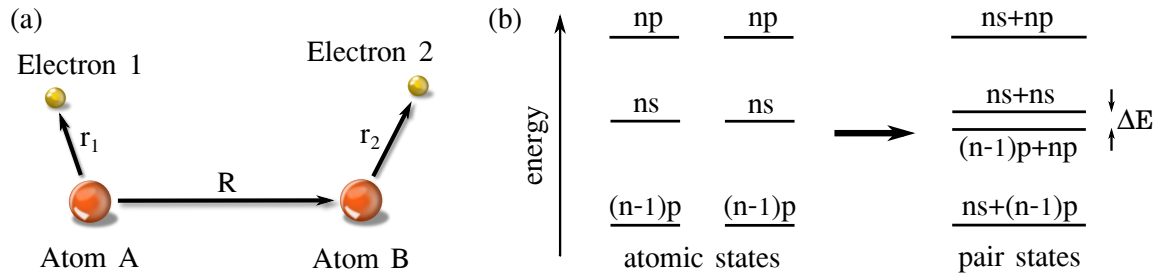

Figure 2.2: (a) Sketch of two interacting Rydberg atoms. In the field-free case the expectation value of the dipole moment of each atom is zero, such that there is no direct dipole-dipole interaction. (b) The product states $ns + ns$ and $(n-1)p + np$ are near degenerate and coupled by the interaction Hamiltonian H_{dd}, which leads to strong, long-range interactions.

We also comment on permanent dipoles induced by external fields and the notion of a Förster resonance.

The total Hamiltonian of the two Rydberg atoms is

$$H_{\text{tot}} = H_A + H_B + H_{\text{int}}\,, \tag{2.3}$$

where H_A and H_B are the single-atom Hamiltonians of atoms A and B. In a notation that becomes obvious from Fig. 2.2(a) the interaction Hamiltonian between the two atoms is

$$H_{\text{int}} = \frac{e^2}{R} - \frac{e^2}{r_{A2}} - \frac{e^2}{r_{B1}} + \frac{e^2}{r_{12}}\,. \tag{2.4}$$

Here, the internuclear distance is R, with $\mathbf{R} = R\mathbf{n}$. If $R \gg r_1, r_2$, a multipole expansion can be performed, which, in leading order, yields the dipole-dipole Hamiltonian [23]

$$H_{dd} = \frac{\boldsymbol{\mu_1}\cdot\boldsymbol{\mu_2} - 3(\boldsymbol{\mu_1}\cdot\mathbf{n})(\boldsymbol{\mu_2}\cdot\mathbf{n})}{R^3}\,. \tag{2.5}$$

This approximation is only valid as long as the Rydberg wave functions do not overlap and electron 1 is always closer to core A than to core B and vice versa. Note that for the calculation of Rydberg-Rydberg bound states one would have to take into account the full Hamiltonian (2.3).

Van der Waals interactions

In the total Hamiltonian (2.3) the interaction Hamiltonian $H_{\text{int}} \simeq H_{dd}$ can be treated as a perturbation. Assuming that the atomic Rydberg states (eigenstates of $H_{A,B}$) are known, the level shift of a given product state $|ns, ns\rangle$ can be calculated. If there is no degeneracy, the first and second order energy shifts are

$$E_i^{(1)} = \langle i|\, H_{dd}\, |i\rangle\,, \tag{2.6a}$$

$$E_i^{(2)} = \sum_{k\neq i} \frac{|\langle i|\, H_{dd}\, |k\rangle|^2}{E_i^{(0)} - E_k^{(0)}}\,. \tag{2.6b}$$

As the diagonal element $\langle ns, ns| H_{dd} |ns, ns\rangle$ vanishes due to parity, the first order term is zero. In the second order term, a sum over all possible pair states has to be carried out. However, in the case of $|i\rangle = |ns, ns\rangle$, the dominating contribution comes from the energetically close $|(n-1)p, np\rangle$ states with $\Delta E = 2E_{ns} - (E_{(n-1)p} + E_{np})$. All other states are energetically far away as illustrated in Fig. 2.2(b). Thus, the leading order energy shift becomes

$$E^{(2)}_{ns,ns} = \sum_{m,m'} \frac{|\langle ns, ns| H_{dd} |(n-1)p_m, np_{m'}\rangle|^2}{\Delta E} = \frac{\mathcal{D}_\varphi (\mu_1\mu_2/R^3)^2}{\Delta E} = \frac{\hbar C_6}{R^6} \tag{2.7}$$

where the $\mu_i = \langle P_{ns}| er |P_{n_i p}\rangle$, $n_i \in \{n, n-1\}$, with the radial wave functions $|P_{nl}\rangle$, and $\mathcal{D}_\varphi$ is the angular part that depends on the Zeeman sublevels of the perturbing state. In the second expression of Eq. (2.7) we sum over the Zeeman sublevels m, m' of the state $|(n-1)p, np\rangle$. The interaction coefficient C_6 appearing in Eq. (2.7) is defined as

$$C_6 = \frac{(\mu_1\mu_2)^2}{\hbar \Delta E} \mathcal{D}_\varphi \,. \tag{2.8}$$

The sign of C_6 depends on the sign of ΔE. For $|ns, ns\rangle$ interactions in ^{87}Rb with $n < 235$ [57, 62], and in particular in all cases discussed in this thesis, one finds $\Delta E > 0$ and thus *repulsive* van der Waals interactions. Substituting the scalings of μ_i and ΔE from Tab. 2.1, the scaling $C_6 \propto n^{11}$ is obtained, which means that extremely large C_6 coefficients arise for large n. Note that in Ref. [62] the Förster defect ΔE is defined with opposite sign.

Of course, the interaction also leads to an admixture of the $|(n-1)p, np\rangle$ states to the $|ns, ns\rangle$ state. However, in the following, this admixture is assumed to be small and, for the calculation of the atom-light interaction it is neglected. In Chap. 4 the validity of this approximation (three-level approximation) will have to be questioned. The reason is that in the above calculation, the fine structure was neglected. Taking into account the electron spin, the ns-level ($j = 1/2$) splits into two degenerate Zeeman sublevels. Taking this degeneracy into account in the second order perturbation theory, the different Zeeman levels of $|ns, ns\rangle$ become mixed [62]. The experimental results presented in Sec. 4.3 will show that, if only one Zeeman component is laser excited, the van der Waals interaction leads to a population transfer to the other Zeeman sublevels [60, 103, 111, 191].

Figure 2.3 shows the result of a numerical diagonalization of the full Hamiltonian (2.3) for energies around the $\left|45s_{1/2}, 45s_{1/2}\right\rangle$ level of ^{87}Rb. It is obvious that the state $\left|44p_{3/2}, 45p_{3/2}\right\rangle$ is not the only one energetically close to $\left|45s_{1/2}, 45s_{1/2}\right\rangle$. However, the nearby $\left|44s_{1/2}, 47f_{7/2}\right\rangle$ state is not dipole coupled with $\left|45s_{1/2}, 45s_{1/2}\right\rangle$ and therefore they only mix very weakly and suffer a narrow avoided crossing at $R \approx 1.1\,\mu$m. We thus find that our above assumption of a two-state picture is justified since the $\left|45s_{1/2}, 45s_{1/2}\right\rangle$ potential is dominated by the repulsion from $\left|44p_{3/2}, 45p_{3/2}\right\rangle$. For internuclear distances smaller than $1\,\mu$m a tangle of states is encountered. Here, already the description of the interactions by the dipole-dipole Hamiltonian (2.5) is not adequate any more. The inset shows that the potential curve coincides well with a van der Waals potential for $R \gtrsim 1.5\,\mu$m. The fitted interaction coefficient was $C_6/2\pi = 4.35\,\mathrm{GHz}\,\mu\mathrm{m}^6$. Recently, Rydberg-Rydberg interaction potentials could be measured by observing Rabi oscillations of two interacting atoms [63].

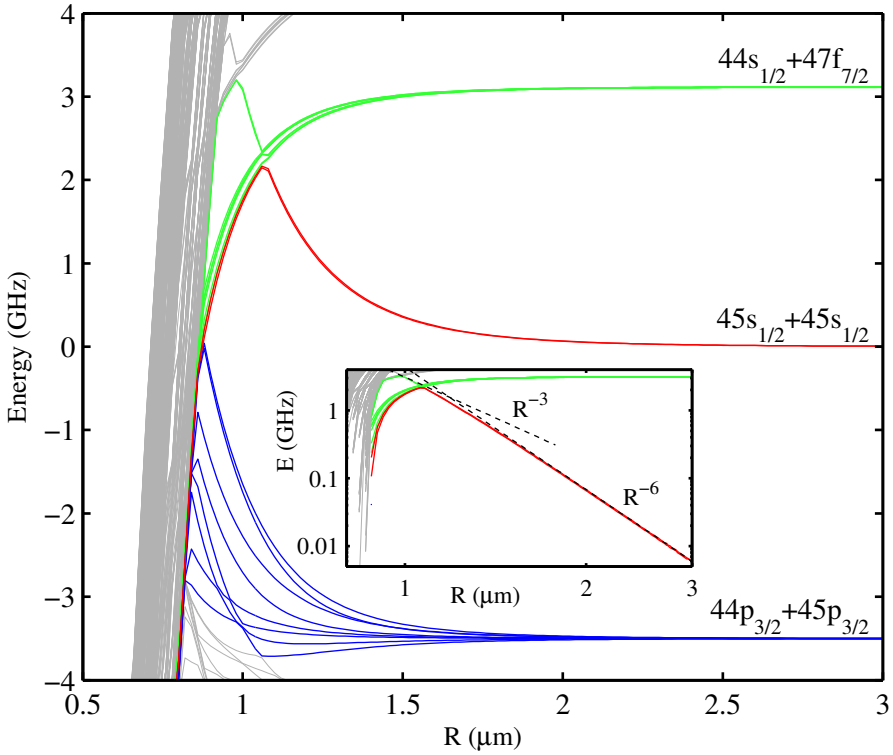

Figure 2.3: Potential energies of rubidium around $|45s_{1/2}, 45s_{1/2}\rangle$ [81]. The inset shows a double logarithmic plot illustrating the van der Waals behavior in a large range of internuclear distances, and the R^{-3} behavior at short distances. We thank L. Marcassa for providing the data for this figure.

Permanent dipoles and Förster regime

In the presence of an external static electric field or a microwave field coupling adjacent s- and p-states, the spatial isotropy is broken and the atoms acquire permanent dipole moments. In this case the atomic s- and p-levels are mixed which means that the first order energy correction in Eq. (2.6a) does not vanish. The resulting interaction potential $V(R) \propto R^{-3}$ is then anisotropic. This case has been studied in Refs. [55,58,82,83,85,277] for E-field induced dipoles and in Refs. [84,130,137,251,278] for microwave dressing.

A second case, in which a R^{-3} potential arises, is what is called a Förster resonance. It occurs when two pair states, e.g., $|ns, ns\rangle$ and $|(n-1)p, np\rangle$, are (near) degenerate. Then, perturbation theory for degenerate states has to be applied. This means that we have to diagonalize H in the basis of degenerate levels. The resulting matrix

$$H = \begin{pmatrix} 0 & \frac{C_3}{R^3}\sqrt{\mathcal{D}_\varphi} \\ \frac{C_3}{R^3}\sqrt{\mathcal{D}_\varphi} & -\Delta E \end{pmatrix} \tag{2.9}$$

with $C_3 = \mu_1\mu_2$ [22] can be diagonalized to give the eigenenergies

$$V_\pm(R) = -\frac{\Delta E}{2} \pm \frac{1}{2}\sqrt{\Delta E^2 + 4\frac{C_3^2}{R^6}\mathcal{D}_\varphi}\,. \tag{2.10}$$

For $\Delta E > 0$ the potential $V_+(R)$ is connected to the $|ns, ns\rangle$-state. In the limit of $\Delta E \gg 2C_3/R^3$ the van der Waals case is recovered, while in the opposite limit $V_+(R) \approx C_3/R^3$. In this limit the interaction eigenstates are (anti)symmetric superpositions of the bare product states. The critical radius at which one expects the van der Waals potential to turn into a R^{-3}-potential is $R_c = (2C_3/\Delta E)^{1/3}$. The inset of Fig. 2.3 shows that the $|45s, 45s\rangle$ potential indeed approaches a R^{-3} behavior at small R.

2.3 Laser excitation of Rydberg atoms

In this section the Hamiltonian describing the interaction of a single three-level atom with a two-mode classical light field is derived. It is shown how the intermediate state can be adiabatically eliminated in the case of large single-photon detuning. Also, the master equation description, taking into account spontaneous decay and dephasing caused by finite laser line width, is introduced. We mainly follow Refs. [271, 272] in our presentation.

Single atom in a laser field

The Hamiltonian describing a single atom interacting with an electric field is

$$H = H_0 + H_L \,, \tag{2.11}$$

where H_0 denotes the atomic Hamiltonian, and $H_L = -e\mathbf{r}\cdot\mathbf{E}(\mathbf{r_0}, t)$ the atom-field interaction in dipole approximation [271]. The two driving lasers are described by the two-component field

$$\mathbf{E}(\mathbf{r_0}, t) = \boldsymbol{\mathcal{E}}_p \cos(\omega_p t) + \boldsymbol{\mathcal{E}}_c \cos(\omega_c t) \,. \tag{2.12}$$

We assume that the two field components are near resonant with the transitions from $|g\rangle$ to $|e\rangle$ (probe laser) and from $|e\rangle$ to $|r\rangle$ (coupling laser), respectively, as sketched in Fig. 2.4, but not resonant with any other atomic transition. Under these conditions a three-level description can be adopted. Defining $s_{ab} = |a\rangle\langle b|$, the atomic Hamiltonian can be written as

$$H_0 = E_g s_{gg} + E_e s_{ee} + E_r s_{rr} \,. \tag{2.13}$$

The atom-field interaction becomes

$$H_L = \hbar(\Omega_p s_{eg} + \Omega_p^* s_{ge})\cos(\omega_p t) + \hbar(\Omega_c s_{re} + \Omega_c^* s_{er})\cos(\omega_c t) \,, \tag{2.14}$$

where the Rabi frequencies are defined as

$$\Omega_p = -\frac{\boldsymbol{\mu}_{eg}\cdot\boldsymbol{\mathcal{E}}_p}{\hbar} \,, \tag{2.15a}$$

$$\Omega_c = -\frac{\boldsymbol{\mu}_{re}\cdot\boldsymbol{\mathcal{E}}_c}{\hbar} \,. \tag{2.15b}$$

Here, $\boldsymbol{\mu}_{ab} = \boldsymbol{\mu}_{ba}^* = \langle a|\, e\mathbf{r}\,|b\rangle$ are the dipole matrix elements. In the following $\hbar$ is set to unity for convenience.

In order to eliminate the explicit time dependence from the Hamiltonian, we perform a

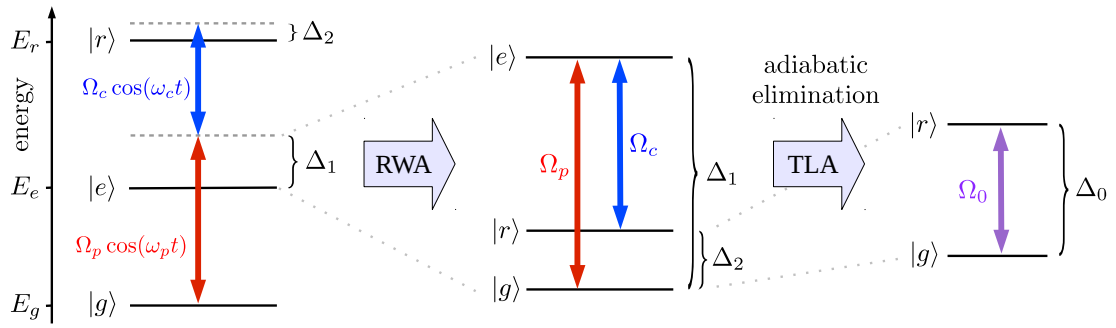

Figure 2.4: Level scheme of a three-level atom. Rabi frequencies, laser detunings, and decay rates are shown. The effect of the rotating wave approximation and the adiabatic elimination of the intermediate level (two-level approximation, TLA) on the diagonal elements of the Hamiltonian is illustrated.

unitary transformation to a frame rotating with the laser:

$$|\psi(t)\rangle \to \left|\psi'(t)\right\rangle = U(t)\,|\psi(t)\rangle \tag{2.16}$$

with the unitary transformation $U(t)$ which is explicitly given as

$$U(t) = e^{iE_g t}\left(s_{gg} + e^{i\omega_p t}s_{ee} + e^{i(\omega_p+\omega_c)t}s_{rr}\right) . \tag{2.17}$$

Evaluating the time derivative of $|\psi'(t)\rangle$ using that $|\psi(t)\rangle$ obeys the time dependent Schrödinger equation, one obtains

$$\begin{aligned} i\partial_t\left|\psi'(t)\right\rangle &= i\partial_t U(t)\,|\psi(t)\rangle \\ &= i\left[\partial_t U(t)\right]|\psi(t)\rangle + iU(t)\partial_t\,|\psi(t)\rangle \\ &= \left[i\partial_t U(t) + U(t)H\right]|\psi(t)\rangle \\ &= \left\{i\left[\partial_t U(t)\right]U^\dagger(t) + U(t)HU^\dagger(t)\right\}\left|\psi'(t)\right\rangle . \end{aligned} \tag{2.18}$$

Thus, the transformed Hamiltonian, governing the time evolution of $|\psi'(t)\rangle$, is

$$\begin{aligned} H_{\rm rot} &= U(t)HU^\dagger(t) + i\left[\partial_t U(t)\right]U^\dagger(t) \\ &= H_0 + U(t)H_L U^\dagger(t) - E_g\mathbb{1} - \omega_p s_{ee} - (\omega_p+\omega_c)s_{rr} . \end{aligned} \tag{2.19}$$

The second term in this expression results in

$$U(t)H_L U^\dagger(t) = \frac{1}{2}\left[\Omega_p\left(1+e^{2i\omega_p t}\right)s_{eg} + \Omega_c\left(1+e^{2i\omega_c t}\right)s_{re} + \text{h.c.}\right] , \tag{2.20}$$

where 'h.c.' denotes the hermitian conjugate. The *rotating wave approximation* (RWA) now consists in dropping the fast rotating terms $e^{2i\omega_i t}$. This is justified since the Rabi frequencies Ω_i that govern the dynamics of the population transfer between the levels are much smaller than the transition frequencies ω_i. Therefore, $H_{\rm rot}$ is time averaged over a period $\omega_i^{-1} \ll T \ll \Omega_i^{-1}$, which lets the exponentials vanish. This coarse graining of the time

evolution does not affect the slow dynamics. Typically $\omega_i \sim 10^9\,\mathrm{MHz}$, and $\Omega_i \sim 1\,\mathrm{MHz}$, so this approximation is well justified for our system.

Thus, the final Hamiltonian is

$$H_{\mathrm{RWA}} = \langle H_{\mathrm{rot}} \rangle_T = -\Delta_1 s_{ee} - \Delta_2 s_{rr} + \frac{1}{2}\left(\Omega_p s_{eg} + \Omega_c s_{re} + \mathrm{h.c.}\right) , \tag{2.21}$$

where Δ_i denote the one- and two-photon detunings defined as

$$\Delta_1 = \omega_p - (E_m - E_g) , \tag{2.22a}$$
$$\Delta_2 = \omega_p + \omega_c - (E_r - E_g) . \tag{2.22b}$$

In matrix notation, the final Hamiltonian reads

$$H_{\mathrm{RWA}} = \begin{pmatrix} 0 & \Omega_p^*/2 & 0 \\ \Omega_p/2 & -\Delta_1 & \Omega_c^*/2 \\ 0 & \Omega_c/2 & -\Delta_2 \end{pmatrix} . \tag{2.23}$$

An additional approximation, that has been made tacitly, is the classical treatment of the light field. In many experiments (see Chap. 4) extremely weak probe intensities are used, such that only a few photons are present in the atomic medium at a time. In such a setup, which is designed to observe quantum features of the light field (e.g., single-photon sources), of course, the semi-classical description employed here will break down.

The Rabi frequencies $\Omega_{p,c} = |\Omega_{p,c}| e^{i\varphi_{p,c}}$ are in general complex. However, the constant phases φ_p, φ_c can simply be absorbed into the states $|m\rangle$ and $|r\rangle$ by applying the unitary transformation

$$U_\varphi = e^{-i\varphi_p} |m\rangle \langle m| + e^{-i\varphi_c} |r\rangle \langle r| . \tag{2.24}$$

In the description of an ensemble of atoms, the phases $\varphi_p^{(i)}, \varphi_c^{(i)}$ associated with the ith atom will depend on the position of the atom: $\varphi_{p,c}^{(i)} = \mathbf{k}_{p,c} \cdot \mathbf{R}_i$. However, as long as the atoms can be treated as independent with respect to the atom-light interactions, the phases can still be transformed away. We will therefore assume real Rabi frequencies in the following. A discussion of the validity of the assumption of independent atoms can be found in Sec. 4.1.

Elimination of the intermediate level

In the following we show how an effective two-level description can be obtained by adiabatic elimination of the intermediate level $|e\rangle$ (*two-level approximation*, TLA). This is possible if the intermediate state is far off-resonant ($|\Delta_1| \gg |\Delta_2|, |\Omega_p|, |\Omega_c|$). In this case, the states $|g\rangle$ and $|r\rangle$ are nearly degenerate in the rotating frame, while $|e\rangle$ is comparably far detuned, see Fig. 2.4. As a consequence, the laser driving will lead to direct excitation from $|g\rangle$ to $|r\rangle$ without significantly populating the intermediate state. The formal procedure we use to obtain an effective Hamiltonian describing the dynamics in the subspace spanned by $|g\rangle$ and $|r\rangle$ is called *quasi degenerate perturbation theory*. More precisely, we employ the *canonical van-Vleck formalism* as described in Ref. [279].

The basic idea is to find a unitary transformation S that transforms the Hamiltonian into a block-diagonal form, where the couplings between the quasi-degenerate subspace and its

complement vanish. Splitting the Hamiltonian into a diagonal part and a part containing the unwanted couplings between the subspaces

$$H = H_0 + V \tag{2.25}$$

we get

$$H \to H_{ad} = SHS^\dagger = H_0 + W\,. \tag{2.26}$$

In the van-Vleck formalism W is now calculated as a power series, where the small parameters are the ratios of the off-diagonal couplings to the block-diagonal ones.

Applying this to the Hamiltonian (2.23), one obtains

$$H_0 = \begin{pmatrix} 0 & 0 & 0 \\ 0 & -\Delta_2 & 0 \\ 0 & 0 & -\Delta_1 \end{pmatrix} \quad \text{and} \quad V = \frac{1}{2}\begin{pmatrix} 0 & 0 & \Omega_p \\ 0 & 0 & \Omega_c \\ \Omega_p & \Omega_c & 0 \end{pmatrix}\,, \tag{2.27}$$

where we have rearranged the basis to $\{|g\rangle, |r\rangle, |e\rangle\}$, anticipating the block-diagonal form. With this, the transformed matrix W to lowest order (Eq. (2.2.69) in Ref. [272]) is obtained:

$$W = \begin{pmatrix} 2\frac{\Omega_p^2}{\Delta_1} & \Omega_p\Omega_c\left(\frac{1}{\Delta_1} + \frac{1}{\Delta_1-\Delta_2}\right) & 0 \\ \Omega_p\Omega_c\left(\frac{1}{\Delta_1} + \frac{1}{\Delta_1-\Delta_2}\right) & 2\frac{\Omega_c^2}{\Delta_1-\Delta_2} & 0 \\ 0 & 0 & -2\left(\frac{\Omega_p^2}{\Delta_1} + \frac{\Omega_c^2}{\Delta_1-\Delta_2}\right) \end{pmatrix}\,. \tag{2.28}$$

The transformed Hamiltonian therefore reads

$$H_{ad} = H_0 + W = \begin{pmatrix} 0 & 0 & 0 \\ 0 & -\Delta_2 & 0 \\ 0 & 0 & -\Delta_1 \end{pmatrix} + \begin{pmatrix} \delta_g & \Omega_0/2 & 0 \\ \Omega_0/2 & \delta_r & 0 \\ 0 & 0 & \delta_e \end{pmatrix} \tag{2.29}$$

with the definitions ($\epsilon = \Delta_2/\Delta_1$)

$$\delta_g = \frac{\Omega_p^2}{4\Delta_1}\,, \tag{2.30a}$$

$$\delta_r = \frac{\Omega_c^2}{4(\Delta_1-\Delta_2)} = \frac{4\Omega_c^2}{\Delta_1}\left[1 + \mathcal{O}(\epsilon)\right]\,, \tag{2.30b}$$

$$\delta_e = -\left(\frac{\Omega_p^2}{4\Delta_1} + \frac{\Omega_c^2}{4(\Delta_1-\Delta_2)}\right) = -\frac{\Omega_p^2+\Omega_c^2}{4\Delta_1}\left[1 + \mathcal{O}(\epsilon)\right]\,, \tag{2.30c}$$

$$\Omega_0 = \frac{\Omega_p\Omega_c}{4}\left(\frac{1}{\Delta_1} + \frac{1}{\Delta_1-\Delta_2}\right) = \frac{\Omega_p\Omega_c}{2\Delta_1}\left[1 + \mathcal{O}(\epsilon)\right]\,. \tag{2.30d}$$

The upper block, describing the effective two-level system, becomes

$$H_{ad}^{[1]} = \begin{pmatrix} 0 & \Omega_0/2 \\ \Omega_0/2 & -\Delta_0 \end{pmatrix} + \begin{pmatrix} \delta_g & 0 \\ 0 & \delta_g \end{pmatrix}\,, \tag{2.31}$$

where we have defined the effective detuning $\Delta_0 = \Delta_2 - \delta_r + \delta_g$. The second term is just an

overall energy shift, which can be dropped. This leads to the final Hamiltonian

$$H_{\text{final}} = \begin{pmatrix} 0 & \Omega_0/2 \\ \Omega_0/2 & -\Delta_0 \end{pmatrix} \tag{2.32}$$

with the effective Rabi frequency and detuning

$$\Omega_0 = \frac{\Omega_p \Omega_c}{2\Delta_1}\,, \tag{2.33a}$$

$$\Delta_0 = \Delta_2 + \frac{\Omega_p^2 - \Omega_c^2}{\Delta_1}\,. \tag{2.33b}$$

An alternative way to obtain the effective Hamiltonian (2.32) is the following [280,281]: We write down the Schrödinger equation in terms of the coefficients c_a in $|\psi\rangle = c_g\,|g\rangle + c_r\,|r\rangle + c_e\,|e\rangle$, which reads

$$i\dot{c}_g = \frac{1}{2}\Omega_p c_e\,, \tag{2.34a}$$

$$i\dot{c}_r = \frac{1}{2}\Omega_c c_r - \Delta_2 c_r\,, \tag{2.34b}$$

$$i\dot{c}_e = \frac{1}{2}\Omega_p c_g + \frac{1}{2}\Omega_c c_r - \Delta_1 c_e\,. \tag{2.34c}$$

Recognizing that the last term in Eq. (2.34c) causes c_e to oscillate rapidly compared to the timescale on which the other amplitudes change, we can take another time average under which leading to $\dot{c}_e = 0$. Solving this for c_e, we get

$$c_e = \frac{\Omega_p c_g + \Omega_c c_r}{2\Delta_1} \tag{2.35}$$

which can be substituted back into Eq. (2.34) to recover the result $i\partial_t\,|\psi\rangle = H_{\text{final}}\,|\psi\rangle$ with the Hamiltonian from Eq. (2.32).

Including dissipation

An isolated physical system is described completely by the state vector $|\psi\rangle$ and its dynamics is governed by the Schrödinger equation

$$i\hbar\partial_t\,|\psi\rangle = H\,|\psi\rangle\ . \tag{2.36}$$

Any observable is represented by a Hermitian operator O and its expectation value can be calculated as

$$\langle O\rangle = \langle\psi|\,O\,|\psi\rangle\ . \tag{2.37}$$

In many situations, however, the system we want to describe, will not be isolated from the environment, but coupled to an infinite bath. In this case the quantum state of the system is in general unknown. It is only know that the system is in state $|\psi\rangle$ with a certain (classical) probability P_ψ. In this case, in order to calculate the expectation value, we have to sum over

all possible realizations $|\psi\rangle$ of the system weighted with their respective probabilities:

$$\langle O\rangle = \sum_{\psi} P_{\psi} \langle\psi| O |\psi\rangle = \mathrm{Tr}[O\rho]\,, \tag{2.38}$$

where we have defined the density operator

$$\rho = \sum_{\psi} P_{\psi} |\psi\rangle \langle\psi| \ . \tag{2.39}$$

More formally, one would start with the quantum state of the total system (system and bath) $|\Psi_{\mathrm{tot}}\rangle$ and define the density operator of the system $\rho_{\mathrm{tot}} = |\Psi_{\mathrm{tot}}\rangle \langle\Psi_{\mathrm{tot}}|$. The density operator of the system we are interested in is then obtained by taking the trace over the bath degrees of freedom [271, 282].

The coherent time evolution of the density operator can immediately be derived from the Schrödinger equation

$$\begin{aligned} \partial_t \rho &= \sum_{\psi} P_{\psi} \left[(\partial_t |\psi\rangle) \langle\psi| + |\psi\rangle (\partial_t \langle\psi|) \right] \\ &= -\frac{i}{\hbar} \sum_{\psi} P_{\psi} \left(H |\psi\rangle \langle\psi| + |\psi\rangle \langle\psi| H \right) \\ &= -\frac{i}{\hbar} [H, \rho]\,, \end{aligned} \tag{2.40}$$

which is called the *Von Neumann equation*. The trace of ρ always equals unity since the probability distribution P_{ψ} is normalized. If it is possible to write the density operator as $\rho = |\psi\rangle \langle\psi|$, we call ρ a pure state, which is equivalent to the requirement $\mathrm{Tr}[\rho^2] = 1$. Otherwise the system is in a mixed state. For a three-level atom, it is natural to write the density operator in the basis $\{|g\rangle, |e\rangle, |r\rangle\}$. The density matrix elements

$$\rho_{ab} = \langle a| \rho |b\rangle \tag{2.41}$$

are called populations for $a = b$ (diagonal elements) and coherences for $a \neq b$ (off-diagonal elements), since the probability to find the atom in state $|a\rangle$ is

$$\langle s_{aa}\rangle = \mathrm{Tr}[s_{aa}\rho] = \rho_{aa}\,. \tag{2.42}$$

What makes a density matrix description necessary in an atomic multilevel system, is the first of all the spontaneous decay from excited levels that is induced by coupling to the bath of vacuum electric field modes. Since we work in a semi-classical framework of atom-light interactions, we trace over the bath of vacuum field modes [271]. The resulting time evolution in terms of the atomic levels is nonunitary and leads to the evolution of an initially pure state into a mixed state. In order to include spontaneous emission, a *Lindblad term* can be added to the Von Neumann equation. Such a term preserves the trace of ρ and has the otherwise quite general form [283]

$$\mathcal{L}_{\alpha\beta}[\rho] = C_{\alpha\beta}\rho C_{\alpha\beta}^{\dagger} - \frac{1}{2}\left(C_{\alpha\beta}^{\dagger} C_{\alpha\beta}\rho + \rho C_{\alpha\beta}^{\dagger} C_{\alpha\beta} \right)\,. \tag{2.43}$$

The derivation of the Lindblad term involves the *Born approximation* (the bath is not affected by changes in the system) and the *Markov approximation* (reservoir correlation time is much smaller than the typical time scales of the system). A detailed discussion of this derivation can be found in Refs. [282, 284]. In the case of spontaneous emission from a level $|a\rangle$ to $|b\rangle$, the projector $C_{\alpha\beta}$ reads

$$C_{\alpha\beta} = C_{ab} = \sqrt{\gamma_{ab}} s_{ab} = \sqrt{\gamma_{ab}} \, |a\rangle \langle b| \tag{2.44}$$

with the spontaneous decay rate $\gamma_{ab} = \tau_a^{-1}$ that equals the natural line width of state $|a\rangle$. τ_a is the life time of the state. Such a term leads to a population transfer from state $|a\rangle$ to $|b\rangle$ and to a decay of the coherence ρ_{ab} between the two states.

An additional source of decoherence is the finite laser line width. We assumed initially that each laser field only consists of a single field mode. The fact that a realistic laser field possesses an approximately Lorentzian line profile of finite width leads to an additional decay of the coherences. The line width of the laser driving a transition from $|a\rangle$ to $|b\rangle$ can be taken into account by the additional term [266, 285]

$$\mathcal{L}_{ab}^{d}[\rho] = -\frac{\Gamma_{ab}}{2} \left(s_{aa} \rho s_{bb} + s_{bb} \rho s_{aa} \right) \tag{2.45}$$

where Γ_{ab} is the full width of the spectral laser profile. This term just leads to a decay of the coherence ρ_{ab}. In the three-level system, the probe laser has a bandwidth Γ_p, leading to a dephasing $\Gamma_{ge} = \Gamma_p$, and the coupling laser bandwidth makes a dephasing $\Gamma_{er} = \Gamma_c$. In the case of independent lasers, the dephasing of the coherence between $|g\rangle$ to $|r\rangle$ is just the sum of the two laser line widths $\Gamma_{gr} = \Gamma_p + \Gamma_c$. The super-operator $\mathcal{L}_{ab}^{d}[\cdot]$ does not have Lindblad form, but it can be expressed as a sum of Lindblad terms

$$\mathcal{L}_{ab}^{d}[\rho] = \frac{1}{2} \left(\mathcal{L}_{aa}[\rho] + \mathcal{L}_{bb}[\rho] - \mathcal{L}_{cc}[\rho] \right) \tag{2.46}$$

with $\gamma_{aa} = \gamma_{bb} = \gamma_{cc} = \Gamma_{ab}$, where (a, b, c) are permutations of (g, e, r). This is important for the applicability of the Monte Carlo wave function method, that will be introduced Chap. 3.

The resulting *master equation* describing a laser driven three-level atom including spontaneous decay from the Rydberg and intermediate level as well as laser line widths is

$$\begin{aligned} \partial_t \rho &= -\frac{i}{\hbar} [H_{\mathrm{RWA}}, \rho] + \mathcal{L}[\rho] \\ &= -\frac{i}{\hbar} [H_{\mathrm{RWA}}, \rho] + \mathcal{L}_{eg}[\rho] + \mathcal{L}_{re}[\rho] + \mathcal{L}_{ge}^{d}[\rho] + \mathcal{L}_{er}^{d}[\rho] + \mathcal{L}_{gr}^{d}[\rho] \end{aligned} \tag{2.47}$$

In the case of far off-resonant intermediate state, in which one can reduce the coherent dynamics to an effective two-level system, spontaneous decay is very small, since the Rydberg state is long-lived as was shown in Sec. 2.1. Laser dephasing might still be present and can be included phenomenologically analogous to the three-level case. It shall be noted, however, that the adiabatic elimination of the intermediate level in the density matrix formalism, is not straight froward and in general the effective master equation will not have Lindblad form.

2.4 Ensembles of ultracold Rydberg atoms

So far, we have shown only the single-atom Hamiltonian for atom-laser interaction and derived the binary interaction potentials between Rydberg atoms. In this section we will write down the equations governing the many-body dynamics of an ensemble of motionally frozen atoms, which will be our working equations in Chaps. 3 and 4, respectively. In the second part we describe the typical setup of an ultracold gas of alkali atoms laser excited to a Rydberg state. We revisit all the approximations that have been made in the course of this chapter and compare the relevant energy and length scales. All parameters given in this section refer to an experiment carried out in the group of M. Weidemüller [286].

Many-body quantum dynamics in a frozen gas

The general Hamiltonian describing an ensemble of N interacting atoms is

$$H_{\text{tot}} = \sum_{i=1}^{N} \left(H_{cm}^{(i)} + H_0^{(i)} + H_L^{(i)} \right) + \sum_{i<j} H_{\text{int}}^{(ij)} , \tag{2.48}$$

where $H_{cm}^{(i)}$ describes the center of mass motion of atom i, possibly in an external potential, $H_0^{(i)} + H_L^{(i)}$ is the internal atomic Hamiltonian and the atom-light interaction discussed in Sec. 2.3, and $H_{\text{int}}^{(ij)}$ accounts for the interactions between the Rydberg states of the atoms introduced in Sec. 2.2. In an ultracold gas the kinetic energy of the atoms will be negligibly small and the distances ΔR they travel during the time of a typical experiment are small compared to the interatomic distances. Also the Rydberg-Rydberg interaction potential $V(R)$ around the characteristic distances between the Rydberg atoms changes little (e.g., compared to Ω) if R it is varied by ΔR. Therefore, we can neglect $H_{cm}^{(i)}$ and assume that the atoms are fixed in space over the time of our simulation, i.e., that the interatomic distances $R_{ij} = |\mathbf{R}_i - \mathbf{R}_j|$ are constant parameters. This is the so called *frozen gas approximation*. Its validity will be discussed in detail in Chap. 4. In addition, we assume that the local phases of the of light field can be absorbed in the state vectors and the interaction of any atom with the laser field is independent from the other atoms as already mentioned in Sec. 2.3.

Combining this with the results of the previous sections we obtain the following many-body Hamiltonian for the case of two-level atoms

$$\begin{aligned} H_{2L} &= \sum_{i=1}^{N} H_{\text{final}}^{(i)} + \sum_{i<j} H_{\text{int}}^{(ij)} \\ &= \sum_{i=1}^{N} \left[-\Delta_0 s_{rr}^{(i)} + \frac{\Omega_0}{2} (s_{gr}^{(i)} + s_{rg}^{(i)}) \right] + \sum_{i<j} \frac{C_6}{R_{ij}^6} s_{rr}^{(i)} \otimes s_{rr}^{(j)} . \end{aligned} \tag{2.49}$$

Since there is only one detuning and Rabi frequency in the two-level case, we will drop the index 0. In general, the laser parameters can be time dependent and the laser intensity can vary spatially. The resulting Schrödinger equation, the solution of which Chap. 3 deals with,

is

$$i\partial_t |\psi\rangle = \left[\sum_{i=1}^{N}\left(-\Delta s_{rr}^{(i)} + \Omega^{(i)}\sigma_x^{(i)}\right) + \sum_{i<j}\frac{C_6}{R_{ij}^6}s_{rr}^{(i)}\otimes s_{rr}^{(j)}\right]|\psi\rangle\ , \tag{2.50}$$

where $\sigma_x^{(i)} = (s_{rg}^{(i)} + s_{gr}^{(i)})/2$ and $|\psi\rangle$ is the many-body wave function.

Chapter 4 is dedicated to the case of resonant two-step excitation. In this case including decoherence is crucial due to the fast spontaneous decay from the intermediate level $|e\rangle$. This makes a master equation treatment necessary. The full many-body Hamiltonian, in analogy to Eq. (2.49), is

$$\begin{aligned} H_{3L} &= \sum_{i=1}^{N} H_{\mathrm{RWA}}^{(i)} + \sum_{i<j} H_{\mathrm{int}}^{(ij)} \\ &= \sum_{i=1}^{N}\left[-\Delta_1 s_{ee}^{(i)} - \Delta_2 s_{rr}^{(i)} + \left(\frac{\Omega_p^{(i)}}{2}s_{ge}^{(i)} + \frac{\Omega_c^{(i)}}{2}s_{er}^{(i)} + \mathrm{h.c.}\right)\right] + \sum_{i<j}\frac{C_6}{R_{ij}^6}s_{rr}^{(i)}\otimes s_{rr}^{(j)}\,. \end{aligned} \tag{2.51}$$

The resulting many-body master equation reads

$$\partial_t\rho = -i\,[H_{3L},\rho] + \sum_{i=1}^{N}\mathcal{L}^{(i)}[\rho]\,. \tag{2.52}$$

Developing methods to solve this equation is the subject of Chap. 4.

Typical parameters and scales

In the experiments which we refer to in the following chapters [38, 43, 286, 287] ^{87}Rb atoms are trapped in an optical dipole trap at temperatures of a few μK and at densities of typically 10^9-$10^{12}\,\mathrm{cm}^{-3}$. These atoms are then excited from the $|5s\rangle$ ground state to the $|55s\rangle$ Rydberg state via the intermediate state $|5p\rangle$. In such a setup various energy and length scales arise. In the following, all energies will be given in units of MHz ($\hbar = 1$).

The ground-state binding energy as well as the transition energies between ground state and (Rydberg-) excited state are on the order 1 eV or 10^9 MHz. As the typical Rabi frequencies that can be reached are

$$\Omega_{p,c} \sim 0.1 - 10\,\mathrm{MHz} \tag{2.53}$$

the rotating wave approximation is well justified in our system. We have seen that the Förster defect ΔE, which is in any case smaller than the typical level spacings, is on the order of

$$\Delta E \sim 10^3\,\mathrm{MHz} \tag{2.54}$$

for a $|55s\rangle$ state, which is much larger than the Rabi frequencies and the typical laser line widths

$$\Gamma \sim 0.1 - 1\,\mathrm{MHz}\,. \tag{2.55}$$

Therefore, Rydberg states can usually be treated as isolated form other atomic levels. Note that in the case of s-states there is only one fine structure component, so the fine-structure

splitting is not an issue, and the Zeeman sublevels $m = \pm 1/2$ can be selected by the laser polarizations. Going to higher lying Rydberg states, this changes and extremely narrow banded lasers are required to address a specific Rydberg state [288]. Rydberg state lifetimes are $\tau \sim 100\,\mu$s for $n \approx 55$, corresponding to line widths of

$$\gamma \sim 0.01\,\text{MHz}\,, \tag{2.56}$$

which is much larger than the typical experimental time scale of $1\,\mu$s. Also, at $T = 5\,\mu$K the Doppler width is on the order of

$$\Delta\omega_{\text{doppler}} \sim 0.01\,\text{MHz} \tag{2.57}$$

and thus negligible. With a detuning $\Delta_1 \sim 100\,\text{MHz}$ from the intermediate state, the effective two-level Rabi frequency becomes

$$\Omega_0 \sim 0.1 - 1\,\text{MHz}\,, \tag{2.58}$$

which is comparable to the laser line width, so decoherence due to laser dephasing will usually not be negligible. Smaller line widths and higher intensities (larger Rabi frequencies) have been achieved in recent experiments [48, 248]. For very high principal quantum numbers ($n \gtrsim 100$), the line width is limited by the electric field control due to the huge polarizabilities of the Rydberg atoms [288].

In a cloud of ultracold atoms several characteristic length scales arise: The orbital radius for a $|55s\rangle$ state is

$$r_a \sim 0.1\,\mu\text{m} \tag{2.59}$$

but can be much larger for higher principal quantum numbers [288]. For densities $n_0 \lesssim 10^{13}\,\text{cm}^{-3}$ this radius is much smaller than the mean interparticle distance (Wigner-Seitz radius)

$$r_s \sim n_0^{-1/3} \sim 1\,\mu\text{m}\,. \tag{2.60}$$

If the r_a exceeds r_s a regime is entered where our description of the Rydberg-Rydberg interaction breaks down, and additional decoherence occurs due to scattering of the Rydberg electron off the ground-state atoms [288]. Our description of the atom-light interactions requires that the wave lengths of the excitation lasers

$$\lambda_p = 780\,\text{nm}\,, \tag{2.61a}$$

$$\lambda_c = 480\,\text{nm} \tag{2.61b}$$

are smaller than the mean interparticle spacing. If the volume λ^3 contains several particles, collective effects will arise that are not included in a description that treats the atoms as interacting with the light field independently from each other [289, 290]. A further crucial length scale is the blockade radius R_b that we define as the minimal distance at which two Rydberg atoms can be excited simultaneously for given interaction strength and laser parameters. It is typically

$$R_b \sim 5\,\mu\text{m} \tag{2.62}$$

for the parameters of Ref. [38]. By varying the atomic density, we can observe the transition

from the noninteracting ($r_s \gg R_b$) to the strongly interacting regime $r_s \ll R_b$.

At $T = 5\,\mu$K the mean velocity of the particles is

$$v_{\text{mean}} = \sqrt{\frac{8kT}{\pi m}} = 0.03\,\frac{\mu\text{m}}{\mu\text{s}}\,. \tag{2.63}$$

This means that an atom moves over a distance of 30 nm in a typical excitation time of 1 μs which is much smaller than the interparticle distance. Thus the frozen gas approximation is justified for excitation times on the order of 1 μs. An exception is the off-resonant excitation of pairs [192], which we discuss in Sec. 3.7. The typical experimental time scale is given by the time that the system needs to reach the steady state, which in turn depends on the laser parameters. All Rabi frequencies and line widths are of the order of 1 MHz resulting in typical time scales of 1 μs. If, however, the experiment is carried out on longer timescales $\sim 100\,\mu$s, motional effects, such as collisions between Rydberg atoms, might become important, cf. Chap. 4.

Chapter 3

Coherent dynamics of two-level Rydberg atoms

This chapter is based on the following publications:

Finite size effects in strongly interacting Rydberg gases
M. Gärttner, K. P. Heeg, T. Gasenzer, and J. Evers
Physical Review A **86**, 033422 (2012)

Dynamic formation of Rydberg aggregates at off-resonant excitation
M. Gärttner, K. P. Heeg, T. Gasenzer, and J. Evers
Physical Review A **88**, 043410 (2013)

Full counting statistics of laser excited Rydberg aggregates in a one-dimensional geometry
H. Schempp, G. Günter, M. Robert-de-Saint-Vincent, C. S. Hofmann, D. Breyel, A. Komnik, D. W. Schönleber, M. Gärttner, J. Evers, S. Whitlock, and M. Weidemüller
arXiv:1308.0264 (2013), submitted for publication

Towards the scaling limit in dense gases of Rydberg atoms
M. Gärttner, D. W. Schönleber, and J. Evers
in preparation

This chapter deals with the many-body effects arising in a cloud of atoms coherently excited to a Rydberg state. In contrast to Chap. 4, we only take into account the ground and Rydberg state of the atoms. First, the structure of the Hamiltonian (2.49) and the underlying basis of many-body states is described and the techniques that are used for the truncation of this basis are introduced. We explain the computational methods that are employed in our simulations and discuss various observables that can be extracted from them. The presentation of the simulation results starts with the case of a resonantly driven one-dimensional sample, where we discuss effects of finite size and finite density. The second part of the results deals with the emergence of spatial structure that arises in an off-resonantly driven ensemble. Such a system has been recently studied experimentally [42,43] in the presence of strong decoherence due to finite laser line width. The modeling of this dissipative dynamics is discussed in the last section of this chapter.

3.1 State space and Hamiltonian

Many-body basis and Hamiltonian

An ensemble of N van der Waals interacting two-level atoms, subject to coherent laser driving, is described by the many-body state vector

$$|\psi\rangle = \sum_{k=1}^{n} c_k |\phi_k\rangle \tag{3.1}$$

with n basis states $|\phi_k\rangle$ and their corresponding complex amplitudes c_k. A priori, any atom of the gas can be either in the ground state or in the Rydberg state, which leads to a total number of 2^N canonical basis states

$$|\phi_k\rangle = \bigotimes_{i=1}^{N} |\alpha_i\rangle = |\alpha_1 \alpha_2 \dots \alpha_N\rangle \tag{3.2}$$

where $\alpha_i \in \{g, r\}$. Typically, due to the dipole blockade, only a small number of atoms will be in the Rydberg state $|r\rangle$, while the majority resides in the atomic ground state $|g\rangle$. We will therefore sometimes use the following alternative notation to describe the basis states: The many-body ground state of the ensemble, i.e., all N atoms in $|g\rangle$, is denoted as $|0\rangle$. A state with m Rydberg excited atoms is then labeled as

$$|\phi_k\rangle = |g_1 g_2 \dots g_{i_1-1} r_{i_1} g_{i_1+1} \dots g_{i_m-1} r_{i_m} \dots g_N\rangle = |m; i_1, \dots, i_m\rangle \ , \tag{3.3}$$

where the indices $i_1, \dots, i_m$ indicate which atoms are in the Rydberg state. The first notation is as in Eq. (3.2). The second notation is more compact, especially if $m \ll N$, and also corresponds to the way the basis states are stored in our numerical simulation. In our convention the atom excited indices i_s always increase monotonically, $i_s < i_{s+1}$.

We now recall the many-body Hamiltonian (2.49) and explain its structure. In the canonical product basis

$$H_{2L} = H_\Delta + H_\Omega + H_{\text{int}} \tag{3.4}$$

has a diagonal part

$$H_\Delta + H_{\text{int}} = -\sum_{i=1}^{N} \Delta s_{rr}^{(i)} + \sum_{i<j} V_{ij} s_{rr}^{(i)} \otimes s_{rr}^{(j)} \tag{3.5}$$

and an off-diagonal part

$$H_\Omega = \sum_{i=1}^{N} \frac{\Omega}{2} \sigma_x^{(i)} \tag{3.6}$$

coupling states with m Rydberg excitations to states with $m \pm 1$ excitations. Two states are only coupled if they differ in the state of exactly one atom, i.e., the state $|m; i_1 \dots i_m\rangle$ is coupled to $|m+1; i_1 \dots i_{m+1}\rangle$ if and only if $\{i_1 \dots i_m\} \subset \{i_1 \dots i_{m+1}\}$. The diagonal matrix

Table 3.1: Structure of the Hamiltonian matrix in the excitation-number-sorted basis. $\omega = \Omega/2$, $\delta = -\Delta$. By E_3 and E_4 we denote the sum of pairwise interaction term as in Eq. (3.7). We only write down the off-diagonal couplings for the upper right part, since the matrix is Hermitian and even symmetric in the case of real a Rabi frequency Ω. The corresponding basis states are shown on the right.

$m=0$	0	ω	ω	ω	ω	0	0	0	0	0	0	0			0	$\lvert gggg\rangle$
$m=1$	ω	δ	0	0	0	ω	ω	ω	0	0	0					$\lvert rggg\rangle$
	ω	0	δ	0	0	ω	0	0	ω	ω	0		0		0	$\lvert grgg\rangle$
	ω	0	0	δ	0	0	ω	0	ω	0	ω					$\lvert ggrg\rangle$
	ω	0	0	0	δ	0	0	ω	0	ω	ω					$\lvert gggr\rangle$
$m=2$						$2\delta+V_{12}$						ω	ω	0	0	$\lvert rrgg\rangle$
							$2\delta+V_{13}$					ω	0	ω	0	$\lvert rgrg\rangle$
	0		...					$2\delta+V_{14}$				0	ω	ω	0	$\lvert rggr\rangle$
									$2\delta+V_{23}$			ω	0	0	ω	$\lvert grrg\rangle$
										$2\delta+V_{24}$		0	ω	0	ω	$\lvert grgr\rangle$
											$2\delta+V_{34}$	0	0	ω	ω	$\lvert ggrr\rangle$
$m=3$												$3\delta+E_3$			ω	$\lvert rrrg\rangle$
	0		0					...					$\ddots$		ω	$\lvert rrgr\rangle$
															ω	$\lvert rgrr\rangle$
															ω	$\lvert grrr\rangle$
$m=4$	0		0					0					...		$4\delta+E_4$	$\lvert rrrr\rangle$

element can immediately be evaluated to give

$$\langle m; i_1 \dots i_m | \, H_{2L} \, | m; i_1 \dots i_m \rangle = -m\Delta + \sum_{s<t}^{m} V_{i_s j_t} = -m\Delta + E_{\text{int}} \,. \tag{3.7}$$

Thus the Hamiltonian matrix can be divided into blocks of basis states sharing the same number of Rydberg excitations. The matrix is tridiagonal in these blocks. The blocks on the diagonal are themselves diagonal, containing the detuning part of the laser Hamiltonian and the interaction part. The off-diagonal blocks contain the Rabi frequency, coupling states differing by only one excitation. An example for a typical matrix for a system of 4 atoms is given in Tab. 3.1.

3.2 Technical aspects and implementation

State space truncation

In the previous section it was shown that the dimension of the Hilbert space grows exponentially with the number of atoms N. This would limit numerically feasible calculations to atoms numbers of $N \lesssim 20$. However, we can exploit the dipole blockade to exclude certain states from the computational basis and thereby reduce the dimension tremendously [48, 101, 103, 104, 112, 114, 144, 291].

If two atoms are very close to each other, their Rydberg-Rydberg interaction energy is large, and we know that they will never be excited simultaneously. Therefore we can exclude all states in which both of these atoms are in the Rydberg state $|r\rangle$ from the computational

Table 3.2: Illustration of the state space reduction with $N = 4$. The cutoff distance R_c is larger than R_{12} and R_{23} as illustrated in Fig. 3.1. The number of basis states is reduced from 16 to 10. The number of Rydberg excitations in a given basis state is m.

$m = 0$	$m = 1$	$m = 2$	$m = 3$	$m = 4$
$\|gggg\rangle$	$\|rggg\rangle$	~~$\|rrgg\rangle$~~	~~$\|rrrg\rangle$~~	~~$\|rrrr\rangle$~~
	$\|grgg\rangle$	$\|rgrg\rangle$	~~$\|rrgr\rangle$~~	
	$\|ggrg\rangle$	$\|rggr\rangle$	$\|rgrr\rangle$	
	$\|gggr\rangle$	~~$\|grrg\rangle$~~	~~$\|grrr\rangle$~~	
		$\|grgr\rangle$		
		$\|ggrr\rangle$		

Figure 3.1: Example of a quasi one-dimensional trap containing $N = 4$ atoms. States containing pairs of excited atoms with distance smaller than the cutoff R_c are discarded.

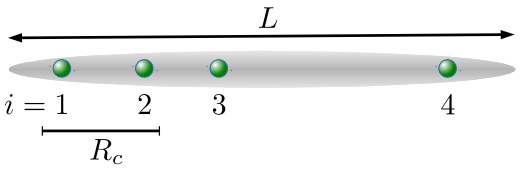

basis. This state space truncation is realized by introducing a cutoff radius R_c and excluding excited pairs with $R_{ij} < R_c$. We need to choose the cutoff distance smaller than the "physical" blockade radius in order to ensure that the result of the simulation is not biased by the state space reduction. Alternatively, one can introduce a cutoff energy E_c and exclude states $|\phi_k\rangle$ if their interaction energy exceeds this cutoff:

$$E_{\text{int}}^{(k)} = \langle\phi_k| H_{\text{int}} |\phi_k\rangle = \sum_{\substack{i<j \\ \alpha_i=\alpha_j=r}} V_{ij} = \sum_{s<t}^{m} V_{i_s j_t} > E_c \tag{3.8}$$

where we have written the sum over the pairwise interaction terms $V_{ij} = C_6/R_{ij}^6$ in two different ways, referring to the two different notations introduced above. Such an energy cutoff will obviously lead to a maximal number of excitations of $m_{\max} = \lfloor L/R_c \rfloor + 1$ in a one-dimensional sample, where the symbol $\lfloor x \rfloor$ denotes the largest integer smaller of equal to x.

An example of $N = 4$ atoms is given in Fig. 3.1 and Tab. 3.2 to illustrate the truncation.

For one-dimensional systems an estimate for the number of remaining states can be derived from combinatoric arguments. In a trap of length L containing N atoms, the number n of remaining states after truncation is approximately

$$n_{\text{est}} = \sum_{m=0}^{m_{\max}} \frac{(N + N_c - mN_c)!}{m![N + N_c - m(N_c + 1)]!}\,, \tag{3.9}$$

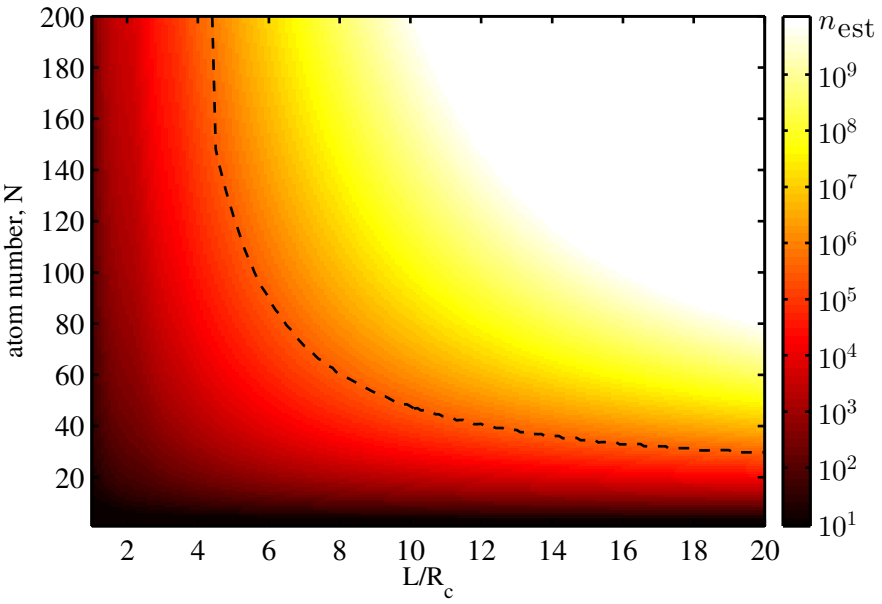

Figure 3.2: Estimate for the number of basis states n_{est} for a homogeneous one-dimensional sample of length L containing N atoms. The trap length L is scaled by the cutoff distance R_c to give the maximal number of excitations $m_{\max}$ that fit into the trap. The color scale is logarithmic. The dashed line shows the limit of 10^6 states beyond which simulations typically become unfeasible.

where $N_c = \lfloor R_c N/L \rfloor$ [138]. This estimate assumes a homogeneous distribution of the atoms in the trap. The dimension of the physically relevant Hilbert space which is used for the computation thus depends on two parameters in one-dimensional geometry: the number of atoms N and the maximal number of excited states $m_{\max} = \lfloor L/R_c \rfloor + 1$. In other geometries the dependence can differ from Eq. (3.9). In Fig. 3.2 we show n_{est} as a function of these parameters. This illustrates that for $N \lesssim 20$ atoms arbitrary densities can be simulated, while for $N = 200$ we are limited to volumes containing at most 5 excitations. In the most costly simulations that have been done, the parameters were $m_{\max} \approx 11$ and $N = 64$ atoms, leading to $n_{\mathrm{est}} \approx 5 \times 10^6$ basis states, see Sec. 3.5.

In addition to reducing the number of basis states and thus the size of the Hamiltonian matrix, the state space reduction has another advantage: If states with very large interaction energies are included, these energies appear as diagonal elements in the Hamiltonian, rendering the matrix stiff, i.e., having a large ratio of largest over smallest eigenvalue, and thus requiring very small time steps in the time integration. This is avoided by excluding states with high E_{int}.

Technically, the buildup of the state space is done recursively. We start with the ground state $|0\rangle$ and from there build up all singly excited states by changing the state of each atom from $|g\rangle$ to $|r\rangle$. Then, starting from the first singly excited state $|1;1\rangle$, we build up the doubly excited ones by converting atoms $j > 1$ to state $|r\rangle$. When doing so we check for any newly crated state, whether it should be excluded because the distance between the two excited atoms is smaller than the cutoff distance, $R_{1j} < R_c$ (or $V_{1j} > E_c$ for the energy cutoff). If this is the case, the state is not stored. In the same way we proceed with all singly excited states $|1,i\rangle$, trying to create doubly excited states by exciting atoms $j > i$. For $i = N$, there

are no further atoms, so the recursion stops. From the doubly excited states the triply excited ones are built up analogously by exciting atoms $k > j$ and so on. This recursive method works since the interaction energy increases monotonically with the number of excitations. By only adding excited atoms with atom index i_{m+1} higher than the highest index in the initial state i_m, it is guaranteed that there are no double occurrences of states in our *state tree*. The recursive state space construction is illustrated in Fig. 3.3. It becomes obvious that in the recursive scheme, the number of states we generate and then discard again since they are blockaded is small compared to the total number of states we generate. This is due to the fact that each blockaded state cuts off a whole branch of the state tree that does not have to be considered. Thus, the complexity of the state space buildup scales as $nm_{\max}$, with the number of valid basis states n. The term $m_{\max}$ stems from the number of operations that are required to check the exclusion criterion for a newly generated state.

It should be noted that whole state space truncation and recursive buildup procedure gets more difficult for large positive detuning Δ since in this case the detuning term and the interaction term can compensate and the value of the diagonal elements does not increase monotonically with n any more. In this case the state space buildup has to be done first without taking into account the detuning part of the diagonal element and using a cutoff energy $E_c > m_{\max}\Delta$ in order not to discard states with diagonal elements ≤ 0. Then, further states can be discarded a posteriori by going through all generated states again and discarding the ones with diagonal elements larger than a reduced cutoff. In the second step, also a lower energy cutoff may be used since now, due to the detuning part $-m\Delta$, states can have very small diagonal elements $\ll 0$, and thus will not take part in the dynamics if the initial state is $|0\rangle$.

The exact choice of the truncation parameters depends on the physical parameters. The numerical cutoff distance R_c should always be smaller than the blockade radius R_b, or, in the case of off-resonant excitation, smaller than the pair resonant distance $r_{\mathrm{res},2}$, see Sec. 3.7. The pair correlation function $g^{(2)}$, which we introduce below, is a very useful observable for verifying that the cutoff distance has been chosen adequately. In our simulations we always verified that all observables are converged with respect to the numerical cutoff parameters.

Buildup and efficient storage of the Hamiltonian matrix

Having described the buildup of the state space, we now have to determine the Hamiltonian matrix in the canonical product state representation. The diagonal elements have already been evaluated above. Thus, only the off-diagonal part of the Hamiltonian remains to be determined. The values of the nonzero off-diagonal elements are identical for homogeneous intensity profiles of the driving lasers. However, determining which basis state is connected with which can be the most time consuming part of the whole algorithm for large basis size n, if it is not highly optimized.

The straightforward way of determining the Rabi couplings would be the following: For any state $|m; i_1 \dots i_m\rangle$ we search the states that are Rabi coupled to it among the states with $m-1$ and $m+1$ excitations. This can be done by exciting/deexciting one atom i_s and then searching for the resulting state by iterating through the states of the respective block. For this way of determining the off-diagonal elements, the complexity of the matrix buildup scales as n^2, while the number of nonzero off-diagonal elements is limited by nN (since any state can couple at most to N other states by exciting/deexciting any atom). Since usually $n \gg N$

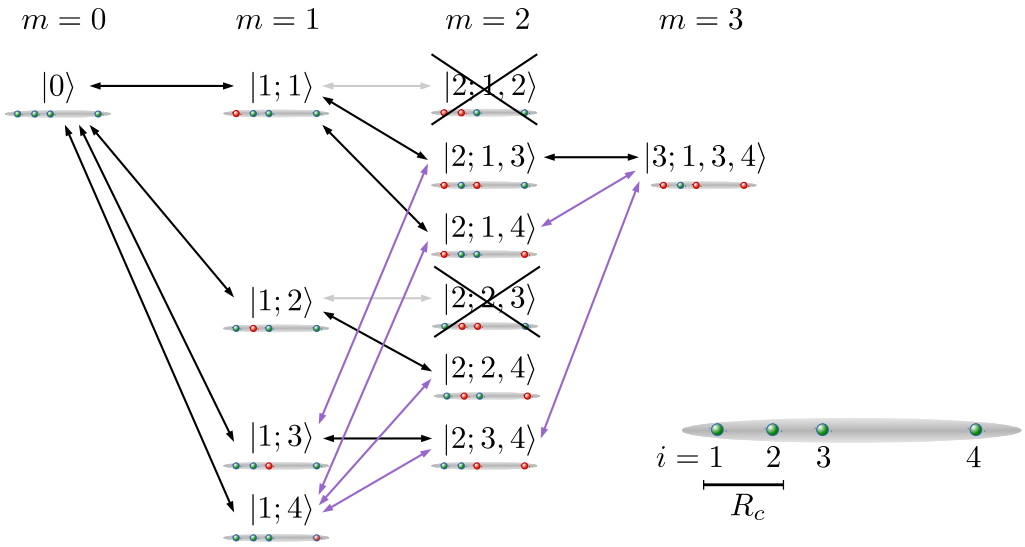

Figure 3.3: Illustration of the recursive buildup of the numerical basis and Hamiltonian. Double-arrows symbolize Rabi-couplings Ω. The black double arrows are the connections found during the recursive buildup of the state tree. The purple ones are found during the second stage of the generation of the Hamiltonian matrix, in which the Rabi couplings are generated using fast-access search in the state tree.

the buildup of the Hamiltonian, if done in this way, will be the most time consuming part of the algorithm for large N.

However, by storing the basis states as a nested linked list (or tree), we can accelerate the search for the Rabi couplings and achieve nN-scaling. The idea is that each state is a node in the state tree. During the recursive buildup of the state space we store which states were generated from a certain state $|\phi_k\rangle = |m; i_1 \dots i_m\rangle$ by storing the pointers to the newly generated states with $|\phi_k\rangle$. When we now search the index k of a certain state during the matrix buildup phase, we can go along the state tree starting at the ground state node $|0\rangle$ and taking the path through the branches specified by the excited atom indices i_s. Using this way of state searching, the buildup of the Hamiltonian matrix scales as $nNm_{\max}$. The performance of this method depends very much on careful memory management. During the recursive buildup of the state tree, memory can easily become fragmented. This has to be avoided by preallocation of memory for the nodes and pointer arrays. An illustration of the algorithm is provided in Fig. 3.3. The different scalings can be measured in terms of CPU-time, which is shown in Fig. 3.4.

The insight that the number of nonzero matrix elements is $\sim nN$ shows that the Hamiltonian matrix will be sparse. Therefore, instead of storing all n^2 matrix elements, we only store the nonzero ones together with their respective column index in each line of the matrix. Technically, the Hamiltonian is then represented by an $n \times N$-array of doublets $(H_{k_r k_c}, k_c) = (\langle \phi_{k_r} | H | \phi_{k_c} \rangle, k_c)$, containing the value and the column index k_c of the matrix element. The state $|\psi\rangle$ of the system is represented by the coefficient vector c_k. In this notation the action of the Hamiltonian operator on a state, $H|\psi\rangle$, is accomplished by the

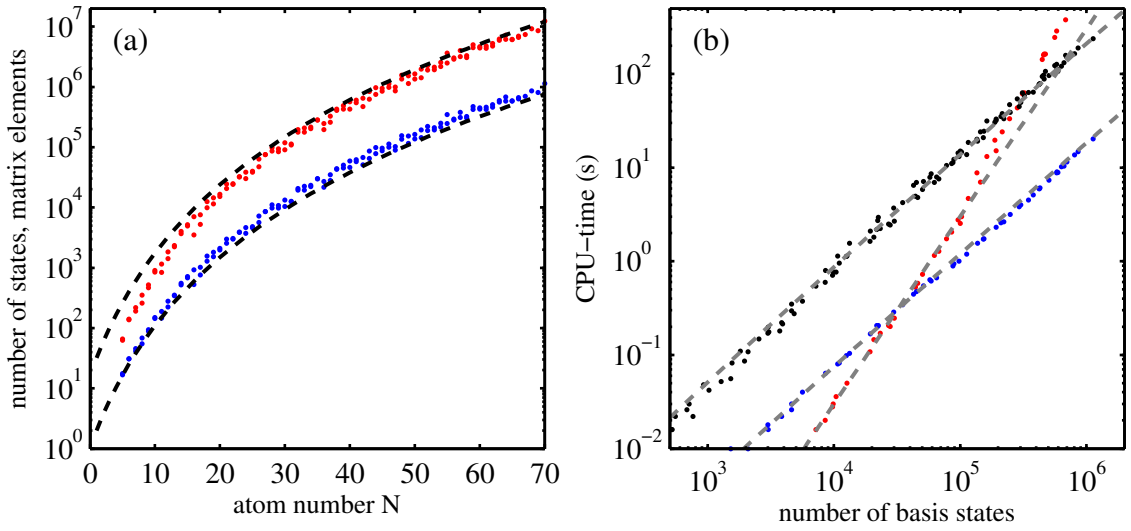

Figure 3.4: (a) The number of basis states and nonzero matrix elements for a one-dimensional trap of length $L/R_c = m_{\text{est}} = 8$ as a function of the atom number. The lower dashed line is the estimate n_{est} from Eq. (3.9) showing that n_{est} underestimates the state number slightly. The upper dashed line is $2m_{\max}n_{\text{est}}$, which turns out to be a good estimate for the number of nonzero matrix elements at large N_b. Thus we obtain an estimate for the memory requirements of the algorithm, since the Hamiltonian matrix is always the dominant object in terms of memory. Note, however that memory is never the limiting factor for our simulations. The basis size limit is set by the maximal computation time that we regard as feasible. (b) CPU-times for time evolution (black) and state space buildup with different methods (red: naive search of Rabi couplings, blue: intelligent search using the state tree). The dashed lines are fits proportional to n^2 and nN, respectively. We have used typical parameters, similar to those of Sec. 3.5 and an integration time of $t_{\text{end}}\Omega = 20$. All results shown here have been obtained on an *Intel®Core™ i7-2600* processor (cache: 8 MB, clock speed: 3.4 GHz).

matrix-vector multiplication

$$\sum_{k_c=1}^{n} H_{k_r,k_c} c_{k_c} = \sum_{s=1}^{n_{k_r}} H_{k_r,k_c(s)} c_{k_c(s)} \,, \tag{3.10}$$

where n_{k_r} is the number of nonzero matrix elements in row k_r and $k_c(s)$ is the column index of the sth element of row k_r of our sparse matrix. The complexity of this operation is thus nN (number of nonzero matrix elements).

Time integration and performance

The algorithm consists of three main parts: The buildup of the state space and Hamiltonian, the time integration of the time dependent Schrödinger equation

$$\dot{\mathbf{c}}(t) = -iH\mathbf{c}(t) \,, \tag{3.11}$$

and the evaluation of the observables. The initial condition for the time integration will always be that all atoms are in the ground state $|g\rangle$, i.e., $c_k(t=0) = \delta_{1,k}$. As shown above, the computation time for the first part scales as nN if implemented cleverly. The second part is just the solution of a system of first order ordinary differential equations, which can be done

using standard techniques. The third part, the evaluation of the observables is discussed in Sec. 3.3. Here, we just note that this part is never a limiting factor in terms of computation time. The computation time needed for the integration depends on the number of time steps and the complexity of the evaluation of the right hand side of Eq. (3.11). As shown above, the Hamiltonian matrix contains $\sim nN$ nonzero matrix elements, and thus the matrix-vector multiplication $H\mathbf{c}(t)$ scales as nN. For the time stepping we use Runge-Kutta methods from the GNU Scientific Library [292], more precisely we used the *embedded 8th order Runge-Kutta Prince-Dormand method with 9th order error estimate (RK8PD)*. We note that if the same methods are employed for propagation in imaginary time, one obtains a brute force method for calculating the ground state of the Hamiltonian. Refining this, one would end up with Lanczos methods for determining the ground state [293].

Figure 3.4(b) illustrates the CPU-times needed for the different parts of the algorithm as a function of the basis size n for a one-dimensional sample with $L/R_c = 8$ and typical parameters for resonant laser excitation ($\Delta = 0$). The time evolution is calculated up to $\Omega t_{\mathrm{end}} = 20$. The matrix buildup and the time propagation both scale as nN. The different prefactors, number of time steps n_{dt} for the time propagation and $m_{\max}$ for the matrix buildup, give an offset of about $n_{\mathrm{dt}}/m_{\max}$ between them. This factor was always large in our simulations such that the time propagation is the bottleneck of the algorithm.

Note that this model exclusively contains the unitary time evolution, i.e., spontaneous emission, dephasing or laser line widths are not explicitly accounted for. A proper treatment of such incoherent processes would require methods such as a master equation or a quantum Monte Carlo simulation of the incoherent jumps, which would considerably increase the computational complexity, see Sec. 3.8. From a physical point of view, this approximation can be justified if the experimental time scales are short compared to the life time of highly excited Rydberg states, and if stabilized laser systems with low line width are used.

Direct integration or diagonalization of the many-body Hamiltonian using truncated Hilbert spaces and related approaches have also been pursued by Hernandez and Robicheaux [110,112, 204], in the groups of T. Pohl [48,101–103,146], T. Pfau [114,115], and I. Lesanovsky [104,105], and in [144, 291].

Monte Carlo position sampling and parallelization

In thermal gas any atom has a well defined position but these positions are unknown. In the density matrix formalism (see Sec. 2.3) this would be described by a statistical mixture of position states. In frozen gas approximation (see Sec. 2.4) the kinetic term of the Hamiltonian is neglected, which means that the total Hamiltonian is diagonal in the position component of the wave function and thus we can calculate the time evolution in the internal states for each possible realization of positions independently and then integrate over all possible position realizations weighted with their respective probabilities [148]. The expectation value of an observable O becomes

$$\langle O \rangle = \int d^{3N}\mathbf{r}\, P_{\mathbf{r}}\, \langle O \rangle_{\mathbf{r}}\,, \tag{3.12}$$

where $\mathbf{r} = (\mathbf{R}_1, \ldots, \mathbf{R}_N)$ is a certain realization of atom positions $\mathbf{R}_i$, $P_{\mathbf{r}}$ the probability for this realization and $\langle O \rangle_{\mathbf{r}}$ the expectation value of the observable for this specific realization of atomic positions. This integral we solve with Monte Carlo techniques [294] for large atom numbers N. This means that we randomly generate atom positions for all atoms in a

given trap volume and with a given density profile and calculate the time evolution of this particular realization. This we do several times (typically 5000 times) with the same physical parameters but other randomly chosen atom positions. At the end we average the outcomes of the observables, such as the number of Rydberg excitations, over all realizations. We only require convergence of this method with respect to the observables we are interested in. For spatially resolved observables such as the local excitation density, this convergence may be slow, depending on the atomic density. Such Monte Carlo methods have also been used for example in Refs. [82, 103, 117, 148].

The Monte Carlo sampling allows for trivial parallelization of our algorithm: As the time evolution can be solved independently for all realizations we can solve each one of them on a different processors and take the Monte Carlo average once all calculations have terminated. With this, the Monte Carlo sampling does not imply an additional factor in computation time as long as enough CPUs are available.

Another, more sophisticated, way of parallelization would be to distribute the matrix-vector multiplication to different processing units. In principle all the lines of the Hamiltonian matrix can be multiplied with the coefficient state vector independently. Using the architecture of graphic cards (GPUs) that possess thousands of parallel processing units (threads) one could assign each of the n lines of the matrix to a distinct thread. Doing the n vector-vector operations in parallel instead of serially would result in a tremendous speedup. The bottleneck here would probably be the time needed to copy the Hamiltonian matrix from the CPU memory to the GPU. Note that the recursive state space buildup can not be parallelized. If the whole time evolution is done on the GPU, and only the final coefficient vector has to be copied back to the CPU at the end, an enormous speedup should be possible. In the end the efficiency will presumably depend on the clever handling of the memory again. However, this a goal for future research and we will not go into further detail here.

3.3 Observables

In this section we introduce the most important observables that we will discuss in the further course of this chapter and explain how they are calculated from the coefficient vector $\mathbf{c}$.

Let us recall that for a single realization of our system, all information is contained in the coefficient vector $\mathbf{c}$, defined via

$$|\psi\rangle = \sum_k c_k |\phi_k\rangle \quad \rightarrow \quad c_k = \langle \phi_k | \psi \rangle \ , \tag{3.13}$$

where the basis states are the product states described above:

$$|\phi_k\rangle = \bigotimes_{i=1}^{N} |\alpha_i\rangle = |\alpha_1 \alpha_2 \dots \alpha_N\rangle \tag{3.14}$$

where N is the number of atoms in the cloud and $\alpha_i \in \{g, r\}$. From this we can calculate expectation values for various observables.

The mean number of Rydberg atoms is

$$N_{\mathrm{ryd}} = \langle \hat{N}_{\mathrm{ryd}} \rangle = \sum_{k=1}^{n} |c_k|^2 m^{(k)} \tag{3.15}$$

where $m^{(k)}$ is the number of excited atoms in state $|\phi_k\rangle$.

In terms of the probability to find exactly m excited atoms,

$$P_{\mathrm{ryd}}(m) = \sum_{k=1}^{n} |c_k|^2 \delta_{m^{(k)} m}\,, \tag{3.16}$$

the q-th moment can be expressed as

$$\langle \hat{N}_{\mathrm{ryd}}^{q} \rangle = \sum_{m=0}^{m_{\max}} m^q P_{\mathrm{ryd}}(m)\,. \tag{3.17}$$

Having calculated the expectation values $\langle \hat{N}_{\mathrm{ryd}} \rangle$ and $\langle \hat{N}_{\mathrm{ryd}}^2 \rangle$, we can in addition evaluate Mandel's Q parameter [295]

$$Q = \frac{\langle \hat{N}_{\mathrm{ryd}}^2 \rangle - \langle \hat{N}_{\mathrm{ryd}} \rangle^2}{\langle \hat{N}_{\mathrm{ryd}} \rangle} - 1\,. \tag{3.18}$$

Q characterizes the excitation statistics, and allows us, e.g., to identify squeezing in the excitation numbers. For a Poisson distribution, Q vanishes while a negative (positive) Q-parameter means sub-Poissonian (super-Poissonian) excitation statistics.

The excitation probability of the ith atom is given by

$$\langle \hat{N}_{\mathrm{ryd}}^{(i)} \rangle = \sum_{k=1}^{n} |c_k|^2 \delta_{\alpha_i^{(k)} r}\,, \tag{3.19}$$

where $\alpha_i^{(k)}$ is the internal state of atom i in state $|\phi_k\rangle$, and the Kronecker delta selects the coefficients of the states in which the ith atom is excited.

The spatial distribution of the Rydberg excitations $N_{\mathrm{ryd}}(\mathbf{R})$ is obtained by dividing the trap volume into small cells and summing up the excitation probabilities of all atoms that lie in such a cell, normalized by their number. Most important in this work are spatial correlations quantified by the pair correlation function $g^{(2)}(\mathbf{R}, \mathbf{R}')$. This function is a measure for the conditioned probability of having an excitation at $\mathbf{R}$ if there is already one at $\mathbf{R}'$. Since the interaction potential in our model only depends on the mutual distance of two atoms, it is valid to assume that also $g^{(2)}$ only depends on $R = |\mathbf{R} - \mathbf{R}'|$. This has been verified numerically. The pair correlation of two particles is defined as [296]

$$g_{i,j}^{(2)} = \frac{\langle s_{rr}^i s_{rr}^j \rangle}{\langle s_{rr}^i \rangle \langle s_{rr}^j \rangle}. \tag{3.20}$$

Discretizing space, we define

$$g^{(2)}(R) = \frac{\sum_{i,j}^{(R,\Delta R)} g_{i,j}^{(2)}}{\sum_{i,j}^{(R,\Delta R)} 1} \tag{3.21}$$

where $\sum_{i,j}^{(R,\Delta R)}$ denotes the sum over all pairs with mutual distance $|\mathbf{R}_i - \mathbf{R}_j|$ lying within the interval $[R, R + \Delta R]$. This means that we sum up the correlations of all these pairs divided by their number. Note that some authors use the alternative definition $\tilde{g}^{(2)} = g^{(2)} - 1$ [46]. According to our definition $g^{(2)}(R) = 1$ corresponds to uncorrelated atoms.

The expectation value of the product operator $s_{rr}^{(k_1)} s_{rr}^{(k_2)}$ is called $G^{(2)}$-function. We can define $G^{(2)}(R)$ in the same way as $g^{(2)}(R)$, only substituting $g_{i_1,i_2}^{(2)}$ with

$$G_{i_1,i_2}^{(2)} = \langle s_{rr}^{i_1} s_{rr}^{i_2} \rangle \tag{3.22}$$

and normalize by multiplying with N_{ryd}^{-2} at the end. Note, that we have chosen R as the center of the ΔR-interval now. In the following we will use the notation $g^{(2)}(R)$ and $G^{(2)}(R)$, respectively, for the correlation functions. The physical meaning of $G^{(2)}(R)$ is the probability density of finding an excited pair with separation R.

A last useful quantity is the energy density of states, i.e., the number of states with an interaction energy E_{int} in a certain energy interval. After building up the basis of the Hilbert space, we can calculates the (diagonal) interaction part of the Hamiltonian for each state. Putting these energies into a histogram to see at which energies the density of states is high an at which it is low, can help to interpret the evolution of the system.

3.4 Effects of finite system size

In a one-dimensional ensemble of atoms, two length scales are naturally present: The system length L and the mean inter-particle spacing n_0^{-1}. For laser excited Rydberg atoms, due to the interplay between long-range interactions and laser driving, a third length scale, the blockade radius R_b arises. Nontrivial dynamics emerge in the case where $L > R_b > n_0^{-1}$. If all the length scales are well separated from each other, i.e.,$L \gg R_b \gg n_0^{-1}$, again the properties of the system simplify, since R_b is the only relevant length scale in the system. This limit is called the scaling limit [114]. Signatures of $L \gg R_b$ not being satisfied are what is meant by finite size effects, whereas R_b not being well separated from n_0^{-1} implies a coarse graining of the medium leading to, as we will call it, finite density effects (see Sec. 3.5).

In this section we study how the dependence of the number of Rydberg excitations in a laser-driven cloud of atoms on the interaction strength is affected by the finite size of the system. A theoretical model predicting a simple power-law dependence is compared with results extracted from numerical many-body simulations. We find that for finite-size systems the numerical results do not agree with the analytical prediction. By individually testing the assumptions leading to the theoretical prediction using the results from the numerical analysis, we identify the origin of the deviations, and explain it as arising from the finite size of the system. Furthermore, finite-size effects in the pair correlation function $g^{(2)}$ are studied.

Here and the following sections we set $\Omega = 1$, which is not a restriction of the parameter space but just a rescaling of time, i.e., we measure energy in units of $\hbar\Omega$ and time in units of

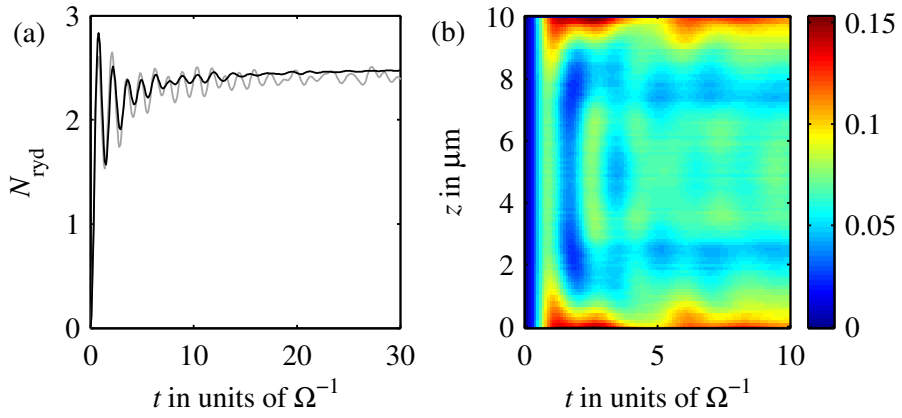

Figure 3.5: (a) Time evolution of the number of Rydberg excitations in an ensemble of $N = 50$ atoms enclosed in a cylindrical trap with radius $r = 1\,\mu$m and length $L = 10\,\mu$m. gray: Single realization. The remaining oscillations at long times reflect the fluctuations of the positions of the Rydberg atoms. black: Average over 1000 Monte Carlo samples. (b) Spatially resolved excitation density for an ensemble of $N = 30$ atoms in a one-dimensional trap of length $L = 10\,\mu$m, averaged over 2000 Monte Carlo samples. Further parameters are: $\Delta = 0$, $C_6 = 900\,\Omega\,\mu\text{m}^6$ in both (a) and (b).

$1/\Omega$. We assume that the intensity and wavelength of the laser is temporally and spatially constant. In experimental terms this means that the exciting lasers are switched on instantly. In this section and in Sec. 3.5 we study resonant excitation ($\Delta = 0$), while in Sec. 3.7 and 3.8 the focus will be on the off-resonant case.

3.4.1 Dynamical properties

A single atom or a gas of noninteracting atoms undergoes simple Rabi oscillations on a time scale short compared to the dephasing time. If the laser is detuned, only a part of the population oscillates between the ground and excited states, while the rest of the population remains in the ground state. The oscillation frequency is modified to $\sqrt{\Delta^2 + \Omega^2}$. In the case of infinite interaction strength, starting from the ground state $|\mathbf{0}\rangle = |gg\ldots g\rangle$, only singly excited states are accessible. Higher excited states can be discarded because they have infinite interaction energy. The resulting dynamics is a Rabi oscillation between the ground state $|\mathbf{0}\rangle$ and the symmetrized singly excited state $|\mathbf{s}\rangle = N^{-1/2}\sum_{i=1}^{N}|1;i\rangle$ [4], with collective Rabi frequency $\Omega_c = \sqrt{N}\Omega$ [204]. Collective Rabi oscillations of two atoms could already be observed in experiment [17, 29, 243].

In the intermediate case, in which several atoms can be excited simultaneously, but interactions are nonzero, the dynamics is more complicated. In the example shown in Fig. 3.5 we use a cylindrical trap of length $10\,\mu$m and diameter $2\,\mu$m. We observe that the Rydberg population of the cloud, initially being in the ground state, shows a saturation behavior. However, even for long times some oscillations remain, cf. Fig. 3.5(a). The strength of these oscillations depends on the number of excitations and on the number of atoms in the trap. This saturation can be interpreted in two ways: On the one hand, the mean-field picture predicts that, due to the disorder induced by the randomness of the atom positions, interaction shifts δ differ from atom to atom, leading to different Rabi frequencies $\sqrt{\delta^2 + \Omega^2}$ for the individual atoms. Consequently, the oscillations dephase over time and lead to a saturation of

the overall excitation. Alternatively, one uses the so-called super-atom picture: Any excited atom in the ensemble blocks the excitation of the surrounding atoms which leads to collective excitation of the atoms within this blockade sphere. Again due to the random positions of the atoms, the number of atoms per blockade sphere and thus the collective Rabi frequency varies across the ensemble. The occurrence of different collective Rabi frequencies leads to a dephasing and thus to saturation. This subject of thermalization in Rydberg gases has been subject of intense studies recently [106, 109, 110, 113, 173].

Averaging over many realizations shows that the mean number of Rydberg excitations saturates fully after some time, cf. Fig. 3.5(a). The timescale of this saturation depends on how many Rydberg excitations are present in the gas, on the system size and also the detuning. Note that for very small traps that confine the gas to near one blockade volume, ongoing strong oscillations are observed even after Monte Carlo averaging. The reason is that in this case, only one or a few different collective Rabi frequencies are possible, depending on the number of atoms in the blockade spheres. In the example shown in Fig. 3.5(a) we find that the excitation number converges to about $N_{\mathrm{ryd}} = 2.5$ Rydberg excitations. This means that $N_b = N/N_{\mathrm{ryd}} = 20$ atoms share one excitation and we expect to observe a collective Rabi frequency of $\Omega_C/\Omega = \sqrt{N_b} = 4.47$. Measuring the period of the initial oscillations in Fig. 3.5(a) we obtain $\Omega_C = 2\pi/T = 4.49\,\Omega$, consistent with the super-atom picture.

It is interesting to note that the inhomogeneity induced be the trap boundaries leads to faster relaxation towards a stationary state compared to a system with closed boundaries. This is illustrated in Fig. 3.5(b). Close to the trap boundaries the excitation density is higher. Thus one excitation is shared between less atoms than in regions of small excitation density. Therefore the collective Rabi frequency is lower close to the trap edges leading to a dephasing of the initial oscillations. This leads to an accelerated decay of the oscillations in N_{ryd}. In a system with closed boundaries the translational symmetry is not broken and the oscillations are spatially in phase across the whole trap.

3.4.2 The concept of blockade spheres and super-atoms

Before starting with the further analysis of our numerical results, we more formally introduce the concepts of blockade spheres and super-atoms, already mentioned in the introduction. By inspecting the Hamiltonian (3.4) one recognizes that two nearby atoms cannot be excited simultaneously by the laser field since the interaction part of the Hamiltonian would become very large in this case. This fact leads to the notion of a blockade volume [22, 23], that is, a volume that can contain at most one excitation due to the interaction. A natural length scale of the system, the blockade radius R_b, emerges by comparing the interaction energy C_6/R_b^6 to the collective Rabi frequency $\sqrt{N_b}\Omega$. With N_b we denote the number of atoms sharing one excitation in such a blockade sphere of volume V_b, see also Sect. 3.4.1. Interestingly, a qualitative understanding of a number of phenomena observed in Rydberg gases can be gained by visualizing the total excitation volume V with atom density n_0 as an arrangement of densely packed blockade spheres. This picture is commonly called the super-atom picture. Throughout this section, we will in particular consider the relations [22]

$$N_{\mathrm{ryd}} \propto V/V_b\,, \tag{3.23a}$$

$$\sqrt{N_b}\Omega = C_6/R_b^6\,, \tag{3.23b}$$

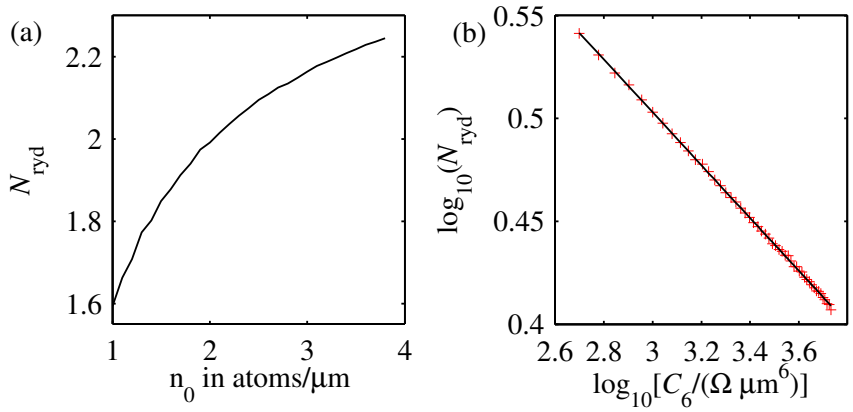

Figure 3.6: Number N_{ryd} of Rydberg excitations in a one-dimensional gas. (a) N_{ryd} as a function of the line density. Parameters: $L = 10\,\mu$m, $C_6 = 900\,\Omega\,\mu\mathrm{m}^6$, $\Delta = 0$. (b) Number of excitations as a function of the van der Waals interaction constant, on a double logarithmic scale. Crosses: numerical simulation. Solid line: power-law fit $N_{\mathrm{ryd}} \sim C_6^{-0.128}$. Parameters: $L = 15\,\mu$m, $N = 45$, $\Delta = 0$ of $N = 45$ atoms.

motivated above. From $N_b = n_0 V_b \propto n_0 R_b^d$ in $d-$dimensional space, and neglecting H_Δ assuming resonant laser driving, we further obtain an estimate of the blockade radius

$$R_b \propto \left(\frac{C_6}{\Omega\sqrt{n_0}}\right)^{2/(d+12)}. \tag{3.24}$$

Eqs. (3.23) and (3.24) can be used to derive a scaling law [29, 114] which we will probe numerically for finite systems in the following. Throughout the following discussion, we in particular refer to Eqs. (3.23) and (3.24) when we mention the super-atom picture.

3.4.3 Signatures of finite system size in bulk properties

In this section we study the properties of the system after is has saturated to its steady state. For sufficiently high atomic density the number of Rydberg excitations does not scale linearly with the number of atoms, as it would be expected for a dilute noninteracting gas. Instead, a reduced Rydberg population is observed as is shown in Fig. 3.6(a). This is caused by the well-known dipole blockade [28] inhibiting the simultaneous excitation of two nearby atoms by means of a large interaction shift. This effect is the more pronounced the stronger the interactions are. Thus N_{ryd} decreases as a function of the interaction parameter C_6, as is illustrated in Fig. 3.6(b). From Eqs. (3.23) and (3.24), one finds that [114]

$$N_{\mathrm{ryd}} \sim \frac{N}{N_b} \sim R_b^{-d} \sim C_6^{-2d/(d+12)}. \tag{3.25}$$

This power-law behavior is the consequence of universal scaling connected to a quantum critical point [114]. For a one-dimensional gas ($d = 1$), one obtains an algebraic scaling of N_{ryd} with C_6, with exponent $\nu = -2/13 \approx -0.1538$.

Fig. 3.6(b) shows the data obtained from our numerical simulations for a one-dimensional trap of length $15\,\mu$m containing 45 atoms. We find that it is consistent with a power-law dependence over the simulated range of interaction strengths covering approximately one decade

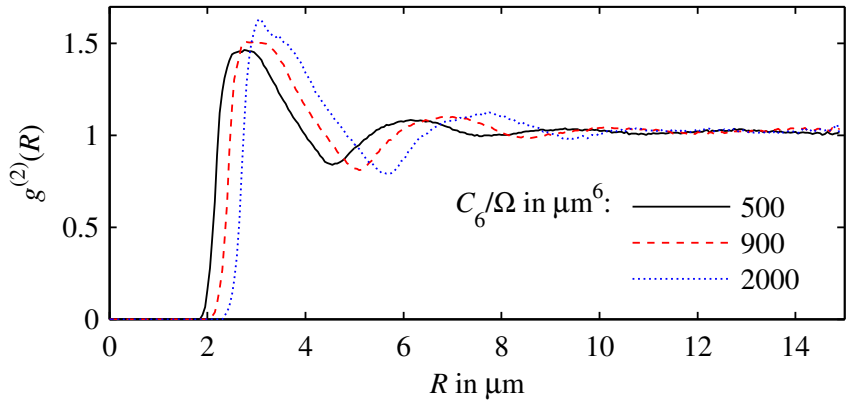

Figure 3.7: Pair correlation function defined in Eq. (3.21) for three different interaction strengths C_6 after $t = 200\,\Omega$ evolution time. One-dimensional trap of length $L = 15\,\mu$m holding $N = 45$ atoms exposed to a resonant laser.

in C_6 ($500 - 5500\,\Omega\mu\text{m}^6$). However, the fitted exponent is found as $\nu_{\text{fit}} = -0.1283 \pm 0.0006$ (errors we give on fitted values just refer to the confidence interval of the fit). At first sight, this result appears to be in contrast to the predicted scaling exponent ν and the calculations reported in [114] where good agreement of numerical simulations with the analytically predicted value was reported. We will analyze this discrepancy in more detail in the following section and show that the deviation from the theoretical prediction is due to finite-size effects arising in our relatively small trap volume. Further calculations simulating larger volumes using closed boundary conditions in Sect. 3.5 will confirm that our numerical model is capable of reproducing the predicted scalings in larger volumes, such that the deviations found here can indeed be attributed to finite size effects in smaller volumes. For now, we summarize that the dependence of the excited fraction on the interaction strength in finite-size systems, although it is consistent to a power law over the considered parameter range, does not show the algebraic scaling predicted for an unbounded homogeneous gas. While our numerical results do not prove the existence of universal scaling in finite systems due to the limited range of C_6 and N_{ryd} accessible to our simulations, the deviation from the scaling law for bulk systems reported here could be probed experimentally already by scanning over a limited parameter range.

3.4.4 Origin of the finite-size effects

In the previous subsection, we found that the scaling exponent ν_{fit} obtained by fitting the numerical data with a power-law did not agree with the value ν predicted and confirmed previously for a homogeneous gas. In the following, we trace back the origin of this discrepancy to finite-size effects. For this, we individually examine the two assumptions which lead to the prediction of the scaling parameter in Eq. (3.25). The first one is the estimate of the blockade radius, Eq. (3.24). The second one is the assumption that the number of Rydberg excited atoms can be obtained from an estimate based on the super-atom picture, $N_{\text{ryd}} \propto m_{\max} = N/N_b = L/R_b$, Eq. (3.23). Note that the effects studied here are physical finite-size effects in the sense that they originate from the finite trap volume rather than from computational

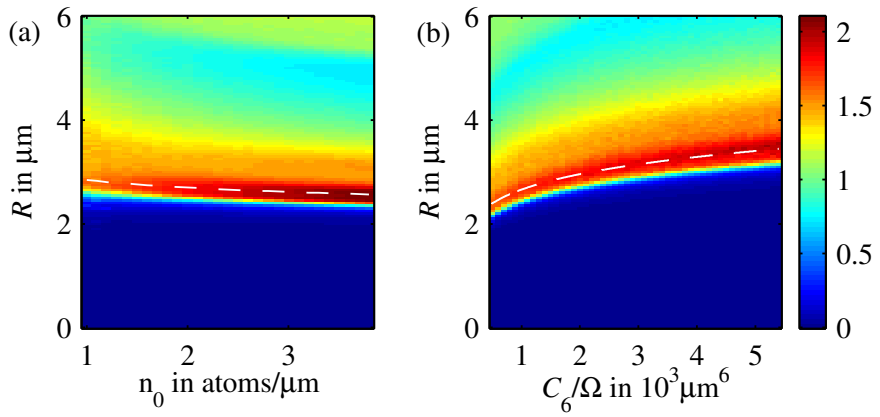

Figure 3.8: Pair correlation function (3.21) as a function of (a) the atom line density, with $C_6 = 900\,\Omega\,\mu\mathrm{m}^6$, $L = 10\,\mu\mathrm{m}$; (b) the interaction constant C_6, with line density $n_0 = 3\,\mu\mathrm{m}^{-1}$ ($L = 15\,\mu\mathrm{m}$, $N = 45$). Dashed lines indicate the estimates for R_b as in Eq. (3.26).

limitations. Therefore, they could possibly be observed in experiments.

Estimate for the blockade radius

In order to analyze the estimate for the blockade radius given in Eq. (3.24) we consider pair correlations. Fig. 3.7 shows the pair correlation function (3.21) of a one-dimensional gas in its stationary state (see also Ref. [138]). Pairs with small mutual distance are never excited simultaneously, hence the $g^{(2)}$-function is zero for small R. Note that the numerical blockade radius R_c was chosen well below the onset of nonzero correlations to ensure that the state space truncation does not affect the outcome of the simulations. The sharp peak which emerges just outside the blockaded region is located precisely at

$$R_b = \left(\frac{C_6}{\Omega \sqrt{N/L}} \right)^{2/13}, \tag{3.26}$$

which was our estimate of the blockade radius (Eq. (3.24)) leading to Eq. (3.25). In order to probe this conjecture more thoroughly we analyze $g^{(2)}$ for varying line density and interaction strength. Results are shown in Fig. 3.8. The predicted blockade radius perfectly matches the first maximum of $g^{(2)}$ in the whole parameter region. This indicates that the estimate for R_b in Eq. (3.24) are reasonable even in finite geometries. We remark that in these figures one can also observe that correlations become stronger as the density or the interaction strength increases. We could also quantitatively verify Eq. (3.26). For this, we extracted the blockade radius from the simulation results shown in Fig. 3.8 by defining it as the pair distance at which the $g^{(2)}$-function reaches its first turning point (point of steepest ascend). This observable shows a power-law dependence over the whole range of parameters and fitting the exponent yields perfect agreement with the results obtained for homogeneous systems in Sect. 3.5. The remaining small deviations from the predicted scaling, cf. Eq. (3.26), can be explained by the finite atom density, see Sect. 3.5.

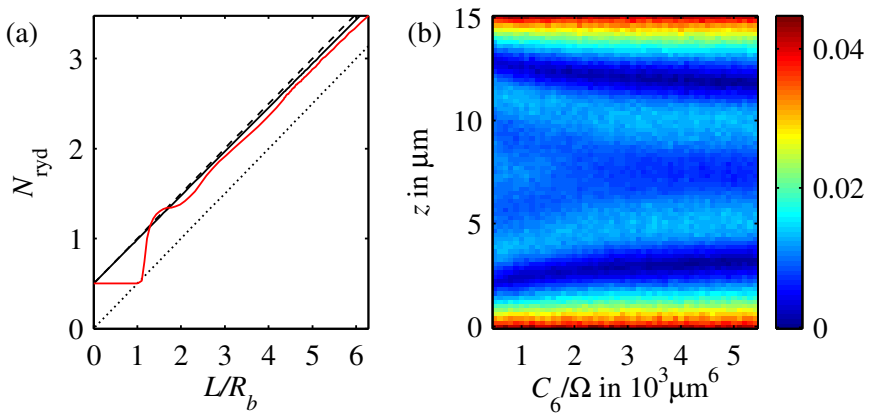

Figure 3.9: Same setup as in Fig. 3.7. (a) N_{ryd} as a function of $L/R_b = L(C_6/\Omega\sqrt{n_0})^{-2/13}$. Red line: Numerical data, obtained by varying C_6. Dotted black line: $0.5\,L/R_b$. Dashed black line: $0.5(L/R_b+1)$. Solid black line: $0.5(L_{\mathrm{eff}}/R_b+1)$. None of these estimates fits the numerically obtained dependence. (b) Spatial distribution of the Rydberg excitations on the string in excitations per μm, divided by the total number of excitations.

Estimate for the number of Rydberg excited atoms

Next, we consider the assumption that $N_{\mathrm{ryd}} \sim m_{\mathrm{max}} = N/N_b = L/R_b$. In Fig. 3.9(a) results are shown for the numerically obtained N_{ryd} as a function of C_6, expressed in units of L/R_b via Eq. (3.24). In order to interpret the numerical data, we approximate the one-dimensional excitation volume as a densely packed array of super-atoms, and estimate that each super-atom in an average over time is excited with a probability of $\gamma^* = 1/2$ since for resonant excitation ($\Delta = 0$) one expects full Rabi oscillations between zero and one excitation. With these model assumptions, we obtain $N_{\mathrm{ryd}} = \gamma^* L/R_b$. This first estimate is shown as a dotted line in Fig. 3.9(a). It can be seen that it does not coincide with the numerically found N_{ryd}.

This failure is due to boundary effects and can be understood in two ways. First, from Fig. 3.9(b) it can be seen that the distribution of excitations on the string shows strong maxima at both ends. These can be understood in the mean-field picture. The interaction shift of atoms close to the border is smaller than that of atoms in the center since they only have potentially excited neighbors to one side. Consistent with the structure of the pair correlation function, the side maxima have to be followed by minima due to the blockade effect and, towards the center of the string, by further maxima corresponding to the first maximum of $g^{(2)}$. The maxima at the edges of the string lead to a higher excited fraction compared with the case of an infinite string. This effect becomes more dominant as C_6 increases since the number of excitations on the string decreases leading to an effectively smaller system.

Secondly, in a system of length L, the assumption of densely packed excitations at distances R_b from each other does not necessarily lead to $N_{\mathrm{ryd}} = \gamma^* L/R_b$. The number of super-atoms fitting on such a string is rather $L/R_b + 1$ due to the excitations sitting at both ends of the string. This would result in $N_{\mathrm{ryd}} = \gamma^*(L/R_b + 1)$ which fits the numerical data much better but overestimates it a bit [dashed black line in Fig. 3.9(a)].

A further correction is connected to the finite density of the gas. The finite atomic line density of $\rho = 3\,\mu\mathrm{m}^{-1}$ implies that it is very unlikely that two atoms are sitting exactly at the trap ends, so the outermost super-atoms are shifted towards the trap center on average

by $0.5\,n_0^{-1}$ leading to an efficient trap length of $L_{\text{eff}} = L - n_0^{-1}$. We therefore show $N_{\text{ryd}} = \gamma^*(L_{\text{eff}}/R_b + 1)$ [solid black line in Fig. 3.9(a)] where again $\gamma^* = 0.5$ was assumed. This line now reproduces the behavior of the numerical data well but still overestimates it slightly. In order to understand this, we should bear in mind that the notion of super-atoms sitting at the edges of the trap is not consistent with the ansatz we used to estimate the blockade radius. R_b is estimated by equating the collective Rabi frequency of N_b atoms to the interaction strength at a distance R_b, i. e., $\sqrt{N_b}\Omega = C_6/R_b$. A super-atom sitting at the edge of the trap would now contain less atoms, leading to a larger blockade radius. We conclude that the super-atom picture is not adequate to explain the effects of the trap boundaries.

We note that also our choice $\gamma^* = 1/2$ should be regarded as a model assumption, as recently it has been predicted that atoms trapped in a lattice potential and interacting with a hard core interaction potential can exhibit $\gamma^* > 1/2$ at higher densities ($N_b \gg 1$) [138]. However, in our system, effects stemming from the finite system size dominate, and render a numerical extraction of γ^* difficult.

In general, the validity of universal scaling laws depends on how well length scales are separated from each other. The blockade radius should be much smaller than the trap size but much larger than the intermediate particle distance [114]. As the simulation in Fig. 3.9 was done at constant atom density and trap size, increasing L/R_b means that the number of atoms per blockade sphere decreases. Thus by increasing L/R_b we effectively move towards the regime of low density, where the inter-atomic distance is of similar size as the blockade radius. In this regime the coarse graining induced by the decreasing ratio of R_b to the intermediate particle distance leads to a smaller number of Rydberg excitation than expected from the picture of densely packed super-atoms.

Fig. 3.9(a) shows yet another interesting property of small clouds. If L/R_b is smaller than one, the cloud is perfectly blocked and Rabi oscillates between the ground state and the fully symmetric singly excited state as mentioned in Sect. 3.4.1. Thus the time average of N_{ryd} is 0.5 as confirmed by the simulation data. As L/R_b increases, N_{ryd} increases steeply but smoothly and reaches values higher than the line $\gamma^*(L/R_b + 1)$. Some more oscillations around the line with slope $\gamma^* = 0.5$ follow before the dependence becomes linear in Fig. 3.9(a). This behavior reflects the structure of the $g^{(2)}$-function. For small pair distances it is zero, meaning that simultaneous excitation of two atoms in a trap of size $L < R_b$ is inhibited. It then increases steeply to values greater than one, indicating enhanced probability of simultaneous excitation at these pair distances. If now the trap size is slightly larger than R_b, the excitations near both trap ends enhance each other due to their positive correlations leading to an enhanced overall excitation probability. This effect is repeated, when three excitations just fit into the trap. We thus see that the oscillatory behavior of N_{ryd} as a function of trap size can be related to the structure of the pair correlation function. It should also be mentioned that, as the trap size is increased holding density and all other parameters constant, for $L/R_b \gtrsim 5.5$, N_{ryd} increases linearly with a slope of $0.5/R_b$ in agreement with the super-atom picture.

Our above findings explain why the slope of $N_{\text{ryd}}(C_6)$ is underestimated if finite-size effects are neglected, and why it is quite difficult in finite systems to find an analytical relation between N_{ryd} and $m_{\max}$ based on simple assumptions. For larger systems, these finite-size effects become negligible relative to the bulk properties of the large ensemble. We thus conclude that the assumptions $N_{\text{ryd}} \sim m_{\max} = N/N_b = L/R_b$ fails for small ensembles, leading to the discrepancy between the numerically obtained scaling parameter ν and the theoretical prediction in Eq. (3.25). It can be expected that in smaller systems, other predictions relying

on this relation would suffer from similar discrepancies as well. Therefore, to the extent to which one can associate this relation to the super-atom model, one can also conclude that this model itself is of restricted validity for small systems.

3.4.5 Finite-size effects in the correlation function $g^{(2)}$

We finally analyze finite-size effects in the pair correlation function. Fig. 3.10(a) shows $g^{(2)}(R)$ for three different trap lengths and a density of $n_0 = 3.33\,\mu\text{m}^{-1}$. We notice that the deviation from $g^{(2)}(R) = 1$, indicating spatial correlations, decrease slightly with increasing L. We now focus on the first maximum of the correlation function, cf. Fig. 3.10(a). This maximum is the feature that depends on the trap size most strongly. Analyzing it more closely, we find a double-peak structure which merges into a single maximum in the limit of large trap size. Splitting up the $g^{(2)}$-function into contributions from the different subspaces with definite excitation number m we find a very pronounced peak in the contributions of the lowest-m parts, especially of the two-fold excited states. This peak is located at the position of the left sub-peak of the first maximum of the full $g^{(2)}$ function in Fig. 3.10(a). The $m = 2$ part of the $g^{(2)}$-function is shown for two examples, $L = 15$ and $L = 18$, in Fig. 3.10(a). This structure was found for all trap lengths considered in our simulations, and even when periodic boundary conditions were used. However, as the relative population of states with a very low number of excitations decreases with increasing trap size, the effect on the structure of the total $g^{(2)}$ becomes weaker for large traps. This explains why the height of the left sub-peak decreases with increasing trap size, whereas the right sub-peak remains constant in size. The structures seen on the $m = 2$ subspace can partly be interpreted in the two-atom picture as arising from different excitation channels, as done in Ref. [118] for the case of $\Delta \gg \Omega$. However, for the $\Omega = 0$ case one expects collective effects to be dominant, and thus it is clear that the structure cannot be fully understood from the perspective of the two-atom problem. As expected, correlation peaks are generally enhanced if the system size is smaller than the range of the correlations. Fig. 3.10(b) confirms that $g^{(2)}(R)$ converges to a smooth function in the limit of large L. In the simulations with largest system sizes in Fig. 3.10(b), the $g^{(2)}$-function saturates to 1 over a distance smaller than the trap length. Nevertheless, some features of the correlation function (visible in Fig. 3.10(a) as discussed above) still depend on the trap length. We note that, in order to experimentally resolve these features in a measurement of $g^{(2)}(r)$, a distance resolution of $\lesssim 1\mu$m will be required.

3.4.6 Concluding remarks

We found finite-size effects in the scaling of N_{ryd} with the van der Waals coefficient C_6 which quantifies the dipole-dipole interaction strength between the excited Rydberg atoms. Our numerical analysis shows that, in the considered range of interaction strengths, the dependence of N_{ryd} on C_6 is still consistent to a power law dependence, but with a scaling exponent different from the analytically predicted value for large ensembles. The analytical prediction relies on two assumptions which can be motivated from the super-atom model: an estimate of the blockade radius, and an estimate of the number of excited Rydberg atoms. We could show that the estimate of the blockade radius provides a reliable prediction of the position of the first maximum of the pair correlation function obtained from the numerical simulations over a wide range of atom densities as well as interaction strengths. In contrast,

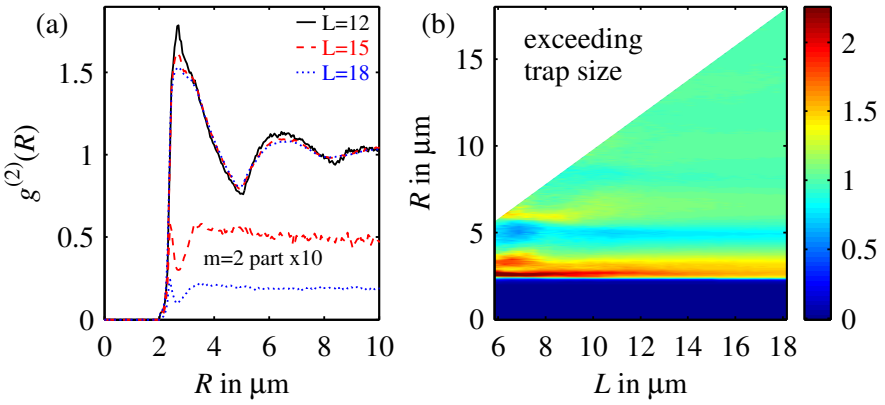

Figure 3.10: Finite-size effects in the $g^{(2)}$-function. If the correlation length is on the order of the trap size, correlations are enhanced by the finite-size effects. The lower two lines are the $g^{(2)}$-functions calculated on the subspace of doubly excited states for $L = 15\,\mu$m and $L = 18\,\mu$m, scaled up by a factor of 10 for better visibility. Parameters are $C_6 = 900\,\text{MHz}\,\mu\text{m}^6$ and $n_0 = 3.33\,\mu\text{m}^{-1}$.

the analytical estimate of the number of excited Rydberg atoms did not agree with our numerical results. This was found to be due to the fact that atoms at the ensemble borders can only interact with other atoms to one side, leading to an overall enhanced Rydberg excitation. Additionally, for a continuously varying ensemble size, the number of super-atoms fitting into the volume is not L/R_b, but rather lies between L/R_b and $L/R_b + 1$, and oscillates, reflecting the oscillations in the pair correlation function. We also predicted finite-size effects in the pair correlation function $g^{(2)}$, for which we have shown that some of its features depend on the ensemble size even for lengths L exceeding the distance range over which $g^{(2)}(R)$ is different from one. We conclude that two conditions are required to eliminate finite-size effects: First, the condition $R_b \gg n_0^{-1}$ needs to be fulfilled, such that the microscopic structure of the atom distribution becomes irrelevant. Second, $L \gg R_b$ is needed in order to eliminate the effects of the trap boundaries. We have shown that for trap sizes of $L/R_b < 6$ finite size effects significantly modify the dependence of the number of Rydberg excitations on the interaction strength. For typical experimental parameters ($R_b = 5\,\mu$m to $10\,\mu$m) this corresponds to $L = 30\,\mu$m to $60\,\mu$m which is an experimentally relevant length scale [34,86,120,207,225,243]. The finite-size effects are most pronounced for spatially homogeneous atom densities and laser intensities. We note that in typical experimental setups both atom density and laser intensities may vary spatially. However, near-homogeneous atom densities can be achieved by defining the excitation volume via laser beam cross sections small compared to the atom cloud extend. In combination, e.g., with flat-top beam shapers, an excitation volume with well defined boundaries and homogeneous atom density and laser intensity can be achieved [31]. Alternatively, atomic vapor microcells can be used to achieve homogeneous densities and excitation laser intensities [225].

3.5 Effects of finite density

Having understood the effects of finite system size in a one-dimensional setup with open boundary conditions, we now want to focus on systems that are large enough for finite size ef-

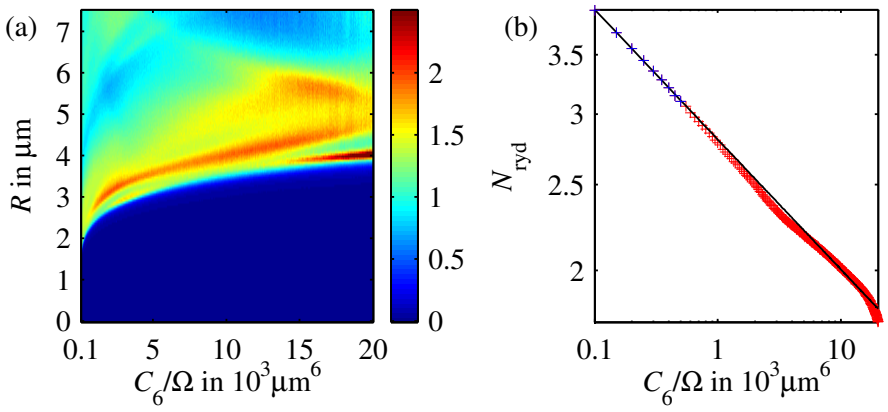

Figure 3.11: Same setup as in Fig. 3.7, but with periodic boundary conditions. (a) Pair correlation function as a function of C_6. Effects of artificial self coupling due to finite system size are visible particularly at high C_6. (b) Crosses: Number of Rydberg excitations obtained from numerical simulations. Solid line: Power law fit. Only the first nine points are used for the fit.

fects to be irrelevant. This is accomplished by choosing closed (periodic) boundary conditions that render the system homogeneous and by using large system sizes ($L/R_b \gtrsim 6$). We will revisit the dependence on C_6 that was studied in the previous section, but now for periodic boundary conditions, and find that for large system size and density the predicted scaling exponents are reproduced by the numerical simulations. In a second step we will introduce rescaled units in order to obtain effective, dimensionless parameters and find that, for resonant excitation ($\Delta = 0$) and in the large-trap regime (no finite size effects), we are left with only one parameter. This dimensionless parameter is the number of atoms per blockade volume N_b. If this parameter becomes large, the so called scaling limit is approached [114], in which the scaling laws discussed in the previous section are expected to hold strictly. In this limit the relevant length scales in the systems are well separated from each other: $L \gg R_b \gg n_0^{-1}$. This means that the only relevant scale is R_b. We study the effects of not being perfectly in the scaling limit, i.e., effects of finite density, meaning that the coarse graining of the atomic medium plays a role since $N_b \gg 1$, i.e., $R_b \gg n_0^{-1}$, is not fulfilled.

3.5.1 Large ensembles via periodic boundary conditions

If periodic boundary conditions are used, the spatial excitation density is perfectly flat. However, if strong correlations are present, large system sizes are required in order to eliminate artificial self-coupling effects. The latter are also known as aliasing effects that are caused by atoms correlated with a neighboring atom twice, inside the string and across the string boundary. Therefore the string length has to be at least twice as large as the range of the correlations. This is illustrated in Fig. 3.11(a). At large values of the interaction strength, for which the blockade radius is large and correlations are long-range, the $g^{(2)}$-function deviates strongly from the case without periodic boundaries. Only at small values of C_6 the system seems to become free of artificial self-coupling effects. Note that in contrast to the finite-size effects without periodic boundary conditions discussed above, these self-couplings cannot be observed in a linear 1D ensemble. They could, however, be observed if instead the gas was arranged in a suitable 1D ring trap as, e.g., in Ref. [176]. In our case the self coupling effects

observed at large C_6 values are unphysical effects. Therefore, to avoid these unwanted effects, we fitted the algebraic scaling law to the nine points with lowest C_6 shown in Fig. 3.11(b) and obtained $\nu \approx -0.146 \pm 0.003$. The line density is $\rho = 3\,\mu m^{-1}$ as in the fixed-boundary case. For larger densities, i.e., larger N_b, the scaling exponent obtained from our numerical simulations approaches the predicted value of $\nu = -2/13 \approx 0.154$ as we will see in Sec. 3.5.5. For the parameters of Fig. 3.11, the nearest-neighbor distances between ground-state atoms is much smaller than R_b, while the trap length is much larger than R_b. In this case, the system appears homogeneous, as neither the finite trap size nor the coarseness of the atom distribution are relevant. In the following we provide a more systematic analysis of the question how the scaling limit is approached, i.e., what happens if the two effective parameters L/R_b and $N_b = n_0 V_b$ become large.

3.5.2 Effective parameters and scaling laws

In the following we will generalize the reasoning about the blockade radius as a characteristic length scale of the system from Sec. 3.4 to the case of a d-dimensional system with binary interactions of the form $V_{ij} = C/R_{ij}^p$. Three length scales arise in such a system: The system size L, the mean inter-particle distance n_0^{-d}, and the blockade radius R_b arising from comparing the characteristic energy scales, collective Rabi coupling and interaction strength. In the general case we have

$$C/R_b^p = \Omega\sqrt{N_b} = \Omega\sqrt{n_0 R_b^d}\,, \tag{3.27}$$

where constant factors (2 in 1d, π in 2d, $4\pi/3$ in 3d) have been dropped in the last expression, since we are only interested in the scaling laws. This results in the blockade radius

$$R_b = \left(\frac{C}{\Omega\sqrt{n_0}}\right)^{\frac{2}{2p+d}}\,. \tag{3.28}$$

Different regimes are defined by comparing these length scales: The presence of finite size effects will depend on the relative size of L and R_b, and the high density regime will be defined by $R_b \gg n_0^{-d}$.

We now want to write the Hamiltonian (3.4) in dimensionless units using R_b as a length scale and $\hbar\Omega$ as an energy scale. This results in the rescaling

$$R \to R/R_b \tag{3.29a}$$
$$H \to H/\hbar\Omega \tag{3.29b}$$
$$t \to \Omega t\,. \tag{3.29c}$$

Alternatively, one could use the collective Rabi frequency $\sqrt{N_b}\Omega$ to define time and energy units.

Rewriting the time dependent Schrödinger equation in these units, we obtain

$$i\partial_t\,|\Psi\rangle = \sum_{i=1}^{N}\left(\frac{1}{2}\sigma_x^{(i)} - \frac{\Delta}{\Omega}s_{rr}^{(i)} + \sum_{i<j}\frac{C/\Omega}{R_b^p R_{ij}^p}s_{rr}^{(i)}s_{rr}^{(j)}\right)|\Psi\rangle \tag{3.30}$$

Thus, as long as the system is sufficiently homogeneous, such that the precise atomic positions do not matter, we are left with three physical parameter, namely, the dimensionless detuning $\Delta^* = \Delta/\Omega$ and the interaction parameter $\alpha^* = C/(\Omega R_b^p)$, and the system size L/R_b. Note that in the case of off-resonant excitation the detuning Δ sets an additional energy scale, such that also other length and time scales arise from comparing Δ with $V(R)$, namely the resonant distance $r_{\text{res}} = (C/\Delta)^{1/p}$ and the oscillation frequency of resonantly excited pairs $\Omega_{\text{res}} = \Omega^2/\Delta$, see Sec. 3.7. In the following, however, we are only concerned with the case $\Delta = 0$ and thus work with R_b as the characteristic length. The rescaling of units we have introduced corresponds to setting $\hbar = \Omega = R_b = 1$.

We now discuss the physical meaning of the effective interaction parameter α^*. Expressed in terms of the original parameters, the parameter α^* reads

$$\alpha^* = \frac{C}{\Omega R_b^p} = \left[\left(\frac{C}{\Omega}\right)^d n_0^p\right]^{\frac{1}{2p+d}} = \alpha^{-\frac{d}{2p+d}} \tag{3.31}$$

where we have defined $\alpha = \Omega/(C n_0^{p/d})$ to be consistent with [114]. The number of atoms per blockade sphere

$$N_b = n_0 R_b^d = \left[\frac{C}{\Omega} n_0^{p/d}\right]^{\frac{2d}{2p+d}} = \alpha^{-\frac{2d}{2p+d}} = (\alpha^*)^2 \tag{3.32}$$

turns out to be just the square of the dimensionless interaction parameter α^*. This means that the collective Rabi frequency is $\Omega_c = \Omega\alpha^*$. The excited fraction can be estimated as

$$f_R = \frac{N_{\text{ryd}}}{N} = \frac{1}{N_b} = \alpha^{\frac{2d}{2p+d}} = (\alpha^*)^{-2} \tag{3.33}$$

if we assume a dense packing of super-atoms.

In summary, we found that in the case of zero detuning, all properties of the system should follow a simple algebraic dependence on the parameter α [114]. Here we should point out that the relations between the observables and α are to be understood rather as proportionalities than equalities since dimensionality dependent constant factors have been neglected and for the estimation of f_R we assumed that in the steady state the super-atoms are densely packed hard spheres and all of them are excited. In reality only a fraction of the super-atoms will be excited, but the scaling dependence on α should hold. We want to stress again that this universal scaling behavior can only be expected to be observed when the length scale R_b is the only relevant length scale in the system. This means two things: First, the mean nearest neighbor distance must be much smaller than R_b such that the system can be regarded as homogeneous and the coarse graining in terms of atom positions does not matter. Second the system size L must be much larger than the blockade radius. The second prerequisite can be fulfilled by using periodic boundary conditions. However, still some requirements have to be accounted for. To be precise, correlations between particles should have decayed completely on a length scale of half of the trap length (or equivalently the ring circumference) in order to avoid so called aliasing effects that come about when particles can be correlated with themselves via the periodic boundaries. In this limit in which both these requirements ($L/R_b \gg 1$ and $N_b \gg 1$) are fulfilled, we should expect that all properties of the system solely depend on α^*.

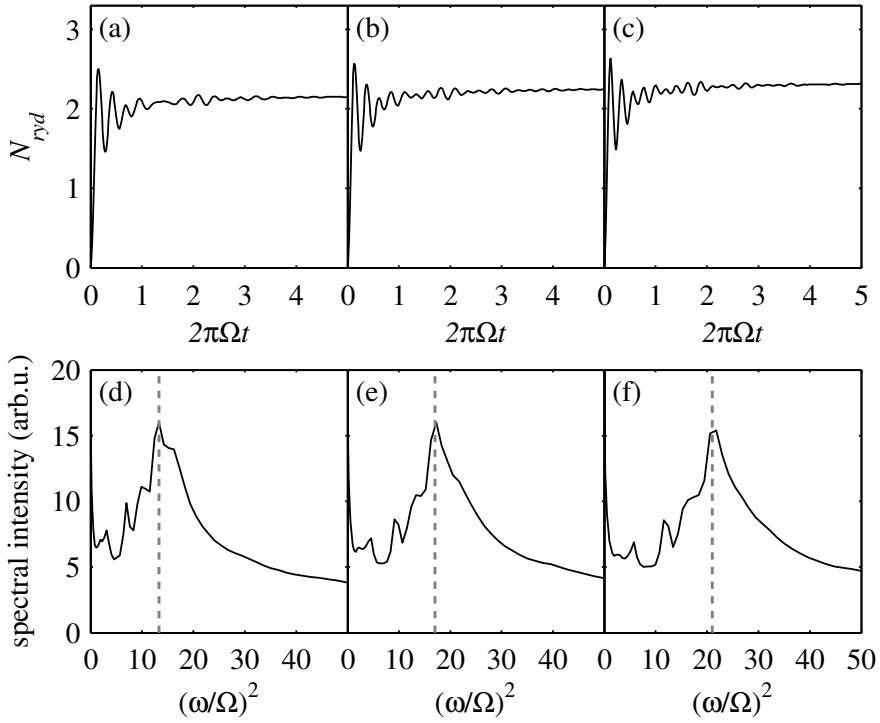

Figure 3.12: Time dependence of the number of Rydberg excitations for a one-dimensional sample of length $L \approx 4R_b$ containing $N = 30$, 40, 50 atom for (a), (b), (c), respectively. (d)-(f) show the Fourier transform of the above time dependence. The dashed lines mark the measured N_b.

Fulfilling both requirements poses substantial challenges for numerical simulations since both, large numbers of particles per blockade sphere and a large number of excitations $m_{\max}$ are required, and thus large total atom numbers N, which results in huge state spaces despite of all truncations methods (see Fig. 3.2). In the following, we study how the universal scaling regime is approached for increasing N_b in the case of van der Waals interactions ($p = 6$) in a one-dimensional system ($d = 1$). It is important to realize that by varying C_6 for otherwise constant parameters, as it was done in Sec. 3.4, we change both L/R_b and N_b at the same time, which makes it difficult to separate finite size from finite density effects. In order to study effects of finite density we want L/R_b to be large and constant.

Table 3.3: Comparison of observed and estimated collective Rabi frequency. N_b is calculated as in Eq. (3.32). N_b^{obs} is extracted from the time evolution as explained in the text.

N	N_b	N_b^{obs}	N_b^{obs}/N_b
30	7.85	13.3	1.69
40	10.2	17.0	1.66
50	12.6	21.0	1.67

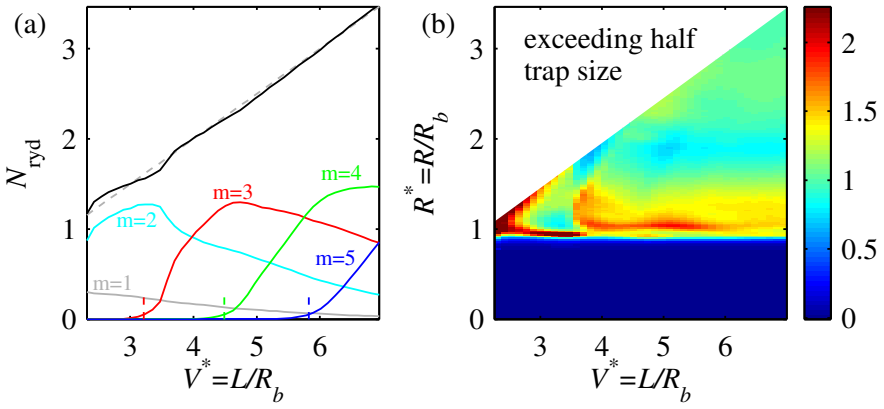

Figure 3.13: Varying the trap size. One-dimensional trap with periodic boundary conditions, atomic density $\rho = 3.3\,\mu\text{m}^{-1}$, $C_6 = 900$ (corresponds to $\alpha^* = 2.94$ or $N_b = 8.65$). The trap length is increased from $6\,\mu$m to $18\,\mu$m while the atom number N increases from 20 to 60. (a) Number of Rydberg excitations, also resolved for contributions from subspaces with definite excitation number m. (b) Pair correlation function. Effects of artificial self coupling due to finite system size are visible particularly for small L/R_b

3.5.3 Collective oscillations in a homogeneous system

In order to verify that the definitions of R_b and the collective Rabi frequency $\Omega_c = \Omega\sqrt{N_b}$ are reasonable in the sense that they have a physical meaning, we analyze the time evolution of N_{ryd} in a dense one-dimensional sample. Figure 3.12(a)-(c) shows an example of a trap of length $L \approx 4R_b$ containing $N = 30$, 40, and 50 atoms, respectively. In order to extract the collective Rabi frequency, we can read off the period of the initial oscillations of N_{ryd}. It is well visible that this period becomes shorter as the density (atom number) increases. A more systematic way to extract Ω_c is to Fourier transform $N_{\text{ryd}}(t)$ and determine the position of the peak in the spectrum. This is done in lower row of Fig. 3.12. Note that we plot over the squared frequency, such that the peak position should be directly proportional to N_b. The collective Rabi frequencies measured in this way are compared to the estimated ones in Tab. 3.5.3. We observe that the observed collective enhancement of the Rabi frequency is about $N_b^{obs} = (\Omega_c^{obs}/\Omega)^2 = 1.7N_b$. This indicates that the number of atoms that act collectively in a one-dimensional sample is rather $2R_bn_0$ than R_bn_0 in consistence with the fact that we overestimate R_b slightly when comparing to the onset of nonzero correlations in $g^{(2)}$, cf. Fig. 3.8. The fact that we obtain the same proportionality factor for all different densities confirms again that the general scaling of N_b with the parameters is described correctly by Eq. (3.32).

3.5.4 System size dependence

Before analyzing the dependence on N_b, we first discuss the system size dependence for periodic boundary conditions. We thereby assure that, for our later analysis of finite density effects, the requirement of large system size with negligible finite size effects is met. The results are summarized in Fig. 3.13.

For large trap size the number of excitations is expected to increase linearly with the trap size. The gray dashed line shows $L/(2R_b)$. At low densities fluctuations due to finite size

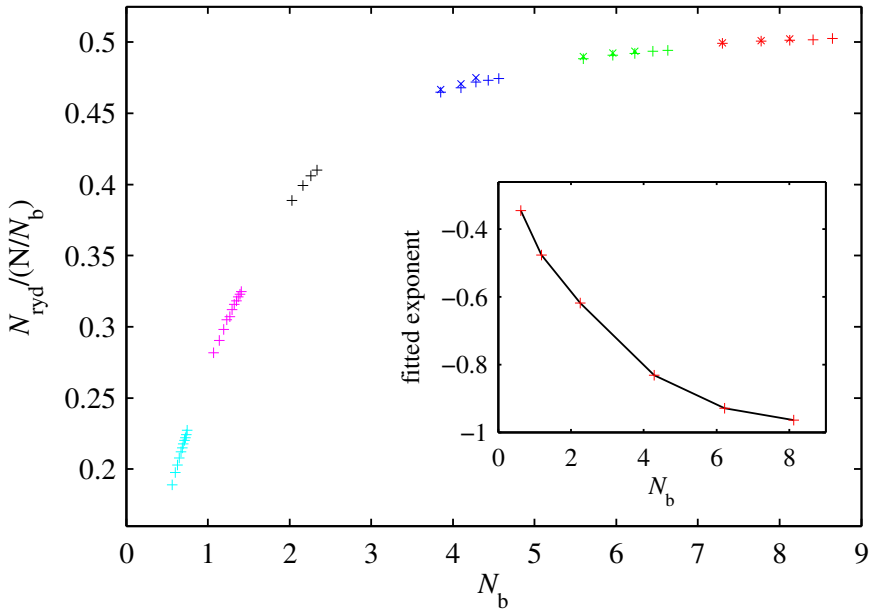

Figure 3.14: Same setup as in Fig. 3.13 but varying the interaction strength (or α^*, or N_b) instead. Each group of data points corresponds to a simulation with fixed tap length and atom number and varying C_6. For all points $L/R_b > 6.5$, so finite size effects should be negligible. We checked this by redoing some of the simulations with larger trap size but otherwise equal parameters (crosses). From left to right: $L/R_b \approx 20$ (cyan), $L/R_b \approx 15$ (magenta), $L/R_b \approx 10$ (black), $L/R_b \approx 7.5$ (blue pluses), $L/R_b \approx 9$ (blue crosses), $L/R_b \approx 7.9$ (green pluses), $L/R_b \approx 9.2$ (green crosses), $L/R_b \approx 8.0$ (red pluses), $L/R_b \approx 8.5$ (red crosses). Inset: Local fits of the exponent ν in $f_R = N_{\mathrm{ryd}}/N = N_b^{\nu}$. In the limit of high density the expected scaling of $\nu = -1$ is reached asymptotically.

effects are visible. The later analysis of density dependent scaling exponents will be done in the region of $L/R_b \gtrsim 6$. The contributions from different subspaces with definite excitation number m are also shown in Fig. 3.13(a). The dashed vertical lines are obtained as follows: We assume that m-fold excited states start to become populated when the ones with minimal interaction energy lie lower than twice the *collective* Rabi frequency (collective power broadening), $E_{\min}(m) < 2\sqrt{N_b}\Omega$. The minimal energy state is the one with equidistant excitations, i.e., $E_{\min}(m) = mC_6/(L/m)^{1/6}$. Solving for L gives a critical length of $L_{\mathrm{crit}}(m) = 2^{-1/6} R_b m^{7/6}$. For trap lengths larger than this, m-fold excited states should become populated. The positions of the $L_{\mathrm{crit}}(m)$ indeed coincide with the onset of the contribution of the respective state to N_{ryd}, as depicted in Fig. 3.13(a). Figure 3.13(b) shows that for small trap size correlations are present beyond the half trap length. This means that unwanted aliasing effects are present here. However, for large trap length ($L \gtrsim 5.5R_b$) the $g^{(2)}$-function has leveled out to unity before reaching $L/2$ and the artificial effects vanish.

3.5.5 Dependence on effective interaction parameter

Having quantified the effects of finite trap size in the case of periodic boundary conditions, we now want to investigate the effect of finite density, i.e., the dependence on α^* (or equivalently on $N_b = (\alpha^*)^2$). For this, we vary C_6 for fixed trap length and atom number. The trap length is chosen large enough to ensure that finite size effects do not significantly distort the

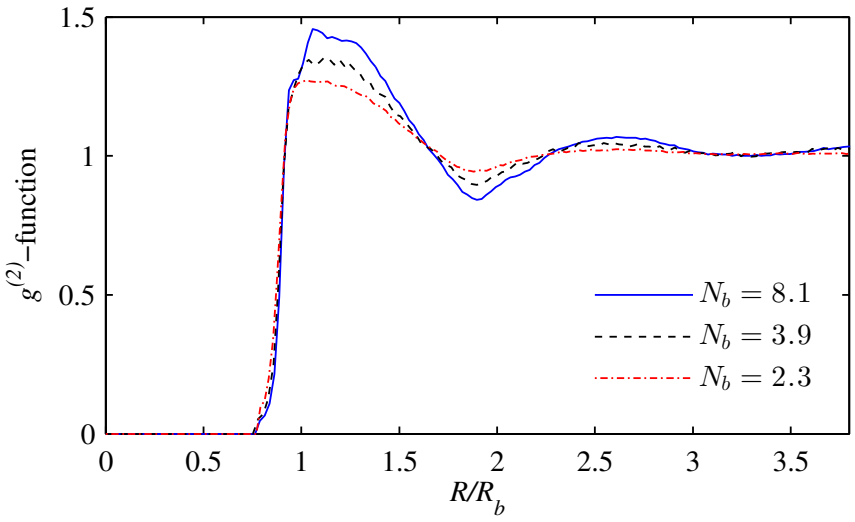

Figure 3.15: Same setup as in Fig. 3.14. Pair correlation function for various interaction parameters N_b. The trap length is $L/R_b \approx 8$ in all cases. The height and correlation length increases with the effective atomic density N_b.

dependence on N_b. This has been checked by redoing the simulations for larger trap size (and atom number) but otherwise identical parameters. We found that f_R increases slightly with increasing trap size even at $L/R_b \gtrsim 7$, but this effect is much smaller than the dependence on N_b. Figure 3.14 shows the dependence of the ratio of N_{ryd} over the expected number of super-atoms N/N_b. We observe that the curve saturates at high N_b and interestingly slightly exceeds the value of 0.5, which means that the super-atom excitation probability can exceed the limit of 1/2 that one naively expects for super-atoms undergoing coherent Rabi oscillations. This will be further discussed in Sec. 3.6. The inset of Fig. 3.14 shows the fitted exponent in $f_R = N_b^{\nu}$ for each group of data points. This exponent depends on N_b and seems to converge to the universal scaling value of -1 in the limit of large N_b. We thus observe that at low atomic densities $N_b \sim 1$, the coarse graining of the atomic medium leads to a reduced excitation probability.

Figure 3.15 shows the pair correlation function for different values of N_b, but same L/R_b. We observe that spatial correlations become stronger and their range longer as N_b is increased. At very low density the $g^{(2)}(R)$ becomes a step function in the sense that it never significantly exceeds unity, but the transition from $g^{(2)} = 0$ and $g^{(2)} = 1$ is still smooth, depending on the potential shape (see Sec. 3.6). It seems that the height of the first maximum of $g^{(2)}$ increases about linearly with N_b. We can, however, not conclude from our numerical data if the correlation height will keep increasing for ever increasing N_b or if it will saturate at some finite value. This will be further discussed in Sec. 3.6. For the largest value of N_b some small sub-peaks are visible. These are system-size dependent features and will vanish for even larger trap size. The overall trend of correlations increasing with density is not affected by this. The onset of nonzero correlations is independent of N_b if we plot $g^{(2)}$ over the rescaled length R/R_b. This confirms that the density dependence of this onset is correctly described by R_b as estimated above. If plotted over R in non-rescaled units, the onset of $g^{(2)} > 0$, and thus the blockade radius, would decrease with increasing N_b. Fitting the point of steepest

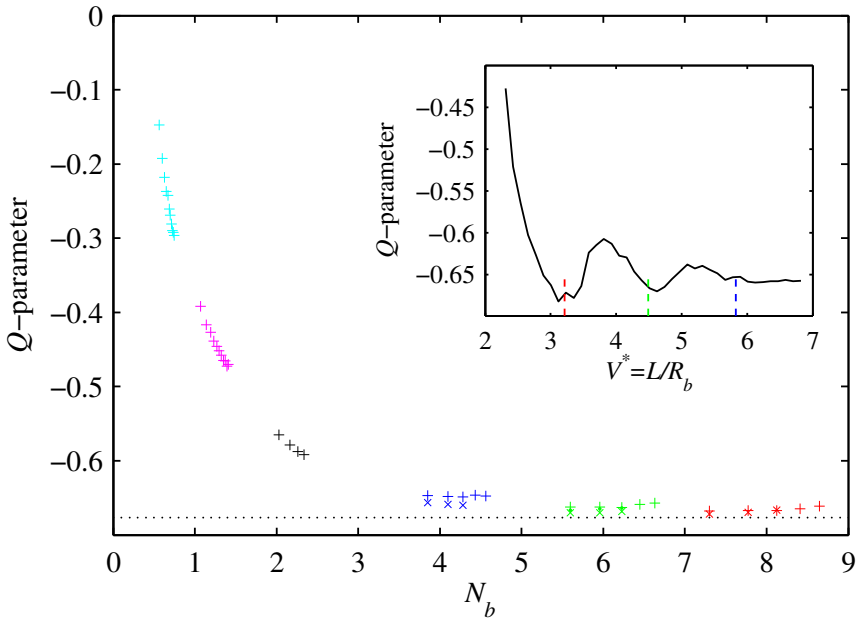

Figure 3.16: Same setup as in Fig. 3.14. Mandel Q-parameter as a function of the interaction parameter. The dotted line marks the value $Q_{\text{analyt}} = (\sqrt{5}-9)/10$ obtained for a hard dimer model [109]. Inset: trap size dependence of the Q-parameter. Same parameters as in Fig. 3.13. The vertical lines indicate the onset of contributions of higher m-fold excited states as in Fig. 3.13.

ascent of $g^{(2)}$, which would be a natural definition for a phenomenological blockade radius, we obtain the turning point distance $R_{tp} \approx 0.9R_b$.

Usually, increasing correlations are associated with increasingly dense packing of excitations. Thus, one would expect that the Mandel Q-parameter quantifying excitation number squeezing becomes smaller with increasing N_b. This is indeed the case, as Fig. 3.16 shows. However, there seems to be a lower limit larger than -1 for Q to which it converges at large N_b. This is surprising, since thermodynamic arguments [138] suggest that for a hard core potential (and with closed boundaries), Q should tend to -1 as the density tends to infinity. There is no obvious reason why this should not be the case for a van der Waals potential. We observe that for our parameters larger trap sizes can still lead to slightly lower Q-values, so finite trap size could be a reason why Q does not decrease further. However, as shown in the inset of Fig 3.16, for increasing trap size, the Q parameter just shows oscillations with decreasing amplitude but no global trend to lower values at large trap size. This indicates that in our case the value of Q is indeed has a lower bound. Interestingly, the Q-parameter seems to converge to

$$Q_{\text{analyt}} = \frac{\sqrt{5}-9}{10}\,, \tag{3.34}$$

which is the analytical value that one obtains from a hard dimer model of a hard core nearest neighbor interacting chain [109]. In this model, one uses purely classical arguments, essentially counting the number of states and connections in the state tree (see Sec. 3.2) to obtain a master equation for the probabilities $P(m)$ of m-fold excitation. Calculating the steady state of this master equation for a chain with N equidistant atoms, one obtains the equilibrium

values

$$P(m) = \left(\frac{2}{1+\sqrt{5}}\right)^L \frac{N}{N-m}\binom{N-m}{m} \tag{3.35}$$

from which we calculated Q_{analyt} in the limit of large N. It should be emphasized that we have not strictly proven the existence of a lower bound of Q since due to the high computational complexity, we are limited to relatively small values of N_b. It could well be a coincidence that our numerical results for Q seem to converge to Q_{analyt}. Note that Ref. [138] predicts that for a lattice gas of with hard core interactions Q can come arbitrarily close to -1 for increasing N_b. The question arises if this is also the case for non-hardcore potentials, such as the van der Waals potential. This question and the relation to the results of [138] and [109] will be discussed further in Sec. 3.6.

3.6 Effects of potential shape

This section discusses the question in what way the exponent p in the potential $V(R) = CR^{-p}$ influences the properties of our one-dimensional system. How does the softness of the potential manifest in the dynamics, the pair correlations, and the scaling laws discussed in the previous section? Is there a fundamental difference between finite p and the case of a hard core potential $p = \infty$? This discussion is mainly motivated by the findings of Ref. [138]: For a lattice system with hard core interactions, all accessible states have zero interaction energy. It is argued that therefore in thermal equilibrium all states should be occupied with the same probability. Thus, the equilibrium properties of the system can be deduced just by counting the states with a certain number of excitations m (micro-canonical ensemble). From this reasoning one can derive that for increasing N_b, the excitations should become more and more closely packed, such that the Mandel Q-parameter can get arbitrarily close to -1 and the spatial correlations become arbitrarily strong. These are the properties of a maximum entropy state of a Tonks gas. We previously argued that in the scaling limit ($N_b \gg 1$), the number of excitations approaches $N_{\text{ryd}} = \gamma N/N_b$, with the packing fraction that was found to be $\gamma \approx 0.5$, i.e., every blockade sphere is excited with a probability of $1/2$. The entropic arguments of Ref. [138] now suggest that γ can exceed the value $1/2$ and even approaches unity in the limit $N_b \to \infty$. The question now is if the classical entropic arguments still apply if the dynamics is fully quantum, and if the potential has a finite exponent p. We will not be able to give a definite answer to this question here. The numerical results give some indications but are not conclusive.

For the numerical simulations of this section we varied N, adjusting α^* such that R_b stays constant, by just choosing $C/\Omega = \sqrt{N/L} = \sqrt{n_0}$. That way, we keep the ratio L/R_b constant and vary $N_b = n_0 R_b$. As before, periodic boundary conditions and a relatively large trap size are used in order to eliminate finite size effects. The observables are evaluated after a simulation time that is sufficiently large to assure that the system has evolved into a stationary state. Note that the numerical blockade radius R_c used as a truncation parameter has to be chosen smaller than one for $p < \infty$. For smaller p, i.e., softer potential, the correlation will rise more smoothly outside the blockade region, so we have to choose a smaller R_c. We usually chose R_c such that $V(R_c) = 10V(R_b) = 10\sqrt{N_b}\Omega$.

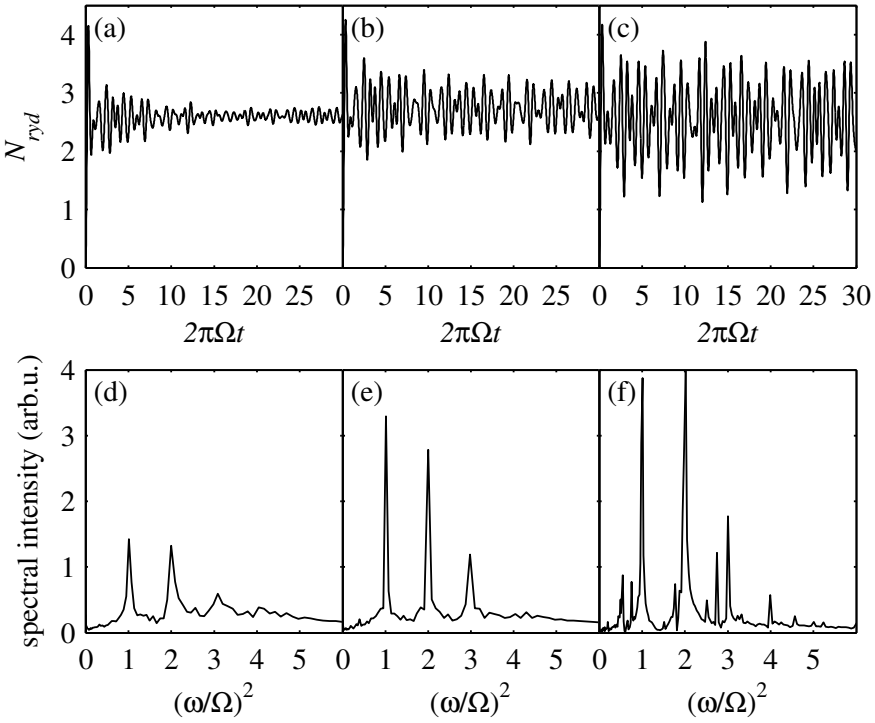

Figure 3.17: Time dependence of the number of Rydberg excitations for a one-dimensional sample of length $L = 10R_b$ containing $N = 10$ atoms. The potential is $V(r) \sim 1/R^p$ with $p = 3$, 6, ∞ in (a), (b), and (c), respectively. (d)-(f) show the Fourier transform of the above time dependence.

3.6.1 Dynamical properties

Here, we study the dynamical properties of the system in the dilute regime ($N_b \sim 1$). Figure 3.17 shows the time evolution of the number of Rydberg excitations in a sample of $N = 10$ atoms in a trap of length $L = 10R_b$. We observe that the larger p, i.e., the more hard core like the potential, the larger the remaining oscillations. This can be understood since for a soft core potential a continuum of interaction energies of the states taking part in the time evolution is probed, while in the case of a hard core potential, all states have vanishing diagonal elements. Calculating the Fourier transform we observe sharp peaks at integer values of $(\omega/\Omega)^2$. The peak at $(\omega/\Omega)^2 = 1$ corresponds to isolated atoms oscillating with the single-atom Rabi frequency Ω. The other peaks correspond to pairs, triples, and so on, of atoms that are within one blockade volume and undergo collective Rabi oscillations, enhanced by a factor of $\sqrt{2}$, $\sqrt{3}$, etc. The fact that for a soft core potential, there will be sets of atoms that are neither perfectly blockaded nor noninteracting, leads to a broadening of the peaks. In other words, the presence of off-resonantly excited atoms adds more frequency components to the system, which leads to a stronger dephasing and flattening of the temporal oscillations.

3.6.2 Pair correlation function

Next, we study the influence of the potential shape on the pair correlation function $g^{(2)}$. In Fig. 3.18 we show the result of a simulation with $N = 30$ atoms in a trap of length $L = 8R_b$,

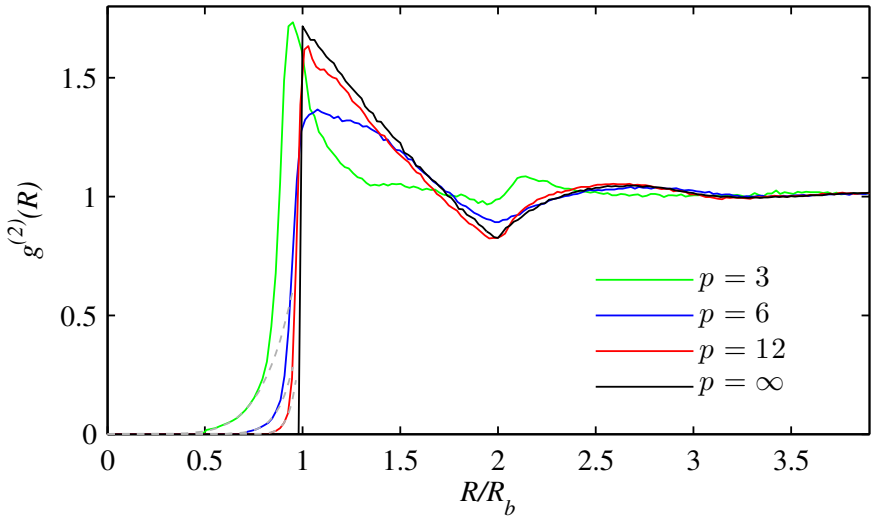

Figure 3.18: Pair correlation function $g^{(2)}$ in a sample of length $L = 8R_b$ containing $N = 30$ atoms for varying potential shape, $V(r) \propto r^{-p}$. These parameters correspond to $N_b = 3.75$. The gray dashed lines are $(R/R_b)^{2p}$. They fit the onset of the correlation function perfectly.

i.e., $N_b = 3.75$. Here, we used the definition $R_b = [C/(\Omega\sqrt{2n_0})]^{1/(2p+1)}$ to scale the abscissa. This choice has proven to be sensible in Sec. 3.5.3. If the exponent p is varied, it makes a difference if the factor of 2 in the denominator is included or not. It turns out that the onset of nonzero correlations is described better by including the 2, as the steepest point of $g^{(2)}(R)$ in Fig. 3.18 is at $R/R_b = 1$ for $p = 6, 12$. For a very soft potential ($p = 3$), the blockade radius is still overestimated. As p becomes larger, the shape of the pair correlation function approaches the hard core case. We can quantify this by observing that for $R \lesssim R_b$ the $g^{(2)}(R)$ is very well approximated by $(R/R_b)^{2p}$, cf. the dashed lines in Fig. 3.18. Note that similar observations have been made for the pairs correlations of the system ground state [291]. We observe that the first correlation peak gets more strongly peaked as p increases, $p = 3$ being an exception again. We conclude that there seems to be a smooth crossover from soft to hard core potential as the exponent p is increased. For very soft potentials ($p = 3$), the shape of $g^{(2)}$ is qualitatively different, from which we conclude that the simple arguments that lead to the estimate of R_b probably are not valid any more in this case.

3.6.3 Excitation number

In order to assess the question whether the packing fraction $N_{\mathrm{ryd}}/m_{\max}$ of excitations can become arbitrarily large in a dense sample, we study this quantity and the Mandel Q-parameter for various potential shapes and varying N_b. The results are shown in Fig. 3.19. As N_b increases, the packing fraction increases in all cases. The larger p, the faster the increase. However, at very large p, the overall value of $N_{\mathrm{ryd}}/m_{\max}$ becomes smaller again. Also the Mandel Q-parameter is minimal for some intermediate p at finite N_b. Here, the fact that for soft potentials, states with $m > m_{\max}$ can be populated, outweighs the effect of smaller probability to populate highly excited states due to their nonvanishing interaction energy. We notice that for $p = 12$, the limit $\gamma = N/m_{\max} = 0.5$ is slightly exceeded, and probably can be exceeded also for lower p at sufficiently large N_b (see also Sec. 3.5, Fig. 3.14). This means that

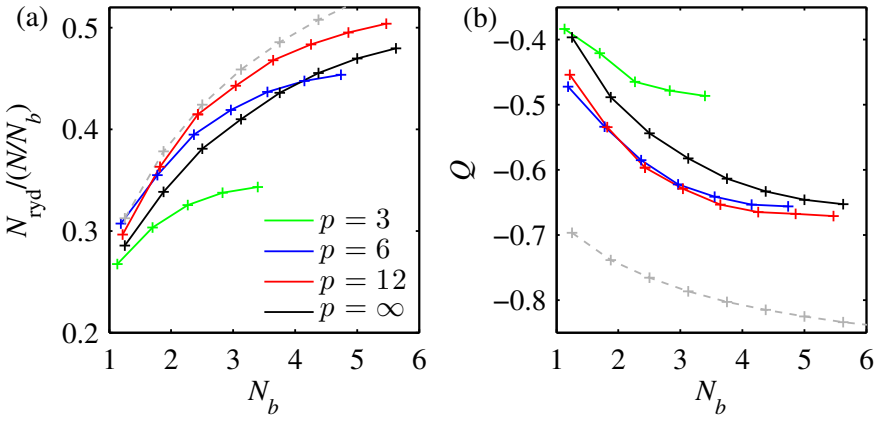

Figure 3.19: (a) Number of Rydberg excitations per blockade sphere and (b) Mandel Q-parameter for varying interaction parameter N_b and potential shape. The sample length is held constant at $L = 8R_b$. Here we used the definition $R_b = [C/(\Omega\sqrt{2n_0})]^{1/(2p+1)}$, including the 2 in the denominator, since for different exponents p this will result in different factors. The gray dashed lines show the predictions of a classical hard rod model.

for soft potentials and fully coherent dynamics, entropic effects, i.e., the fact that there are more accessible states for high excitation numbers than for small ones, can in principle lead to an enhancement of the excited fraction beyond the expectation from a simple super-atom picture. However, the question if there is a limit on the packing fraction for finite p which is smaller than what is expected from the classical arguments, cannot be answered.

In the following, we provide a quantitative comparison to the hard rod model from Ref. [138]. For increasing N_b (increasing atomic density), the scaling limit is approached and microscopic structure of the atomic gas should become irrelevant. In this limit the deviations between lattice case and disordered sample should vanish. Based on this argument it makes sense to compare our numerical findings to the predictions of an analytical calculation that can be done in the case of a lattice gas with hard core interactions and with classical arguments [138]. For a lattice with N sites and periodic boundaries, the number of m-fold excited states, where any excitation blocks l_b neighboring sites from being excited, is

$$\Lambda(m, N, l_b) = N \frac{(N - ml_b - 1)!}{m![N - m(l_b + 1)]!} \,. \tag{3.36}$$

This can be calculated using combinatoric arguments similar to the ones used in Ref. [138]. Under the assumption that all accessible states are populated with same probability, we can immediately deduce the number of Rydberg excitations

$$N_{\text{ryd}} = \frac{\sum_m m\Lambda(m, N, l_b)}{\sum_m \Lambda(m, N, l_b)} \tag{3.37}$$

and similarly the Mandel Q-parameter.

The analytic prediction is depicted as a gray dashed line in Fig. 3.19. We observe that the qualitative behavior is predicted correctly, however, the number of excitations is overestimated, and the Q-parameter strongly underestimated. Thus, the hard rod model fails to describe the dynamics in a fully coherent system, which one should probably expect due to

the purely classical nature of this ansatz. Nevertheless, it would be interesting to investigate if consistency with the hard rod model is reached in the presence of strong dissipation, e.g., caused by laser dephasing.

3.7 Off-resonant excitation of Rydberg aggregates

In this section we allow the laser detuning Δ to be different from zero. In the blue detuned case ($\Delta > 0$) we encounter completely different physics than in the resonant case. We find that the dynamics is dominated by resonant excitation channels in this regime. These lead to strongly peaked spatial correlations associated with characteristic features in the spatial excitation density, the Mandel Q parameter, and the total number of excitations. As an application an implementation of the three-atom CSWAP or Fredkin gate with Rydberg atoms is discussed. The gate not only exploits the Rydberg blockade, but also utilizes the special features of an asymmetric geometric arrangement of the three atoms.

Our discussion of quasi-crystalline structures is partly motivated by previous work that we shortly outline in the following. It has been predicted that spatial pair correlations can be induced in a three-level Rydberg gas via the so-called anti-blockade arising from resonant excitations due to single-atom Autler-Townes splitting [99]. These correlations could be measured based on mechanical forces due to the vdW interaction. The induced particle motion leads to an encoding of position correlations into a time-dependent Penning ionization signal [40]. Interestingly, in this way, spatial information is gained without a spatially resolved measurement. Following these works on spatial properties of pairs of Rydberg atoms in large ensembles, it was subsequently shown that also the Rydberg ensemble as a whole could form crystalline structures in the Rydberg excitation density [146, 148]. In a repulsive vdW gas of Rydberg atoms, it can be energetically favorable for a given number of excitations to assume a highly ordered, crystalline state, with distances between the excitations maximized. If the laser detuning acts opposite to the interaction contribution, these ordered states become the quantum mechanical ground state of the system. It was proposed that such ground-state crystals (GSC) could be produced using chirped laser pulses [142, 146, 148]. The chirp of the laser driving induces adiabatic passage to the energetically most favorable state corresponding to the crystalline excitation structure. For dipole-dipole interacting spins in a lattice configuration a scheme for growing ordered structures by using resonant excitation processes similar to the ones discussed here has been proposed recently [297].

Here, we systematically discuss the properties of a one-dimensional sample of van der Waals interacting atoms subject to off-resonant coherent laser driving. We start by recalling the state space and Hamiltonian and show how it is affected by changing the laser detuning. We show for few atoms how resonant excitation channels arise and discuss the characteristic distances and time scales that are associated with these. Studying the time evolution in an extended sample, we re-encounter these time scales. Furthermore we show how resonant excitation channels manifest themselves in different observables like pair correlation function, excitation density, and excitation statistics. Finally, we show how the emerging resonantly excited spatial structures can be exploited to implement a quantum gate.

Note that in this section, we will denote the inter-atomic distance with r instead of R, and the Rydberg state will be called $|e\rangle$ instead of $|r\rangle$.

3.7.1 State space and resonant excitation channels

In order to be able to interpret the numerical results obtained in this section we will revisit the structure of the Hamiltonian and introduce some useful ways to visualize the state space and Hamiltonian. Recall that the system Hamiltonian written in canonical product states has the diagonal elements

$$E_{\text{diag}} = \langle m; i_1 \dots i_m | \, H \, | m; i_1 \dots i_m \rangle = -m\Delta + \sum_{s<l} V_{i_s i_l} \,, \tag{3.38}$$

where we sum over the interaction energies of all pairs of Rydberg excited atoms. Two basis states are Rabi coupled if they differ only in the state of one atom. For $\Delta \neq 0$ it is convenient to employ a bare state picture in which one depicts the diagonal elements of each state. The Rabi couplings then mix energetically close states. An example is given in Fig. 3.20, where the bare energies of all states in a sample of $N = 20$ atoms in a trap of length $L \approx 3r_b$ are depicted. The gray dashed line shows the cutoff energy E_{cut}. States with higher energies are discarded since they will not be populated during the time evolution. In the case of $\Delta = 0$, the singly excited states are degenerate with the zero-excitation state. In each m-manifold, the state with lowest energy is the one with maximal distances between the interactions. These are the crystalline states that can be prepared by a chirped laser pulse as mentioned above [142, 146, 148]. If we now add a detuning $\Delta > 0$, the m-fold excited states get shifted down in energy by $m\Delta$. We note that now in our example in Fig. 3.20, the $m = 3$ minimal energy state is the ground state of the system. If the detuning is negative, the states shift upwards and the ground state is always the state $|0\rangle = |g \dots g\rangle$. Therefore, doing an adiabatic sweep from $\Delta < 0$ to $\Delta > 0$, one can prepare the crystalline ground state. In our case, however, we switch on the excitation laser instantaneously, meaning that we quench the system from $\Delta = \Omega = 0$ to some finite values of these parameters. In this case, the relevant states are the ones that are near degenerate with the initial state $|0\rangle$. The singly excited states are always detuned by Δ. For higher excited states, at positive detuning, the interaction energy can compensate the detuning and, for example, atom pairs can be excited resonantly. In Fig. 3.20 we highlighted two states: First, the resonantly excited pairs, fulfilling

$$0 = -2\Delta + V(r_{\text{res},2}) = -2\Delta + \frac{C_6}{r_{\text{res},2}^6} \rightarrow r_{\text{res},2} = \left(\frac{C_6}{2\Delta}\right)^{1/6} , \tag{3.39}$$

are resonantly excited from $|0\rangle$ by a two-photon process. Second, if there is already an excitation present, further excitations can be created resonantly at a distance defined by

$$-\Delta = -2\Delta + V(r_{\text{res},1}) = -2\Delta + \frac{C_6}{r_{\text{res},1}^6} \rightarrow r_{\text{res},1} = \left(\frac{C_6}{\Delta}\right)^{1/6} . \tag{3.40}$$

These two characteristic distances will be crucial for interpreting the many-body dynamics of extended samples. In principle, there could also be higher order resonant processes, like the simultaneous excitation of three atoms. However, if more than two excitations are involved, there is no unique resonant distance, which makes it very difficult to observe these processes. Moreover, the resonances would be very narrow and the corresponding process would take place on a very slow timescale as we will see in the following.

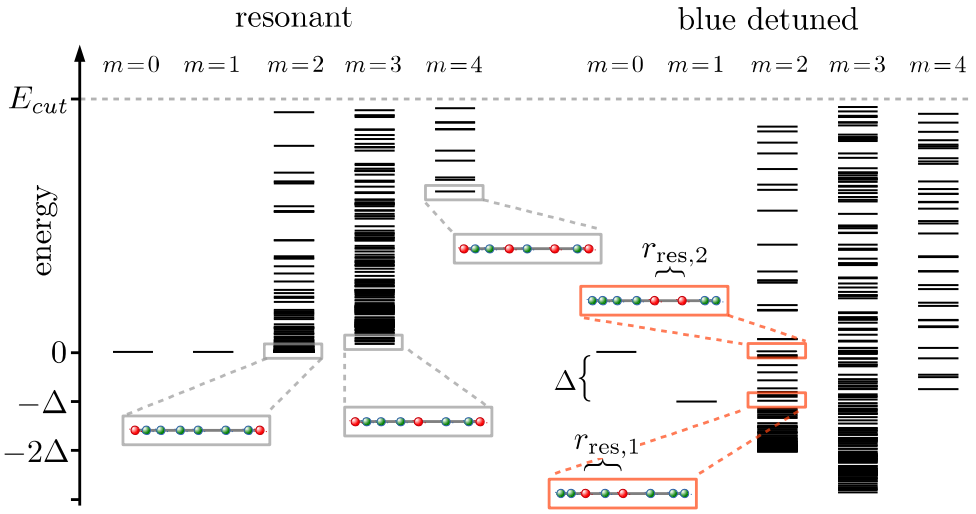

Figure 3.20: Bare energies (diagonal elements) for a one-dimensional sample of length $L \approx 3r_b$ containing $N = 20$ atoms. The lowest energy states of every manifold of m-fold excited states show a crystalline structure of excitations. In the blue detuned case the states are shifted to lower energies by $m\Delta$. Pair states ($m = 2$) are degenerate with the state $|0\rangle$ if the two excitation are at the resonant distance $r_{\mathrm{res},2}$. For the chosen detuning the state with lowest energy is the triply excited state with maximal distance between the excited atoms.

Already in the two-atom case $r_{\mathrm{res},2}$ and $r_{\mathrm{res},1}$ are encountered. In this case we can exploit the symmetry of the system and use the symmetric and anti-symmetric singly excited states

$$|s\rangle = \frac{1}{\sqrt{2}}(|ge\rangle + |eg\rangle) \tag{3.41a}$$

$$|a\rangle = \frac{1}{\sqrt{2}}(|ge\rangle - |eg\rangle) \tag{3.41b}$$

instead of $|g\rangle$ and $|e\rangle$. The anti-symmetric state is not Rabi-coupled to $|gg\rangle$ or $|ee\rangle$, so we can neglect it. Then, in the basis $\{|gg\rangle, |s\rangle, |ee\rangle\}$, the Hamiltonian for two atoms reads

$$H_{\text{2-atom}} = \begin{pmatrix} 0 & \Omega/\sqrt{2} & 0 \\ \Omega/\sqrt{2} & -\Delta & \Omega/\sqrt{2} \\ 0 & \Omega/\sqrt{2} & -2\Delta + V \end{pmatrix}. \tag{3.42}$$

Figures 3.21(a) and (b) illustrate the spectrum of this Hamiltonian for varying detuning (a) and varying inter-atomic distance (b). This shows that our picture of bare states being coupled only if they are near degenerate with each other is valid if $\Delta \gg \Omega$ (here $\Delta/\Omega = 5$): Deviations from the bare energies (dashed lines) only happen at avoided crossings, i.e., when two bare states become degenerate, which was exactly the resonance condition we introduced above. We notice that the avoided crossing between $|gg\rangle$ and $|rr\rangle$, corresponding to the pair resonance, is much narrower than the other ones. This is because those states are only indirectly coupled via the singly excited one. For $V = 2\Delta$, the eigenvalues can indeed be calculated analytically, yielding a width $\Delta E = 2\Omega^2/V$ of the crossing in the limit for $\Omega \ll \Delta$.

Having diagonalized the Hamiltonian, we can do some simple quantum mechanics and write

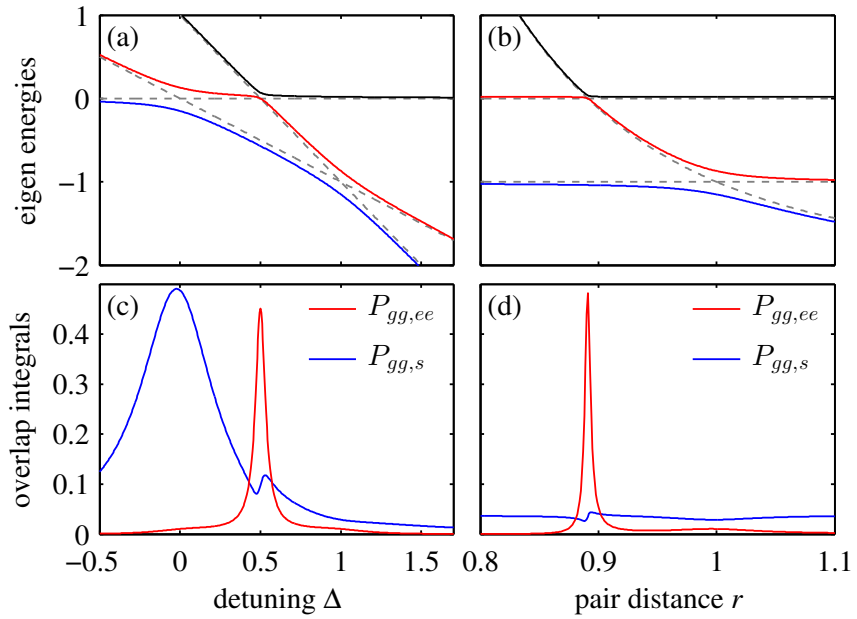

Figure 3.21: Eigenenergies and overlap integrals of the two-atom Hamiltonian. The dashed lines denote the bare state energies. In (a) and (c) the interaction energy is fixed at $V = 1$, while the detuning is varied. In (b) and (d) we vary the pair distance r in $V(r) = r^{-6}$, while the detuning is fixed at $\Delta = 1$. The Rabi frequency is $\Omega = 0.2$ in both cases.

down the time-evolution for the initial state $|gg\rangle$ in terms of the eigenstates $|\phi_k\rangle$:

$$|\psi(t)\rangle = e^{-iHt}\,|gg\rangle = e^{-iHt}\sum_k |\phi_k\rangle\,\langle\phi_k\,|gg\rangle = \sum_k e^{-iE_k t}\langle\phi_k\,|gg\rangle\,|\phi_k\rangle\,. \tag{3.43}$$

The probability of finding the system in some final state $|f\rangle$ after time t is

$$\begin{aligned} |\langle f\,|\psi(t)\rangle\,|^2 &= \left|\sum_k e^{-iE_k t}\langle\phi_k\,|gg\rangle\,\langle f\,|\phi_k\rangle\right|^2 \\ &= \sum_k |\langle\phi_k\,|gg\rangle\,|^2\,|\langle f\,|\phi_k\rangle\,|^2 + \text{terms} \propto \cos\left(\Delta E_{kl} t\right). \end{aligned} \tag{3.44}$$

Upon taking the time average over this expectation value, the oscillating terms will vanish and only the first term

$$\left\langle |\langle f\,|\psi(t)\rangle\,|^2\right\rangle_t = \sum_k |\langle\phi_k\,|gg\rangle\,|^2\,|\langle f\,|\phi_k\rangle\,|^2 \equiv P_{gg,f}\,, \tag{3.45}$$

which we call the *overlap integral*, remains. This quantity is a measure for degree to which the base states $|gg\rangle$ and $|f\rangle$ get mixed by the Rabi coupling. In Figs. 3.21(c) and (d) we show the overlap between the ground state and the singly and doubly excited state. The width of the pair resonances can be calculated analytically by calculating the Taylor series of $P^{-1}_{gg,ee}$ in $\delta = V - 2\Delta$ to second order around $\delta = 0$. Expanding numerator and denominator to second

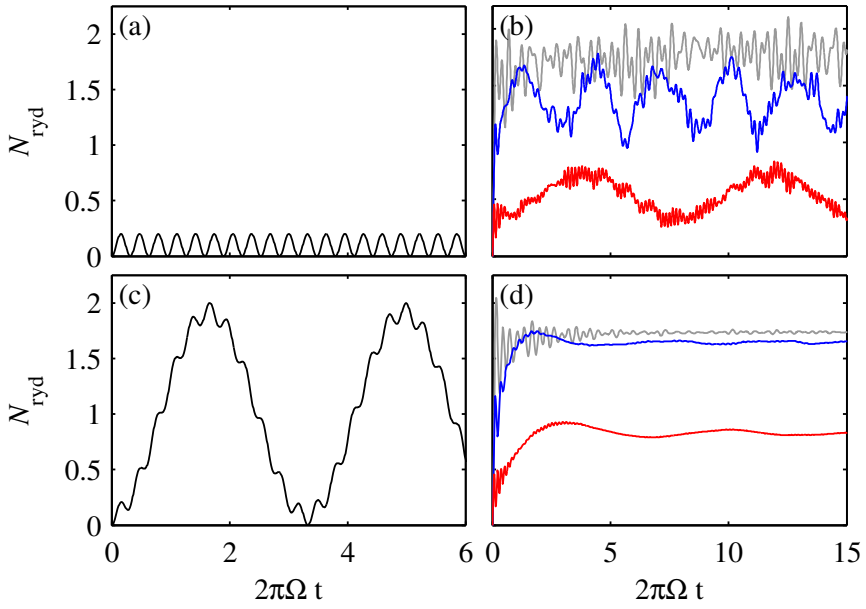

Figure 3.22: (a) and (c) show the time evolution of the number of Rydberg excitations for two atoms with $V = 0$ (a) and $V = 2\Delta$ (c). The detuning is $\Delta = 3\Omega$ in both cases. (b) shows the time evolution for the sample from Fig. 3.20 for different detunings: $\Delta = 0$ (gray), $\Delta = 3\Omega$ (blue), and $\Delta = 6\Omega$ (red). In (d) we have averaged the result from (b) over 1000 random position samples.

order in Ω/Δ and neglecting terms proportional to $\delta^2\Omega^2/\Delta^2$ one obtains a Lorentzian

$$P_{gg,ee} \approx \frac{1}{2}\frac{1-\frac{\Omega^2}{\Delta^2}}{1+\frac{\delta^2}{\Omega^2}\left(1+\frac{\Delta^2}{\Omega^2}\right)} = \frac{1}{2}\frac{1-\frac{\Omega^2}{\Delta^2}}{1+\frac{\delta^2}{(\Gamma_\delta/2)^2}} \tag{3.46}$$

with the energetic resonance width

$$\Gamma_\delta = \frac{2\Omega^2}{\sqrt{\Omega^2+\Delta^2}}\,. \tag{3.47}$$

We have checked that this fits the numeric values of $P_{gg,ee}$ around the two-photon resonance perfectly for large Δ/Ω. Linearizing the potential around $r_{\mathrm{res},2}$ we can translate this into the spatial resonance width

$$\Gamma = \Gamma_\delta \left(\frac{dV}{dr}\right)^{-1}_{r=r_{\mathrm{res},2}} = \frac{1}{6}\frac{\Omega^2}{\Delta\sqrt{\Omega^2+\Delta^2}}\left(\frac{C_6}{2\Delta}\right)^{1/6}. \tag{3.48}$$

This result will be used in Sec. 3.7.3 to fit the resonance width of the pair correlation function in the many-atom case. We also observe, that there is a flat maximum in $P_{gg,ee}$ at $V = \Delta$. Thus, pair excitation is also slightly enhanced at the one-photon resonance. In extended samples, this will be buried in the resonant excitation to higher excited states ($m > 2$), that happens at a distance $r_{\mathrm{res},1}$ from a previously present excitation.

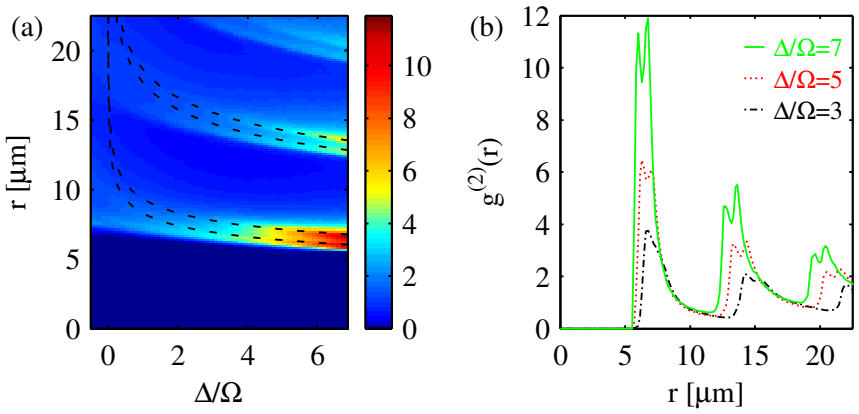

Figure 3.23: (a) Pair correlation function $g^{(2)}(r)$ as a function of interparticle distance r and detuning Δ. Dashed lines are theoretical prediction for resonance positions as explained in the main text. (b) Sections through (a) at detunings $\Delta/\Omega = 3, 5, 7$. Parameters are $L = 30\,\mu$m, $N = 30$, $\Omega = 10\,$MHz, and $C_6 = 6.6\,\text{THz}\,\mu\text{m}^6$.

3.7.2 Time dependence of the excitation number

The spectral features encountered in the previous section translate into characteristic time scales in the time evolution: For noninteracting atoms, the detuning leads to fast off-resonant Rabi oscillations with amplitude $\Omega^2/(\Omega^2+\Delta^2)$ and frequency $\sqrt{\Omega^2+\Delta^2}$. The sharp avoided crossing associated with resonant pair excitation on the other hand leads to the emergence of slow oscillations between $|gg\rangle$ and $|ee\rangle$ with frequency Ω^2/Δ, that completely invert the population. This is shown in Figs. 3.22(a) and (c), where the time evolution for $V = 0$ and $V = 2\Delta$ is shown. The Rabi frequency is $\Omega = \Delta/3$ in this case. These time scales are again encountered in an extended sample as illustrated in Figs. 3.22(b) and (d). Here, we simulated the dynamics of a one-dimensional sample of $N = 20$ atoms in a trap of length $L \approx 3R_b$ as in Fig. 3.20 for different detunings. We also show the resonant case ($\Delta = 0$) for comparison. In the resonant case, the collective Rabi frequency $\Omega_c = \sqrt{N_b}\Omega$ was the characteristic time scale of oscillations. In the detuned case we observe slow oscillation stemming from resonant pairs, modulated by fast oscillation from off-resonantly excited atoms. This shows that in the detuned case a lot of the physics going on in the many-body case is already captured by the two-atom case. For the time scale of thermalization this implies that for large detuning it can take exceedingly long to reach a steady state of the Rydberg population. This observation will be discussed further in Sec. 3.7.4 and 3.8.

We thus found that resonant excitation of pairs is associated with a very sharp resonance peak and a slow time evolution for $\Delta \gg \Omega$. For higher order processes, e.g., the direct excitation of triples, the resonance width would be even smaller and the corresponding time scale even slower. Also, such higher order processes are suppressed in the presence of decoherence as we will find in Sec. 3.8.

3.7.3 Spatial correlations

Here we show that characteristic geometric excitation structures form out of the homogeneous cloud of atoms under continuous laser driving. For this we study the pair correlation function

that was introduced in Sec. 3.3 as

$$g^{(2)}(r) = \frac{1}{N_p(r)} \sum_{i,j}{}' \frac{\langle s_{ee}^i s_{ee}^j \rangle}{\langle s_{ee}^i \rangle \langle s_{ee}^j \rangle} , \tag{3.49}$$

where $\sum_{i,j}'$ sums over pairs with distance in $[r, r + \Delta r]$ and $N_p(r)$ is the total number of such pairs. Recall that $g^{(2)}(r)$ is a measure for the conditioned probability for an excitation if another excitation is already present at a distance r. As shown in Fig. 3.23, pronounced resonances emerge in $g^{(2)}$ at regularly spaced distances for detunings $\Delta > \Omega$. A closer look at Fig. 3.23 reveals a sequence of double resonances. The first resonance at lowest inter-particle distance is caused by resonant pair excitation in which the ground state is resonantly coupled to a doubly excited state via two-photon excitation if $2\Delta = C_6/r_{\mathrm{res},2}^6$. We identified the second maximum at slightly higher r as the resonant transition from an m-fold to an m+1-fold excited state, satisfying $\Delta = C_6/r_{\mathrm{res},1}^6$. The two conditions are shown as dashed lines in Fig. 3.23(a) and coincide very well with the maxima of $g^{(2)}$ from the numerical simulation results. We can thus directly trace back the emergence of spatial correlations in a homogeneous many atom sample to resonant excitation channels. Starting from a doubly-excited state with inter-atomic distance $r_{\mathrm{res},2}$, a triply excited state emerges by resonant excitation of a third atom at a distance $r_{\mathrm{res},1}$ from one of the original Rydberg excited atoms. This is also illustrated in Fig. 3.24(a) where we show the bare energies (diagonal elements of the Hamiltonian) as a function of the detuning. This is basically the same as Fig. 3.20 but now with continuously varying Δ. It can be seen that, as long as the density of states is sufficiently high around zero energy, pair states and triplet states are available that can be excited resonantly. For the later analysis it is crucial to note that due to the mutual interaction shifts, the third atom has distance $r_{\mathrm{res},1} \neq r_{\mathrm{res},2}$, such that an asymmetric three-particle structure is created. This triplet causes the third resonance line at $r_{\mathrm{res},1} + r_{\mathrm{res},2}$ in Fig. 3.23(a). Subsequent resonances originate from higher-excited states, which most likely occur again at distances $\approx r_{\mathrm{res},1}$ from the respective previous structures. In total, for highly excited states, a regular chain of atoms with a single "defect" formed by the initial pair of atoms is created.

Interestingly, the triply excited state is distinguished by a ratio $r_{\mathrm{res},1}/r_{\mathrm{res},2} = 2^{1/d}$ for an interaction potential $V \sim 1/r^d$, independent of the trap size and the laser parameters. In this sense, the interaction potential leads to a self-assembly of asymmetric excitation structures. This invites applications exploiting the robust and definite asymmetric spatial configuration with distances $r_{\mathrm{res},1}$ and $r_{\mathrm{res},2}$ between the excitations, created out of a homogeneous cloud of atoms. An example for this will be discussed in Sec. 3.7.6.

Next, we analyze the structure of the spatial correlations at high detunings in more detail. Figure 3.23(b) shows that the pair correlation resonances become narrower with increasing detuning. The origin of this effect is illustrated in the inset of Fig. 3.24(b). The resonances are of Lorentzian shape in energy space as a function of the detuning. The interaction potential $V(r)$ translates this dependence on the detuning into a distance dependence. For the same energy-resonance width, the position-space resonances become narrower as the distance decreases at which the laser moves into resonance. Hence, an increase of the detuning leads to a reduction of the resonant width. For the particular case of a two-photon resonance, the energetic resonance width depends on the detuning itself. To quantify this, we studied the width of the resonance in the overlap integral $P_{gg,ee}$ above, see Eq. (3.48). Alternatively, one

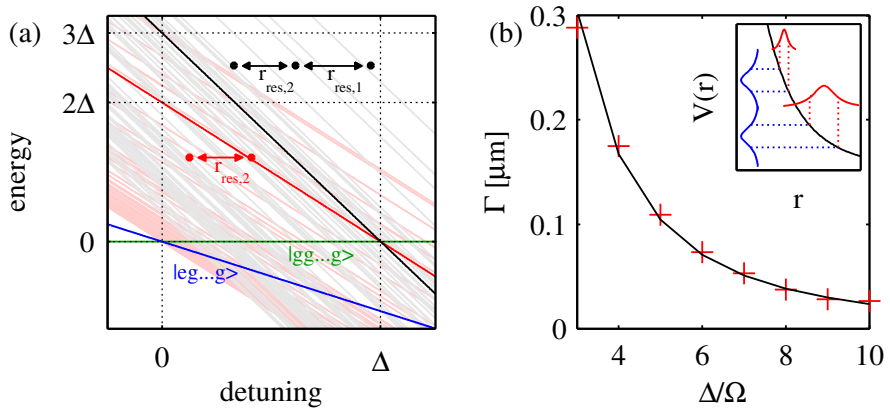

Figure 3.24: (a) Illustration of the resonant excitation channels. Bare state energies [diagonal part of the Hamiltonian (3.38)] as a function of the laser detuning. We used a sample of 16 atoms randomly placed in a one-dimensional trap. The energy of m-fold excited states decreases with slope m. The solid red and black line mark states that can be resonantly couples to from the ground state for a certain detuning Δ. Note that in a dressed state picture (eigenstates of the Hamiltonian) all the crossings would become avoided. (b) Dependence of the two-photon excitation line width on the detuning. The solid line is obtained from Eq. (3.50), red crosses are obtained from the numerical simulations. The inset shows the detuning-dependent transformation of energetic resonances into spatial resonances via the interaction potential $V(r) = C_6/r^6$.

can adiabatically eliminate the singly excited states in the two-atom problem. This is valid if Δ is much larger than both, Ω and the two photon detuning $V - 2\Delta$. The resulting effective Rabi frequency is Ω^2/Δ, which means that the full width of the resonance with respect to the two photon detuning (power broadening) is $2\Omega^2/\Delta$. Linearizing the potential around $r_{\mathrm{res},2}$ we obtain the position-space width of the two photon resonance

$$\Gamma = \frac{2\Omega^2}{\Delta}\left(\frac{dV}{dr}\right)_{r=r_{\mathrm{res},2}} = \frac{1}{6}\frac{\Omega^2}{\Delta^2}\left(\frac{C_6}{2\Delta}\right)^{1/6}. \tag{3.50}$$

As shown in Fig. 3.24(b), the numerical simulation data fully agrees with Eq. (3.50) up to an overall prefactor of about 2 due to additional atoms in the trap which broaden the resonance compared to the idealized two-atom case. Note that, since the potential is not strictly linear across the width of the resonance, the spatial shape of the resonance peaks is asymmetric.

In summary, we find that in the limit of large Δ, the position-space two-photon resonance width decreases as $\Delta^{-13/6}$. Therefore, in our model, resonant excitations are only possible at definite positions with lattice spacings determined by the shape of the interaction potential. In the limit of large detuning all features of the pair correlation function can be understood in terms of two-atom properties.

3.7.4 Excitation density and excitation statistics

Number of Rydberg excitations

After having established the formation of stronger spatial ordering with increasing detuning, we now address the question how this ordering manifests itself in various observables related to the spatial distribution of Rydberg excitations. We start with the number of Rydberg

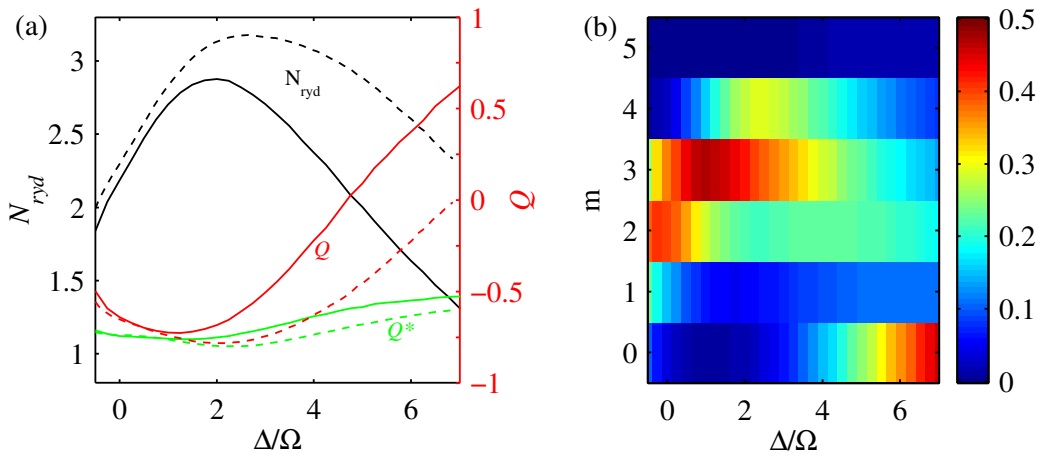

Figure 3.25: (a) Total number of excited atoms and Mandel Q parameter as a function of the detuning. Q^* is the corresponding parameter evaluated without the ground state fraction. Solid lines show $N = 30$; dashed lines show $N = 45$. C_6 and L are as in Fig. 3.23. (b) The probabilities P_m to find exactly m excitations for the case of $N = 30$ atoms.

excitations N_{ryd}. Fig. 3.25(a) shows that N_{ryd} increases with detuning starting from the resonant case, at some positive detuning assumes a maximum, and then decreases towards larger values of Δ. The initial increase can be attributed to the presence of the off-resonant excitation channels at positive detuning, which also lead to a better packing of the Rydberg excitations. However, with increasing detuning, the spatial excitation resonances become more narrow, as shown in Fig. 3.24(b). Therefore, the number of atom pairs with distance compatible with the resonant distance reduces. Consequently, starting from a certain critical detuning, the total number of excited atoms decreases with increasing Δ. For higher densities, this effect is expected to set in at higher detunings, since at a given resonance width, the number of pairs having a distance within the resonant range increases with density. This is supported by our numerical simulation data, as the maximum of the number of Rydberg excitations N_{ryd} is shifted to higher detunings for higher densities, see Fig. 3.25(a).

Rydberg excitation statistics

Next we investigate the distribution of the number of excitations, which is characterized by the Mandel Q parameter which was defined in Sec. 3.3 as

$$Q = \frac{\langle \hat{N}_{\mathrm{ryd}}^2 \rangle - \langle \hat{N}_{\mathrm{ryd}} \rangle^2}{\langle \hat{N}_{\mathrm{ryd}} \rangle} - 1 \,. \tag{3.51}$$

For a Poissonian distribution of excitation numbers, like in a coherent state, the Q parameter is zero, while for sub-Poissonian statistics it is negative. In previous proposals on GSC, for a given detuning, a definite number of excitations was predicted in the system, as illustrated in Fig. 3.20. Then, ideally Q reaches the value -1 for a Fock state.

In contrast, Fig. 3.25(a) shows that in our setup, the Q parameter assumes a minimum at a detuning close to that of the maximum in N_{ryd}, but then increases again towards larger Δ.

The interpretation of this result is related to the behavior of N_{ryd}. The underlying mechanism is connected to the slowdown of the dynamics that we observed in Fig. 3.22 and finite density of pair state that decreases as Δ is increased. For small positive detuning, the resonant channels for ordered excitation structures lead to a decrease of Q.

However, towards larger detunings, i.e., smaller spatial resonance widths (or equivalently decreasing state space density of pair states around zero energy), there is an increasing probability that there are few or even no atom pairs at the resonant distance in the ensemble. Furthermore, the spatial width of the resonant pair excitation (aggregate nucleation) decreases faster with the detuning than the width for subsequent resonant excitation of further atoms (aggregate growth). Therefore, once a resonant pair is excited, there is a high probability that further atoms connected to this initial seed are excited subsequently. This then leads to a nonzero probability to detect no excitation at all and at the same time to the emergence of aggregates of size two and higher, while the population of singly excited states is very low. Another effect reducing excitation density at finite time is the slowdown of the dynamics at large detuning. In terms of the bare state picture: In order to reach higher excited states the population has to pass the bottleneck of the far detuned singly excited state, which gets increasingly difficult as Δ/Ω is increased. A signature for this effect is that at large detunings, the system evolves into a bimodal excitation distribution, with one fraction in the ground state, and the second fraction distributed around a parameter-dependent excitation number. This observation is supported by corresponding results shown in Fig. 3.25(a) for Q^*, which is the ordinary Q parameter evaluated without the ground state fraction. It can be seen that Q^* remains low even for higher detunings Δ. The probability of m-fold excitation is depicted in Fig. 3.25(b) clearly showing that at large detuning the population of the zero-excitation state increases again. Another way of interpreting the bimodality, or suppression of the singly excited state, is already possible in the two-atom picture: In the regime, where resonant excitation of pairs is the dominant mechanism, these pairs will evolve into a superposition of $|gg\rangle$ and $|ee\rangle$, as we have learned from the two-atom case. The singly excited states can even be eliminated. If resonant pair excitation dominated over off-resonant excitation of single atoms, this effect will lead to a suppression of the population of singly excited states. This interpretation is in principle equivalent to the picture of a slowdown of the excitation transport from $m = 0$ to $m = 2$ due to the large detuning intermediate state with $m = 1$.

We thus conclude that in the present case of off-resonantly excited Rydberg gases, super-Poissonian rather than sub-Poissonian excitation statistics are a sign of ordered structures and the buildup of strong correlations, in contrast to the properties of the GSC.

Position-resolved Rydberg excitation density

The sharply peaked $g^{(2)}$-function in Fig. 3.23 indicated that the distances between excitations predominantly are multiples of the resonant excitation distances. However, interestingly, this does not translate into a peaked structure in the spatially resolved excitation density. Fig. 3.26(a) shows that at high detuning, the excitation density has a rather complicated step-like dependence on the position. This can be explained with a geometric argument: If we consider, e.g., the doubly excited states, we notice that these are only populated if the distance between the excited atoms is the resonant one. If we now ask how such a pair of excitations with fixed distance can be placed in the 1d ensemble volume, and assume that each

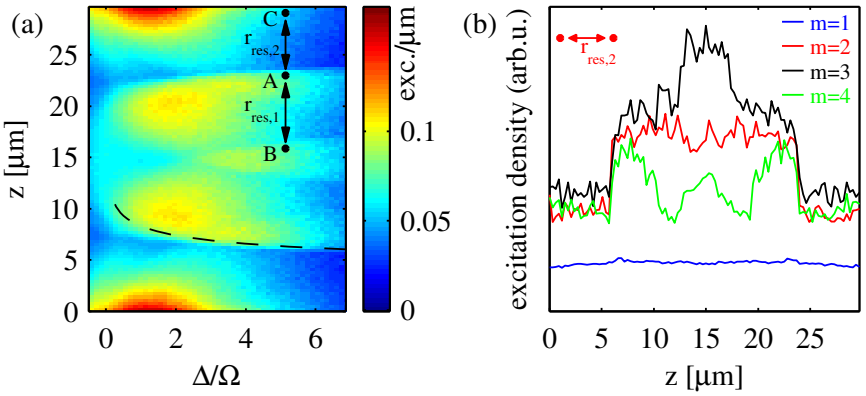

Figure 3.26: (a) Rydberg excitation density in excitations per μm vs. position in the 1d trap and detuning. Dashed line: resonance line corresponding to $2\Delta = C_6/r^6$ as explained in the text. (b) Excitation density for $\Delta/\Omega = 7$ split into excitation-number subspaces.

of these possibilities is realized with equal probability, it becomes clear that atoms located within one resonant radius from the ends of the trap are excited only half as often as atoms at the center. This explains the outermost edges in the excitation density. The dashed line in Fig. 3.26(a) indicates the position $r_{\mathrm{res},2}$ away from one edge of the ensemble coinciding with the position of the step in excitation density, clearly supporting this interpretation. The other edges can be explained analogously, taking into account higher excited states. Note that this reasoning only applies if the detuning is significantly larger than the Rabi frequency and sharp spatial resonances are present. For small detuning $|\Delta| \lesssim \Omega$ the excitation density is maximal at the edges of the trap. This is the kind of finite size effect that was discussed is Sec. 3.4. In a mean field picture it can be understood as follows: For atoms close to the edges the interaction shift is smaller since they only have potentially excited neighbors only to one side. The characteristic features of excitation density at large detuning are also illustrated in Fig. 3.26(b) in which the excitation density is split up into contributions of states with different excitation numbers. Again, e.g., the plateau-structure of the doubly excited states confirms the above reasoning. In higher dimensions the condition of resonant excitation is fulfilled for various positions of the third excitation and thus it is less localized. These results indicate a second fundamental difference of the regular structures found in our setup from previous proposals. The GSC are located at fixed positions relative to the trap borders. In our case, however, the resonant excitation structures are not fixed relative to the ensemble, but can *float* over a certain position range in the atom gas from realization to realization. This leads to the characteristic differences in the excitation density shown in Fig. 3.26.

3.7.5 Dynamical buildup of correlations

To reveal the emergence of spatial order in our setup, a measurement as illustrated in Fig. 3.27 could be performed. In each run, a certain excitation pattern is obtained. To compensate for the floating, the positions of the leftmost excited atoms in the different runs are matched by a shift of the position axis. Then, the shifted data of the different runs are averaged. A histogram of 2000 runs analyzed in this way is shown in Fig. 3.27 and clearly shows the

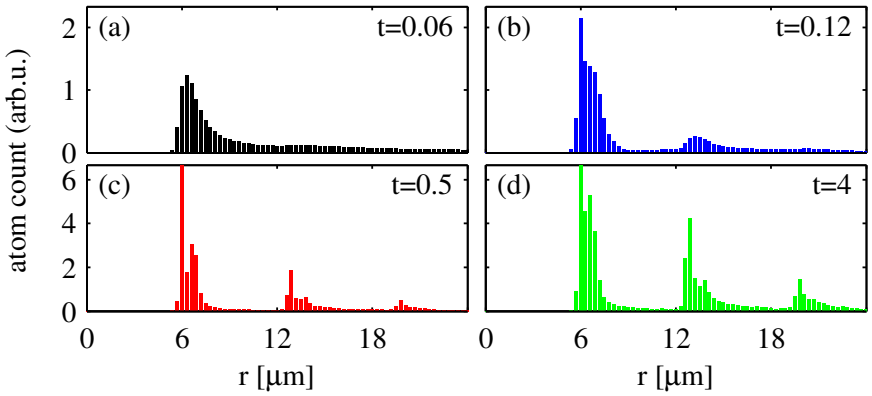

Figure 3.27: Illustration of the aggregate formation: Positions of the excitations are determined from the exact quantum state by a Monte Carlo procedure mimicking a measurement. The distances of the excitations to the leftmost excitation are collected in a histogram. Note that the scale of the ordinate in (c) and (d) differs from (a) and (b). The height of the two-photon resonance is 12 in (c) and 19 in (d). Parameters are as in Fig. 3.23, $\Delta/\Omega = 6$. In (d) the steady state has been reached. Excitation times are given in μs.

strongly peaked structure at long times. At short excitation times the correlation peaks build up successively. Remarkably, after 500 ns the qualitative features of the steady-state situation are present already. Thereafter, only the absolute height of the peaks increases. This successive buildup of correlation peaks can be attributed to a finite propagation speed of entanglement, that was studied in lattice geometries recently [298].

It can be seen from Fig. 3.27 that the correlations decrease with increasing distance, unlike in an ideal crystal. the correlations extend over a multiple of the interaction length scale. In consistence with our interpretations, we found that the characteristic distances between excitations are independent of the ensemble volume.

3.7.6 Quantum gate with asymmetric structures

We now turn to a specific application exploiting the spatially asymmetric excitation structure, and show that the generated spatial structures are optimal in the sense that they maximize the success probability of our proposed application. For this we consider an implementation of a three-particle quantum gate [22, 206, 214, 217]. Based on the approach used in Ref. [48], the excitation structure generated in the first step can be isolated by removing ground-state atoms with a resonant laser pulse, and subsequently mapped onto ground states by resonantly driving a transition to a rapidly decaying p-state. That way, a spatial arrangement of ground-state atoms is prepared, that corresponds to one specific realization of the original excitation structure. In the case that three atoms survive this procedure, their mutual distances are $r_{\mathrm{res},2}$, $r_{\mathrm{res},1}$, and $r_{\mathrm{res},2} + r_{\mathrm{res},1}$, and we denote the three atoms as C, A and B as indicated in Fig. 3.26(a), respectively.

We exploit this asymmetric arrangement of atoms to implement a controlled SWAP or Fredkin gate. Depending on the state of the control atom C, atoms A and B shall interchange their states or not. The qubits are stored in two hyperfine components of the ground state $|0\rangle$ and $|1\rangle$ that can both be coupled to the Rydberg state $|e\rangle$. The gate protocol consisting of five laser pulses is illustrated in Fig. 3.28(a). As an example, two possible evolution sequences

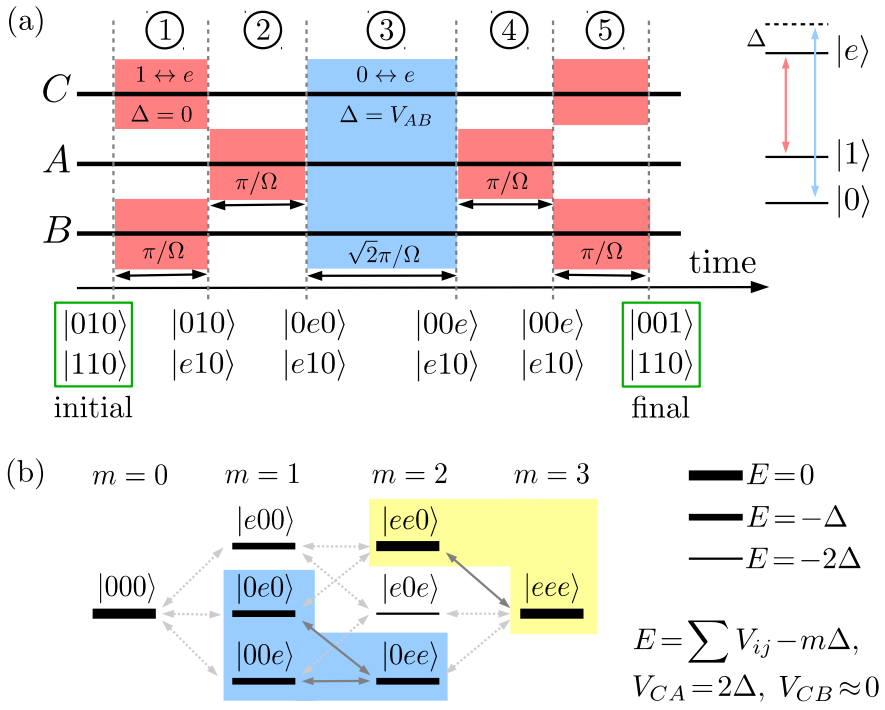

Figure 3.28: (a) Illustration of the gate protocol and level scheme of a single atom. The truth table is given for two exemplary initial states $|CAB\rangle = |010\rangle$ and $|110\rangle$. Depending on the control bit C bits A and B interchange their states, or not. (b) Hamiltonian of the detuned pulse (blue in gate protocol). The thickness of the bars stands for the value E of the diagonal element of the corresponding state (with m Rydberg excitations). Double arrows indicate laser couplings. In the blue subspace, the state $|0e0\rangle$ evolves into $|00e\rangle$ under the $\sqrt{2}\pi$-pulse.

for initial states $|CAB\rangle = |010\rangle$ or $|110\rangle$ out of the full truth table are shown in the bottom part of Fig. 3.28(a).

In step 1, a resonant π-pulse on atoms C and B evolves them to $|e\rangle$ if they are initially in $|1\rangle$, but leaves them untouched if they are in $|0\rangle$. Step 2 is a resonant π-pulse on atom A. Again, it induces excitations of A from $|1\rangle$, but not from $|0\rangle$. However, due to the excitation blockade, in addition the excitation only occurs if neither C nor B are excited. Therefore, atom A is excited in this step for initial state $|010\rangle$, but not for initial state $|110\rangle$, see Fig. 3.28(a). The crucial step is the detuned $\sqrt{2}\pi$-pulse (step 3) in the middle of the sequence applied to all three atoms. The corresponding effective Hamiltonian is shown schematically in Fig. 3.28(b). Because of the detuning, it decomposes into several approximately independent subspaces. Due to this separation, its main effect is an interchange of states $|0e0\rangle$ and $|00e\rangle$. Besides this desired exchange, also $|ee0\rangle$ would be resonantly coupled to $|eee\rangle$ causing unwanted dynamics. However, due to the blockade in the second step, $|ee0\rangle$ and $|eee\rangle$ are never accessed, such that this channel can be neglected. Steps 4 and 5 repeat the first two steps in reverse order, and effectively evolve the atoms back into a superposition of ground states $|0\rangle$ and $|1\rangle$.

We have implemented this five-step sequence on the full three-atom state space and numerically simulated the dynamics. To quantify the quality of the gate for arbitrary input states,

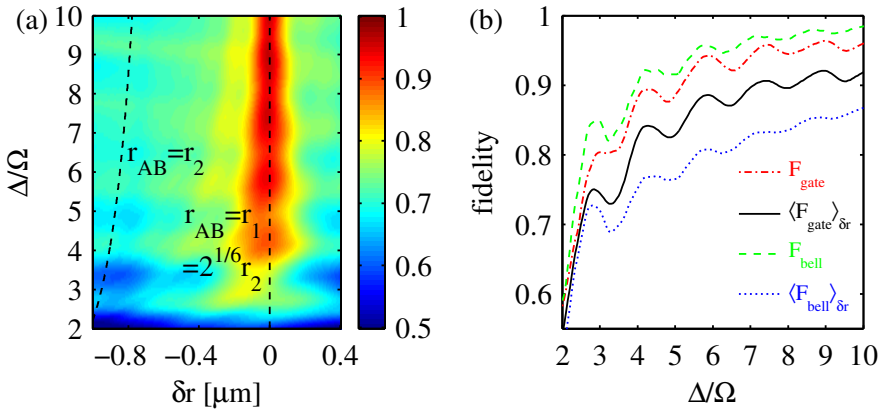

Figure 3.29: (a) Fidelity F_{gate} of the CSWAP gate against detuning Δ and imperfections δr of the spatial arrangement of the three atoms. (b) F_{gate} and F_{bell} for the optimal r_{AB} and averaged over a Lorentzian distribution of distances r_{AB}. The fidelity is relatively insensitive to variations in r_{CA}.

we use the gate fidelity

$$F_{\text{gate}} = \frac{1}{8}\sum_i |\langle\Psi^{(i)}|\Psi_{\text{id}}^{(i)}\rangle|^2\,, \tag{3.52}$$

where $\Psi_{\text{id}}^{(i)}$ and $\Psi^{(i)}$ are the ideal target and the numerically obtained output state, respectively, as well as the confidence F_{bell} with which a maximally entangled state $|\Psi\rangle_{\text{bell}} = (|001\rangle - |110\rangle)/\sqrt{2}$ can be prepared from the unentangled initial state $(|010\rangle + |110\rangle)/\sqrt{2}$. Figure 3.29(a) shows F_{gate} as a function of Δ/Ω and the deviation δr of r_{AB} from $r_{\text{res},1}$. The fidelity increases with Δ/Ω since the decomposition of the Hamiltonian into independent subspaces improves with Δ. We also find that F_{gate} is very sensitive to variations in r_{AB}, and reaches the optimum value only for $\delta r = 0$. In Fig. 3.29(b) results for both, F_{gate} and F_{bell}, with optimized r_{AB} and integrated over the distribution of distances r_{AB} that results from the preparation using the resonant excitation scheme are shown. We notice that the entanglement fidelity is even more sensitive to variations in r_{AB} than the gate fidelity. The reason is that the Bell state preparation strongly depends on the relative phases that the different product states acquire during the gate operation. These phases are more difficult to control, the higher Δ/Ω becomes. Thus they counteract the decreasing coupling between the subspaces of the Hamiltonian and decrease the fidelity.

It is crucial to realize that the required separation of the Hamiltonian into different subspaces only arises due to the asymmetric distances $r_{CA}/r_{AB} \neq 1$. Furthermore, already small deviations in the optimum distance δr lead to a significant degradation of the gate fidelity. In our setup this optimum distance is automatically achieved for each given laser detuning, because the resonantly excited correlated structures are created with atomic distances such that the laser detuning condition required for the gate operation is satisfied. It is in this sense, that the self-assembly of the excitation structures is optimal.

An obvious drawback of the proposed scheme is, that after generating the resonantly excited triples out of a homogeneous sample, one does not know where exactly the atoms are localized due to the floating nature of the excitation structures. This will spoil the required single-atom

addressability. A solution could be to use a dense sample in a small trap that accommodates at most 3 excitations, such that the range for the floating is smaller than the distances between the excitations. However, this still leaves two possible orientations for the created resonant structure. Alternatively, one could use a lattice geometry for the whole protocol. This would have the advantage that after preparing the asymmetric structure, one could determine the positions of the individual atoms, e.g., by fluorescence imaging. The disadvantage would be that the irrational distance ratio of $2^{1/6}$ is difficult to realize. If single-site addressability is achieved, the initial state preparation can be realized by coupling the two hyperfine states by a microwave field. For readout, one could employ state selective fluorescence imaging, as described in Ref. [48].

We also note that there can be additional sources of decoherence that lead to a decrease of the gate fidelity. Decoherence effects beyond the uncertainty of the inter-atomic distances have not been accounted for in our three atom simulations, cf. Fig. 3.29. First, finite laser linewidth could lead to dephasing. Note, however, that state of the art experiments use lasers with linewidths on the order of a few tens of kHz, which should be sufficient to not significantly deteriorate our gate fidelity. Second, probably more severe, is the effect of atomic motion. It has been shown recently [192], that resonantly excited pairs can suffer strong decoherence due to the mechanical repulsion between the Rydberg atoms. Since our gate is an interaction gate, meaning that for certain initial states, the doubly excited state $|0ee\rangle$ is temporarily populated. In this state, the two excited atoms A and B having a distance $r_{\mathrm{res},1} = (V_6/\Delta)^{1/6}$ repel each other due to the van der Waals potential, and will thus start to accelerate. We can use simple classical arguments to estimate how far they can move during the gate time $t_{\mathrm{gate}} = \sqrt{2}\pi/\Omega$. The acceleration they experience initially is

$$a = -\frac{1}{m}\left.\frac{dV}{dr}\right|_{r=r_{\mathrm{res},1}} = \frac{\hbar\Delta}{\mu}\left(\frac{\Delta}{C_6}\right)^{1/6}, \tag{3.53}$$

where $\mu = M_a/2$ is the reduced mass which equals half the atomic mass. The repulsion thus makes the atoms travel a distance

$$dr = \frac{1}{2}at_{\mathrm{gate}}^2 = \frac{\pi^2\hbar}{\mu}\frac{\Delta}{\Omega^2}\left(\frac{\Delta}{C_6}\right)^{1/6} = \frac{\pi^2\hbar}{\mu C_6^{1/6}}\left(\frac{\Delta}{\Omega}\right)^{7/6}\Omega^{-5/6}. \tag{3.54}$$

The last expression shows that dr can be reduced by increasing Ω and keeping Δ/Ω constant. The length scales (resonant distance $r_{\mathrm{res},1}$ and the resonance width Γ) only decrease as $\Omega^{-1/6}$. For the parameters used for the simulations of Fig. 3.29 ($C_6 = 6.6\,\mathrm{THz}\,\mu\mathrm{m}^6$, $\Omega = \Delta/10 = 10\,\mathrm{MHz}$), we obtain $dr = 14\,\mathrm{nm}$, which is much smaller than the width of the fidelity peak in Fig. 3.29(a). However, this does not mean that motional effects are negligible. In order to investigate this thoroughly a full quantum mechanic simulation including the motional degrees of freedom would be necessary. Note, that not only the gate protocol itself but also the preparation of the resonant structures will be influenced by mechanical effects.

3.7.7 Discussion of possible experimental implementations

In summary, we have shown that regular Rydberg excitation structures form at off-resonant laser driving. These structures differ from previously studied ground-state crystals, as their

characteristic distances are independent of the ensemble length, as they are not localized relative to the gas, and as the Mandel Q parameter, the Rydberg excitation density and the total number of Rydberg excitations yield qualitatively different results. We have shown how these structures build up dynamically and found that the ratio of the two different emerging characteristic lengths depends on the interaction potential only.

As an application, we have shown that excitation structures generated by off-resonant laser driving can be used to implement an efficient three-qubit quantum gate, because the excitation scheme automatically generates an asymmetric spatial arrangement out of a homogeneous atom cloud such that an optimum gate operation is achieved for the given laser parameters. This asymmetry that the gate protocol relies on, is a feature that is inherent to resonantly generated structures and cannot be found in ground-state crystals. Extensions to other gates like CNOT or Toffoli are straight forward. We also expect that the general concept of self-assembly of optimum asymmetric excitation structures will find other applications.

Experimentally, laser excited Rydberg atoms in a quasi one-dimensional dipole trap could be used to verify our theoretical predictions. Depending on the capabilities of the experimental setup, different predictions can be probed. As the simplest observable, the total number of excited atoms could be measured as a function of the detuning and the density. This way, the shift of the maximum of the Rydberg excitation to higher detunings with increasing density and the increasingly super-Poissonian excitation statistics at very high detuning could be verified as a first manifestation of the resonant excitation channels. A position-resolved measurement of the excitations would allow to verify the predicted resonance peaks in $g^{(2)}$, and the formation of the ordered structure as described in Sec. 3.7.5. By determining the position of the resonances as a function of the detuning, also the precise structure of the interaction potential could be probed. Furthermore, the spatial dependence of the various excitation-number subspaces arising from the floating nature of our aggregates could be analyzed. Realizing an excitation volume with sharp boundaries, for example by using flat top beams, one could investigate the enhanced excitation density close to the trap border in the case of resonant excitation which is suppressed in the far off-resonant case (see Fig. 3.26). The resonant excitation aggregates are formed dynamically throughout the time evolution and do not require a thermalization of the system. This invites a time-resolved study of the dynamic formation of spatial correlations.

In approximately 1D systems or higher-dimensional systems, the higher-order resonance conditions do not uniquely determine the positions of all involved particles. This leads to a broadening of the corresponding resonances in $g^{(2)}$. Also decoherence due to spontaneous emission, finite laser line width, or effects of atomic motion will lead to a broadening of the resonance peaks in $g^{(2)}$. All these effects lead to a suppression of the resonant two photon processes compared to the off-resonant single-photon excitation, which sets limits to the observation of higher-order resonance peaks in experiments.

Finally, we note that very recently, super-Poissonian excitation statistics have been observed in experiments operating at off-resonant driving in the strongly dissipative regime [42, 43]. We expect that the mechanism of aggregate formation discussed here leading to a bimodal distribution of excitation numbers still applies in the presence of substantial decoherence. The main difference would be that, rather than resonantly excited pairs, off-resonantly excited single atoms function as initial grains for the aggregate formation [43]. The results reported in Ref. [43] are discussed in detail in the next section.

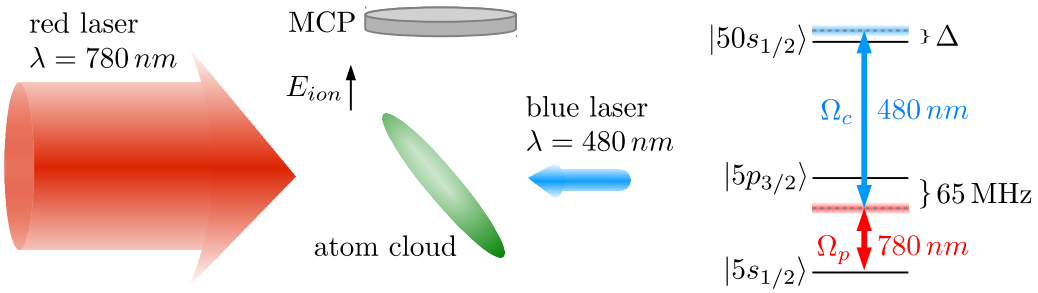

Figure 3.30: Schematic sketch of the experimental setup of Ref. [43]. A cloud of ^{87}Rb atoms, initially prepared in a quasi one-dimensional dipole trap, is Rydberg excited by two counter-propagating laser beams far detuned from the intermediate state. After the excitation sequence the Rydberg atoms are ionized by an electric field ramp and the ions are collected in a micro channel plate detector (MCP). The sketch of the level scheme illustrates the two step excitation process.

3.8 Effects of dissipation and experimental realization

In this section we report on the recent experimental observation of some of the phenomena predicted in the previous section. In this experiment the full counting statistics of Rydberg excitations, i.e., the excitation number histogram $P(m)$ can be measured [43]. The observed shape of $N_{\rm ryd}$, Q, and even higher order moments as a function of the detuning show all qualitative features predicted in Sec. 3.7.4. An important difference between the experimental parameters and the coherently evolving system is the presence of dissipation due to finite laser line widths and possibly other effects. This requires a more involved treatment of the many-body dynamics including these decoherence effects. The basic mechanism of aggregate formation due to resonant excitation channels is expected to work still, but the resonant pair excitation will be suppressed in favor of sequential excitation of single atoms in the presence of strong dissipation. After shortly introducing the experimental setup we will describe two different ways to model dissipative many-body dynamics in strongly interacting Rydberg gas. These models are the subject of the Master thesis of David Schönleber[1], so we will just give a brief description of these here and refer the interested reader to Ref. [299] for further details.

3.8.1 Experimental setup

The experiments we describe here, have been carried out in the group of M. Weidemüller at the University of Heidelberg. In the following their measurement procedure is described briefly. Further details can be found in Refs. [266, 286]. First, approximately 1.5×10^4 ^{87}Rb atoms are prepared in the state $|g = 5S_{1/2}, F = 2, m_F = 2\rangle$ in a tightly focused optical dipole trap. This results in an elongated atom cloud with $e^{-1/2}$ radii of $\approx 240\,\mu$m (axial) $\times 1.65\,\mu$m (radial). Due to the finite optical resolution of the imaging system, the radial size cannot be precisely measured, therefore we adjust this parameter in the comparison with theory. However, it is smaller than the range of the Rydberg-Rydberg interactions given by the blockade radius, giving rise to a quasi-1D geometry with respect to the Rydberg excitations.

[1] The numerical models have been developed by D. Schönleber in close collaboration with the author. All results presented here have been discussed and interpreted jointly.

The maximal peak density of ground-state atoms is $\approx 1.5 \times 10^{12}\,\mathrm{cm}^{-3}$, corresponding to a mean inter-particle spacing at the trap center of approximately $0.9\,\mu$m. Lower densities are achieved by reducing the time taken for initial loading of the dipole trap.

Rydberg atoms in the state $\left|50S_{1/2}\right\rangle$ are excited by first turning off the optical trap and then applying a two-photon laser pulse for 5 μs. The lasers are close to two-photon resonance, detuned $\Delta_1/2\pi = 65\,\mathrm{MHz}$ below the intermediate $|5P_{3/2}, F = 3, m_F = 3\rangle$ state. The first laser at 780 nm uniformly illuminates the cloud, while the second excitation laser at 480 nm is focused to an elliptical region of size $\approx 27\,\mu\mathrm{m} \times 11\,\mu\mathrm{m}$ (vertical $\times$ horizontal Gaussian beam waists). The two excitation laser beams counter-propagate and cross the atomic cloud perpendicular to its long axis, see Fig. 3.30. The effective (single-atom) two-photon Rabi frequency is $\Omega/2\pi \approx 0.4\,\mathrm{MHz}$ and the line width related dephasing between ground and Rydberg state is $\Gamma_{\mathrm{deph}}/2\pi \approx 1\,\mathrm{MHz}$. The two-photon detuning Δ can be varied by scanning the frequency of the second step excitation laser (blue laser). The Rydberg atoms interact repulsively with the van der Waals coefficient $C_6/2\pi = 16\,\mathrm{GHz}\,\mu\mathrm{m}^6$. In the low density limit this gives a blockade radius of $R_b \approx 5.3\,\mu$m. At a density of $1.5 \times 10^{12}\,\mathrm{cm}^{-3}$ however we calculate approximately $N_b \approx 160$ atoms per blockade sphere. As a result the Rabi frequency is collectively enhanced $\sqrt{N_b}\Omega/2\pi \approx 5.0$ MHz and correspondingly $R_b \approx 4.1\,\mu$m. Given the extent of the excitation region we anticipate that $10 - 15$ Rydberg excitations are possible. After excitation the Rydberg atoms are field ionized and one counts the number of ions detected on a MCP detector, with an estimated detection efficiency of $\eta \approx 0.4$ [38]. By repeating the experiment several hundred times statistical distributions of the Rydberg number are built up from which the mean number of excitations (N_{ryd}), and higher moments can be extracted.

3.8.2 Modeling of dissipative many-body dynamics

If the system is subject to dissipation, in principle, a master equation description has to be employed to model its dynamics, see Sec. 2.3. For a many-body system, this quickly becomes computationally hard as the atom number increases, since the number of density matrix elements, i.e., the size of the system increases as n^2, where n is the dimension of the relevant state space. There are two possible ways to overcome this problem. One is the solution of the master equation using the Monte Carlo Wave Function (MCWF) technique, which is in principle exact. The second is the reduction of the master equation to a rate equation that can be solved with kinetic Monte Carlo methods. In this method multi-atom coherences and thus quantum correlations are neglected and interactions are only included as local mean field shifts of the Rydberg level.

Monte Carlo Wave Function methods

Here we introduce the so called MCWF technique for the solution of a master equation including Lindblad terms. This method [300–303] allows for the numerical solution of the many-body master equation (3.55) without employing the density matrix formalism. Instead, a Schrödinger equation is solved and incoherent processes are included via non-Hermitian time evolution and additional random quantum jumps. Averaging over many such random trajectories allows to obtain a mixed state that can be shown to solve the corresponding master equation. In that way, the problem of solving a system of n^2 coupled ordinary differential

equations can be reduced repeatedly solving a system of n equations.

Recall once more that the master equation describing the evolution of an ensemble of interacting two-level atoms (see Sec. 2.3) reads

$$\dot{\rho} = -i[H, \rho] + \mathcal{L}[\rho] \tag{3.55}$$

with the Hamiltonian

$$H = \sum_{i=1}^{N} \left[H_L^{(i)} + H_\Delta^{(i)} \right] + \sum_{i<j} \frac{C_6}{|\mathbf{r}_i - \mathbf{r}_j|^6} s_{ee}^{(i)} \otimes s_{ee}^{(j)} \,, \tag{3.56}$$

where $H_L^{(i)} = \Omega/2(s_{ge}^{(i)} + s_{eg}^{(i)})$, with $s_{ab} = |a\rangle \langle b|$, describes the coupling of the atoms to the laser field and $H_\Delta^{(i)} = -\Delta s_{ee}^{(i)}$ accounts for the detuning from the two photon resonance. The Lindblad terms accounting for spontaneous decay and dephasing have the form

$$\mathcal{L}_{ab}[\rho] = C_{ab}\rho C_{ab}^\dagger - \frac{1}{2}\left(C_{ab}^\dagger C_{ab}\rho + \rho C_{ab}^\dagger C_{ab} \right) . \tag{3.57}$$

In the MCWF model, in each step of the time evolution the system can either undergo a deterministic time evolution or perform a random jump associated with incoherent processes such as dephasing or decay. To include reservoir effects, the system Hamiltonian governing the deterministic time evolution is replaced by a non-Hermitian Hamiltonian including the anti-commutator part (second part) of the Lindblad term in Eq. (3.57). The incoherent processes, namely dephasing and decay, are included via the constants Γ_{deph} and γ_{dec}. Thus, the non-Hermitian Hamiltonian becomes

$$H \to \tilde{H} = H - \frac{i}{2}(\Gamma_{\text{deph}} + \gamma_{\text{dec}}) \sum_{j=1}^{N} s_{ee}^{(j)}. \tag{3.58}$$

The jump operators associated with dephasing and decay, respectively, of the ith atom are given accordingly by

$$C_{\text{deph}}^{(i)} = \sqrt{\Gamma_{\text{deph}}} s_{ee}^{(i)}, \quad C_{\text{dec}}^{(i)} = \sqrt{\gamma_{\text{dec}}} s_{ge}^{(i)}. \tag{3.59}$$

In each time step the wave function is either propagated non-unitary with $\exp[-i\tilde{H}\,\delta t]$, or projected by applying one of the jump operators $C_{\text{k}}^{(i)}$ to it. Whether or not a jump occurs in a single time step is determined stochastically by a Monte Carlo method, which randomly selects the jumping atom as well as the jump operator according to the jump probability given by $\delta p_{i,\text{k}} = \langle \psi(t)| \, C_{\text{k}}^{(i)\,\dagger} C_{\text{k}}^{(i)} \, |\psi(t)\rangle \, \delta t$, where $\psi(t)$ denotes the many-body wave function and δt is chosen such that $\sum_{i,\text{k}} \delta p_{i,\text{k}} \ll 1$.

As the norm of a wave function undergoing non-Hermitian time evolution is not conserved, the wave function is normalized after each time step, yielding a single (stochastic) wave function trajectory for each time evolution. By averaging over the quantum trajectories, the master equation result is obtained in the limit of large sample size. For further details on the numerical modeling, see Refs. [118, 299, 303, 304].

In our simulation we employed state space truncation to improve the performance, excluding states that cannot be populated due to the Rydberg blockade effect, see Sec. 3.2.

A fully correlated many-body simulation for three-level atoms is numerically demanding since the state space truncation technique can only be applied to strongly interacting states, so the noninteracting intermediate state would cause a state space growing exponentially with the atom number. This will be discussed in Chap. 4. However, as for the present experimental parameters the intermediate state can be adiabatically eliminated, we expect to obtain good results with an effective two-level approach.

Rate equation kinetic Monte Carlo methods

For the experimental setup described above, the excitation volume typically contains on the order of $N = 10^3$ atoms in and accommodates about $m_{\max} = 20$ excitations. With the MCWF technique such large system sizes cannot be treated due to the huge Hilbert space. A method that can deal with very large system sizes, as its complexity only scales linearly with the atom number N, is the rate equation method [98,99,270]. The basic idea of this approach is that in the presence of strong dephasing, the coherences in the density matrix decay fast and the system is close to a maximally mixed state, in which the density matrix is diagonal in the canonical product states $|\alpha_1 \dots \alpha_N\rangle$, $\alpha_i \in \{g, m, e\}$. Thus the master equation can be reduced to a rate equation between the populations (diagonal elements of ρ) by adiabatic elimination of the coherences (off-diagonal elements). In the following we show how such a rate equation can be obtained in the noninteracting case, where the full density matrix is separable into atomic density matrices, and thus the master equation reduces to a single-atom problem. In the case of a fast decaying intermediate state, this rate equation can be reduced to a two-level one. Subsequently, we show how interactions can be taken into account in order to generalize to a many-body rate equation, which involves a further approximation. Finally we explain how to solve the resulting equation by Monte Carlo methods.

We start from the single-atom master equation (2.47). The dynamics of the Rydberg population is governed by the slow effective two-photon Rabi frequency $\Omega = \Omega_p \Omega_c/(2\Delta_1)$, which is smaller than the spontaneous decay from the intermediate level and also smaller than the laser dephasing rates Γ_{deph}. Under these conditions the coherences between the levels and the population difference between the ground and intermediate state equilibrate fast such that we can assume

$$\dot{\rho}_{ab} = 0 \quad \text{for} \quad a \neq b \qquad \text{and} \qquad \dot{\rho}_{mm} - \dot{\rho}_{gg} = 0\,. \tag{3.60}$$

Exploiting in addition the trace conservation $\sum_a \rho_{aa} = 1$ the single-atom master equation reduces to the two-level rate equation

$$\dot{\rho}_{ee} = \gamma_\uparrow \rho_{gg}^{\text{eff}} - \gamma_\downarrow \rho_{ee}\,, \tag{3.61}$$

where we have defined the effective ground-state population $\rho_{gg}^{\text{eff}} = 1 - \rho_{ee}$. The rates $\gamma_\uparrow$ and $\gamma_\downarrow$ are known functions of the laser parameters [98].

In the case of noninteracting atoms this can be easily generalized to the many-body case. Introducing the populations $P(\boldsymbol{\alpha}) = \rho_{\boldsymbol{\alpha}\boldsymbol{\alpha}}$, where $\boldsymbol{\alpha} = \{\alpha_1 \dots \alpha_N\}$ corresponds to the many-body state $|\alpha_1 \dots \alpha_N\rangle$, $\alpha_i \in \{g, e\}$, where g is now the effective ground state, the rate

equation can be written as

$$\frac{dP(\boldsymbol{\alpha})}{dt} = -\left(\sum_{i=1}^{N} \gamma_{\alpha_i,\bar{\alpha}_i}\right) P(\boldsymbol{\alpha}) + \sum_{i=1}^{N} \gamma_{\bar{\alpha}_i,\alpha_i} P(\boldsymbol{\alpha}_i)\,. \tag{3.62}$$

We have introduced the inverted state $\bar{\alpha}_i = e\delta_{\alpha_i g} + g\delta_{\alpha_i e}$ and the rates $\gamma_{\alpha_i,\bar{\alpha}_i} = \gamma_\uparrow \delta_{\alpha_i g} + \gamma_\downarrow \delta_{\alpha_i e}$, i.e., $\gamma_{ge} = \gamma_\uparrow$ and $\gamma_{eg} = \gamma_\downarrow$. The symbol $\boldsymbol{\alpha}_i$ denotes the configuration where the ith atom has changed its state with respect to $\boldsymbol{\alpha}$, i.e., $\boldsymbol{\alpha}_i = \{\alpha_1 \dots \bar{\alpha}_i \dots \alpha_N\}$. This just means that any configuration is coupled to any other configuration that only differs in the state of one atom and the rate connecting them is just the single-atom rate $\gamma_{\uparrow\downarrow}$ of the corresponding atom.

If the interaction Hamiltonian is included, this results in two additional terms, one being just an interaction induced shift of the Rydberg level, the second one accounting for two atoms changing their state simultaneously [98]. The second contribution was crucial for off-resonant excitation in the coherent case (see Sec. 3.7.1), since it accounts for the pair excitation. We will see later in this section that for large dephasing the direct pair excitations become suppressed in favor of sequential excitation of the single atoms. This is because direct pair excitation is associated with a two-atom coherence, that becomes strongly suppressed if dissipation is dominant. We can therefore neglect direct two-atom processes and thus only include interactions as local level shifts. This means that in the configuration $\boldsymbol{\alpha}$ the detuning Δ of the ith atom is modified to the effective detuning

$$\Delta \to \Delta_i = \Delta - \sum_{j,\, j\neq i} V_{ij} \delta_{\alpha_j e}\,. \tag{3.63}$$

With this, the rate equation (3.62) becomes

$$\frac{dP(\boldsymbol{\alpha})}{dt} = -\left(\sum_{i=1}^{N} \gamma^{(i)}_{\alpha_i,\bar{\alpha}_i}\right) P(\boldsymbol{\alpha}) + \sum_{i=1}^{N} \gamma^{(i)}_{\bar{\alpha}_i,\alpha_i} P(\boldsymbol{\alpha}_i)\,. \tag{3.64}$$

The rates $\gamma^{(i)}_{\bar{\alpha}_i,\alpha_i}$ are now calculated with the local detuning Δ_i of atom i and depend on the configuration $\boldsymbol{\alpha}$. Note that this rate equation still has the same simple structure as in the noninteracting case, with the only difference that local, configuration dependent level shifts appear.

Equation (3.64) is still a system of n first order linear equations, where n is the dimension of the Hilbert space. Thus the complexity for solving it by direct time integration is still the same as in the case of solving the time dependent Schrödinger equation. However, due to its simple structure (every configuration is only coupled to N other configurations), this rate equation can be solved very efficiently by Monte Carlo methods [132, 305]. The idea is to perform a random walk through the space of configurations $\boldsymbol{\alpha}$ where the system is in a discrete configuration all the time and jumps to another configuration randomly with a probability determined by the rates $\gamma^{(i)}_{\alpha_i,\bar{\alpha}_i}$. In this way the system is propagated up to the end time and then the observables are evaluated for the discrete configuration it ends up in. Many such random trajectories are calculated and the outcomes are averaged, which gives expectation values for all desired observables. What is special about the kinetic Monte Carlo approach pursued here [132], is that, instead of determining if a jump occurs or not in every

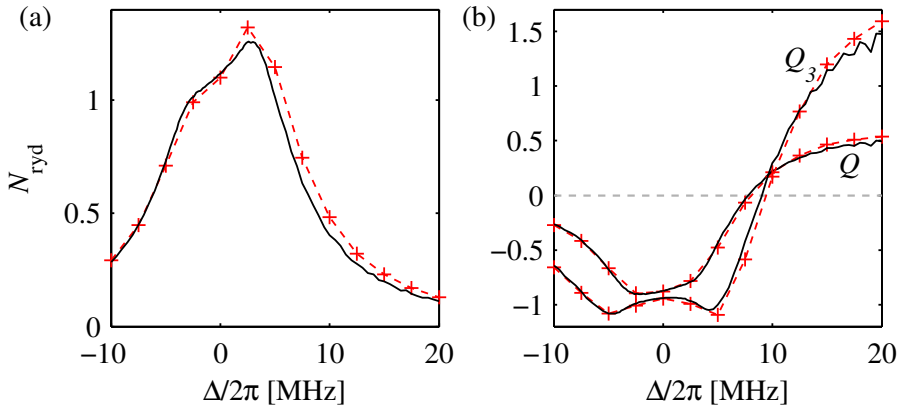

Figure 3.31: Number of excitations and Mandel Q-parameter and Q_3 in a spherical cloud of radius 2.3 μm after 5 μs evolution time. Solid black line: Rate equation model. Red dashed lines and crosses: MCWF simulation. Parameters: $\Omega/2\pi = 0.3\,\mathrm{MHz}$, $\Gamma_{\mathrm{deph}}/2\pi = 1\,\mathrm{MHz}$, $\gamma_{\mathrm{dec}}/2\pi = 4\,\mathrm{kHz}$, $C_6/2\pi = 16\,\mathrm{GHz}\,\mu\mathrm{m}^6$, $N = 50$ atoms corresponds to a density of $10^{12}\,\mathrm{cm}^{-3}$.

(fixed) time step, we randomly determine the time at which the next jump occurs and then in a second stochastic process determine which atom changes its state (see Ref. [299]).

In Chap. 4 we will use a modified version of this Monte Carlo rate equation model, that can handle the full three-level case but is not capable of simulating the time evolution of the system but only predicts its steady state.

Comparison between the models

As a first benchmark of the rate equation model, we simulate a spherical volume containing $N = 50$ atoms. The parameters are the same as in the experiment and are given in the caption of Fig. 3.31. The number of excitations, the Mandel Q-parameter and the third moment Q_3 coincide very well for the two model. Only at large detuning, N_{ryd} is slightly underestimated by the rate equation model. The third moment is defined as

$$Q_3 = \frac{\langle\langle m^3 \rangle\rangle}{\langle m \rangle} - 1 = \frac{\langle (m - \langle m \rangle)^3 \rangle}{\langle m \rangle} - 1 \tag{3.65}$$

in analogy to the Q-parameter. $\langle\langle m^i \rangle\rangle = \langle (m - \langle m \rangle)^i \rangle$ is called the ith cumulant of the distribution $P(m)$.

An observable that is more sensitive to the presence of higher order processes like resonant pair excitation, is the pair correlation function. First we justify that we can neglect two photon processes for large dephasing by calculating the $g^{(2)}$-function for two atoms in their steady state by solving for the steady state of the full two-atom master equation. Precisely, we calculated the steady state for fixed inter-atomic distance r between the two atoms and from this

$$g^{(2)}(r) = \frac{\rho_{ee,ee}}{(\rho_{eg} + \rho_{ee})(\rho_{ge} + \rho_{ee})} \tag{3.66}$$

for several distances r. If laser dephasing and spontaneous decay is included, this steady state always exists and is unique. The results are presented in Fig. 3.32(a). The spontaneous

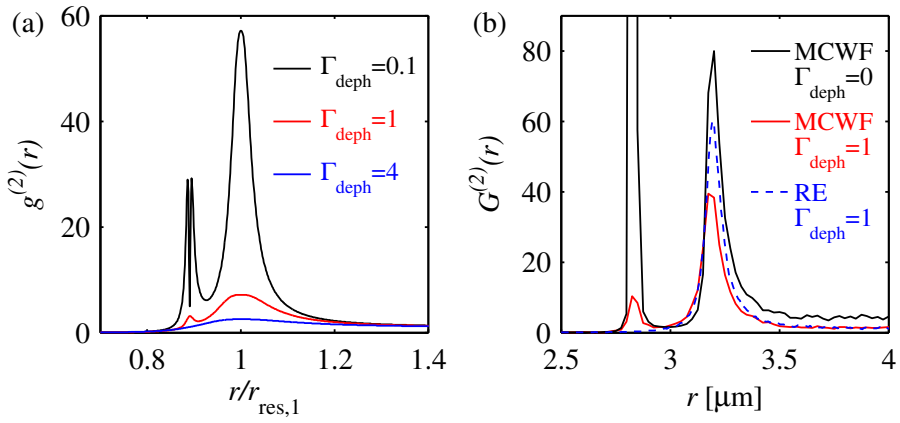

Figure 3.32: (a) Pair correlation between two atoms in steady state for different values of the laser dephasing $\Gamma_{\rm deph}$ (in units of 2π MHz). Full master equation calculation. Parameters are as in Fig. 3.31, except $\Omega/2\pi = 0.4$ MHz. (b) $G^{(2)}$ function with and without dephasing and comparison between MCWF simulation and rate equation model. The atoms are placed in a cylindrical volume with homogeneous density. Parameters are as in Fig. 3.31. The excitation time was 5 μs as in the experiment.

decay from the Rydberg level is very small ($\gamma_{\rm dec} = 15.5$ kHz). We used the effective Rabi frequency $\Omega/2\pi = 0.4$ MHz as in the experiment. The interaction strength is absorbed in the rescaling of length by $r_{\rm res,1}$. The detuning is $\Delta/2\pi = 10$ MHz $= 25\Omega$. For small dephasing we observe a very sharp peak at the pair resonant distance $r_{\rm res,2} = 2^{-1/6} r_{\rm res,1} \approx 0.89 r_{\rm res,1}$. Note that there is a dip in the center of this peak. This behavior is also found in the many-body case for small dephasing and is due to the small kink in the singly exited component around $r_{\rm res,2}$ (see Fig. 3.21). For larger dephasing, the dip vanished and the pair-resonance peak decreases much faster than the peak at $r_{\rm res,1}$ due to off-resonant single excitation and subsequent resonant excitation of the second atom.

In a second step we compare the pair correlation functions predicted by the two models for parameters that are very close to the experimental ones in Fig. 3.32(b). Namely, we use a cylindrical volume and its radius equals the radial $e^{1/2}$ width of the real atomic cloud but the height is only 6 μm, which is much smaller than the horizontal beam waist of the blue laser defining the axial extent of the excitation volume. The density is homogeneous and equals the mean density of the corresponding section of the real (experimental) cloud. Also the intensity profile of the laser was taken as homogeneous for the benchmark calculations. Here, we used $\Omega/2\pi = 0.3$ MHz , which can be thought of as a mean value of the effective Rabi frequency over the relevant excitation region. Recall that the peak effective Rabi frequency is 0.4 MHz. Note also that here, we use $G^{(2)}$ instead of $g^{(2)}$ since in the rate equation model it is difficult in terms of numerics to extract $g^{(2)}$. The function $G^{(2)}$ is just the normalized distribution of excited pairs (see Sec. 3.3). $G^{(2)}$ typically shows much higher correlation peaks than $g^{(2)}$ and can be biased by finite size effects in samples with inhomogeneous atomic density. Nevertheless, it is the observable that would be accessible much more easily in an experiment with position resolved detection of Rydberg excitations. Note that in Ref. [48] yet another definition of the pair correlation function was used. Setting the dephasing to zero we obtain an extremely strong peak at the pair resonance distance $r_{\rm res,2}$ in Fig. 3.32(b) (black line). Switching on the laser dephasing (red line), the pair resonance peak is strongly reduced

but still a small peak survives. The rate equation model naturally does not reproduce this peak and overestimates the peak at $r_{\mathrm{res},1}$ slightly. In the experiment the pair excitation peak could be suppressed even more due to additional dephasing effects, e.g., due to atomic motion (see also Sec. 3.8.3).

3.8.3 Experimental results

Figure 3.33(a) shows the measured mean Rydberg atom number $\langle m \rangle$ as a function of the detuning Δ for different atomic densities. At the lowest atomic densities (blue) the excitation spectrum is narrow and almost symmetric, reflecting the single-atom excitation probability. As the density is increased we observe a pronounced asymmetry extending to higher detunings, despite the fact that the single-atom excitation probability is almost zero. This is consistent with the simple picture for the excitation of aggregates comprised of several nearby Rydberg atoms.

The mean number of Rydberg excitations only provides partial information on the underlying many-body correlations. To learn more about the nature of the excitation process we analyze the second statistical moment quantified by the Mandel Q parameter. We also analyze the third moment characterized by the quantity Q_3. This quantity gives an additional measure of the nature of the correlations in our system and can be related to the three-body spatial correlation function $G_3(r_1, r_2, r_3)$ [97]. For uncorrelated excitation of single-atoms we expect $Q_3 = 0$ (Poissonian limit), and assuming independent excitation of m-atom aggregates $Q_3 = m^2 - 1$. Estimating our statistical errors using bootstrap re-sampling [306], we conclude that measurements of fourth-order and higher statistical moments are not statistically significant for our sample sizes.

In order to directly compare the measured with the simulated statistical moments we have to take into account the finite detection efficiency $\eta = 0.4$ of detecting a Rydberg excitation as an ion reaching the MCP detector. We assume the detection process to be independent for each Rydberg atom and also to not be influenced by the total number of Rydberg atoms, which excludes saturation effects. In this case we can model the detector operation as a binomial process. The probability distribution of physically present Rydberg atoms $P(m)$ and the probability distribution of the detected Rydberg atoms $P'(m)$ are related by

$$P'(m) = \sum_{k=0}^{\infty} f_\eta(m|k) P(k), \tag{3.67}$$

where for all practical purposes the upper limit of the sum may be set to a finite value and the kernel $f_\eta(m|k)$ of this transformation is given by

$$f_\eta(m|k) = \left(\begin{array}{c} k \\ m \end{array} \right) \eta^m (1-\eta)^{k-m}. \tag{3.68}$$

Assuming η is known, equation (3.67) now allows to relate the p-th order physical moments $\langle m^p \rangle = \sum m^p P(m)$ to the measured moments $\langle m^p \rangle' = \sum m^p P'(m)$ of their respective distri-

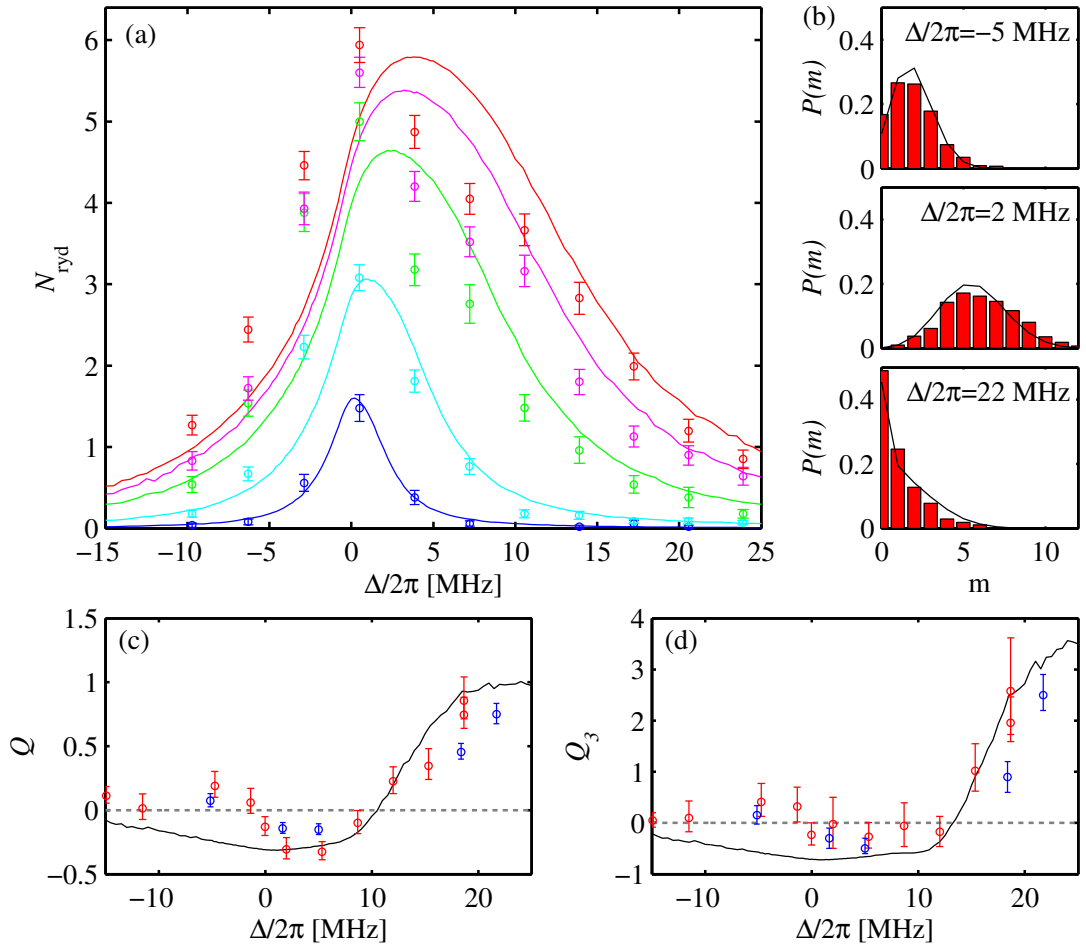

Figure 3.33: (a) Rydberg excitation spectra for different atomic densities: $5 \times 10^{10}\,\mathrm{cm}^{-3}$ (blue), $2 \times 10^{11}\,\mathrm{cm}^{-3}$ (cyan), $8 \times 10^{11}\,\mathrm{cm}^{-3}$ (green), $1.2 \times 10^{12}\,\mathrm{cm}^{-3}$ (magenta) and $1.5 \times 10^{12}\,\mathrm{cm}^{-3}$ (red). With increasing density we find enhanced excitation probabilities on the blue side of the resonance due to repulsive Rydberg-Rydberg interactions. The solid lines show the result of the rate equation model. (b) Measured histograms of the Rydberg atom number distribution for different detunings (normalized). The solid lines are the results of the rate equation simulations. The finite detection efficiency was accounted for by convolving the simulated histograms with a binomial distribution. (c) Second and (d) third-order statistical moments of the distributions as a function of the detuning Δ of the excitation lasers at a density of $1.5 \times 10^{12}\mathrm{cm}^{-3}$. The red (blue) circles are extracted from a dataset with 200 (800) experiments per data point. Error bars represent 68% confidence intervals determined via bootstrapping. The solid lines show the statistical moments as obtained from the rate equation model. The experimental data presented in this figure has been obtained in an experiment performed in the group of M. Weidemüller [43]. We thank our collaborators for providing the original datasets.

butions. The results read

$$\begin{aligned}
\langle m\rangle' &= \eta\langle m\rangle \\
\langle m^2\rangle' &= \eta^2\left(\langle m^2\rangle - \langle m\rangle\right) + \eta\langle m\rangle \quad \text{and} \\
\langle m^3\rangle' &= \langle m\rangle(\eta - 3\eta^2 + 2\eta^3) + \langle m^2\rangle(3\eta^2 - 3\eta^3) + \eta^3\langle m^3\rangle,
\end{aligned} \tag{3.69}$$

and can be used to calculate the corresponding cumulants $\langle\langle m^p\rangle\rangle'$. Subsequently the measured

Mandel-Q-parameter, generalized to p-th order,

$$Q'_p = \frac{\langle\langle m^p \rangle\rangle'}{\langle m \rangle'} - 1. \tag{3.70}$$

can be related to the Q_p of the true distribution. Evaluating the above for variance $\langle\langle m^2 \rangle\rangle'$ and third cumulant $\langle\langle m^3 \rangle\rangle'$ we get

$$\begin{aligned} Q'_2 &= \eta Q_2 \quad \text{and} \\ Q'_3 &= 3Q_2(\eta - \eta^2) + Q_3\eta^2. \end{aligned} \tag{3.71}$$

where $Q_2 := Q$. Note that in Fig. 3.33 the measured values Q'_p are shown but the primes have been dropped in the axis labels.

The comparison of the first statistical moment (the Rydberg population) in Fig. 3.33(a) shows that for low atomic density one gets good agreement between experiment and theory while at high densities the shift of the line is not as strong in the experimental data as predicted by theory. Also the measured profile appears to be more strongly broadened than the simulated one. One reason for these discrepancies could be the breakdown of the frozen gas approximation. It was shown recently that the resonant excitation mechanism leading to the line shift can be deteriorated by the mechanical repulsion between the nearby atoms [192]. Also collisions between Rydberg atoms can lead to additional dephasing effects in the high density regime [253] that would lead to an additional broadening of the line. In order to check if such effects are indeed to be expected in the parameter regime of the experiment, simulations including the atomic motion in some way should be done.

In Fig. 3.33(b) the full histograms are shown for some specific values of the detuning. The data used here is the same as for the blue circles in Fig. 3.33(c) and (d). The comparison with the rate equation result show very good agreement. We will see in the next section that, while in the case of $\Delta/2\pi = -5$ and 2 MHz the system is already more or less in its steady state after 5 μs, the low excited fraction for $\Delta/2\pi = 22$ MHz and the peak at zero excitations is due to the slowdown of the dynamics at large detuning, and in this case the population would still evolve towards higher excited states at longer times.

Figure 3.33(c) shows the measured Q parameter as a function of detuning at the highest density of 1.5×10^{12} cm^{-3}. The red circles show results averaged over 200 experimental realizations while the blue circles are based on a larger sample with 800 measurements per point. We observe a clearly asymmetric dependence of Q on the detuning. This is in marked contrast to recent observations involving Rydberg $|nD\rangle$ states in a three-dimensional system, where large fluctuations were observed either side of the resonance [39]. For negative detunings we find $Q \approx 0$ which reflects Poissonian fluctuations in the limit of weak excitation. For excitation frequencies around resonance we find Q factors clearly below 0, which reflect anti-bunching of excitations induced by the Rydberg blockade [38, 39, 59]. For positive detunings the statistical distributions become clearly super-Poissonian ($Q > 0$), which we attribute to the slowdown of the dynamics due to the small transition rate from zero to one excitation and subsequent fast excitation of aggregates comprised of multiple Rydberg atoms. Figure 3.33(d) shows Q_3 as extracted from our measured distributions. We observe qualitatively similar behavior to Q, with $Q_3 \approx 0$ for $\Delta < 0$, suggesting independent (Poissonian) excitation of Rydberg atoms. For $\Delta > 0$ we find that Q_3 rapidly increases also indicating the presence of

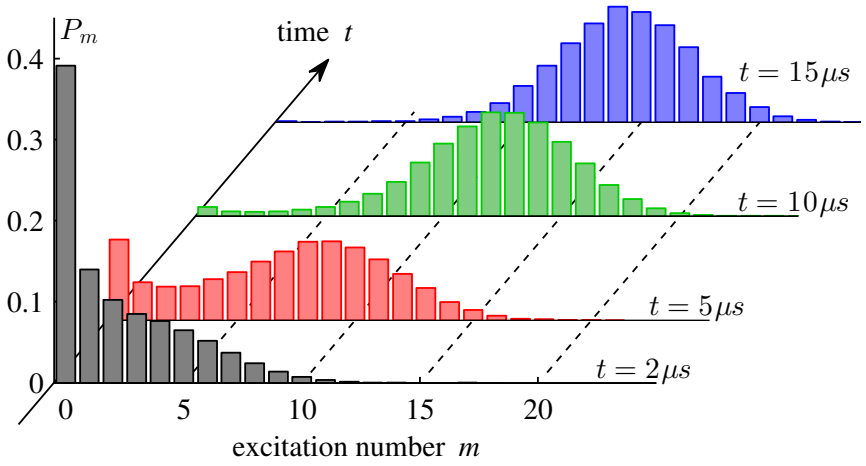

Figure 3.34: Stroboscopic time evolution of the excitation number histogram (rate equation simulation) for the parameters of the experimental run with the highest density of $1.5 \times 10^{12}\,\mathrm{cm}^{-3}$ and detuning $\Delta/2\pi = 15\,\mathrm{MHz}$. It is clearly visible that the bimodal structure leading to the high Q value is a transient feature and vanishes again at long times.

larger aggregates. The agreement with the simulation results is very good for both Q and Q_3.

3.8.4 Discussion

Despite the fact that the RE model does not capture multi-atom coherences which would be present in a direct multi-photon excitation, we find that the results of the RE model reproduce the full statistical distributions including higher order correlations quite well (see Fig. 3.33). Especially the features on the blue detuned side, i.e., the asymmetry increasing with atomic density and the super-Poissonian behavior visible in Q and Q_3, which show the excitation of Rydberg aggregates, are reproduced nicely. From this we infer that coherent multi-photon excitation is not required to explain the experimental observations. Instead, the dominant mechanism by which aggregates are formed at large detuning is via sequential (single-atom) excitations around an initial grain seeded by off-resonant excitation. While the excitation of the initial grain is strongly suppressed, the excitation of additional Rydberg atoms at well defined distances from the grain is resonant, and hence happens on faster time scales.

To further analyze the mechanism and to illustrate how it leads to the large Q-parameter and bimodality in the excitation number distribution, we study the time evolution of the full histograms predicted by the rate equation model. Figure 3.34 shows a stroboscopic time evolution for the case of high atomic density and large positive detuning. It is obvious that the decay of the zero excitation probability $P(0)$ decays slowly while the population that leaves $m = 0$ is quickly distributed into higher excitation numbers. This leads to a transient bimodal structure that leads to the large values of the Mandel Q-parameter observed in the experiment. At long times $P(0)$ eventually goes to zero and the bimodal structure disappears again. The reason for this behavior is a separation of time scales. As already mentioned, the rate at which population is transfered from $m = 0$ to $m = 1$ slows down at large detuning since they are separated by Δ in energy. For transitions from $m = 1$ to $m = 2$ and subsequently

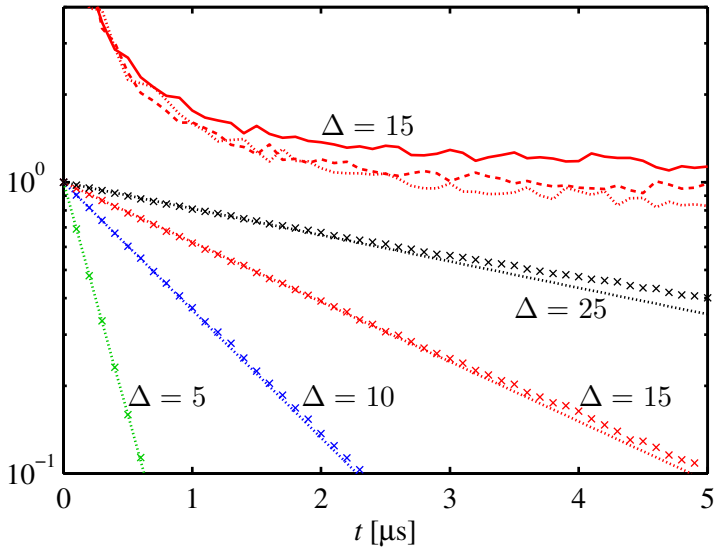

Figure 3.35: Time evolution of the populations of the different excitation number subspaces $P(m)$ with m excitations. The four curves (crosses) in the lower part of the figure show the time evolution of the zero excitation subspace $P(0)$ for different detunings of the incident laser field. The data points obtained from the RE model are overlaid with an exponential fit (dotted). The three red curves (solid, dashed, dotted) in the upper half of the figure show the time evolution of ratios $P(m)/P(m+1)$ of excitation probabilities of adjacent subspaces for $m \in \{1, 2, 3\}$. From top to bottom, ratios with increasing m are shown.

to higher excited states, there are always resonant channels, as long as the atomic density is high enough such that any atom has neighbors located at the resonant distance $r_{\mathrm{res},1}$. In short, aggregate nucleation slows down at large Δ, while aggregate growth is always fast.

In order to analyze this mechanism more quantitatively, we show $P(0)$ as a function of time for different detunings $\Delta/2\pi = \{5, 10, 15, 25\}$ MHz on a logarithmic scale in Fig. 3.35. In all cases the population in the zero-excitation state decreases exponentially until a significant part of the population is excited to higher N values. Furthermore, the depopulation of the zero-excitation state becomes slower with increasing detuning. Fitting the exponential decay rates, we find that the obtained rates approximately scale with $1/\Delta^2$, in particular for higher detunings. This is compatible with the expectation for a detuning-dominated rate equation modeling.

Next, the time evolution of the higher excited subspaces $P(N > 0)$ is analyzed with fixed detuning $\Delta/2\pi = 15$ MHz. Rather than studying them individually, Fig. 3.35 shows ratios $P(N)/P(N+1)$ for $N \in \{1, 2, 3\}$. Initially, these ratios are large, and they rapidly converge to an approximate stationary state $\gtrsim 1$ on a time scale much faster than the decay out of the zero-excitation subspace $P(0)$. This confirms the above reasoning about the separation of time scales of aggregate nucleation and aggregate growth.

Considering the good agreement between the theory and experimental data, we can extract more information about the underlying many-body correlations in the system from the results of the RE model. Specifically, we extract the second order spatial correlation function $G_2(r)$, as defined in Sec. 3.3, and shown in Fig. 3.36. For $\Delta/2\pi = +15$ MHz we observe strong liquid-like correlations which are responsible for the large measured Q values. The pronounced peak

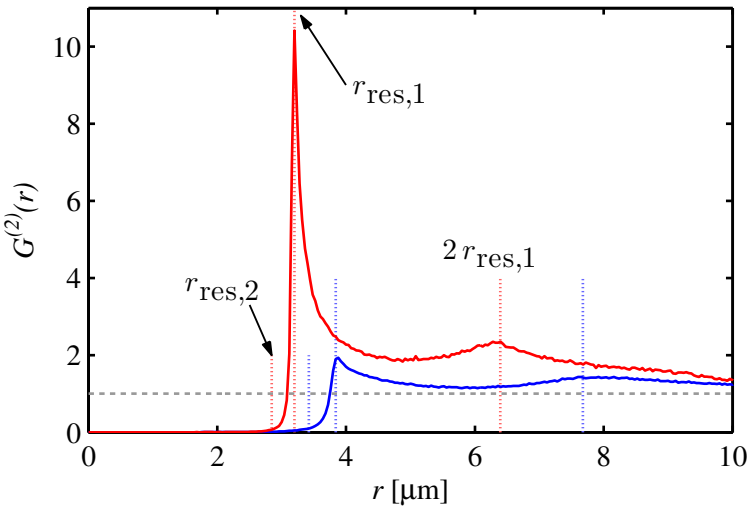

Figure 3.36: Pair correlation functions $G_2(r)$ obtained from the rate equation model using parameters from the experiment. The blue curve shows the correlation function for $\Delta/2\pi = 5\,\mathrm{MHz}$, the red curve for $\Delta/2\pi = 15\,\mathrm{MHz}$. The atomic density is $1.5 \times 10^{12}\,\mathrm{cm}^{-3}$.

at $r_{\mathrm{res},1} = (C_6/\Delta)^{1/6} \approx 3.2\ \mu$m reflects a strongly preferred pair distance. A second smaller peak at $2\,r_{\mathrm{res},1} \approx 6.4\,\mu$m is evidence for higher order correlations for $m > 2$. This feature would be more pronounced in a truly one-dimensional system. However, in higher dimensions the distance of the third resonantly excited atom in an aggregate to the other atoms is not uniquely determined, and therefore the second order peak becomes smeared out. Both features are strongly reduced for near resonant excitation ($\Delta = +5$ MHz). There is of course no peak at the position of the pair resonance $r_{\mathrm{res},2}$ since simultaneous multi-photon processes are not included in the rate equation model. These spatial correlations could be exploited in other areas of physics such as in the creation of strongly-coupled plasmas [149, 150, 307].

It should be noted that there are also some discrepancies between theory and experiment (see Fig. 3.33). Most prominently, the number of Rydberg excitations is systematically underestimated by our model on the red detuned side. On this side also Q and Q_3 are underestimated. While the measured data shows Poissonian statistics for $\Delta < 0$, the simulations predict sub-Poissonian ones in a relatively broad region around $\Delta = 0$. Furthermore, at high atomic densities a shoulder or side peak seems to develop in N_{ryd} at some positive detuning. In oder to explore the reasons for these discrepancies, we, on the one hand, varied all the experimental parameters entering in our simulations within the uncertainties to which they could be determined in independent measurements. We found that the observed N_{ryd} on the red detuned side can only be reproduced by the rate equation model if very low atomic densities and large laser line widths are assumed. These parameters are already outside the credibility region given by the their experimental uncertainties. The perfectly Poissonian Q and Q_3 and the onset of a double peak structure in N_{ryd} can not be reproduced at all by our rate equation simulations. On the other hand, we checked by various benchmark calculations in smaller systems that in the parameter regime under consideration the rate equation model coincides with the solution of the full three-level master equation. From this we conclude that the observed deviations must be due to physics beyond the master equation description

of a frozen gas of three-level Rydberg atoms.

An obvious candidate for an approximation entering in the master equation description, is the frozen gas approximation. Considering the mechanical forces that act on a resonantly excited pair due to the repulsive van der Waals potential one finds that these forces cause the atoms, within a typical time scale of $1\,\mu$s, to acquire velocities well above the mean thermal velocity at $5\,\mu$K and travel across distances much larger than, e.g., the spatial resonance width of the pair excitation resonance. This implies that motional dephasing and/or other motion induced effects should play a role in this parameter regime.

A second approximation that might break down at high atomic density is the one of a single Rydberg level. At small interatomic distances interaction induced couplings to additional Rydberg states might become important, which could, in principle, explain the emergence of the side lobe at high densities.

Chapter 4

Nonlinear optics and Rydberg EIT

This chapter is based on the following publications:

Hybrid model for Rydberg gases including exact two-body correlations
K. Heeg, M. Gärttner, and J. Evers
Physical Review A **86**, 063421 (2012)

Sub-Poissonian Statistics of Rydberg-Interacting Dark-State Polaritons
C. S. Hofmann, G. Günter, H. Schempp, M. Robert-de-Saint-Vincent, M. Gärttner, J. Evers, S. Whitlock, and M. Weidemüller
Physical Review Letters **110**, 203601 (2013)

Nonlinear absorption and density dependent dephasing in Rydberg EIT-media
M. Gärttner and J. Evers
Physical Review A **88**, 033417 (2013)

Rate equation models and the breakdown of universality in Rydberg gases
M. Gärttner, D. W. Schönleber, S. Whitlock, and J. Evers
in preparation

Electromagnetically induced transparency (EIT) is a well studied phenomenon in quantum optics [308] having a multitude of consequences and applications. Using this effect an opaque atomic medium can be rendered transparent by switching on a control laser coupling to an additional metastable level. The group velocity of light pulses traveling through a medium can be controlled and the pulses can even by stopped completely allowing for storage and retrieval of optical signal pulses. EIT in Rydberg gases has been the subject of intense studies both theoretically [100, 230, 233, 241, 242, 250, 251, 256–258, 263, 309, 310] and experimentally [38,247–249,261,287,311] in the recent years. One motivation is to achieve strong interactions between photons by interfacing them with interacting states of matter. In particular, based on the excitation blockade [4], non-classical states of light can be prepared out of an initially classical driving field [38, 247, 261, 311]. Possible applications include deterministic single-photon sources, storage and retrieval of photons, as well as quantum gates based on photon-photon interactions. However, already the simulation of classical light propagating through a strongly interacting medium is a substantial theoretical challenge due to the high complexity of the underlying many-body physics. At the heart of this is the exponential complexity

of the quantum many-body problem of interacting 3-level atoms and the non-linearity and non-locality of the propagation equations of the light related to the long-range interactions.

In the present chapter we introduce the basic principles of light propagation in three-level Rydberg gases such as EIT and the Maxwell-Bloch equations. We briefly introduce the methods that have been used to calculate the medium response, i.e., to solve the many-body master equation of interacting three-level atoms. We focus on the rate equation methods that have been developed in Refs. [98–100, 119] and reveal the limitations of this approach by comparing to full master equation calculations with few atoms [312]. We then show how the back-action of the medium response on the light field can be included in the rate equation model self consistently [253]. The resulting model is employed to reproduce recent experimental findings [38].

4.1 Light propagation and electromagnetically induced transparency

In classical electrodynamics, light traveling through a polarizable medium gets absorbed and diffracted according to the complex refractive index n of the medium. The refractive index is defined via the complex electric susceptibility χ as

$$n = \sqrt{1+\chi} \simeq 1 + \frac{\chi_R + i\chi_I}{2}\,, \tag{4.1}$$

where the approximation is valid as long as $|\chi| \ll 1$, which is fulfilled in conventional media [285]. We assume for now that the medium response is linear; i.e., the susceptibility is independent of the strength of the input field. Then, a probe field with E traveling through a homogeneous medium of length L is modified as

$$E = E_0 e^{i(knL-\omega t)} = E_0 e^{-k\chi_I L/2} e^{i(k\chi_R L/2-\omega t)}\,. \tag{4.2}$$

Thus it is possible to obtain the electric susceptibility of the medium by measuring the transmission

$$T = \frac{I}{I_0} = \frac{|E|^2}{|E_0|^2} = e^{-k\chi_I L} \tag{4.3}$$

and phase shift

$$\Delta\phi = k\chi_R L/2\,. \tag{4.4}$$

Two-level case: Absorption

The electromagnetic susceptibility χ is in general a tensorial quantity that quantifies the response of a dielectric medium to an electric field

$$\mathbf{P} = \epsilon_0 \chi \mathbf{E}\,. \tag{4.5}$$

In an atomic medium in which the probe field E drives a transition between two levels a and b (see Fig. 4.1) the polarization is caused by the induced atomic transition dipoles $\langle \mathbf{d} \rangle$. Thus we have

$$\mathbf{P} = n_0 \langle \mathbf{d} \rangle\,, \tag{4.6}$$

where n_0 is the atomic density. In rotating wave approximation the complex susceptibility of an atomic medium therefore equals the mean induced dipole density per field amplitude $\mathcal{E}$ [24, 271, 285, 313]

$$\chi = \frac{n_0\langle d\rangle}{\epsilon_0\mathcal{E}} = \frac{2n_0\mu_{ab}}{\epsilon_0\mathcal{E}}\mathrm{Tr}[\rho s_{ab}] = -\frac{2n_0|\mu_{ab}|^2}{\hbar\epsilon_0\Omega}\rho_{ba} = -\frac{3\lambda^2\gamma n_0}{2\pi k\Omega}\rho_{ba} \tag{4.7}$$

where we have used the definition (2.15) of the Rabi frequency $\Omega = -\mu_{ba}\mathcal{E}/\hbar$ in the third equality. To obtain the last equality, we have rewritten the dipole matrix element μ_{ab} in terms of the spontaneous decay rate γ, given by

$$\gamma = \frac{|\mu_{ab}|^2k^3}{3\epsilon_0\hbar}\,, \tag{4.8}$$

where $k = 2\pi/\lambda$ is the wave vector of the transition. For two-level atoms, neglecting the laser dephasing, the steady-state value of the coherence ρ_{ba} is

$$\rho_{eg}^{(ss)} = \frac{\Omega}{2}\frac{\Delta - i\gamma/2}{\Omega^2/2 + (\gamma/2)^2 + \Delta^2} \tag{4.9}$$

and thus the complex susceptibility

$$\chi = -\frac{\sigma_{\mathrm{abs}}n_0\gamma}{2k}\frac{\Delta - i\gamma/2}{\Omega^2/2 + (\gamma/2)^2 + \Delta^2} \tag{4.10}$$

where we have defined the absorption cross section $\sigma_{abs} = 3\lambda^2/2\pi$. We thus find that the absorption, i.e., the imaginary part of χ, is just a Lorentzian with width $\sqrt{2\Omega^2 + \gamma^2}$. For weak driving, $\Omega \ll \gamma$, the absorption is linear as χ does not depend on Ω. On resonance ($\Delta = 0$) the laser intensity $I \propto |E|^2$ is thus attenuated as

$$I(L) = I(0)e^{-\sigma_{\mathrm{abs}}n_0L}\,, \tag{4.11}$$

which justifies the definition of σ_{abs} as the two-level resonant absorption cross section. The real part of χ vanishes on resonance. The shapes of the real and imaginary part of χ are illustrated in Fig. 4.2. In the later discussion we will refer to the resonant two-level response as $\chi_{2L} = \chi(\Delta = 0)$.

Three-level case: Transparency

If an additional laser coupling to a third metastable level is added to the simple two-level system, the absorption on resonance vanishes. This effect is called electromagnetically induced transparency (EIT) [308]. Originally EIT was studied in Λ-systems, where the third level is energetically lower than the decaying level. However, EIT is also possible in a ladder scheme, if the upper level is metastable, which is the case for Rydberg states as we have seen in Sec. 2.1. The different schemes are shown in Fig. 4.1, also to recall the nomenclature of levels

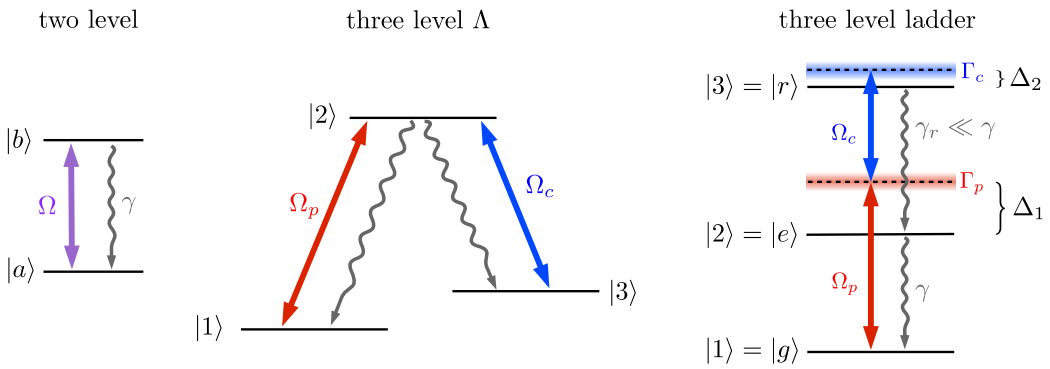

Figure 4.1: Level scheme of two-level atoms and three-level atoms in EIT configuration. A two-level atom just scatters light due to the spontaneous emission. In the three-level Λ-scheme the system evolves into the dark state $|d\rangle \propto \Omega_c |1\rangle - \Omega_p |3\rangle$. In the ladder scheme the upper state $|r\rangle$ is meta-stable and the dark state becomes $|d\rangle \propto \Omega_c |g\rangle - \Omega_p |r\rangle$. Definitions of Rabi frequencies, laser detunings, line widths, and decay rates are illustrated.

and parameters. The Hamiltonian of this three-level system was derived in Sec. 2.3 and reads

$$H = \begin{pmatrix} 0 & \Omega_p/2 & 0 \\ \Omega_p/2 & -\Delta_1 & \Omega_c/2 \\ 0 & \Omega_c/2 & -\Delta_2 \end{pmatrix} . \tag{4.12}$$

It is easy to see that on the two-photon resonance ($\Delta_2 = 0$) H possesses an eigenstate with eigenvalue zero, namely the state

$$|d\rangle = \frac{\Omega_c |g\rangle - \Omega_p |r\rangle}{\sqrt{\Omega_c^2 + \Omega_p^2}} . \tag{4.13}$$

This state is called a dark state. In the case of perfect EIT, meaning that there is no decay from the Rydberg state $|r\rangle$ and no dephasing of the coherence between $|g\rangle$ and $|r\rangle$, this state is also the steady state of the system. The laser Hamiltonian does not couple it to other states and the it does not contain the fast decaying state $|e\rangle$ which means that dark state is immune to decay. We are interested in the effect of the atomic medium on the probe beam, which is quantified by the susceptibility $\chi_{ge} \propto \rho_{eg}$. It is obvious that, once the system is in the dark state $|d\rangle$, the coherence ρ_{eg} vanishes. Thus the probe beam is neither absorbed nor diffracted and the medium becomes transparent.

Figure 4.2 shows the dependence of the real and imaginary part of χ_{ge} on the detuning $\Delta_p = \Delta_1$ of the probe laser, while the detuning of the coupling laser $\Delta_c = \Delta_2 - \Delta_p$ is kept at zero. The width w of the dip at $\Delta_1 = 0$ (EIT window) depends on the strength of the coupling laser as

$$w = \gamma_{rg} + \frac{\Omega_c^2}{\gamma_{eg}} , \tag{4.14}$$

where the $\gamma_{rg} = \gamma_r + \Gamma_2 = \gamma_r + \Gamma_p + \Gamma_c$ and $\gamma_{eg} = \gamma + \Gamma_p$ are the full line widths of the one-photon and two-photon transition respectively. Here, γ_r and γ are the spontaneous decay

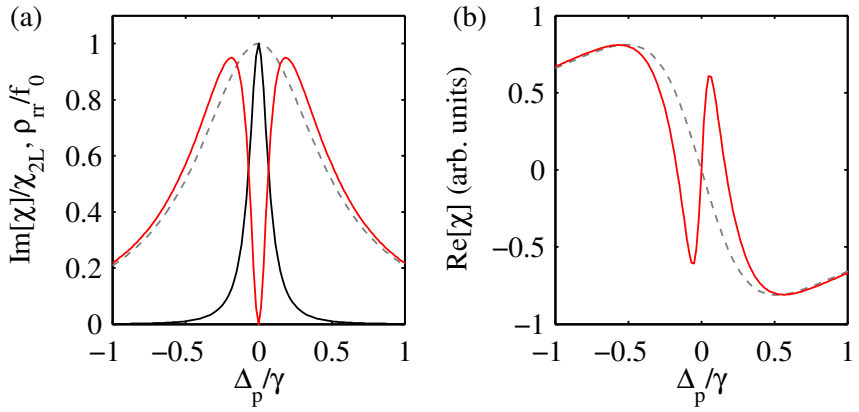

Figure 4.2: (a) Imaginary and (b) real part of the electromagnetic susceptibility χ (steady states). The dashed lines show the two-level case ($\Omega_c = 0$). Here, the maximum dispersion, i.e., the steepest slope of the real part, is accompanied by a maximum in absorption (large imaginary part). The black line in (a) shows the Rydberg excitation probability in the tree-level case. Parameters are $\gamma = 3\Omega_c = 6\Omega_p$. γ_r and the laser dephasings have been set to zero.

rates and Γ_p and Γ_c the laser line widths (see Fig. 4.1). Note that we always refer to the full line width of a transition or laser, while sometime the laser line width is defined as the half width of the spectral laser profile in the literature. The EIT width w is also equal to the width of the Rydberg population $\rho_{rr}(\Delta_p)$ which has approximately Lorentzian shape (see Fig. 4.2). From the steady state $|d\rangle$ we immediately find $\rho_{rr}(\Delta_p = 0) = (\Omega_p/\Omega_c)^2$ in the weak (and strong) probe limit. This means that for weak probe intensity the Rydberg population per atom is small while in the strong probe case ($\Omega_p \gg \Omega_p$) the ground state is depopulated. This technique of inverting the population from the from $|g\rangle$ to $|r\rangle$ by driving the lower transition more strongly than the upper one, is called coherent population trapping (CPT) [314]. Adiabatically sweeping from the weak to the strong probe limit the population can be transfered from $|g\rangle$ to $|r\rangle$ without ever populating $|e\rangle$, which is called stimulated Raman adiabatic passage (STIRAP) [315, 316].

Another interesting observation in Fig. 4.2 is that the real part of χ has a zero crossing with very steep slope at $\Delta_1 = 0$. This slope relates to the propagation speed of the electromagnetic wave [308]

$$v_g = \frac{c}{n(\omega_p) + \omega_p \frac{dn}{d\omega_p}} \,. \tag{4.15}$$

The slope of Re[χ] can be increased by decreasing the EIT width w, which can be accomplished by reducing the coupling strength Ω_c. Thus, by dynamically changing the intensity of the coupling laser, light pulses can be decelerated and even stored in an atomic medium and retrieved again [317–320].

At this point we should comment on cooperative effects that can arise in dense atomic media even in the absence of Rydberg excitations. In principle the dipoles induced in the atoms not only weaken the probe field but also irradiate themselves. This radiation could in principle influence the atoms in their vicinity and lead to dipole-dipole interactions similar to the mechanism leading to the Rydberg-Rydberg interactions, but with a much shorter wave length. This leads to cooperative effects like super-radiance [289, 290]. However, such

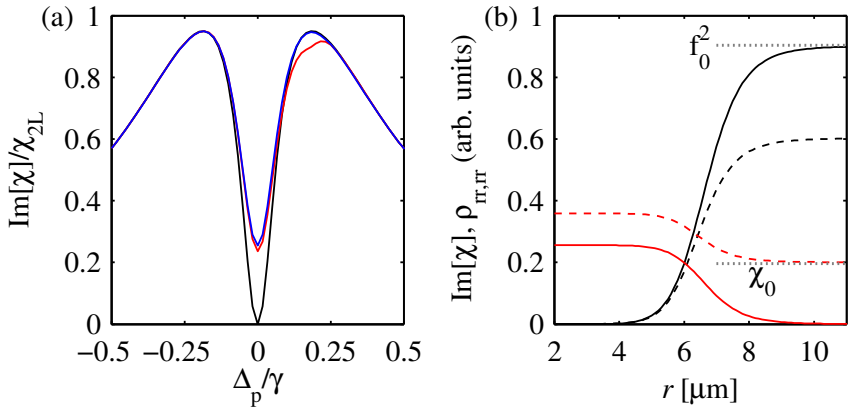

Figure 4.3: (a) Susceptibility as a function of probe laser detuning for two atoms. The different lines correspond to different interaction strengths between the atoms. Black, non-interacting; red, $V = \Omega_c$; blue, $V = 5\Omega_c$. The parameters are as in Fig. 4.2. If the interaction strength is comparable to the EIT width an asymmetry arises due to resonant excitation channels. (b) Susceptibility (red) and doubly excited fraction (black) as a function of the interatomic distance. The interaction potential is $V(r) = C_6/r^6$ with $C_6/2\pi = 50\,\mathrm{GHZ}\,\mu\mathrm{m}^6$, which corresponds to the Rydberg state $|55s\rangle$ of ^{87}Rb. Solid lines are for perfect EIT conditions ($\Gamma_p = \Gamma_c = 0$), dashed lines for $\Gamma_p = \Gamma_c = 0.05\Omega_c$.

effects are only relevant if the interatomic distance is smaller than the wavelength of the radiation mediating the dipole-dipole coupling. Also, effects like super-radiance are easily destroyed by decoherence effects like van der Waals dephasing or dephasing by the finite laser line widths [285]. We will therefore neglect those effects and treat the atoms as independent with respect to the atom-light interactions. The only interactions between the atoms that we take into account are the van der Waals interactions between the Rydberg atoms. Note, however, that it is interesting to examine the irradiated field of a sample of Rydberg atoms since information about interatomic correlations can be obtained from the correlations in the detected light field [226, 237, 250, 321].

EIT with interacting atoms

The previous discussion illustrated the principle of EIT for non-interacting atoms. In the following it is shown how Rydberg-Rydberg interactions destroy transparency again, which leads to non-linear absorption. The basic mechanism already becomes obvious in the case of two atoms. If the atoms are close to each other, they cannot be excited simultaneously. The steady state can therefore not be $|d_1\rangle \otimes |d_2\rangle$, since this state would contain an $|rr\rangle$ component. The fact that the state $|rr\rangle$ is far detuned due to the interaction shift leads to a steady state with nonzero population of the intermediate state $|m\rangle$ and nonzero coherence ρ_{eg}. Therefore, EIT is not perfect anymore and the probe beam gets absorbed. This is illustrated in Fig. 4.3 where we show how the spectral shape of the susceptibility changes if interaction is included. An increasing interaction strength leads to increasing absorption on resonance ($\Delta_p = 0$). In the non-interacting case [$V = 0$, black line in Fig. 4.3(a)] and in the case of full blockade ($V \gg \Omega_c, \gamma$, blue line), the spectrum is symmetric. For intermediate interaction strength (red line) one observes an asymmetry. This feature is due to degeneracies similar to the resonant excitation channels studied in Sec. 3.7 that arise at positive detuning where detuning and

interaction shift can cancel each other. We also show the population of the state $|rr\rangle$ and the susceptibility as a function of the interatomic distance. At small distance the atoms are perfectly blockaded and therefore the double excitation probability is zero, while $\mathrm{Im}[\chi_{ge}]$ approaches a finite limiting value. At large distance double excitation is possible and the susceptibility vanishes, as the EIT condition ($\Delta_2 = 0$) is recovered. For nonzero dephasing of the coherence between $|g\rangle$ and $|r\rangle$ the susceptibility tends to the single-atom value χ_0. The distance at which the crossover happens is what we define as the two-atom blockade radius here.

Going from two to many atoms the following picture arises: Any Rydberg excitation created by the incident laser field blocks N_b neighbors from being excited and thus generates N_b two-level absorbers. As the number of generated excitations depends on the probe field intensity, $\rho_{rr} = (\Omega_p/\Omega_c)^2$, this results in a strong optical non-linearity. This optical non-linearity not only depends on the strength of the incident probe field but also on N_b and therefore on the density of the medium. Note also that the effect is nonlocal in the sense that the blockade radius R_b, the characteristic distance over which atoms influence each other, is typically on the order of several micrometers. For high atomic densities (large optical depth) the nonlinearity can be strong enough to be observable on the single-photon level [247, 261, 311]. This is the idea of a single-photon switch [262]. A first photon creates an excitation and a second photon can herald the presence of the first one by getting absorbed or not. In order to account for effects involving non-classical photon statistics one should start from the propagation equations for a quantized light field. In the non-interacting case this leads to stable propagating solutions, that are superpositions of photonic excitation and atomic coherences [317]. These solutions are called *dark-state polaritons*. The relative weight of the photonic and matter-like components can be tuned by the coupling field. That way it is possible to store and retrieve single photons in an atomic medium. In the presence of Rydberg interactions, the matter-part of the polaritons will induce interactions between them. Thus, effectively, one obtains interactions between photons and a photon blockade (anti-bunching of photons) can be realized [247, 261, 311].

In the experimental setup this chapter refers to, the photon blockade could not be observed. This was mainly due to the unsuited cloud geometry, but also because of strong dephasing due to the finite laser line width that destroys the coherence and leads to scattering of the polaritons. It is therefore justified to employ a description based on classical light fields, but keep in mind that the effects of non-classical photon statistics could still have an impact on the experimental observations that is not captured by our model.

Maxwell-Bloch equations

The fact that we deal with a nonlocal optical nonlinearity makes the problem of light propagation in an extended Rydberg gas computationally challenging. The propagation equation for the probe Rabi frequency (proportional to the probe field amplitude) in slowly-varying-amplitude approximation is [309, 317]

$$\left(\frac{1}{c}\frac{\partial}{\partial t} - \frac{i}{2k}\nabla_\perp + \frac{\partial}{\partial z}\right)\Omega_p(\mathbf{r},t) = \frac{ik}{2}\chi_{ge}(\mathbf{r},t)\Omega_p(\mathbf{r},t)\,. \tag{4.16}$$

We are interested in the steady-state solution and assume that the medium is sufficiently homogeneous such that transverse dynamics can be neglected. Furthermore we will only be concerned with the case of resonant probe and coupling fields. In this case the real part of χ_{ge} vanishes and we define $\chi = \mathrm{Im}[\chi_{ge}]$. Thus the propagation equation reduces to

$$\frac{\partial}{\partial z}\Omega_p(\mathbf{r}) = -\frac{k}{2}\chi(\mathbf{r})\Omega_p(\mathbf{r})\,. \tag{4.17}$$

This equation might look simple but the complexity is hidden in the local medium response χ. The local susceptibility depends on the local atomic coherence ρ_{ge}, which has to be calculated from the full many-body master equation. For atom i at position $\mathbf{r}_i$ this equation reads (see Sec. 2.3) [100, 269, 310]

$$\frac{\partial}{\partial t}\rho_{ge}^{(i)} = i\frac{\Omega_p(\mathbf{r}_i)}{2}\left(\rho_{gg}^{(i)} - \rho_{ee}^{(i)}\right) + i\frac{\Omega_c}{2}\rho_{gr}^{(i)} - i\Delta_p\rho_{ge}^{(i)} - \frac{1}{2}(\gamma+\Gamma_p)\rho_{ge}^{(i)} \tag{4.18a}$$

$$\frac{\partial}{\partial t}\rho_{gr}^{(i)} = -i\frac{\Omega_p(\mathbf{r}_i)}{2}\rho_{er}^{(i)} + i\frac{\Omega_c}{2}\rho_{ge}^{(i)} - i(\Delta_p+\Delta_c)\rho_{gr}^{(i)} - \frac{1}{2}(\gamma_r+\Gamma_2)\rho_{gr}^{(i)} + i\sum_{j\neq i}V_{ij}\rho_{gr,rr}^{(i,j)} \tag{4.18b}$$

$$\frac{\partial}{\partial t}\rho_{er}^{(i)} = i\frac{\Omega_c}{2}\left(\rho_{ee}^{(i)} - \rho_{rr}^{(i)}\right) - i\frac{\Omega_p(\mathbf{r}_i)}{2}\rho_{gr}^{(i)} - i\Delta_c\rho_{er}^{(i)} - \frac{1}{2}(\gamma+\gamma_r+\Gamma_c)\rho_{er}^{(i)} + i\sum_{j\neq i}V_{ij}\rho_{er,rr}^{(i,j)} \tag{4.18c}$$

$$\frac{\partial}{\partial t}\rho_{gg}^{(i)} = i\frac{\Omega_p(\mathbf{r}_i)}{2}\left(\rho_{ge}^{(i)} - \rho_{eg}^{(i)}\right) + \gamma\rho_{ee}^{(i)} \tag{4.18d}$$

$$\frac{\partial}{\partial t}\rho_{ee}^{(i)} = -i\frac{\Omega_p(\mathbf{r}_i)}{2}\left(\rho_{ge}^{(i)} - \rho_{eg}^{(i)}\right) + i\frac{\Omega_c}{2}\left(\rho_{er}^{(i)} - \rho_{re}^{(i)}\right) - \gamma\rho_{ee}^{(i)} + \gamma_r\rho_{rr}^{(i)} \tag{4.18e}$$

$$\frac{\partial}{\partial t}\rho_{rr}^{(i)} = -i\frac{\Omega_c}{2}\left(\rho_{er}^{(i)} - \rho_{re}^{(i)}\right) - \gamma_r\rho_{rr}^{(i)}\,. \tag{4.18f}$$

The single-atom and two-atom density matrix elements are defined as

$$\rho_{ab}^{(i)} = \mathrm{Tr}[\rho\, s_{ba}^{(i)}] \quad \text{and} \quad \rho_{ab,cd}^{(i,j)} = \mathrm{Tr}[\rho\, s_{ba}^{(i)} \otimes s_{dc}^{(j)}]\,, \tag{4.19}$$

which is consistent with $\rho_{ab} = \langle a|\,\rho\,|b\rangle$ in the single-atom case. The interaction potential is $V_{ij} = C_6/|\mathbf{r}_i - \mathbf{r}_j|^6$. From Eq. (4.18) some important insights can be gained. Equation (4.18d) shows that in the steady-state ($\partial\rho/\partial t = 0$) we have

$$i\frac{1}{2}\left(\rho_{ge}^{(i)} - \rho_{eg}^{(i)}\right) = \mathrm{Im}[\rho_{eg}^{(i)}] = -\mathrm{Im}[\rho_{ge}^{(i)}] = -\frac{\gamma}{\Omega_p(\mathbf{r}_i)}\rho_{ee}^{(i)}\,. \tag{4.20}$$

The last relation will be used in Secs. 4.2 and 4.3 to calculate the local susceptibility from rate equation simulations. Equation (4.18) also shows how the nonlocality and complexity of the problem arises. The interaction terms in Eqs. (4.18b) and (4.18c) connect the state of atom i to distant atoms j and the equations for single-atom matrix elements always involve couplings to the two-atom matrix elements. The equations for the two-atom matrix elements would in turn be coupled to the three-atom ones and so on. This is usually called the hierarchy problem and makes the solution of Eq. (4.18) in long-range interacting Rydberg media very challenging. In the following we briefly discuss some of the approaches that have been pursued in order to solve this problem.

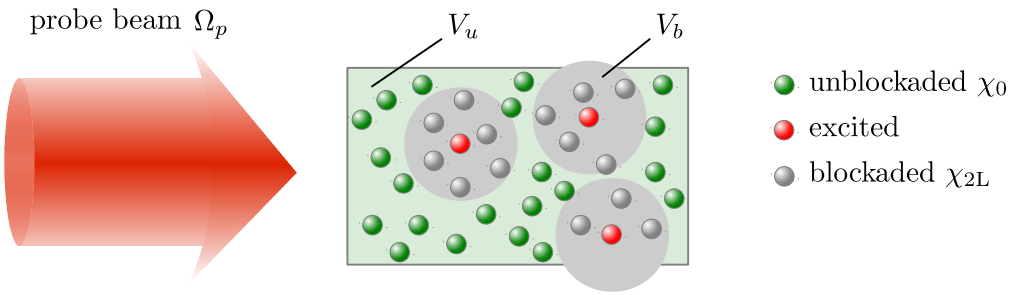

Figure 4.4: Illustration of the super-atom picture. Any excitation blocks volume V_b from containing further excitations. The walls of this volume are hard, meaning that any atom is either blockaded or unblockaded.

The simplest way to overcome the hierarchy problem is a mean field approximation or Hatree-Fock approximation [55]. By imposing

$$\rho_{ab,cd}^{(i,j)} \approx \rho_{ab}^{(i)} \otimes \rho_{cd}^{(j)} \tag{4.21}$$

one obtains a closed set of equations for the single-atom density matrix elements [28, 114, 132, 265]. The mean field approach, however, turns out to break down already at moderate densities. In order to improve this one can take into account the two-atom density matrix elements and truncate the hierarchy problem one order higher by employing the approximation (cluster expansion) [269, 287]

$$\rho^{(i,j,k)} \approx \rho^{(i)}\rho^{(j,k)} + \rho^{(j)}\rho^{(i,k)} + \rho^{(k)}\rho^{(i,j)} - 2\rho^{(i)}\rho^{(j)}\rho^{(k)} \,. \tag{4.22}$$

This was used in Ref. [309] to derive an analytical expression for the third order optical nonlinearity. However, at high atomic densities the cluster expansion approach breaks down [100].

In the weak probe regime, where the probe field consists only of a few photons a treatment of the quantum dynamics is possible [258, 261]. However, for more than two photons in the probe field and imperfect EIT, numerical calculations become very demanding. Petrosyan *et al.* [242] developed a model including correlations in the light field. This model is based on coarse graining the atomic medium by introducing super-atoms.

Simple hard sphere models

An alternative approach to calculate the optical response χ of an interacting EIT medium is the introduction of a simple super-atom picture [228, 230]. This view is based on rather heuristic arguments and starts by a coarse graining of the medium into blockade spheres, which is illustrated in Fig. 4.4. We give the details of this approach here since it will be shown later in this chapter, that a modified version of the hard sphere model reproduces the results of the rate equation model introduced in Sec. 4.2 surprisingly well. The argument given in the following assumes resonant probe and coupling lasers.

Without the Rydberg interactions, the fraction of excited atoms would be f_0, which is the steady-state excitation probability of a single atom, $f_0 = \rho_{rr}^{(ss)}$. So the total number of Rydberg excitations would be $N_{\mathrm{ryd}} = Nf_0 = f_0 n_0 V$ where n_0 the atomic density and V the trap volume. Assuming that the only effect of the interaction is that every Rydberg excitation

prevents a certain volume V_b surrounding it from containing further excitations, the number of Rydberg excitations becomes $N_{\mathrm{ryd}} = f_0 n_0 V_u$, where $V_u = V - V_b N_{\mathrm{ryd}}$ is the unblocked volume. Solving these equations self consistently and using that the Rydberg excited fraction is $f_r = N_{\mathrm{ryd}}/N = N_{\mathrm{ryd}}/(V n_0)$, we find

$$f_r = \frac{N_{\mathrm{ryd}}}{N} = f_0 n_0 \frac{V - V_b N_{\mathrm{ryd}}}{N} = f_0 - f_0 n_0 V_b f_r \,, \tag{4.23}$$

which we can rearrange to

$$f_0 V_b n_0 = \frac{f_0 - f_r}{f_r} = \frac{f_0}{f_r} - 1 \,. \tag{4.24}$$

Defining the blockaded fraction $f_{bl} = f_0/f_r - 1$ and the critical density $n_{\mathrm{crit}} = (f_0 V_b)^{-1}$ one obtains the extremely simple relation

$$f_{bl} = n_0/n_{\mathrm{crit}} \,. \tag{4.25}$$

In the later discussion we show that this relation is indeed reproduced by many-body calculations using rate equations, at least as long as $n_0 < n_{\mathrm{crit}}$. At higher densities the assumption that the blockade volume is a constant parameter and that blockade spheres do not overlap is expected to break down. However we find that in this regime rate equation models are still consistent with a modified version of Eq. (4.25) that takes into account collective effects.

In the framework of the hard sphere picture, also the optical response can be estimated [228,230]. For any blockaded atom the Rydberg level is inaccessible and thus it acts as a two-level absorber with susceptibility χ_{2L} for the probe field. The susceptibility of unblockaded atoms is just the non-interacting three-level response $\chi_0 \propto \mathrm{Im}[\rho_{ge}]$ which vanishes for perfect EIT. As there are $N_{\mathrm{ryd}} N_b$ two-level absorbers, the susceptibility per atom becomes

$$\begin{aligned} \chi &= \chi_{2L} f_r N_b + \chi_0 (1 - f_r N_b) \\ &= \chi_{2L} f_r f_{bl}/f_0 + \chi_0 (1 - f_r f_{bl}/f_0) \\ &= \frac{\chi_{2L} f_{bl} + \chi_0 (1 + f_{bl} - f_{bl})}{1 + f_{bl}} \\ &= \frac{\chi_0 + \chi_{2L} f_{bl}}{1 + f_{bl}} \,, \end{aligned} \tag{4.26}$$

where we have used Eq. (4.25) as $f_{bl} = f_0 N_b$ and $f_r/f_0 = (f_{bl} + 1)^{-1}$ from the definition of f_{bl}. In Sec. 4.2.4 we show that this relation is always fulfilled in rate equation simulations in the case of vanishing χ_0 (perfect EIT). It is an intrinsic property of the rate equation model.

Equations (4.25) and (4.26) can be used to calculate the medium response in Eq. (4.17). That way one obtains a very simple model for light propagation in a Rydberg EIT medium, where the local susceptibility can be calculated analytically. In the following the already mentioned rate equation model that solves Eq. (4.18) without employing the very simplified view of the super-atom model, is introduced. The range of validity of this model and relation to hard sphere models, cf. Eqs. (4.25) and (4.26), is discussed. Thereafter it is shown how the absorption of the probe light can be included self-consistently into the rate equation model to solve Eq. (4.17) simultaneously. The resulting model is applied to recent experimental findings [38] and is compared to other state of the art models. Finally, reasons for deviations

from the experimental observations are discussed.

4.2 Rate equation models for strongly interacting three-level atoms

The rate equation (RE) approach [98–100,119,136] may be used to calculate the steady state of a cloud of two- or three-level atoms subject to near resonant laser driving by adiabatic elimination of all coherences and including interactions as level shifts of the Rydberg level of individual atoms (see also Sec. 3.8.2). This model is fast, simple to implement and allows to treat up to 10^5 atoms and thus the susceptibility χ of an extended atomic cloud at high density ($N_b \gg 1$) can be calculated very efficiently. The model is therefore directly applicable to many experimental setups. There is, however, a lack of understanding of many properties of the model, and, more importantly, of its validity range with respect to the system parameters.

We therefore study an ensemble of resonantly driven atoms in different density regimes using the RE model and thereby point out the characteristic properties of the model. First, at low atomic densities the results of the RE model are consistent with a pure blockade picture, leading to a simple relation between the Rydberg excited fraction and the atomic density [228,230] (see Eq. (4.25)). The RE model reproduces this relation for any trap dimensionality. In the high density regime we show that the RE model is capable of reproducing collective many-body features, namely the scaling laws discussed previously in Secs. 3.4 and 3.5 and reported in Ref. [114]. We give an explanation of this based on a super-atom picture that uses the intrinsic properties of the RE model as a starting point. The different regimes are further characterized by studying pair correlations and excitation statistics as complementary observables to the Rydberg excited fraction.

Next, we discuss the universal dependence of the electromagnetic susceptibility on the fraction of blockaded atoms [100,310] (see Eq. (4.26)) and show that it is an intrinsic property of the RE model. Combining this result with the extended hard sphere model show how this universal relation can be exploited to construct a simple model for light propagation in Rydberg EIT media.

In summary we show that all features of the RE model can be understood from classical statistical arguments. The question that arises immediately is, whether those properties are only valid if the system indeed behaves classically due to strong decoherence or if they also hold in largely coherent systems. In other words: In which parameter regime is the (classical) RE model valid? In Sec. 4.2.5 we therefore benchmark the RE model by comparing it to full master equation simulations with few atoms. We find that the RE model is expected to perform well whenever strong decoherence effects are present, or more precisely, whenever interatomic coherences are small. If the system is rather coherent, the RE can fail dramatically and even lead to qualitatively wrong predictions. As a consequence, for unfavorable parameters also the universal relation between scaled susceptibility and blockaded fraction breaks down.

4.2.1 Rate equation model

The RE model provides a way to calculate the steady state of a strongly interacting many-body system subject to lasers in EIT configuration that scales almost linearly with the atom

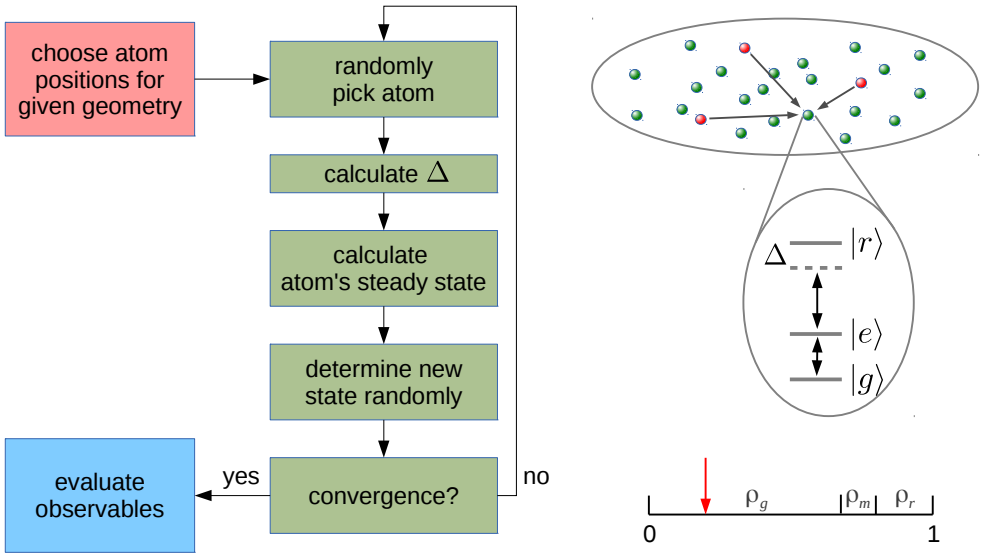

Figure 4.5: Illustration of the RE model. Starting with all atoms in the ground state the loop is typically executed $10N$ times. This guarantees that a global steady state has been reached. For each set of parameters we average over on the order of 1000 Monte Carlo samples of randomly chosen atom positions.

number as long as the Rydberg excited fraction is small. The setup we have in mind is as in Ref. [38] (and Sec. 3.8) and is illustrated in Fig. 4.1 (three-level ladder system). The spontaneous decay of the intermediate and Rydberg state plus the dephasings caused by the finite laser bandwidths lead to the total line widths γ_{eg} and γ_{gr} of the probe transition and the two-photon transition, respectively. Two atoms that are in the Rydberg state show repulsive van der Waals interactions.

The Hamiltonian of an ensemble of N three-level atoms, in rotating wave approximation, was introduced in Sec. 2.3. Writing out the projectors s_{ab} it reads ($\hbar = 1$)

$$H = \sum_{i=1}^{N} \left[H_L^{(i)} + H_\Delta^{(i)} \right] + \sum_{i<j} \frac{C_6 \left| r_i r_j \right\rangle \left\langle r_i r_j \right|}{|\mathbf{r}_i - \mathbf{r}_j|^6} \tag{4.27}$$

where $H_L^{(i)} = \Omega_p/2 \left| g_i \right\rangle \left\langle e_i \right| + \Omega_c/2 \left| e_i \right\rangle \left\langle r_i \right| + h.c.$ describes the coupling of the atoms to the laser fields and $H_\Delta^{(i)} = -\Delta_1 \left| e_i \right\rangle \left\langle e_i \right| - (\Delta_1 + \Delta) \left| r_i \right\rangle \left\langle r_i \right|$ accounts for the laser detunings. Here, $\Delta_1 = \Delta_p$ denotes the probe detuning and $\Delta_1 + \Delta$ is detuning from the two-photon resonance, where $\Delta = \Delta_c$ is the detuning of the coupling laser. Incoherent processes can be included as Lindblad terms [308] leading to the master equation for the density matrix

$$\dot{\rho} = -i[H, \rho] + \mathcal{L}[\rho]. \tag{4.28}$$

For a single atom ($N = 1$) one can transform this into a RE for the populations of the atomic levels by adiabatically eliminating the coherences ($\dot{\rho}_{ij} = 0$ for $i \neq j$) [98]. For the many-body case one can generalize this to a RE for the populations of the product states $|\boldsymbol{\sigma}\rangle = |\sigma_1, \sigma_2, \ldots, \sigma_N\rangle$, where $\sigma_i \in \{g, e, r\}$. We employ a Monte Carlo technique for the

solution of the many-body RE, that is, starting in the global ground state $|g, g, \ldots, g\rangle$ we perform a random walk through the configuration space of states $|\boldsymbol{\sigma}\rangle$ and average over many such trajectories, ensuring the convergence to a global steady state. The Hamiltonian H as well as the Lindblad operators couple two such many-body states only if they differ solely in the state of one atom. Therefore, in order to calculate the transition rates between two states, one only has to take into account the jump probability of the atom the state of which is changing. The interaction between atoms in the Rydberg state is incorporated as a shift of the Rydberg level of the considered atom $\Delta_{\text{int}}^{(i)} = \sum_{j\neq i}' V_{ij}$, where the sum only runs over atoms that are currently in the Rydberg state. $\Delta_{\text{int}}^{(i)}$ enters as an additional detuning into the master equation of atom i, i.e., $\Delta \to \Delta^{(i)} = \Delta - \Delta_{\text{int}}^{(i)}$, where $\Delta^{(i)}$ is the local detuning at atom i. This approximation clearly leads to an exclusion of true quantum correlations. Technically, in a single step of the Monte Carlo procedure, an atom is picked randomly, its transition rates to other states are calculated based on the local interaction shift and the single-atom master equation, and in a further random process the decision is made on whether the atom changes its state and, if it does, which state it jumps to. Figure 4.5 illustrates the different steps of this algorithm. The calculation of the jump rates by the adiabatic elimination procedure is quite time consuming and negative rates can occur, which makes the application of Monte Carlo methods impossible [100]. Therefore, we use the steady-state values of the populations of the considered atom directly as jump probabilities, which obviously leads the same steady-state values after Monte Carlo averaging as described in Ref. [119]. The use of this fast method enables us to simulate atomic ensembles consisting of up to 5×10^4 atoms in reasonable computation times on the cost of abandoning any physical dynamics and restricting only to the calculation of the global steady state. Further details of the algorithm can be found in Refs. [119, 269].

4.2.2 Blockade physics in the low density regime

At low atomic densities the steady-state properties of a resonantly excited Rydberg gas ($\Delta_1 = \Delta = 0$) can be interpreted purely in terms of the dipole blockade. As we have shown in the previous section, this results in the very simple relation

$$V_b f_0 n_0 = \frac{f_0}{f_R} - 1 = f_{bl}\,. \tag{4.29}$$

We show in the following that this is consistent with the predictions of the RE model at low atomic densities.

We simulated an ensemble of 5×10^4 atoms in a box with periodic boundary conditions and varied the density n_0 by decreasing the box size. The parameters are given in the caption of Fig. 4.6 and are the same as in the experiment in Ref. [38] except that we use a higher probe Rabi frequency. The results are shown in Fig. 4.6. We plot over the number of blockaded atoms $N_b = n_0 V_b$ to show that the curves obtained for different trap dimensionalities collapse to a single line for low densities, confirming the linear density dependence anticipated by the simple blockade argument. This line turns out to be $N_b f_0$ (dashed line) as predicted. V_b equals $2r_b$, πr_b^2 and $4\pi r_b^3/3$ for 1D, 2D and 3D, respectively. The blockade radius is obtained by comparing the EIT width $w = \gamma_{gr} + \Omega_c^2/\gamma_{eg}$ [width of single-atom steady-state population $\rho_{RR}(\Delta)$] to the interaction strength at the blockade distance C_6/r_b^6, which yields the numerical

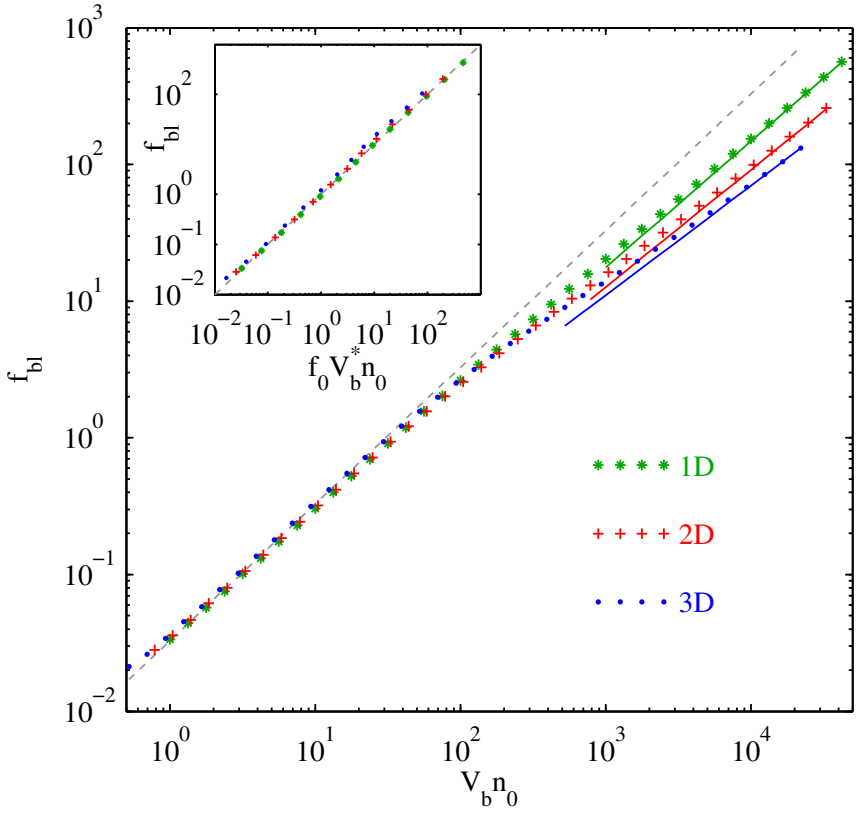

Figure 4.6: Blockade fraction as a function of atomic density for different trap geometries. Parameters as in [38]: $C_6/2\pi = 50\,\mathrm{GHz}\mu\mathrm{m}^6$, $\Omega_p/2\pi = 1\,\mathrm{MHz}$, $\Omega_c/2\pi = 5.1\,\mathrm{MHz}$, $\gamma/2\pi = 6.06\,\mathrm{MHz}$, dephasing of the probe transition 0.33 MHz, dephasing of the two-photon transition 1.7 MHz. The density is varied by changing the edge length of the cube/square/string for a fixed atom number of $N = 5 \times 10^4$. Densities are multiplied with $V_b = 2r_b$, πr_b^2, $4\pi/3 r_b^3$ for 1D, 2D, 3D, respectively. The dashed line has unit slope and corresponds to $N_b f_0$. The solid lines have slopes 12/13, 6/7, and 4/5, corresponding to the predicted scaling exponents. The inset shows f_{bl} plotted over n_0/n_{crit}, where n_{crit} is obtained from the *collective* blockade radius as described in Sec. 4.2.3.

value

$$r_b = \left(\frac{2C_6\gamma_{eg}}{\gamma_{eg}\gamma_{gr} + \Omega_c^2} \right)^{1/6} \approx 5\,\mu\mathrm{m} \tag{4.30}$$

for the given parameters. The high density behavior shown in Fig. 4.6 will be discussed in Sec. 4.2.3.

To further illustrate the low density behavior we discuss how variations in the parameters affect the density dependence. Figure 4.7(a) shows the dependence on the probe Rabi frequency. It is obvious that for smaller probe Rabi frequency the blockaded fraction is reduced, as f_0 gets smaller. Note that in the weak probe limit $f_0 \sim (\Omega_p/\Omega_c)^2$ the regime, in which $f_{bl} = n_0/n_{\mathrm{crit}}$ holds, extends to higher atomic density, consistent with our claim that deviations are to be expected when f_{bl} exceeds one, i.e., when the density exceeds n_{crit}. We have plotted over the atomic density here in order to illustrate up to which densities the linear density dependence holds for typical parameters, however, plotting over n_0/n_{crit} instead, the

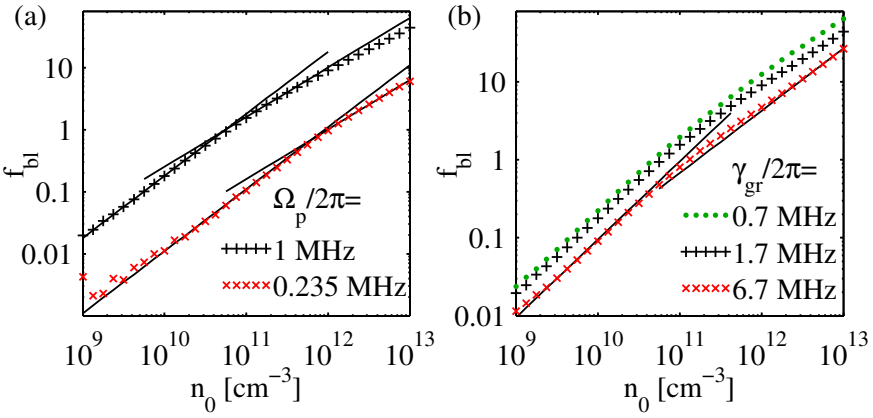

Figure 4.7: Blockade fraction as a function of density for different probe Rabi frequencies (a) and gr-dephasings (b). The trap geometry is 3D (cube). Parameters are as in Fig. 4.6. The solid lines show the linear density dependence and the $n_0^{4/5}$-scaling for high densities.

data points would again collapse to a single line in the low density regime. This shows that in the weak probe or low density regime ($n_0 < n_{\mathrm{crit}}$) the RE model is consistent with the simple relation $f_{bl} = n_0/n_{\mathrm{crit}}$. As mentioned above, one can exploit this fact in combination with Eq. (4.26) to construct a simple model for light propagation in Rydberg media. This is discussed in detail in Sec. 4.2.4.

In Fig. 4.7(b) we vary the dephasing of the Rydberg level. For larger dephasing f_{bl} gets smaller as f_0 is reduced, in consistence with $f_{bl} \propto f_0$. For small decoherence, however, it is questionable whether the RE model gives an adequate description of the strongly correlated quantum dynamics, as we discuss in Sec. 4.2.5.

4.2.3 Collectivity in the high density regime

So far we have only discussed the low density regime in Fig. 4.6. Moving to high atomic densities, where $n_0 > n_{\mathrm{crit}}$, we encounter genuine collective many-body effects associated with a density dependent blockade radius. In this regime we recover scaling laws that have been obtained from mean field models in Ref. [114]. Reinspecting Fig. 4.6 we observe that in the high density limit f_{bl} is proportional to $n_0^{2p/(2p+d)}$, where d is the system dimensionality and p is the exponent in the interaction potential. As we used a van der Waals potential ($p = 6$) for all simulations, this yields exponents 12/13, 6/7, and 4/5 for 1D, 2D, and 3D, respectively.

The observation that the slope of f_{bl} becomes smaller than one in the high density limit is connected to the blockade radius becoming smaller for high densities. For low densities it was sufficient to deduce the blockade radius from binary interaction shifts between atoms, which results in a density independent r_b [cf. Eq. (4.30)]. In the collective regime this is not the case any longer. To illustrate this, we show the pair correlation function $g^{(2)}(r)$ as a function of atomic density in the 3D case in Fig. 4.8. The $g^{(2)}$-function is defined as [119]

$$g^{(2)}(r) = \frac{\sum_{i,j}{}^{(r)} \left\langle |r_i r_j\rangle \langle r_i r_j| \right\rangle}{f_r^2 \cdot \sum_{i,j}{}^{(r)} 1} \,. \tag{4.31}$$

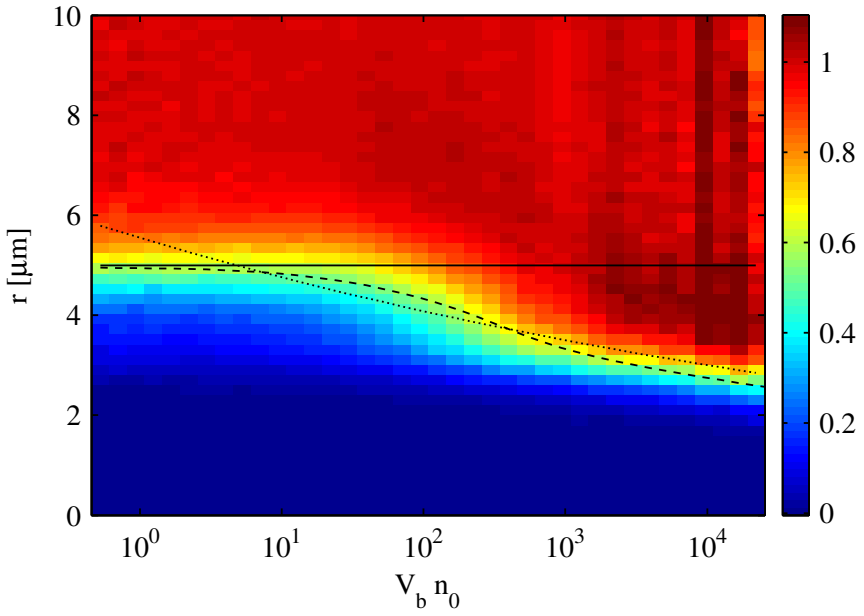

Figure 4.8: Pair correlation function for varying density. Solid line: pair-blockade radius [cf. Eq. (4.30)]; dashed line: collective blockade radius; dotted line: $n_0^{-1/15}$-scaling (see main text for details). For the highest simulated density values, fluctuations in f_r due to non-perfect convergence of the Monte Carlo sampling cause fluctuations in the height of the correlation function. Parameters are as in Fig. 4.6.

Here, $\sum_{i,j}{}^{(r)}$ denotes the sum over all pairs of atoms with distance r. We indeed observe that for low density, the blockade radius is constant (solid line), whereas for high density it decreases as $n_0^{-1/15}$ (dotted line). The high density behavior can be understood by comparing the collective Rabi frequency $\sqrt{N_b}\Omega_p$, where $N_b = V_b n_0 = 4\pi r_b^3 n_0/3$, to the interaction strength at the blockade radius C_6/r_b^6. In the intermediate region we observe an arched feature, a region where r_b decreases faster with density than predicted by this estimate.

It seems very surprising at the first glance that the RE model can reproduce this kind of collective effect since it is rooted in the $\sqrt{N_b}$-enhancement of the Rabi frequency due to coherent collective excitation that does not enter explicitly in the RE model. In the following we will show why the RE model behaves like this starting by considering a single fully blockaded ensemble and using a mean field model to explain the density dependence of r_b over the full range of densities shown in Fig. 4.8.

We start by examining the case of a perfectly blockaded ensemble of N_b atoms. In terms of single-atom properties, there is only one relevant quantity, namely the steady-state population of the Rydberg level for zero interaction shift f_0. With respect to the Rydberg excitations the ensemble can only be in two states: one atom is excited or no atom is excited. We now want to analyze the probability to find an excitation after k Monte Carlo steps of the RE model. If the ensemble is in the (singly) excited state, the probability to still find an excitation after the next Monte Carlo step becomes $(N_b - 1)/N_b + f_0/N_b$ (either we pick one of the non-excited atoms, then the ensemble stays in its state, or we pick the excited one, which then stays excited with a probability f_0). If all atoms are non-excited, the probability to create an excitation in the next step is f_0. The probability P_k to find an excited atom

after k Monte Carlo steps thus follows the recursive relation

$$P_{k+1} = P_k \left(\frac{N_b - 1 + f_0}{N_b} \right) + (1 - P_k) f_0 \tag{4.32}$$

with $P_0 = 0$ if we start with all atoms in the ground state. For k going to infinity this series converges to the super-atom excitation probability

$$P_{\mathrm{ryd}} = \frac{f_0 N_b}{f_0 N_b + 1 - f_0}. \tag{4.33}$$

Note that this result coincides with what is found by adiabatically eliminating all but the collective excited state and the ground state of a super-atom in the weak probe limit [128,242], which explains why the RE model coincides with the super-atom model proposed in Ref. [242] (see also Ref. [253]). This expression is also consistent with $P_{\mathrm{ryd}} = N_b/(N_b+1)$ found in [238] for $f_0 = 1/2$ (resonant driving and strong dephasing), and for the case of perfect EIT (no decay of the gr-coherence) coincides with the steady-state population obtained for a single atom with $\sqrt{N_b}$-enhanced probe Rabi frequency. A similar argument leads to an analytic expression for the intermediate-state population predicted by the RE model for a fully blockaded ensemble

$$P_e = \rho_{ee}^{2L}(N_b - 1)P_{\mathrm{ryd}} + \rho_{ee}^{0}[1 - (N_b - 1)P_{\mathrm{ryd}}], \tag{4.34}$$

where ρ_{ee}^{2L} (ρ_{ee}^{0}) is the steady-state value of the intermediate-state population of a single atom in the limit of infinite (zero) interaction shift. Studying the series (4.32) we can estimate the convergence properties of the RE model with respect to the number of required Monte Carlo steps.

We now want to determine the blockade radius r_b self-consistently by viewing a homogeneous atomic cloud as an ensemble of super-atoms including interactions as mean field shifts. In this picture, any super-atom is surrounded by other super-atoms that induce a shift Δ_{MF} of the Rydberg level of the atomic constituents of the super-atom. Thus, the excitation probability f_0 in P_{ryd} changes to $f = f(\Delta_{MF})$ which is the steady-state value of the Rydberg population for a given detuning of the Rydberg state. The mean field shift of a super-atom is obtained by integrating over the space surrounding it. Assuming a homogeneous medium and a step-like pair correlation function $g^{(2)}(r) = \Theta(r - r_b)$ [114] yields

$$\Delta_{MF} = \int_V g^{(2)}(r) n_{\mathrm{ryd}} V(r) dV = \int_{r>r_b} n_{\mathrm{ryd}} V(r) dV, \tag{4.35}$$

where n_{ryd} is the density of Rydberg atoms, which can be written as $n_{\mathrm{ryd}} = V_b^{-1} \propto r_b^{-d}$ where d is the dimensionality of the system. For potentials $V(r) = C_p r^{-p}$ the mean field shift becomes

$$\Delta_{MF} = \zeta(p, d) C_p r_b^{-p}, \tag{4.36}$$

where the prefactor $\zeta(p, d)$ depends on the dimensionality and the potential shape. In three dimensions and with van-der-Waals interactions we obtain $\zeta(p, d) = 1$, since $V_b = 4\pi r_b^3/3$. The super-atom excitation probability P_{ryd} has an approximately Lorentzian shape as a function of the detuning from the Rydberg level (just as f). Equating the half width of P_{ryd} to the mean field shift, one can self consistently determine r_b, which means one has to solve the

equation

$$P_{\mathrm{ryd}}[\Delta = \Delta_{MF}(r_b)] = \frac{1}{2} P_{\mathrm{ryd}}[\Delta = 0] \tag{4.37}$$

for a given atomic density n_0. Solving Eq. (4.37) for r_b numerically for several atomic densities one obtains the dashed line in Fig. 4.8, which reproduces the low density case as well as the scaling in the high density case well and even reproduces an arched structure in the intermediate region. Thus, the behavior of the RE model an be understood in terms of a mean field model of super-atoms and reproduces the scaling laws predicted by Weimer *et al.* [114] in the collective regime. It should be noted that the assumption of a step-like $g^{(2)}$-function is not quite justified since the many-body RE simulation shows that the onset of non-zero correlations is smooth and also since for very high densities the pair correlation develops peaks as the excitations become densely packed. So we cannot expect that the mean field model holds at very high densities, however, the predicted scaling behavior is still expected to be recovered qualitatively. We note that this feature is not restricted to the case of three-level atoms. Our derivation only assumed that there is exactly one interacting level (Rydberg level).

Thus, in summary, we have shown numerically and understood semi-analytically, that the rate equation model reproduces the expected universal scaling in the high density limit correctly.

We now want to come back once more to Fig. 4.6. From Eq. (4.37) one can analytically deduce that in the limit of large n_0 (large N_b), r_b scales as $n_0^{-1/(2p+d)}$, and thus the Rydberg density $n_{\mathrm{ryd}} \propto r_b^{-d} \propto n_0^{d/(2p+d)}$, and the Rydberg excited fraction $f_r = n_{\mathrm{ryd}}/n_0 \propto n_0^{-2p/(2p+d)}$. Since $f_{bl} \approx f_0/f_r$ in the high density regime ($f_{bl} \gg 1$), we obtain $f_{bl} \propto n_0^{2p/(2p+d)}$, which is the scaling observed in Fig. 4.6. The inset of Fig. 4.6 shows the same data as the main frame, but now plotted over $f_0 V_b^* n_0$, where V_b^* is the blockade volume obtained with the density dependent blockade radius determined from Eq. (4.33). We observe that all data point now lie on the diagonal, which means that f_{bl} predicted by the RE model is nicely modeled by $f_{bl} = f_0 V_b^* n_0$. Note, that we calculated r_b from (4.33) by setting $\zeta(p, d) = 1$ for all dimensionalities, which rather corresponds to a picture of binary interactions between super-atoms than to a mean field of super-atoms. Note, however, that the super-atom picture should not be taken to literal at high densities since super-atoms overlap and the correlation function is far from step-like for low dimensionalities as we show the following.

To further characterize the collective regime, we study the influence of the dimensionality on the shape of the pair-correlation function ($g^{(2)}$-function) at high atomic density. Figure 4.8 shows that in 3D the pair correlation function hardly exceeds unity, except at very high densities. For comparison we show the pair correlation in the 1D case in Fig. 4.9(a). As soon as the collective regime is entered, a clearly visible maximum arises at the onset of non-zero correlations. The comparison between different dimensionalities for a certain value of n_0 in Fig. 4.9(b) shows that the correlations are stronger the smaller the dimensionality. This means that in lower dimensions excitations get more densely packed for the same number of atoms per blockade volume N_b. Arguing again with hard blockade spheres, it is clear that in the process of randomly exciting and deexciting atoms spatial order arises more easily in lower dimensional systems. If the $g^{(2)}$-function shows a strong maximum, our mean field argument using step-like pair correlations will not work any more. Indeed, for the 1D-case Eq. (4.37) with the mean field shift (4.35) would predict a much too small blockade radius

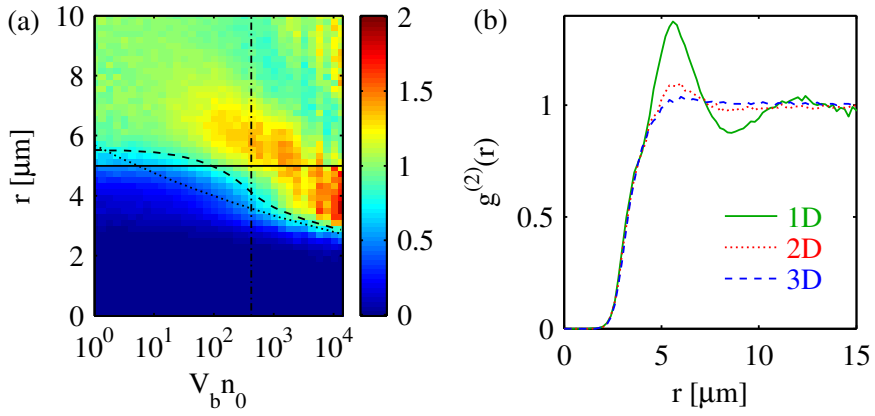

Figure 4.9: (a) Pair correlation function for a one-dimensional trap as a function of line density. Solid line: Blockade radius estimated from two-atom picture. Dotted line: scaling $n_0^{-1/13}$. Dashed line: r_b following from Eq. (4.37) with $\Delta_{\mathrm{MF}} = 2C_6/r_b^6$. (b) Comparison between different dimensionalities for $N_b = V_b n_0 \approx 600$, indicated by the dot-dashed line in (a). Parameters are as in Fig. 4.6.

for high density. Here, a better picture is that of densely packed excitations with distance r_b. In this case the interaction shift would be $\Delta_{\mathrm{int}} = 2C_6/r_b^6$ and the excitation would be shared among $r_b n_0$ atoms. Solving (4.37) under these assumptions gives the dashed line in Fig. 4.9 which nicely agrees with numerical result of the RE simulations.

A further indicator of the degree of dense packing achieved is the Mandel Q-parameter, which quantifies the width of the excitation number distribution. The Q-parameter was defined as $Q = \mathrm{var}(m)/N_{\mathrm{ryd}} - 1$, where m is the number of Rydberg excitations and N_{ryd} its mean (see Sec. 3.3). Figure 4.10(a) shows that, as soon as the collective regime is entered, the lowest Q-parameter is achieved for the 1D setup, which is in accordance with the observations in the $g^{(2)}$-function. In the low density regime, all curves appear to yield the same Q-parameter. To further illustrate the dense packing and the strongly sub-Poissonian character that is associated with it, we show the distribution of excitation numbers in the 1D case in Figs. 4.10(b) and (c). The solid line in (b) is the maximum number of excitations fitting into the volume. For high densities the observed excitation number distribution approaches this limit confirming that excitations become increasingly densely packed. This justifies the dense packing assumption that we used to estimate the blockade radius in Fig. 4.9(a) (dashed line). The dotted lines in (c) show a Poissonian distribution with the same mean for comparison. In consistence with the Q-values observed in (a), we find strong excitation number squeezing at high density and nearly Poissonian behavior at low density.

To conclude, we have shown that the properties of the RE model are determined by simple blockade physics and classical statistical effects that lead to collectivity at high densities. In Sec. 4.2.5, we will pose the question in which parameter regimes such a description is valid and what are the consequences of its breakdown.

4.2.4 Universal light propagation

Having shown the consistency of RE simulations with the simple relation between f_{bl} and the atomic density and f_0 [see Eq. (4.25)], we can use the universal relation between the scaled susceptibility and f_{bl} [see Eq. (4.26)] reported by Ates *et al.* [100] to construct a simple model

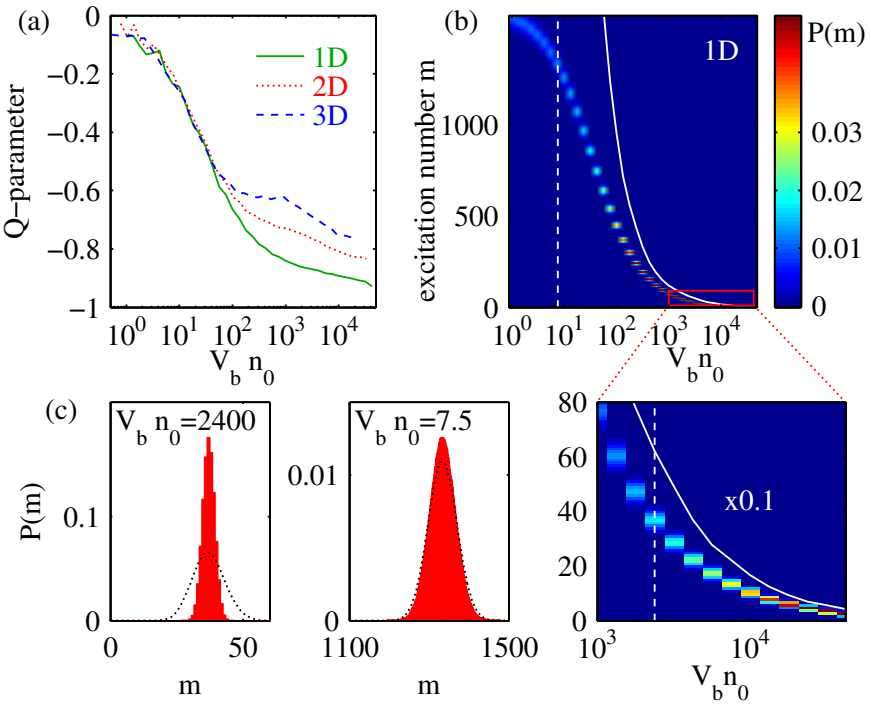

Figure 4.10: Excitation statistics. (a) Density dependence of the Mandel Q-parameter for different dimensionalities. (b) and (c) Excitation number histograms for the 1D case. The dashed lines show the positions of the two histograms of (c). The solid line in (b) indicates the maximum number of excitations $m_{\max} = L/r_b$, where r_b was extracted from the pair correlation function. Parameters are as in Fig. 4.6.

for the absorption of the probe light in a resonantly driven Rydberg medium. Before doing so, we will however illustrate that this universal relation is an intrinsic feature of the RE model.

In the case of perfect EIT the universal relation (4.26) simplifies to

$$\chi/\chi_{2L} = \frac{f_{bl}}{1+f_{bl}}\,. \tag{4.38}$$

In Sec. 4.1 we found that for a single atom χ is proportional to the steady-state population of the intermediate level ρ_{ee}. As in Eq. (4.38) ensemble averaged quantities are used, we obtain $\chi/\chi_{2L} = \langle\rho_{ee}\rangle/\langle\rho_{ee}^{2L}\rangle$ and $f_{bl} = f_0/f_r - 1 = \langle\rho_{rr}^0\rangle/\langle\rho_{rr}\rangle - 1$, where $\langle\cdot\rangle$ denotes the ensemble average. Substituting this into Eq. (4.38), the relation becomes

$$\langle\rho_{ee}\rangle/\rho_{ee}^{2L} = 1 - \langle\rho_{rr}\rangle/\rho_{rr}^{0}\,. \tag{4.39}$$

Note that both the two-level susceptibility $\propto \rho_{ee}^{2L}$ and the non-interacting Rydberg fraction $\rho_{rr}^0 = f_0$ are the same for all atoms, and thus we have dropped the ensemble averages. If this linear relation between the steady-state population of the intermediate level and the Rydberg level holds for the single-atom steady states for any (interaction induced) detuning Δ, then it also holds for the ensemble average obtained from the RE model due to the fact that in the RE model interactions are only taken into account as level shifts of the Rydberg level.

Indeed we find that both sides of Eq. (4.39) are equal to

$$\frac{\Delta^2(\gamma^2+2\Omega_p^2)}{\Delta^2(\gamma^2+2\Omega_p^2)+\frac{1}{4}(\Omega_c^2+\Omega_p^2)^2}, \tag{4.40}$$

in the single-atom case. Thus the universal relation (4.38) is found to be an intrinsic property of the RE model that is due to the fact that in the RE model interactions are included as shifts in the two-photon detuning.

If $\gamma_{gr} > 0$, that is, if dephasings of the gr-coherence lead to nonzero susceptibility on the two-photon resonance (non-perfect EIT), the universal relation the relation has be modified. From a simple hard sphere picture, we obtained

$$\chi/\chi_{2L} = \frac{\chi_0/\chi_{2L} + f_{bl}}{1+f_{bl}}, \tag{4.41}$$

where χ_0 is the remaining absorptivity (imaginary part of the susceptibility) in the noninteracting case [228, 230, 251, 310]. This generalized relation can not be traced back to an analytical equality in the single-atom steady states. However, as long as laser dephasings are not too large, the equality on the single-atom level is still fulfilled to a good approximation. In particular, it is always fulfilled in the limiting cases of zero and infinite interaction shift. For a steep inter-atomic potential, i.e., close to hard core potential, the intermediate region between fully blockaded and non-interacting case where the relation breaks down in general, is small. Therefore the number of atom pairs having a mutual distance within this region is small, too, and the generalized relation (4.41) is expected to hold for the ensemble average.

In the following we show how the insights gained from the preceding discussion can be exploited to develop an efficient model for the absorption of a resonant probe beam in a Rydberg EIT-medium. Our numerical RE simulations confirm that Eq. (4.25) (with density dependent r_b) and Eq. (4.41) hold. Thus, the local susceptibility χ only depends on the local density n_0 and the single-atom quantities f_0, χ_0 and χ_{2L} that are obtained from the laser parameters. We can therefore write down an analytic expression for the local susceptibility $\chi[\Omega_p(\mathbf{r}), n_0(\mathbf{r})]$. Under the assumption that the steady state is reached quickly and n_0 and Ω_p vary slowly spatially, one can calculate the probe beam absorption by integrating

$$\begin{aligned} \partial_z\Omega_p(\mathbf{r}) &= -\frac{k}{2}\chi[\Omega_p(\mathbf{r}), n_0(\mathbf{r})]\Omega_p(\mathbf{r}) \\ \chi[\Omega_p(\mathbf{r}), n_0(\mathbf{r})] &= \frac{\chi_0 + n_0 f_0 V_b^* \chi_{2L}}{1+n_0 f_0 V_b^*} \end{aligned} \tag{4.42}$$

along the propagation direction z. For low atomic density $n_0 < n_{\mathrm{crit}}$ we have $V_b^* = V_b$ and the formula for χ can be calculated analytically for given atomic density and laser parameters. Otherwise one first has to solve Eq. (4.37) to obtain V_b^*. For the setup of Ref. [38] this model yields results identical to the RE simulations including the probe beam attenuation intrinsically [38, 253]. Compared to the extended RE model [253], the continuous model allows to calculate absorption numerically very efficiently. The reliability of this simple model will depend on how well the RE model performs compared to an exact master equation treatment, and on whether the assumption of classical light propagation is justified. We show in the following sections that for small decoherence the first prerequisite can break down

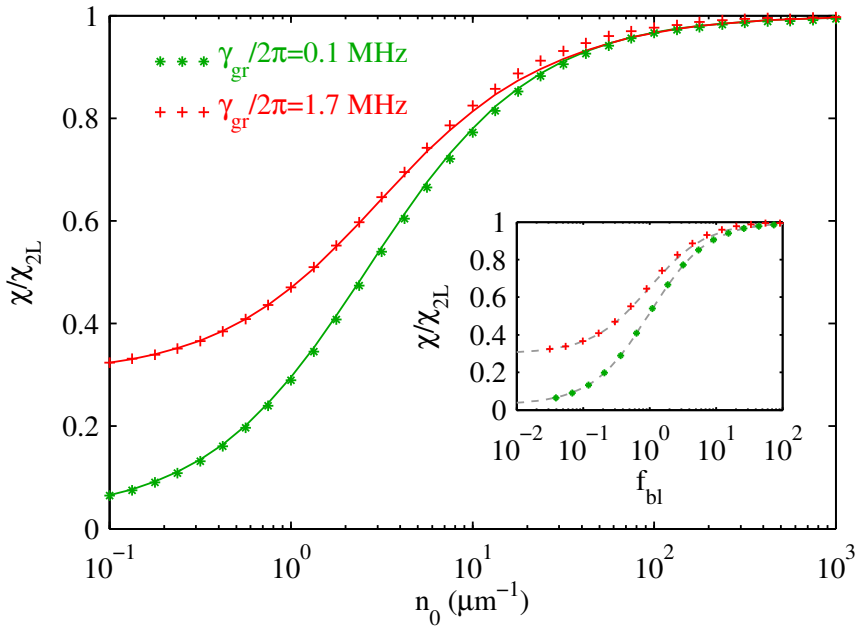

Figure 4.11: Rescaled absorption for varying atomic density. The density has been rescaled with V_{bl}. Solid lines are the result of a semi-analytical model described in Sec. 4.2.4. Parameters as in [38]: $C_6/2\pi = 50\,\mathrm{GHz}\mu\mathrm{m}^6$, $\Omega_p/2\pi = 1\,\mathrm{MHz}$, $\Omega_c/2\pi = 5.1\,\mathrm{MHz}$, $\gamma/2\pi = 6.06\,\mathrm{MHz}$, dephasing of the probe transition $0.1(0.33)\,\mathrm{MHz}$, dephasing of the two-photon transition $0.1(1.7)\,\mathrm{MHz}$ for the green (red) points.

dramatically.

The results of this simple model for χ in the case of a one-dimensional sample are summarized in Fig. 4.11. We observe that for low dephasing (green) the RE result agrees perfectly with the universal curve, while for relatively large dephasing (red) small deviations from the universal curve arise (inset). In the main frame we plot over the atomic density. The solid lines are the result of a semi-analytical model that describes the dependence of f_{bl} on n_0 and the laser parameters and uses Eq. (4.41) to obtain the scaled susceptibility. The deviations that are observed at large dephasing are mainly due to the deviations form Eq. (4.41), that are already visible in the inset.

4.2.5 Comparison to few-atom master equation simulations

We have found in Sec. 4.2.3 that the RE model can be well understood in terms of classical arguments which nonetheless lead to collective effects and non-trivial spatial correlations. In the following we test the validity of the RE model by comparing to full master equation simulations of the steady state of few-atom systems. We will start with the case of a fully blockaded sample and study the full range of laser parameters. Subsequently we show that the characteristic features encountered in the case of full blockade, are still observed if extended samples are used.

Figure 4.12 shows the typical dependence of Rydberg ($\rho_{rr} = f_r$) and intermediate-state population (ρ_{ee}) on the probe Rabi frequency going from the weak probe to the strong probe regime. A fully blockaded sample of 4 atoms under perfect EIT conditions (zero laser dephasings and no spontaneous decay from the Rydberg state) is simulated. In Figs. 4.12(a) and (c)

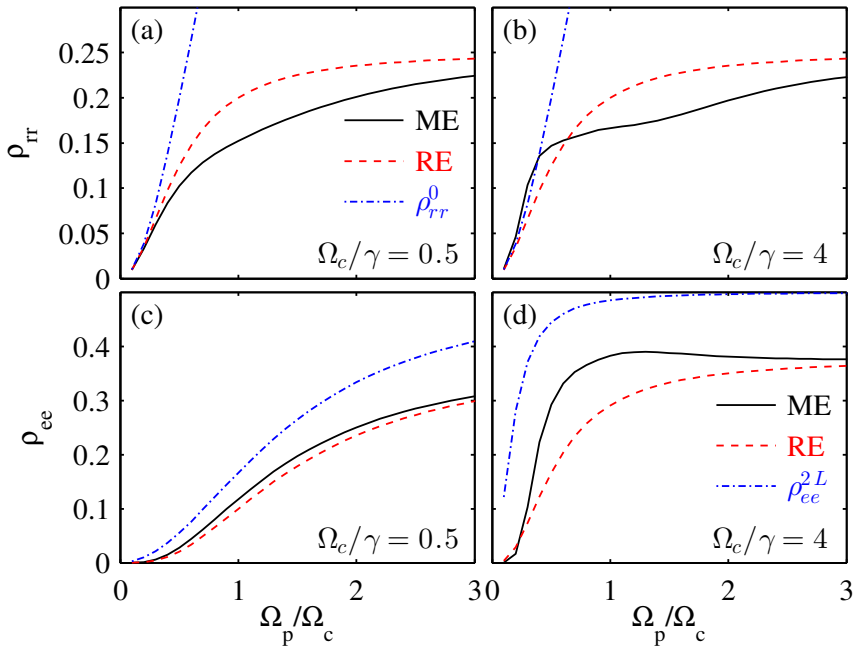

Figure 4.12: Steady-state values of Rydberg population ρ_{rr} and intermediate-state population ρ_{ee} for an ensemble of 4 perfectly blockaded atoms as a function of probe Rabi frequency. Laser dephasings and decay from the Rydberg level are set to zero (perfect EIT). In (a) and (c), the coherent laser driving is weak compared to the decay rate γ of the intermediate level, in (b) and (d) the coherent driving is rather strong. Solid black lines show the exact ME solution, red dashed lines show the RE result. The blue dot-dashed lines show the non-interacting value of ρ_{rr} and the two-level value (without Rydberg level) of ρ_{ee}, respectively, for reference.

we are in the regime of weak driving ($\Omega_c < \gamma$). We observe that the Rydberg population is severely overestimated by the RE model for intermediate Ω_p/Ω_c, while it agrees well with the exact solution in the very weak and in the strong probe regime. For strong coherent driving [Figs. 4.12(b) and (d)] the Rydberg population is still overestimated for intermediate probe frequencies, but underestimated for weak probe. In this case the steady-state Rydberg population of a fully blockaded sample even exceeds the non-interacting value. This means that due the blockade the Rydberg population is enhanced instead of suppressed. This counter-intuitive feature can never be reproduced by the RE model, since f_r is always between f_0/N and f_0, according to Eq. (4.33). If f_r exceeds f_0, it means that f_{bl} becomes negative and the notion of f_{bl} being the fraction of blockaded atoms is not meaningful any more.

Figure 4.13 shows a systematic study of the relative deviation between the RE and the ME result. All qualitative features are present already in the case of two atoms. Note, that Fig. 4.13(c) shows the relative deviation in ρ_{ee}, while the other sub-figures show the deviation in f_r. More precisely, we calculated $|(f_r^{\mathrm{ME}} - f_r^{\mathrm{RE}})/f_r^{\mathrm{ME}}|$. In all plots, two regions can be distinguished: In the weak probe regime, there is a region where the RE model underestimates the exact result, and in the intermediate probe regime, the exact result is overestimated. The two regions are separated by a line of vanishing deviation. The region of underestimated Rydberg population only exists for sufficiently strong coherent driving ($\Omega_c > \gamma$). Comparing Figs. 4.13(a) and (b) we observe that including further decoherence

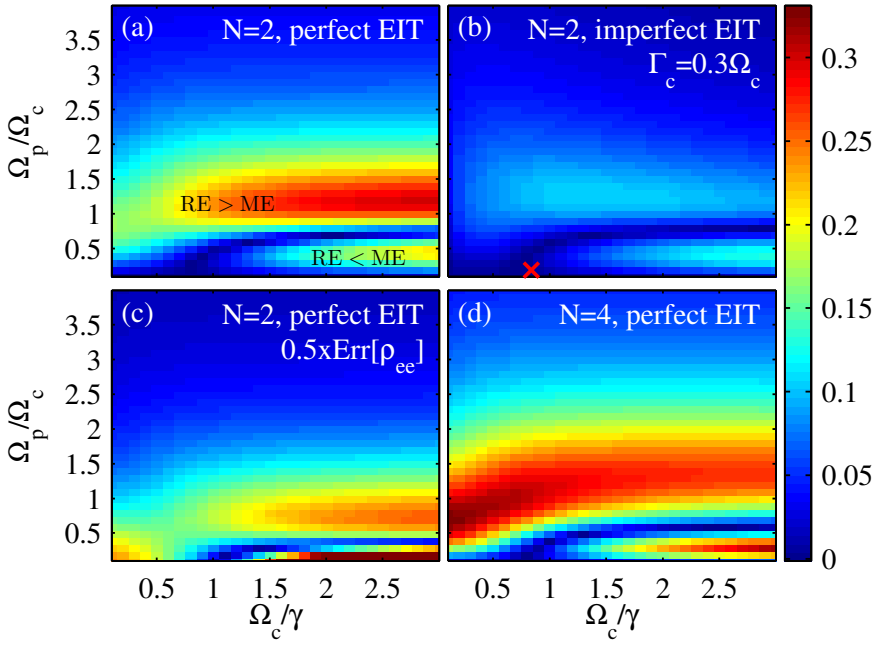

Figure 4.13: Absolute value of the relative deviation between RE and ME, $|(\rho_{\alpha\alpha}^{\mathrm{ME}} - \rho_{\alpha\alpha}^{\mathrm{RE}})/\rho_{\alpha\alpha}^{\mathrm{ME}}|$, $\alpha \in \{e, r\}$ for various parameters. In each figure, the parameters are varied between weak and strong coherent drive from left to right, and between weak and strong probe from bottom to top. We use perfect EIT conditions for all but (b), where a dephasing of the coherences with the Rydberg level $\Gamma_c = 0.3\Omega_c$ is included. The red cross marks (approximately) the parameters used in Fig. 4.6

effects such as finite laser line widths, the deviations decrease, however the qualitative features persist. In (b) we included a dephasing rate of the Rydberg level of $\Gamma_c = 0.3\Omega_c$, which approximately corresponds to the parameters used in Sec. 4.2.1. The red cross marks the parameters used is Fig. 4.6, showing that we are in a region where the RE model performs quite well. Comparing different atom numbers [cf. Figs. 4.13(a) and (d)] it turns out that at weak driving, deviations are globally increased, while at strong driving the deviations increase at weak probe, but decrease at intermediate probe ($\Omega_p \approx \Omega_c$). Interestingly, the weak probe feature, where the RE underestimates the exact result, gets narrower. We will see in the following, that this is due to collective effects beyond classical statistics. The deviations in ρ_{ee} look quite similar, however, here now the population is overestimated by the RE model for weak probe and underestimated for intermediate and strong probe intensity. Additionally, the weak probe feature is much narrower than for f_r. Exceedingly large deviations are possible here for strong driving in the case of perfect EIT. Note, that the data in Fig. 4.13(c) has been scaled down by a factor of two.

In Fig. 4.12(b) we have observed, that in a fully blockaded ensemble the Rydberg population can be larger than the non-interacting case ($f_r > f_0$), resulting in a negative $f_{bl} = f_r/f_0 - 1$. We now analyze this counter-intuitive observation more systematically, by showing f_{bl} as a function of the Rabi frequencies in Fig. 4.14(a) for the case of two fully blockaded atoms. We observe a region of negative f_{bl} for strong driving and weak probe. It is also remarkable that as Ω_p increases f_{bl} exceeds the value $N-1$ and then approaches it from above. In the case of

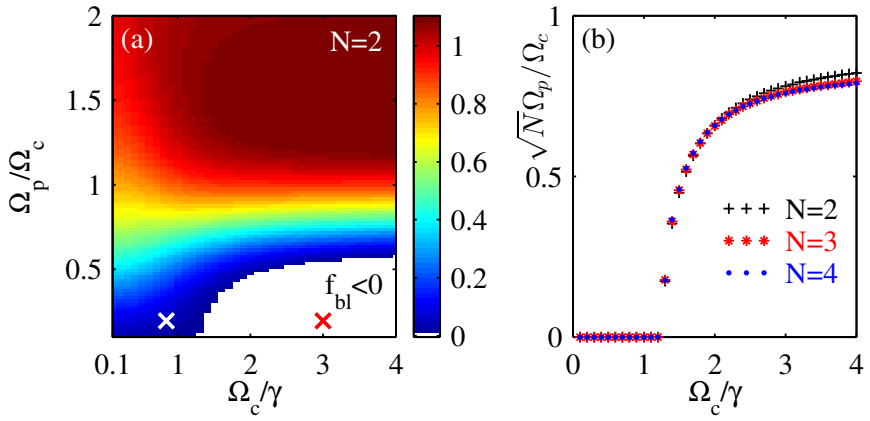

Figure 4.14: (a) f_{bl} as a function of Rabi frequencies. For strong coherent driving and weak probe, a region of negative f_{bl} is encountered. At stronger probe intensity f_{bl} can get larger than $N-1$. Both is impossible for the RE result. (b) Position of the zero crossing of f_{bl} for different atom numbers. Ω_p is rescaled by a factor $\sqrt{N}$ such that the curves collapse to a single one, which shows the intimate collectivity of this feature.

the RE model, using Eq. (4.33) and the fact that $0 < f_0 < 1$ one can show that $f_r = P_{\mathrm{ryd}}/N$ is bounded by f_0 from above and by f_0/N from below. Therefore the RE will always give $0 < f_{bl} < N-1$ in a fully blockaded sample. For $N > 2$, the onset of the region with $f_{bl} < 0$ shifts to smaller Ω_p/Ω_c, while the onset in Ω_c/γ stays constant at about 1. We extracted the zero-line of f_{bl} for different N, and found that if Ω_p is rescaled by $\sqrt{N}$, all these lines collapse to a single one [see Fig. 4.14(b)], indicating that the underlying effects are intimately connected to the collectivity arising due to the blockade.

Having seen that for unfavorable parameters the RE model can show large deviations from exact ME calculations and can even give qualitatively wrong predictions for fully blockaded ensembles, we have to check whether these features also persist for extended samples that admit the population of higher than singly excited states. For this, we first study four atoms on a regular lattice with varying lattice constant in Fig. 4.15. We choose parameters in the strong driving regime ($\Omega_c/\gamma = 3$). The black lines show a simulation in the intermediate probe regime, where the Rydberg population is overestimated considerably by the RE model over the whole range of lattice spacings. Only in the trivial non-interacting limit (large lattice spacing) they coincide. The step like features come from the successive blockade two, three, and eventually all four neighboring sites. The intermediate-state population is strongly underestimated by the RE model in this case, for the case of non-perfect blockade (intermediate lattice spacing) even more than in the perfect blockade case (small spacing). For intermediate lattice spacings with partial blockade (N_b atoms per blockade sphere) the deviation is approximately equal to the case of N_b fully blockaded atoms. Thus our findings for N fully blockaded atoms, provide a good estimate for the deviations in an extended sample with N atoms per blockade volume.

The red curves in Fig. 4.15 show the results for strong driving and weak probe, in the regime where a negative blockade fraction is observed in the fully blockaded case. We see, that this feature is robust with respect to non-perfect blockade as the exact f_r increases monotonically from non-interacting to fully blockaded, while the RE predicts a monotonic decrease.

We further studied the case of a disordered sample of few atoms in a spherical volume

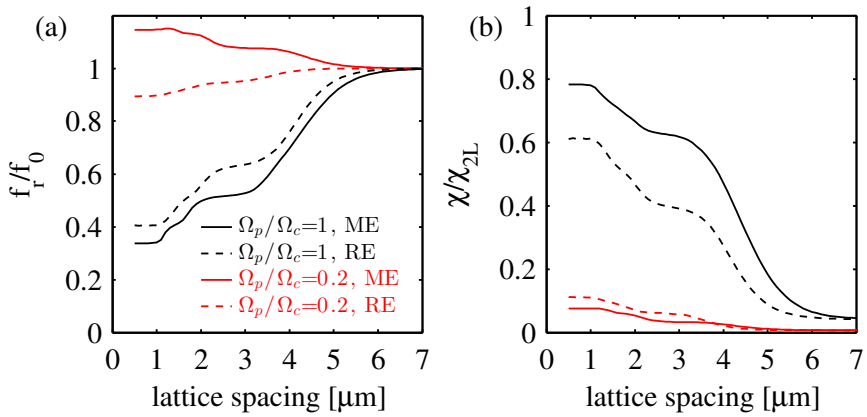

Figure 4.15: Four atoms on a regular lattice with varying lattice constant. (a) Rydberg-state population and (b) intermediate-state population. We exemplify two unfavorable parameter choices in the strong driving regime ($\Omega_c/\gamma = 3$) with small dephasing $\Gamma_c/\gamma \approx 0.02$. The red curves in (a) show, that, even in an extended sample, the RE can lead to qualitatively wrong results for weak probe.

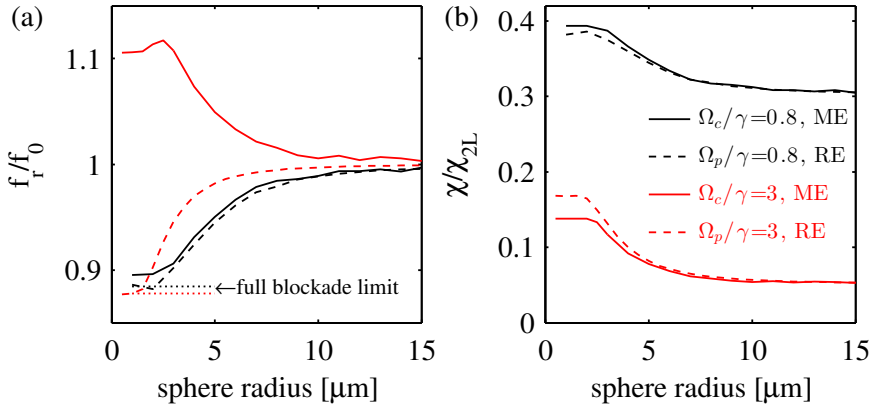

Figure 4.16: Few atoms in a sphere of varying radius with random position sampling. The parameters are as in Fig. 4.6 for the black curves, and have four fold increased Rabi frequencies for the red curves. Increasing both Rabi frequencies brings us in an unfavorable parameter region. We observe that the unintuitive $f_r > f_0$ feature in present at all sphere radii (densities). Note that the black lines have been obtained with an ensemble of five atoms while for the red ones four atoms have been used.

of varying radius. The results are shown in Fig. 4.16. We chose the parameters of Fig. 4.6 (relatively weak probe, black lines in the Figure) and also the same parameters with both Rabi frequencies increased by about a factor of four (red lines in the Figure). In the weak driving case the agreement between RE and ME is fairly good, while for strong driving, again, huge deviations, especially in the number of Rydberg excitations occur. The fluctuations that are visible in the ME data at large sphere radius are due to the finite number of samples of atom positions. Here, laser dephasings are already relatively large, and still the feature of $f_r > f_0$ persists at all densities.

In terms of atoms per blockade, we are still far in the low-density regime with 5 atoms if one reinspects Fig. 4.6. Going to larger densities is however difficult for full quantum calculations due to the exponential growth of the Hilbert space. Alternative methods for benchmarking

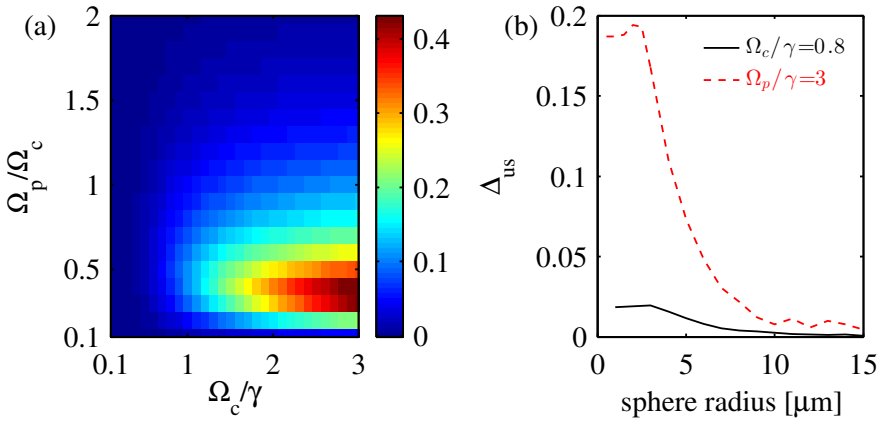

Figure 4.17: (a) The deviations from Eq. (4.39) for varying Rabi frequencies in the case of a perfectly blockaded ensemble of four atoms under perfect EIT conditions. We find that $\chi/\chi_{2L} + f_r/f_0$ is always larger than one. (b) Deviation from Eq. (4.41) for the same setup as in Fig. 4.16.

rate equation models such as Monte Carlo wave function calculations and DMRG methods are currently being pursued [129, 136, 304].

In summary, the rate equation model performs well in the strong probe and very weak probe regime, when f_0 is either close to one or close to zero, where the weak probe regime is defined by $\sqrt{N_b}\Omega_p \ll \Omega_c$ rather than by comparing the bare Rabi frequencies. In these case the inter-atomic coherences are small. In the case of full blockade we looked at the coherence between the ground state $|gg\ldots g\rangle$ and the symmetrized singly excited state (Dicke state) $|s\rangle = \sum_{i=1}^{N} |g_1 \ldots r_i \ldots g_N\rangle$. Large deviations can be expected whenever this coherence is large.

4.2.6 Breakdown of universality

In Sec. 4.2.4 we have found that the universal relation (4.38) between scaled susceptibility ($\chi/\chi_{2L} = \rho_{ee}/\rho_{ee}^{2L}$) and f_{bl} is an intrinsic property of the rate equation model. It remains to be clarified if this relation still holds in an exact model. We have now found in the previous section, that for strong driving f_{bl} can get negative in a large range of parameters already indicating that the answer to this question is going to be no. At least it makes no sense to plot the scaled susceptibility as a function of f_{bl}. We instead test the validity of the reformulated universal scaling relation (4.39) by comparing the sum of χ/χ_{2L} and f_r/f_0 to one. As both summands are positive, and we have learned that f_r/f_0 can become larger than one, it is already clear that, the relation will not hold.

Figure 4.17(a) shows $\chi/\chi_{2L} + f_r/f_0 - 1$ for a fully blockaded ensemble of four atoms as a function of the Rabi frequencies. We observe that there are severe deviations at intermediate probe intensities that increase with the strength of the coherent drive. Interestingly, the observable is always positive. We also study the deviation from universal scaling in an extended sample in Fig. 4.17(b), now referring to Eq. (4.41). The parameters are the same as in Fig. 4.16. We observe that the deviation increases with density (or number of atoms per blockade volume) and is moderate for weak driving while it approaches 20% for strong driving. For the simple model for light propagation (4.42) this means that it will fail for un-

favorable parameters, since both the relation $f_{bl} = n_0/n_{\mathrm{crit}}$ (4.25) and the universal relation (4.41) can break down.

4.2.7 Concluding remarks

In summary we have shown that the RE model is a powerful tool to model the many-body physics of long-range interacting three-level atoms in the frozen gas regime as long a interatomic coherences are small. The smallness of these coherences can be due to strong dephasing effects, or due to strongly differing sizes of the Rabi frequencies, i.e., strong probe ($\Omega_p \gg \Omega_c$) or weak probe ($\Omega_p \ll \Omega_c$). We have found that the RE model is capable of reproducing collective effects that can be understood in terms of classical statistical arguments and resembles the expected steady state for a strongly dissipative fully blockaded ensemble.

The universal relation between the electromagnetic susceptibility χ and the blockade fraction f_{bl} has been shown to be an intrinsic feature of the RE model that can be deduced from the single-atom master equation and appears in RE simulations due to the fact that interactions are included only as level shifts.

Despite the fact that universal scaling relations are reproduced by the RE model, it is questionable if the results obtained in this regime are quantitatively consistent with fully correlated many-body calculations. In order to check this, we have carried out full master equation calculations with few atoms for comparison. We find that for intermediate probe Rabi frequencies, parameter regimes are encountered, where the RE fails severely. We identified a feature occurring in this regime, that cannot be reproduced by the RE model, namely the occurrence of negative values of f_{bl}, implying that the Rydberg excitation of a perfectly blockaded ensemble can exceed the one of a non-interacting one.

We conclude that the universal scaling relation of [100] generally breaks down and is a mere artifact arising from the way the RE model functions.

We note that we have only studied the case of resonant laser excitation here. In the case of off-resonant excitation different physics are to be expected, but again the reliability of the RE model depends on the degree of decoherence and dissipation in the system [43, 119].

The insights about the range of validity are important for the next section, where we apply the RE model to a realistic experimental setup and compare our results to the experimentally measured absorption and excitation number.

4.3 Nonlinear absorption in a Rydberg EIT medium

In this section we show how the effect of probe beam attenuation can be taken into account in the RE model in order to self-consistently solve Eqs. (4.17) and (4.18). This model is analyzed by comparing it to experimental results and other models for light propagation in Rydberg EIT media. As a first example, we compare our results to recent experimental data obtained for resonant probe fields of low intensity [38]. We find that best agreement is achieved if, in addition to the constant dephasing induced by the finite laser line width, also a density-dependent dephasing is introduced. This additional dephasing could arise due motion-induced effects, and we find that the collision rates one obtains from a simple estimate based on kinetic gas theory are comparable to the relevant experimental time scales. Another effect that would also lead to density dependent enhancement of absorption is the coupling

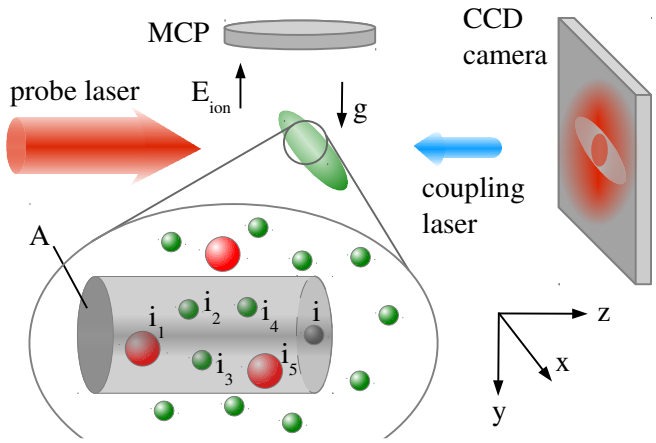

Figure 4.18: (Color online) Setup considered in the numerical calculations, adapted from [38]. A cylindrical cloud of Rydberg atoms interacts with counter-propagating probe and coupling laser fields. We model the attenuation of the probe laser field to evaluate its intensity at the position of atom i by considering an attenuation tube of transverse area A, as explained in the main text. Within this tube, large red spheres represent Rydberg excited atoms, while small green ones are atoms in non-Rydberg states at the time of evaluation. The internal states of the atoms in the tube determines the amount of attenuation. Next to the light absorption, we also calculate the number of Rydberg excitations, indicated by an ionizing field E_{ion} and an ion detector (MCP). g indicates gravitation also included as classical motion in our calculations.

of the Rydberg state excited by the lasers to neighboring Rydberg levels. We further study light propagation with off-resonant probe fields, and compare our results to those of other models [242, 309]. We find that the models disagree at higher probe intensities, as the RE include resonant excitation channels at off-resonant laser driving which are not captured in the other super-atom based models. The resulting asymmetry in the spectra predicted by the RE, however, were not observed in recent experiments [248, 287]. A possible explanation for this discrepancy is that atomic motion could render the resonant excitation channels ineffective [192].

4.3.1 Model description

According to Eq. (4.17) classical light propagating through an atomic medium with electric susceptibility $\chi = \text{Im}(\chi_{eg})$ and thickness L is damped exponentially

$$\Omega_p(L) = \Omega_p(0)e^{-\chi kL/2}\,, \tag{4.43}$$

where k is the wave vector of the light. For resonant probe fields, dispersion and transverse beam dynamics can be neglected [309]. As discussed in Sec. 4.1, χ is given in terms of atomic properties as

$$\chi = \frac{2|\mu_{eg}|^2 n_0}{\epsilon_0 \hbar \Omega_p}\text{Im}(\rho_{\text{ge}}) = \frac{3\lambda^2 n_0 \gamma^2}{2\pi k \Omega_p^2}\rho_{ee} \tag{4.44}$$

where μ_{eg} is the dipole matrix element of the probe transition, n_0 the atomic density, $\lambda = 2\pi/k$ the probe wavelength, and γ the spontaneous decay rate from $|e\rangle$ to $|g\rangle$.

In order to include the propagation effect in the Monte Carlo simulation, we have to calculate the local probe Rabi frequency that a certain atom i experiences. For this, we define

a cylindrical volume (tube) of cross section A located around atom i and extending into the opposite direction of the probe light propagation, see Fig. 4.18. All atoms inside this tubes contribute to the attenuation of the probe beam before it reaches atom i. The attenuation is calculated recursively, starting at the first atom in the tube (i_1), that experiences the full probe laser power corresponding to the Rabi frequency $\Omega_p^{(0)}$. Using $\Omega_p^{(0)}$ we calculate the steady-state value of $\rho_{ee}^{(i_1)}$ for the current configuration $|\boldsymbol{\sigma}\rangle$ and use this to determine the Rabi frequency behind atom i_1 as

$$\Omega_p^{(i_1)} = \Omega_p^{(0)} \exp\left[-\frac{3\lambda^2\gamma^2\rho_{ee}^{(i_1)}}{4\pi A(\Omega_p^{(0)})^2}\right]. \tag{4.45}$$

Using $\Omega_p^{(i_1)}$ this procedure is repeated with the next atom i_2 in the tube and so on until atom i is reached. The local Rabi frequency $\Omega_p^{(i)}$ is then used to determine the steady states and thus the jump probabilities for atom i and to update its state. This procedure is repeated until the global observables converge. Additionally we average over many random Monte Carlo samples of atom positions.

In our numerical routines the recursive calculation of Ω_p is not required in every step. Instead, the values of the local susceptibility and Rabi frequency are stored and reused. They only have to be updated, when an atom jumps into the Rydberg state or out of the Rydberg state, since in this case the interaction shifts of all other atoms change.

The only parameter that we can choose freely is the tube cross section A. We found that the results are independent of the exact choice of A as long as two criteria are fulfilled: A must be large enough to obtain $N_{\text{tube}} \gg 1$ atoms per tube on average, and it must be small enough, such that the atomic density does not vary much over the tube diameter. When simulating samples of varying density, we choose A such that the average N_{tube} is the same for all densities.

4.3.2 Density dependence on resonance

In the first part, we consider the setup in Fig. 4.18, and compare our theoretical predictions to corresponding experimental data reported in [38]. As sketched in Fig. 4.18, a small ensemble of ^{87}Rb atoms is illuminated by counter-propagating probe and coupling lasers, where the coupling laser is focused to a small spot. We calculate the absorption image of the could as well as the number of produced Rydberg excitations, as a function of the atomic density of the Gaussian-shaped cloud. The laser parameters used throughout this section are given in the caption of Fig. 4.19.

Figure 4.19 shows how the probe beam is attenuated while propagating through the atomic cloud. The higher the atomic density, the faster the probe intensity drops. Therefore the maximum of the Rydberg density does not coincide with the maximum of the atomic density. This is indicated by the dashed vertical lines in Fig. 4.19. The next quantity of interest is the transmitted probe intensity relative to the respective intensity observed in the two-level medium obtained in the absence of the coupling beam (without EIT). Figure 4.20 shows the distribution of this relative intensity in a section transverse to the beam propagation direction. In (a), a single Monte Carlo trajectory is shown. The noise is due to fluctuations in the local atomic density. The two dips close to the trap center are signatures of Rydberg excitations

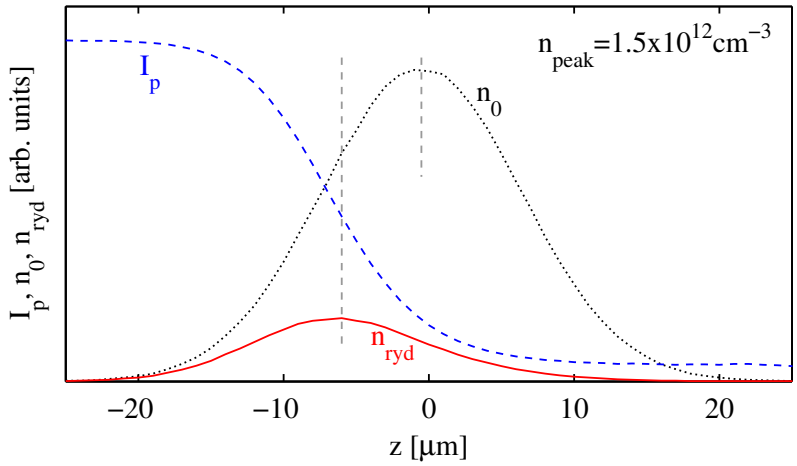

Figure 4.19: (Color online) Probe beam intensity I_p (dashed blue), atomic density n_0 (dotted black), and density of Rydberg excitations $n_{\rm ryd}$ (solid red) along the propagation direction of the probe beam. The Rydberg density has been amplified by a factor of 500 with respect to the atomic density. The peak value of n_0 is $1.5\times10^{12}\,\mathrm{cm}^{-3}$. Parameters are $\Omega_p^{(0)}/2\pi = 0.235\,\mathrm{MHz}$, $\Omega_c/2\pi = 5.1\,\mathrm{MHz}$, $\gamma/2\pi = 6.1\,\mathrm{MHz}$, $\gamma_{eg}/2\pi = 6.4\,\mathrm{MHz}$, $\gamma_{gr}/2\pi = 1.7\,\mathrm{MHz}$, and $C_6/2\pi = 50\,\mathrm{GHz}\,\mu\mathrm{m}^6$.

reducing the transmission in their vicinity. Such images cannot be obtained easily with current state-of-the-art experiments since the exposition time required to obtain an absorption image of sufficient signal to noise ratio is long on the time scale of the excitation dynamics. Thus excitations will vanish and reappear at other positions while the image is acquired making the spatially resolved detection of Rydberg excitations impossible. To overcome this difficulty, alternative imaging schemes have been proposed [46, 176].

In typical experiments, a time-integrated transmission signal is recorded, which is in addition averaged over several repetitions of the experiment. This procedure is mimicked in our Monte Carlo simulation by averaging over several Monte Carlo trajectories and several realizations of randomly chosen atom positions. Such an averaging results in a transmission pattern as shown in Fig. 4.20(b) which can be compared directly to camera images obtained in the experiment reported in [38].

We simulated the probe intensity behind the cloud ($z = \infty$) in the center of the excitation region ($x = y = 0$). The results for the EIT-absorption are divided by the absorption obtained with the coupling laser switched off in order to eliminate trivial density dependences. In the low and high density limit the results (see solid black line in Fig. 4.21) agree well with the experimental data from [38] (red open circles in Fig. 4.21). However, at intermediate densities, the experimentally observed scaled absorption is clearly underestimated by the RE model. In order to understand this discrepancy, we inspect the four major approximations that enter into our calculations. These are, first, the inclusion of interactions as mere level shifts, which is the main approximation of the RE model, second, the classical treatment of the light propagation, third, the frozen gas approximation, and fourth, the assumption of a single Rydberg level. We note that the simulations of the scaled absorption have no adjustable parameters. In [38], all experimental parameters have been determined in independent measurements.

In order to check whether the local medium response is reproduced correctly by the RE model, we benchmark it by comparing it to full ME simulations. For this, we recall that in the

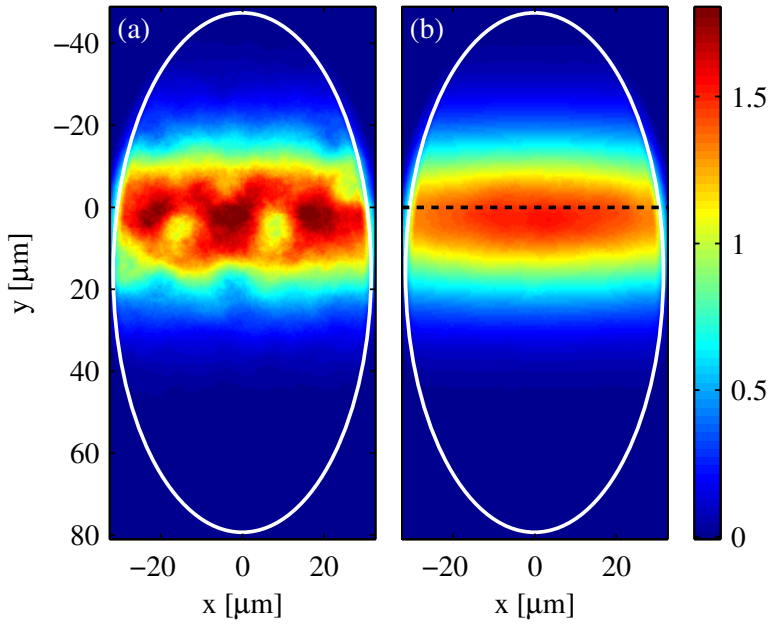

Figure 4.20: (Color online) Simulated absorption images of the atomic cloud. We plot the relative difference between the transmitted probe Rabi frequency and the respective two-level response, $(\Omega_p - \Omega_p^{(2L)})/\Omega_p^{(2L)}$. (a) shows a snapshot of a single Monte Carlo trajectory. We observe two prominent structures near the center stemming from Rydberg excitations that cause enhanced absorption in their vicinity. The peak density is chosen as $2.8 \times 10^{11}\,\mathrm{cm}^{-3}$ in this figure. The white ellipse marks the border of the coupling laser spot. (b) Average over 500 Monte Carlo samples. The dashed line marks the position of the original center of the cloud before falling under gravity.

RE model with probe absorption, the local susceptibility is calculated from the intermediate-state population using $\mathrm{Im}[\rho_{ge}] = \rho_{ee}\gamma/\Omega_p$. We therefore compare the intermediate-state population obtained from the RE model to $\mathrm{Im}[\rho_{ge}]\Omega_p/\gamma$ from full ME calculations. Due to the exponential growth of the state space with the number of three-level atoms, the ME simulations are restricted to only few atoms. The atoms are placed in a regular chain and the distance between neighboring atoms is varied. Small lattice spacing corresponds to high density, while for large lattice spacing the non-interacting regime is approached. The results are shown in Fig. 4.22 for up to 5 atoms. The parameters are as in Figs. 4.21 and 4.23. We find that the probe beam absorption is underestimated systematically by the RE model, and the deviation to the ME result increases with density. The deviations, however, are only on the order of 10^{-3} for five fully blockaded atoms, which corresponds to a density of about $10^{10}\,\mathrm{cm}^{-3}$ (solving $N_b = n_0 V_b = 5$ for n_0 with $V_b = 4\pi r_b^3/3$ and $r_b = 5\,\mu\mathrm{m}$). Higher densities are not accessible for the ME, as then there would be more atoms per blockade radius than included in the simulation. At density $10^{11}\,\mathrm{cm}^{-3}$, where the deviation in scaled absorption between theory and experiment is largest, there are approximately 50 atoms per blockade radius, inaccessible to ME treatments.

For up to 5 atoms, the deviation approximately increases linearly with the number of blockaded atoms. Naively extrapolating this linear dependence to higher densities would lead to a deviation in ρ_{ee} of order of 1% at a density of $10^{11}\,\mathrm{cm}^{-3}$. The relative differences in the Rydberg population are of the same order. This would not be sufficient to explain the deviations

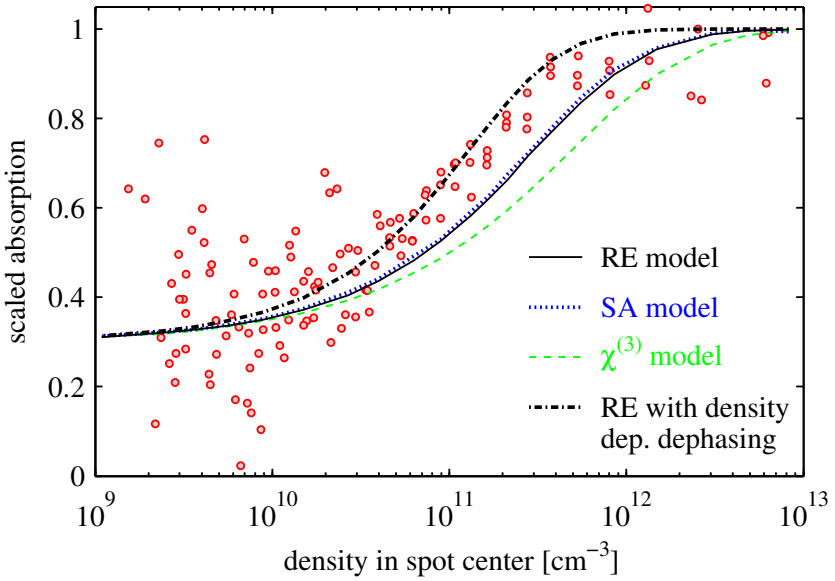

Figure 4.21: (Color online) Density dependence of scaled absorption. Red open circles: experimental data [38], solid black line: RE model, dotted blue line: super-atom model [242], dashed green line: Calculations using the third order susceptibility from [309]. The dot-dashed line is obtained by including additional atomic motion induced dephasings. The experimental data was acquired over an exposure time of 100 μs, much longer than the excitation time 2 μs for the data in Fig. 4.23. The experimental data presented in this figure and in Fig. 4.23 has been obtained in an experiment performed in the group of M. Weidemüller [38, 286]. We thank our collaborators for providing the original datasets.

from the experimental data of $\gtrsim 10\%$. Obviously, this linear extrapolation is expected to break down at higher densities. However, in related calculations, as expected we found that the RE model generally performs better as dephasing rates increase compared to the coherent drive. This was also pointed out in [128] for the case of two-level atoms [312]. In our present calculations, the dephasing rates are quite large compared to the probe Rabi frequency, as $\sqrt{N}\Omega_p^{(0)}$ only exceeds γ_{gr} starting from $N \approx 50$. This explains the good performance of the RE model in the lower density regime, and suggests that its validity range extends into the region of substantial deviation between theory and experiment in Fig. 4.21.

Since a direct benchmark of the RE results to corresponding ME results is possible only over a restricted density range, an alternative strategy to investigate the validity of the RE approach is to compare theory and experiment for other observables in the parameter range inaccessible to ME treatments. In particular, the RE model also gives access to the Rydberg excitations. The predicted number of excitations agrees well with experimental values of Ref. [38] over the entire density range, see Fig. 4.23. Here, we adjusted two parameters that were not determined from independent measurements. Namely, the semi-major axis of the coupling laser spot was found to be 65 μm, and the detection efficiency of the MCP was found to be $\eta = 0.4$, in accordance with Ref. [38]. Note that this data was taken after an excitation of 2μs, such that motional dephasing is not expected to be relevant here. We have added the results for the excitation number that we obtain if we exclude attenuation and interaction effects (green dashed line in Fig. 4.23). The obtained number of excitations is given by $f_0 N$, where f_0 is the single-atom excitation probability. Additionally we simulated the system

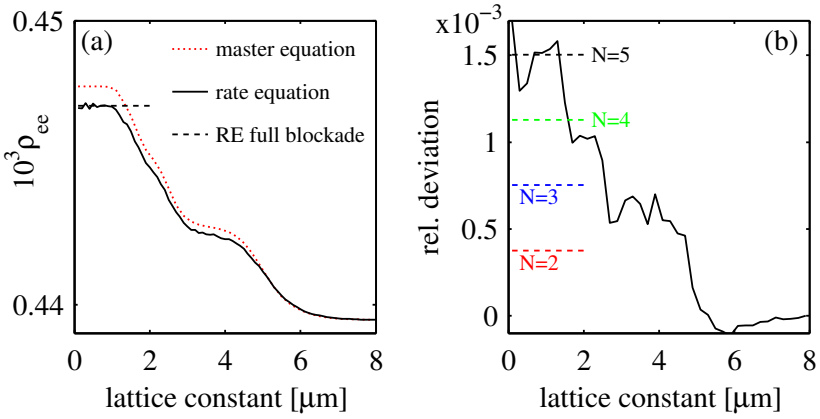

Figure 4.22: (Color online) Comparison between rate equation and master equation for few atoms in a lattice configuration. The parameters are the same as in Fig. 4.21. The atoms are arranged in a regular lattice with varying lattice spacing. The limit of small lattice spacing corresponds to full blockade, while for large spacing the atoms are non-interacting. (a) Intermediate-state population ρ_{ee} and $\mathrm{Im}[\rho_{ge}]\gamma/\Omega_p$ as a function of lattice spacing for $N = 5$ atoms. We additionally show the analytical solution of the rate equation for a fully blockaded ensemble as dashed line. (b) Relative difference between rate equation and master equation. Solid line: $N = 5$, dashed lines: deviation in the full blockade case for other atom numbers.

excluding interactions but including attenuation effects and vice versa. The strong deviations from the experimental data at high densities in both cases show that both, attenuation of the probe beam and interaction between the atoms, have a significant impact on the number of produced Rydberg excitations. This means that including the probe beam attenuation self-consistently in the RE model is indispensable for the simulation of Rydberg EIT in a dense gas. The good agreement of the Rydberg population with the experimental data is a further indication that the comparison between RE theory and experiment in Fig. 4.23 is meaningful.

In order to address possible issues with the light propagation, we compare our results to a model proposed by Petrosyan *et al.* [242]. This work makes use of a simple super-atom model for the atom dynamics and focuses on the propagated light which is characterized via coupled propagation equations for the intensity and the correlation function of the probe light. This way, correlations in the light field going beyond the classical treatment in our approach can be included. The model describes light propagation through a one-dimensional array of super-atoms with diameter $2r_b$. The blockade radius r_b is defined by equating the EIT-width to C_6/r_b^6. Interactions between super-atoms are included as a small mean field shift appearing in the susceptibility, which will be discussed in more detail in Sec. 4.3.3. We extended the original model by replacing the EIT width $w = |\Omega_c|^2/\gamma_{eg}$ by $\gamma_{gr} + |\Omega_c|^2/\gamma_{eg}$ due to the larger dephasing rates in our setup, such that the contribution γ_{gr} can not be neglected. Furthermore we include spatially varying densities, i.e., the number of atoms per super-atom n_{SA} becomes spatially dependent. With the above extensions, we obtain very good agreement for the properties of the propagated light between the two models. However, we found that for our parameters, the simulation results remain unchanged if the photon statistics is forced to remain classical in the extended model of Petrosyan *et al.*. For this, we set the $g^{(2)}$ of the light field to one. This indicates that for the parameters of this experiment, the non-classical character of the light does not influence the total absorption.

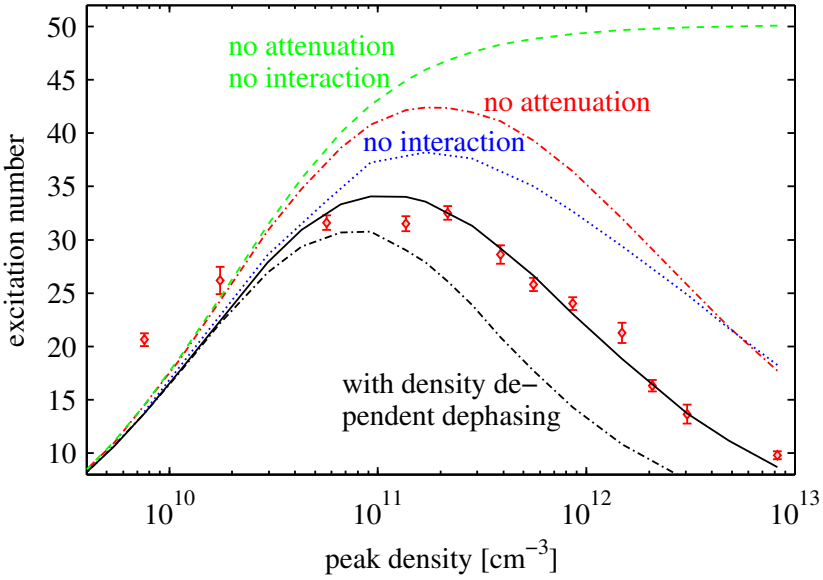

Figure 4.23: (Color online) Number of excited atoms as a function of cloud density. The detector efficiency η and the semi-major axis of the excitation spot used in the simulations are 0.4 and 65 μm, respectively [38]. Red dots show experimental data [38]. In addition to the full simulation results (black solid line), also curves with probe beam attenuation and/or inter-atomic interaction switched off are shown for comparison. As explained in the main text, the dash-dotted curve in addition includes a density-dependent dephasing, which is not expected to occur at the short exposure time of 2μs at which the Rydberg excitations were recorded.

As a further cross check for our model, in Fig. 4.21(a) we show the scaled absorption obtained including the third order non-linear absorption calculated in [309]. However, this model deviates stronger from the experimental data in the relevant density regime. One reason for this could be that the original assumption of neglecting the transverse beam profile exploited in [309] to derive an analytic expression for the nonlinear susceptibility is not satisfied for the present parameters, since the density varies rapidly perpendicular to the propagation direction. Moreover, this model is based on a truncation in the correlation order at the two-particle level, and is thus expected to fail at high densities, where higher order correlations become crucial.

The third key assumption is the frozen gas approximation. Higher absorption could be caused by atomic motion induced dephasing. In the experimental situation under discussion, a thermal cloud of atoms at $T = 5\,\mu$K is considered. The average speed of an atom is thus $v = \sqrt{8kT/\pi m} = 0.035\,$m/s. This means that within the excitation time of 100 μs an atom typically moves across a distance of 3.5 μm. As a consequence, in a binary picture, an atom that is initially unblockaded with respect to second atom, can move towards the second atom within the excitation time and undergo a collision that entangles the internal with the motional degrees of freedom and therefore leads to decoherence of the internal dynamics. Estimating the collision rate from classical kinetic gas theory, we obtain $n_{\rm coll} = \sigma v n_0 \approx 1\,\mu$s^{-1} at a density of $n_0 = 10^{11}\,$cm^{-3}. Here, the scattering cross section $\sigma = \pi r_t^2$ is determined by estimating the classical turning point from $mv^2/2 = \hbar C_6/r_t^6$. This means that after an excitation time of 100 μs, essentially all atoms would have undergone several such collisions. From this estimate, one would expect a motion-induced additional dephasing of

the the Rydberg level which is proportional to the atomic density. We test our hypothesis of an additional dephasing proportional to the atomic density by adding a dephasing rate $\Gamma_{r,mot}/2\pi = \alpha n_0$ to our model. The result is the dot-dashed curve in Fig. 4.21, which shows good agreement with the experimental data. This curve was obtained with $\alpha = 1.2 \times 10^{-11}\,\mathrm{MHz\,cm^3}$, which is of the same order of magnitude as the estimated collision rate $n_{\mathrm{coll}} \approx 10^{-11}\,\mathrm{MHz\,cm^3} n_0$. For the given value of α, the density-dependent dephasing exceeds the constant laser-induced dephasing for densities larger than approximately $1.5 \times 10^{11}\,\mathrm{cm^{-3}}$. It should be noted, however, that a quantitative estimate of such a dephasing rate would require a study of the underlying mechanism of dephasing collisions on the microscopic scale which is beyond the scope of this work.

We also studied the effect of the density dependent dephasing on the number of Rydberg excitations shown in Fig. 4.23 (dot-dashed line). We find that with the additional density-dependent dephasing rate, the Rydberg excitations are severely underestimated at high densities. Since the Rydberg excitations were recorded after a short exposure time of 2μs at which motional effects are not expected to be significant, we interpret this result as a further indication that the deviations in absorption in Fig. 4.21 are caused by a mechanism that is only relevant for long excitation times, consistent with motion-induced dephasing.

Density dependent dephasing effects have recently been studied in hot atomic vapors [222] (see also [33]). The setup in this experiment is different from ours as the excitation lasers are far detuned from the intermediate level. Nevertheless, a linear dependence of the dephasing on the atomic density was found in this work as well. Additionally, in [222], the motional dephasing was found to be proportional to the Rydberg population f_r. While we have employed a motional dephasing that is independent of f_r in our calculations, we note that we checked that an additional dephasing term proportional to the Rydberg density $f_r n_0$ instead of the atomic density n_0 alone would also lead to good agreement between theory and experiment in our case.

Finally, we investigate the truncation of the level space to three-level atoms. In Ref. [38] signatures for transfer of Rydberg excitations to adjacent states have been observed. Such excitations would be excluded from the laser dynamics, and thus effectively become meta-stable. This effect would lead to an increased number of Rydberg excitations at long excitation times and could therefore enhance absorption. The significance of additional Rydberg excitations is expected to depend on the number of particles per blockade volume and thus on the atomic density. Opposite to the motional dephasing, this effect would result in slowly in creasing number of Rydberg excitations and could be checked for experimentally by state selective ionization. Excitation of neighboring Rydberg levels at long excitation times has also been observed in [261].

4.3.3 Dependence on probe field detuning

So far, we have only considered resonant probe and coupling beams. Next, we study the dependence of the transmission through an elongated cloud of length $L = 1.3\,\mathrm{mm}$ and constant density $n_0 = 1.2 \times 10^{10}\,\mathrm{cm^{-3}}$ on the probe field detuning. The laser parameters are as in Refs. [242, 248]. Dephasings are smaller compared to Ref. [38] and C_6 is larger (a $|60s\rangle$-state with $C_6/2\pi = 140\,\mathrm{GHz}\,\mu\mathrm{m}^6$ is used). In the super-atom model of Ref. [242], the correlation function of the light field was included to account for the emergence of non-classical states of light.

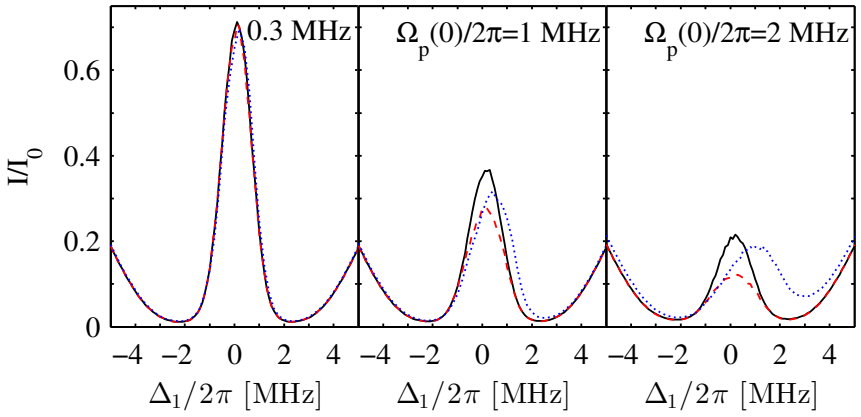

Figure 4.24: (Color online) Transmission through an elongated cloud ($L = 1.3\,\mathrm{mm}$) of density $1.2 \times 10^{10}\,\mathrm{cm}^{-3}$ as a function of probe detuning and intensity. Remaining parameters are $C_6/2\pi = 140\,\mathrm{GHz}\,\mu\mathrm{m}^6$, $\Omega_c/2\pi = 4.5\,\mathrm{MHz}$, $\gamma_{eg}/2\pi = 6.1\,\mathrm{MHz}$, $\gamma_{gr}/2\pi = 0.1\,\mathrm{MHz}$ and $\Delta/2\pi = -0.1\,\mathrm{MHz}$ as in Ref. [248]. Solid black line: super-atom model, dotted blue line: RE model, dashed red line: super-atom model with $g^{(2)} = 1$.

Scanning the probe detuning Δ_1 for various initial probe Rabi frequencies $\Omega_p(0)$, we obtain the transmission curves depicted in Fig. 4.24. For low probe intensity the models agree well. In this case $g^{(2)}$ does not deviate much from unity. As the probe intensity is increased, the transmission on resonance decreases showing the non-linearity of the process. The transmission obtained from the RE model shows a clear shift and broadening of the EIT resonance while the super-atom model does not. If $g^{(2)}$ is set to unity in the super-atom model, the resulting shift and asymmetry is still small, while the main effect is a decrease of transmission near resonance. The asymmetry observed in the RE results is due to higher-order resonant excitation channels. If the interaction shift cancels the detuning, Rydberg excitation is enhanced (anti-blockade) which leads to smaller ρ_{ee} and thus reduces absorption. As this only happens for positive detunings, the curve becomes asymmetric. The asymmetry is not present in the super-atom model since here interactions between different super-atoms are only included as a small mean field shift in the EIT-absorption. This shift is indeed negligible for the parameters studied here and does not account for the anti-blockade.

Nevertheless, the asymmetry predicted by the RE model was not observed in related experiments [248, 287], which invites a further investigation. For this, we next show that this asymmetry is not an artifact of the RE model, but is indeed underestimated by it, by comparing to exact ME calculation with few atoms. Fig. 4.25 shows the result of a simulation with 2 to 5 atoms in a spherical trap with random position sampling. $N = 5$ atoms corresponds to a density of $n_0 = 7 \times 10^9\,\mathrm{cm}^{-3}$. The remaining parameters are the same as in Fig. 4.24(c), except that we ignore the small detuning of the coupling laser ($\Delta = -0.1 \times 2\pi\,\mathrm{MHz}$), in order not to bias our asymmetry parameter by this small shift. Note that the overall shape of the curve is unchanged if we include this detuning. We observe that while for $N = 2$ atoms the asymmetry is still rather small, it becomes increasingly pronounced at larger densities. We also found that increasing the system size holding the density constant renders the asymmetry even more pronounced. In Fig. 4.25(b) we quantitatively analyze the asymmetry by calculating the difference of the integral over the blue detuned side ($\Delta_1 > 0$) and the red detuned side ($\Delta_1 < 0$), normalized by the integral over the full range of $(-5 \le \Delta_1 \le 5) \times 2\pi\,\mathrm{MHz}$. We

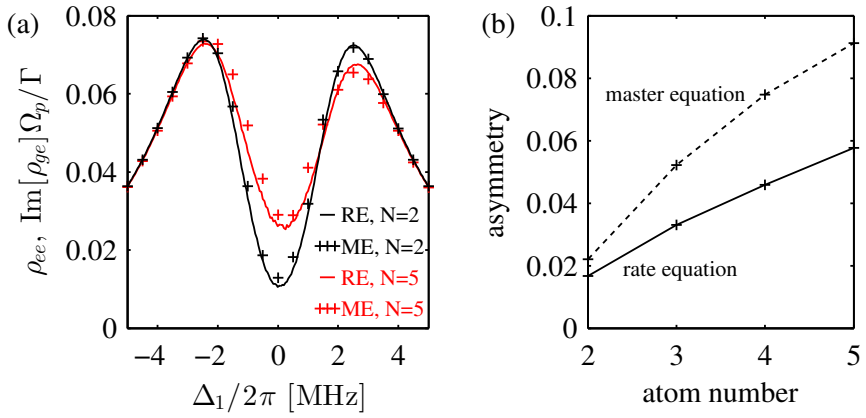

Figure 4.25: Comparison between RE and master equation for few atoms in a spherical trap. The parameters are comparable to the ones of Fig. 4.24(c). The atoms are placed randomly in a spherical trap of radius $5.5\,\mu$m. (a) Intermediate-state population and rescaled imaginary part of the coherence ρ_{ge} (for RE and ME, respectively) as a function of probe laser detuning and for two different atom numbers (densities). (b) Asymmetry of the Rydberg population as a function of atom number.

observe that the asymmetry grows approximately linearly with the atom number (density) and is underestimated by the RE model, which we attribute to the fact that higher order resonant processes relying on higher-order atom correlations are not accounted for [119, 140]. The large relative differences between ME and RE are due to the fact that the asymmetry parameter is very sensitive already to small deviations in the transmission spectra. However, they also show that the predictions of the RE model can not always be trusted, and that the validity also depends strongly on the chosen observable.

This asymmetry is not present in the super-atom model because interactions between different super-atoms are only included as a small mean field shifts in the EIT-absorption which cannot account for an anti-blockade. However, the physical reason why this asymmetry is not observed in experiment [248, 287] must be different. One candidate are again atomic motion and effects beyond the frozen gas approximation. After a pair of atoms is excited resonantly, the atoms start repelling each other as they feel the repulsive force induced by the Rydberg-Rydberg interactions, thereby moving out of the pair excitation resonance. This effect can render resonant excitation processes inefficient for long exposure times. To estimate the relevance of this effect, we consider the case of $\Delta/2\pi = 1\,$MHz. Two atoms can be excited resonantly if they are at a distance $r_{\rm res} = [C_6/(2\Delta)]^{1/6} = 6.4\,\mu$m. Assuming that both atoms get excited initially and calculating the classical trajectory on which the atoms move apart one obtains that after $10\,\mu$s the interatomic distance has increased by about $1\,\mu$m and the atoms have taken up a relative velocity of $0.13\,\mu$m/μs. Thus, they have moved out of the pair resonance, such that the double excitation probability decreases again, and they have received a momentum kick well above the mean thermal momenta at cryogenic temperatures. Thus the effect of resonant processes is rather a heating of the gas than an enhancement of the Rydberg population if excitation times are too long. These mechanisms have been studied recently in microtraps and optical lattice setups, concluding that motional effects can inhibit resonant pair excitation [192]. Recalling that the data of Ref. [248] was taken by scanning $\Delta/2\pi$ from $-20\,$MHz to $20\,$MHz in $500\,\mu$s it becomes clear that such effects should play a role,

possibly enhanced by the dynamic frequency sweep. We note that for the case of attractive interactions it was found that the transmission spectrum strongly depends on the direction of the detuning scan, indicating that mechanical effects come into play [249]. Mechanical effects playing a role in this context have also been mentioned in Ref. [310]. Next to motional effects, there are other possible reasons for the absence of an asymmetry in the experimental results of Ref. [248]. For example, light propagation effects beyond pure absorption could play a role [261]. We further note that by reducing the atomic density, Pritchard *et al.* did obtain an asymmetric transmission profile that matched very well the results of a three-atom master equation calculation, cf. Fig. 4 in Ref. [248].

Chapter 5

Conclusions and outlook

In this chapter the main results of this thesis are summarized and an outlook on future research directions is provided. As the two main parts, Chap. 3 and Chap. 4, treat different parameter regimes and stand for themselves, we summarize them in separate sections. On the technical side, we have developed a powerful toolbox of numerical methods for simulating coherent and incoherent many-body dynamics applicable to a large range of experimental settings currently being studied. This entails efficient methods for Hilbert space truncation, Monte Carlo wave function methods, as well as Monte Carlo rate equation methods for dissipative systems. These tools can not only be applied to ensembles of Rydberg atoms, but to a wide range of many-body systems with discrete internal states and long-range interactions. In both main parts of the thesis we applied the respective models to reproduce recent experimental observations and the comparison between theory and experiment showed good agreement. For both setups we verified that the simplifications we make in our modeling are justified in the sense that the results of our simulations do not deviate significantly from the solution of the full many-body master equation of an ensemble of three-level atoms. This means that the physics responsible for the observed residual deviations between theory and experiment must be physics beyond the employed master equation description. We conclude that, in order to understand the remaining discrepancies, one or several of the approximations that enter into the derivation of this master equation have to be questioned and new fascinating physics are expected to be uncovered. Among the additional effects that might play a role, the most probable candidates seem to be the influence of atomic motion, population of additional Rydberg levels leading to more involved excitation dynamics, and, in the EIT case, the signatures of the non-classical character of the light fields. Thus, there are many open questions that call for further investigation and promise more exciting physics to be discovered.

Coherent dynamics of two-level Rydberg atoms

In Chap. 3 we developed numerical tools for the solution of the time dependent Schrödinger equation of an ensemble of strongly interacting two-level atoms. In order to reduce the Hilbert space, which grows exponentially with the number of particles, to a tractable size, we truncated it by discarding states not being populating during the physical time evolution. This model was then used to provide a detailed parameter study of a one-dimensional gas of two-level Rydberg atoms under coherent laser driving. In the case of resonant laser excitation, we found that the system can be characterized by three length scales, namely the system length L, the mean inter-particle separation (or Wigner-Seitz radius) n_0^{-1}, where n_0 is the atomic (line-) density, and the blockade radius R_b. If all three scales are well separated from each other, the system properties can be described by simple scaling laws with the

number of blockaded atoms N_b being the only relevant parameter [114]. We studied how deviations from $L \gg R_b$ (finite size effects) as well as deviations from $R_b \gg n_0^{-1}$ (finite density effects) influence the properties of the system. In both cases deviations from the predicted scaling laws and signatures in spatially resolved observables and the excitation statistics have been found. Finite size effects, for example, lead to accelerated dephasing of collective Rabi oscillations while for finite atomic density the sub-Poissonian excitation statistics due to dense packing of excitations is imperfect leading to higher values of the Mandel Q parameter than expected in the scaling limit. A detailed understanding of such effects will be beneficial for applications of Rydberg gases, e.g., in quantum information science. Also, effects of potential shapes differing from the usual van der Waals potential have been studied. We found that there are substantial differences between the van der Waals case and the direct dipole-dipole case (R^{-3}) which manifest in a strongly differing shape of the pair correlation function. As consequence, by measuring spatial correlations experimentally it should be possible, in turn, to gain information about the shape of the interaction potential. In the case of a hard core potential, we compared our numerical findings in a disordered gas to a classical argument [138] and found that they disagree for fully coherent laser excitation.

For blue detuned laser excitation the emergence of strong spatial correlations was observed. These quasi-crystalline structures are due to the resonant excitation of aggregates that becomes possible as the detuning can cancel the interaction term in the Hamiltonian. A resonantly excited pair can serve as a seed for the subsequent growth of larger aggregates. As the resonant pair excitation is associated with a different distance between the excitations than the subsequent aggregate growth, two distinct length scales emerge. This was proven by the observation of a double peak structure in the pair correlation function. As a consequence of this mechanism, spatially asymmetric excitation structures emerge. We exploited this asymmetry to construct an efficient three-atom quantum gate, specifically a C-SWAP or Fredkin gate.

In order to realistically model an experimental situation various sources of decoherence, above all laser dephasing, have to be accounted for. Including this in our modeling we found that in the presence of strong dissipation the aggregate formation mechanism still functions, with the only difference that now not pairs but predominantly off-resonantly excited single atoms serve as seeds for the aggregate formation. The comparison to recent experimental observations showed that the characteristic features of the aggregate formation, namely an asymmetry of the Rydberg line and super-Poissonian excitation statistics on the blue detuned side, are clearly present in the measured data. Still some features of the experimental line shape could not be reproduced by our simulations which points to the relevance of additional effects such as mechanical repulsion between resonantly excited pairs or the interaction induced coupling to additional Rydberg levels.

Nonlinear optics and Rydberg EIT

The focus of Chap. 4 was on light propagation through a medium of atoms coupled to a Rydberg state in a two-step excitation process. Without interactions the medium would act as an EIT medium, i.e., it would become transparent for the light that drives the lower transition (probe light). However, due to the Rydberg-Rydberg interactions this transparency is destroyed leading to a strong optical nonlinearity. For three-level atoms, the state space truncation techniques employed in Chap. 3 fails, since only one out of three levels is interacting,

which leads to a still exponentially growing Hilbert space. In addition, incoherent effects, such as spontaneous emission from the intermediate level, have to be taken into account since they are crucial for the EIT effect. This made a master equation treatment necessary which is in general even more demanding than the Schrödinger equation used in Chap. 3. We therefore introduced an alternative approach based on a classical rate equation model for the calculation of the steady state of an ensemble of strongly interacting three-level atoms. Based on this model we studied the properties of the system. It turned out that the optical response predicted by the rate equation model can be reproduced by employing a simple blockade picture including collective effects. The universal relation between electromagnetic susceptibility and Rydberg excited fraction reported previously [100] was shown to be an intrinsic feature of the rate equation model. Employing a full master equation description for small ensembles of up to five atoms we found that this universal relation is violated in large parts of the parameter space. Also, it turns out that the rate equation description only holds in the case of strong probe intensity or in the presence of strong decoherence. In the regime of intermediate probe and strong coherent driving, inter-atomic coherences lead to counter-intuitive effects like an interaction induced enhancement of Rydberg population at resonant laser driving.

In the second part of Chap. 4 we extended the rate equation model to include the effect of attenuation of the probe field self-consistently and applied it to the setup of a recent experiment [38]. For low Rydberg densities (low atomic density or weak probe power) the rate equation modeling reproduces the experimental findings very well. However, at high densities the probe beam absorption is slightly underestimated. This deviation is likely to arise from dephasing effects induced by atomic motion or to the coupling to other Zeeman sublevels of the prepared Rydberg state that are decoupled from the laser driving. Also the assumption of classical light fields might have to be questioned in the regime of large optical depth, since related experiments show that non-classical states of light can emerge under such conditions [247, 261, 311]. The rate equation model also predicts a shift of the Rydberg line that could not yet be observed in experiments [248, 287]. It remains an exciting question if this asymmetry is indeed suppressed due to additional effects or if the parameters of the experiments performed so far are just unsuited for its observation. In any case new fascinating phenomena can be expected as the modeling of such complex many-body physics is still only in the beginning phase and more sophisticated techniques, which include more of the intriguing physics going on in these systems, are to be developed.

Outlook

As already mentioned above, the quantitative comparison to experimental data reveals that a description assuming motionally frozen three-level atoms can be insufficient, especially at high atomic densities. One should question the approximations that enter into this description and think about extensions of the existing models. Particularly interesting seems the study of motional effects in strongly interacting atomic gases. A fully quantum mechanical treatment of the motional and internal dynamics is challenging already for more than two atoms. An efficient, semi-classical modeling, similar to the ansatz used, e.g., in Ref. [197], would be desirable. Tools from quantum chemistry used for the simulation of large molecules might be applicable [322, 323]. In addition it seems promising to exploit the mechanical forces between Rydberg excited atoms as a feature, e.g., for entanglement generation or to implement a

controllable dephasing mechanism. It might also be important to check to what degree the dipole approximation and the use of a single Rydberg level are justified for the parameters used in recent experiments that enter regimes of higher and higher densities. In the very extreme case of Rydberg states with $n \sim 200$ and $n_0 \sim 10^{14}\,\mathrm{cm}^{-3}$ recently reported in Stuttgart [288] the Rydberg electron is scattered off the surrounding ground-state atoms. Here we enter a regime where all the approximations assuming well separated atoms without any spatial overlap of electronic wave functions break down. In this regime very little theoretical work has been done so far.

Besides the aspect of atomic motion, a comprehensive modeling of a quantized light field interacting with a strongly correlated atomic medium is still missing. In the context of light propagation in Rydberg EIT media, advances in this direction would be highly desirable. So far, under realistic conditions, simulations are limited to two photons being described in a quantum mechanical framework.

Apart from the lack of techniques and models, simulations under realistic experimental conditions are usually limited by the available computation power. At this point we can be sure that progress will be made in the near future since most of the numerical techniques employed in our models can easily be parallelized which makes it possible to solve them on massively parallel computation structures like GPUs.

From the point of view of an experimentalists it would be desirable to develop techniques for measuring spatially resolved properties of Rydberg gases. This would enable us to directly probe our predictions about the strong correlations and their formation dynamics made in this thesis. Also experiments in better controllable environments, e.g., with few atoms like in Ref. [63], would enable us to test the approximations that we use in the description of extended ensembles of Rydberg atoms in a controlled fashion. This would give us, as theorists, valuable hints in which direction our models should be extended.

As already pointed out in the introduction of this thesis, there has been a plethora of ideas for applications of Rydberg atoms in many-body physics, quantum optics, solid state physics, quantum simulation and quantum information processing. Current efforts aiming at the experimental realization of these ideas will certainly reveal new interesting effects and challenges for the modeling of quantum many-body systems. For example, in the field of quantum optics further experimental progress into the direction of single-photon switches and photon-photon interactions is to be expected in the near future. Groups working with degenerate quantum gases are pursuing the realization of new phases of matter that emerge in Rydberg-dressed BECs. Also, the recently predicted excitation crystals will presumably soon be realized using optical lattices. In such setups Feynman's vision of a quantum simulator seems to be in reach and the use of Rydberg atoms will pave the road to the simulation of a large class of spin Hamiltonians relevant in solid state physics. This will help to gain a better understanding of material properties of solids and the role of coherence in these. In the realm of quantum information multi-state Rydberg atoms, hybrid systems using Rydberg-Rydberg interactions for entangling operations, and micro-cell arrays of Rydberg ensembles are being worked on in order to push towards the long term goal of a scalable quantum computer. All these promising perspectives make the field of Rydberg physics an exciting research topic for both, theoretical and experimental physicists.

Bibliography

[1] J. R. Rydberg, Phil. Mag. 5th Ser. **29**, 331 (1890).

[2] T. F. Gallagher, *Rydberg Atoms*, Cambridge Monographs on Atomic, Molecular and Chemical Physics, Cambridge University Press, 1994.

[3] D. Jaksch, J. I. Cirac, P. Zoller, S. L. Rolston, R. Côté, and M. D. Lukin, *Fast Quantum Gates for Neutral Atoms*, Phys. Rev. Lett. **85**, 2208 (2000).

[4] M. D. Lukin, M. Fleischhauer, R. Côté, L. M. Duan, D. Jaksch, J. I. Cirac, and P. Zoller, *Dipole Blockade and Quantum Information Processing in Mesoscopic Atomic Ensembles*, Phys. Rev. Lett. **87**, 037901 (2001).

[5] C. H. Greene, A. S. Dickinson, and H. R. Sadeghpour, *Creation of Polar and Nonpolar Ultra-Long-Range Rydberg Molecules*, Phys. Rev. Lett. **85**, 2458 (2000).

[6] M. H. Anderson, J. R. Ensher, M. R. Matthews, C. E. Wieman, and E. A. Cornell, *Observation of Bose-Einstein Condensation in a Dilute Atomic Vapor*, Science **269**, 198 (1995).

[7] K. B. Davis, M. O. Mewes, M. R. Andrews, N. J. van Druten, D. S. Durfee, D. M. Kurn, and W. Ketterle, *Bose-Einstein Condensation in a Gas of Sodium Atoms*, Phys. Rev. Lett. **75**, 3969 (1995).

[8] S. N. Bose, *Plancks Gesetz und Lichtquantenhypothese*, Z. Phys. **26**, 178 (1924).

[9] A. Einstein, Sitz. Ber. K. Preuss. Akad. Wiss. 1924, 261 (1924).

[10] A. Einstein, Sitz. Ber. K. Preuss. Akad. Wiss. 1925, 3 (1925).

[11] M. Nielsen and I. Chuang, *Quantum Computation and Quantum Information*, Cambridge Series on Information and the Natural Sciences, Cambridge University Press, 2000.

[12] A. Ekert and R. Jozsa, *Quantum computation and Shor's factoring algorithm*, Rev. Mod. Phys. **68**, 733 (1996).

[13] P. Shor, Algorithms for quantum computation: discrete logarithms and factoring, in *Proc. 37th Ann. Symp. on the Foundations of Comp. Sci. (FOCS)*, pages 124–134, 1994.

[14] A. Steane, *Multiple-Particle Interference and Quantum Error Correction*, Proceedings of the Royal Society of London. Series A: Mathematical, Physical and Engineering Sciences **452**, 2551 (1996).

[15] I. Mourachko, D. Comparat, F. de Tomasi, A. Fioretti, P. Nosbaum, V. M. Akulin, and P. Pillet, *Many-Body Effects in a Frozen Rydberg Gas*, Phys. Rev. Lett. **80**, 253 (1998).

[16] W. R. Anderson, J. R. Veale, and T. F. Gallagher, *Resonant Dipole-Dipole Energy Transfer in a Nearly Frozen Rydberg Gas*, Phys. Rev. Lett. **80**, 249 (1998).

[17] A. Gaëtan, Y. Miroshnychenko, T. Wilk, A. Chotia, M. Viteau, D. Comparat, P. Pillet, A. Browaeys, and P. Grangier, *Observation of collective excitation of two individual atoms in the Rydberg blockade regime*, Nature Phys. **5**, 115 (2009).

[18] Y. O. Dudin, L. Li, F. Bariani, and A. Kuzmich, *Observation of coherent many-body Rabi oscillations*, Nature Phys. **8**, 790 (2012).

[19] E. P. Gross, *Hydrodynamics of a Superfluid Condensate*, J. Math. Phys. **4**, 195 (1963).

[20] L. P. Pitaevskii, *Vortex lines in an imperfect Bose gas*, Soviet Physics JETP-USSR **13** (1961).

[21] J. Eisert, M. Cramer, and M. B. Plenio, *Colloquium: Area laws for the entanglement entropy*, Rev. Mod. Phys. **82**, 277 (2010).

[22] M. Saffman, T. G. Walker, and K. Mølmer, *Quantum information with Rydberg atoms*, Rev. Mod. Phys. **82**, 2313 (2010).

[23] D. Comparat and P. Pillet, *Dipole blockade in a cold Rydberg atomic sample*, J. Opt. Soc. Am. B **27**, A208 (2010).

[24] J. D. Pritchard, K. J. Weatherill, and C. S. Adams, *Nonlinear optics using cold Rydberg atoms*, chapter 8, pages 301–350, World Scientific, 2013.

[25] M. Müller, S. Diehl, G. Pupillo, and P. Zoller, Engineered Open Systems and Quantum Simulations with Atoms and Ions, in *Advances in Atomic, Molecular, and Optical Physics*, edited by E. A. Paul Berman and C. Lin, volume 61 of *Advances In Atomic, Molecular, and Optical Physics*, pages 1 – 80, Academic Press, 2012.

[26] R. Löw, H. Weimer, J. Nipper, J. B. Balewski, B. Butscher, H. P. Büchler, and T. Pfau, *An experimental and theoretical guide to strongly interacting Rydberg gases*, J. Phys. B **45**, 113001 (2012).

[27] K. Singer, M. Reetz-Lamour, T. Amthor, L. G. Marcassa, and M. Weidemüller, *Suppression of Excitation and Spectral Broadening Induced by Interactions in a Cold Gas of Rydberg Atoms*, Phys. Rev. Lett. **93**, 163001 (2004).

[28] D. Tong, S. M. Farooqi, J. Stanojevic, S. Krishnan, Y. P. Zhang, R. Côté, E. E. Eyler, and P. L. Gould, *Local Blockade of Rydberg Excitation in an Ultracold Gas*, Phys. Rev. Lett. **93**, 063001 (2004).

[29] R. Heidemann, U. Raitzsch, V. Bendkowsky, B. Butscher, R. Löw, L. Santos, and T. Pfau, *Evidence for Coherent Collective Rydberg Excitation in the Strong Blockade Regime*, Phys. Rev. Lett. **99**, 163601 (2007).

[30] R. Heidemann, U. Raitzsch, V. Bendkowsky, B. Butscher, R. Löw, and T. Pfau, *Rydberg Excitation of Bose-Einstein Condensates*, Phys. Rev. Lett. **100**, 033601 (2008).

[31] M. Reetz-Lamour, J. Deiglmayr, T. Amthor, and M. Weidemüller, *Rabi oscillations between ground and Rydberg states and van der Waals blockade in a mesoscopic frozen Rydberg gas*, New J. Phys. **10**, 045026 (2008).

[32] U. Raitzsch, V. Bendkowsky, R. Heidemann, B. Butscher, R. Löw, and T. Pfau, *Echo Experiments in a Strongly Interacting Rydberg Gas*, Phys. Rev. Lett. **100**, 013002 (2008).

[33] U. Raitzsch, R. Heidemann, H. Weimer, B. Butscher, P. Kollmann, R. Löw, H. P. Büchler, and T. Pfau, *Investigation of dephasing rates in an interacting Rydberg gas*, New J. Phys. **11**, 055014 (2009).

[34] M. Viteau, M. G. Bason, J. Radogostowicz, N. Malossi, D. Ciampini, O. Morsch, and E. Arimondo, *Rydberg Excitations in Bose-Einstein Condensates in Quasi-One-Dimensional Potentials and Optical Lattices*, Phys. Rev. Lett. **107**, 060402 (2011).

[35] M. Viteau, M. Bason, J. Radogostowicz, N. Malossi, O. Morsch, D. Ciampini, and E. Arimondo, *Rydberg excitation of a Bose-Einstein condensate*, Laser Physics **23**, 015502 (2013).

[36] T. C. Liebisch, A. Reinhard, P. R. Berman, and G. Raithel, *Atom Counting Statistics in Ensembles of Interacting Rydberg Atoms*, Phys. Rev. Lett. **95**, 253002 (2005).

[37] T. C. Liebisch, A. Reinhard, P. R. Berman, and G. Raithel, *Erratum: Atom Counting Statistics in Ensembles of Interacting Rydberg Atoms [Phys. Rev. Lett. 95, 253002 (2005)]*, Phys. Rev. Lett. **98**, 109903 (2007).

[38] C. S. Hofmann, G. Günter, H. Schempp, M. Robert-de Saint-Vincent, M. Gärttner, J. Evers, S. Whitlock, and M. Weidemüller, *Sub-Poissonian Statistics of Rydberg-Interacting Dark-State Polaritons*, Phys. Rev. Lett. **110**, 203601 (2013).

[39] M. Viteau, P. Huillery, M. G. Bason, N. Malossi, D. Ciampini, O. Morsch, E. Arimondo, D. Comparat, and P. Pillet, *Cooperative Excitation and Many-Body Interactions in a Cold Rydberg Gas*, Phys. Rev. Lett. **109**, 053002 (2012).

[40] T. Amthor, C. Giese, C. S. Hofmann, and M. Weidemüller, *Evidence of Antiblockade in an Ultracold Rydberg Gas*, Phys. Rev. Lett. **104**, 013001 (2010).

[41] M. Reetz-Lamour, T. Amthor, J. Deiglmayr, and M. Weidemüller, *Rabi Oscillations and Excitation Trapping in the Coherent Excitation of a Mesoscopic Frozen Rydberg Gas*, Phys. Rev. Lett. **100**, 253001 (2008).

[42] N. Malossi, M. M. Valado, S. Scotto, P. Huillery, P. Pillet, D. Ciampini, E. Arimondo, and O. Morsch, arXiv:1308.1854 [cond-mat.quant-gas].

[43] H. Schempp, G. Günter, M. R. de Saint-Vincent, C. S. Hofmann, D. Breyel, A. Komnik, D. W. Schönleber, M. Gärttner, J. Evers, S. Whitlock, and M. Weidemüller, arXiv:1308.0264 [physics.atom-ph].

[44] A. Schwarzkopf, R. E. Sapiro, and G. Raithel, *Imaging Spatial Correlations of Rydberg Excitations in Cold Atom Clouds*, Phys. Rev. Lett. **107**, 103001 (2011).

[45] B. Olmos, W. Li, S. Hofferberth, and I. Lesanovsky, *Amplifying single impurities immersed in a gas of ultracold atoms*, Phys. Rev. A **84**, 041607 (2011).

[46] G. Günter, M. Robert-de Saint-Vincent, H. Schempp, C. S. Hofmann, S. Whitlock, and

M. Weidemüller, *Interaction Enhanced Imaging of Individual Rydberg Atoms in Dense Gases*, Phys. Rev. Lett. **108**, 013002 (2012).

[47] M. Valado, N. Malossi, S. Scotto, D. Ciampini, E. Arimondo, and O. Morsch, arXiv:1308.0205 [cond-mat.quant-gas].

[48] P. Schauß, M. Cheneau, M. Endres, T. Fukuhara, S. Hild, A. Omran, T. Pohl, C. Gross, S. Kuhr, and I. Bloch, *Observation of spatially ordered structures in a two-dimensional Rydberg gas*, Nature **491**, 87 (2012).

[49] W. Li, I. Mourachko, M. W. Noel, and T. F. Gallagher, *Millimeter-wave spectroscopy of cold Rb Rydberg atoms in a magneto-optical trap: Quantum defects of the ns, np, and nd series*, Phys. Rev. A **67**, 052502 (2003).

[50] I. I. Beterov, I. I. Ryabtsev, D. B. Tretyakov, and V. M. Entin, *Quasiclassical calculations of blackbody-radiation-induced depopulation rates and effective lifetimes of Rydberg nS, nP, and nD alkali-metal atoms with* $n < 80$, Phys. Rev. A **79**, 052504 (2009).

[51] I. I. Beterov, D. B. Tretyakov, V. M. Entin, E. A. Yakshina, I. I. Ryabtsev, C. MacCormick, and S. Bergamini, *Deterministic single-atom excitation via adiabatic passage and Rydberg blockade*, Phys. Rev. A **84**, 023413 (2011).

[52] I. I. Beterov, M. Saffman, E. A. Yakshina, V. P. Zhukov, D. B. Tretyakov, V. M. Entin, I. I. Ryabtsev, C. W. Mansell, C. MacCormick, S. Bergamini, and M. P. Fedoruk, arXiv:1212.1138 [quant-ph].

[53] D. Tong, S. M. Farooqi, E. G. M. van Kempen, Z. Pavlovic, J. Stanojevic, R. Côté, E. E. Eyler, and P. L. Gould, *Observation of electric quadrupole transitions to Rydberg nd states of ultracold rubidium atoms*, Phys. Rev. A **79**, 052509 (2009).

[54] Z. Feng, H. Zhang, J. Che, L. Zhang, C. Li, J. Zhao, and S. Jia, *Collisional loss of cesium Rydberg atoms in a magneto-optical trap*, Phys. Rev. A **83**, 042711 (2011).

[55] T. J. Carroll, K. Claringbould, A. Goodsell, M. J. Lim, and M. W. Noel, *Angular Dependence of the Dipole-Dipole Interaction in a Nearly One-Dimensional Sample of Rydberg Atoms*, Phys. Rev. Lett. **93**, 153001 (2004).

[56] M. E. Henry and R. M. Herman, *Collisional broadening of Rydberg-atom transitions by ground-state alkali atoms*, J. Phys. B **35**, 357 (2002).

[57] K. Singer, J. Stanojevic, M. Weidemüller, and R. Côté, *Long-range interactions between alkali Rydberg atom pairs correlated to the ns-ns, np-np and nd-nd asymptotes*, J. Phys. B **38**, S295 (2005).

[58] A. Reinhard, T. C. Liebisch, B. Knuffman, and G. Raithel, *Level shifts of rubidium Rydberg states due to binary interactions*, Phys. Rev. A **75**, 032712 (2007).

[59] A. Reinhard, K. C. Younge, and G. Raithel, *Effect of Förster resonances on the excitation statistics of many-body Rydberg systems*, Phys. Rev. A **78**, 060702 (2008).

[60] J. Stanojevic, R. Côté, D. Tong, S. M. Farooqi, E. E. Eyler, and P. L. Gould, *Long-range Rydberg-Rydberg interactions and molecular resonances*, Eur. Phys. J. D **40**, 3 (2006).

[61] T. G. Walker and M. Saffman, *Zeros of Rydberg-Rydberg Förster interactions*, J. Phys. B **38**, S309 (2005).

[62] T. G. Walker and M. Saffman, *Consequences of Zeeman degeneracy for the van der Waals blockade between Rydberg atoms*, Phys. Rev. A **77**, 032723 (2008).

[63] L. Béguin, A. Vernier, R. Chicireanu, T. Lahaye, and A. Browaeys, *Direct Measurement of the van der Waals Interaction between Two Rydberg Atoms*, Phys. Rev. Lett. **110**, 263201 (2013).

[64] B. Olmos, D. Yu, Y. Singh, F. Schreck, K. Bongs, and I. Lesanovsky, *Long-Range Interacting Many-Body Systems with Alkaline-Earth-Metal Atoms*, Phys. Rev. Lett. **110**, 143602 (2013).

[65] R. Mukherjee, J. Millen, R. Nath, M. P. A. Jones, and T. Pohl, *Many-body physics with alkaline-earth Rydberg lattices*, J. Phys. B **44**, 184010 (2011).

[66] W. Li, A. W. Glaetzle, R. Nath, and I. Lesanovsky, *Parallel execution of quantum gates in a long linear ion chain via Rydberg mode shaping*, Phys. Rev. A **87**, 052304 (2013).

[67] W. Li and I. Lesanovsky, arXiv:1306.5953 [quant-ph].

[68] V. Bendkowsky, B. Butscher, J. Nipper, J. P. Shaffer, R. Löw, and T. Pfau, *Observation of ultralong-range Rydberg molecules*, Nature **458**, 1005 (2009).

[69] W. Li, T. Pohl, J. M. Rost, S. T. Rittenhouse, H. R. Sadeghpour, J. Nipper, B. Butscher, J. B. Balewski, V. Bendkowsky, R. Löw, and T. Pfau, *A Homonuclear Molecule with a Permanent Electric Dipole Moment*, Science **334**, 1110 (2011).

[70] M. Kiffner, H. Park, W. Li, and T. F. Gallagher, *Dipole-dipole-coupled double-Rydberg molecules*, Phys. Rev. A **86**, 031401 (2012).

[71] B. Vaucher, S. J. Thwaite, and D. Jaksch, *Ultralarge Rydberg dimers in optical lattices*, Phys. Rev. A **78**, 043415 (2008).

[72] V. Bendkowsky, B. Butscher, J. Nipper, J. B. Balewski, J. P. Shaffer, R. Löw, T. Pfau, W. Li, J. Stanojevic, T. Pohl, and J. M. Rost, *Rydberg Trimers and Excited Dimers Bound by Internal Quantum Reflection*, Phys. Rev. Lett. **105**, 163201 (2010).

[73] M. Kiffner, W. Li, and D. Jaksch, arXiv:1304.1597 [quant-ph].

[74] M. Kiffner, W. Li, and D. Jaksch, arXiv:1306.5892 [quant-ph].

[75] A. Cesa and J. Martin, arXiv:1309.2538 [quant-ph].

[76] P. J. Tanner, J. Han, E. S. Shuman, and T. F. Gallagher, *Many-Body Ionization in a Frozen Rydberg Gas*, Phys. Rev. Lett. **100**, 043002 (2008).

[77] W. Li, P. J. Tanner, and T. F. Gallagher, *Dipole-Dipole Excitation and Ionization in an Ultracold Gas of Rydberg Atoms*, Phys. Rev. Lett. **94**, 173001 (2005).

[78] W. Li, P. Tanner, Y. Jamil, and T. Gallagher, *Ionization and plasma formation in high n cold Rydberg samples*, Eur. Phys. J. D **V40**, 27 (2006).

[79] T. Topcu and A. Derevianko, arXiv:1308.0573 [physics.atom-ph].

[80] X. Zhang, R. R. Jones, and F. Robicheaux, *Time-Dependent Electron Interactions in Double Rydberg Wave Packets*, Phys. Rev. Lett. **110**, 023002 (2013).

[81] J. S. Cabral, J. M. Kondo, L. F. Gonçalves, V. A. Nascimento, L. G. Marcassa, D. Booth, J. Tallant, A. Schwettmann, K. R. Overstreet, J. Sedlacek, and J. P. Shaffer, *Effects of electric fields on ultracold Rydberg atom interactions*, J. Phys. B **44**, 184007 (2011).

[82] I. I. Ryabtsev, D. B. Tretyakov, I. I. Beterov, V. M. Entin, and E. A. Yakshina, *Stark-tuned Förster resonance and dipole blockade for two to five cold Rydberg atoms: Monte Carlo simulations for various spatial configurations*, Phys. Rev. A **82**, 053409 (2010).

[83] I. I. Ryabtsev, D. B. Tretyakov, I. I. Beterov, and V. M. Entin, *Observation of the Stark-Tuned Förster Resonance between Two Rydberg Atoms*, Phys. Rev. Lett. **104**, 073003 (2010).

[84] L. A. Jones, J. D. Carter, and J. D. D. Martin, *Rydberg atoms with a reduced sensitivity to dc and low-frequency electric fields*, Phys. Rev. A **87**, 023423 (2013).

[85] J. Nipper, J. B. Balewski, A. T. Krupp, B. Butscher, R. Löw, and T. Pfau, *Highly Resolved Measurements of Stark-Tuned Förster Resonances between Rydberg Atoms*, Phys. Rev. Lett. **108**, 113001 (2012).

[86] A. Tauschinsky, R. M. T. Thijssen, S. Whitlock, H. B. van Linden van den Heuvell, and R. J. C. Spreeuw, *Spatially resolved excitation of Rydberg atoms and surface effects on an atom chip*, Phys. Rev. A **81**, 063411 (2010).

[87] H. Kübler, D. Booth, J. Sedlacek, P. Zabawa, and J. Shaffer, arXiv:1304.7266 [physics.atom-ph].

[88] J. D. Carter and J. D. D. Martin, arXiv:1308.1945 [physics.atom-ph].

[89] S. E. Anderson, K. C. Younge, and G. Raithel, *Trapping Rydberg Atoms in an Optical Lattice*, Phys. Rev. Lett. **107**, 263001 (2011).

[90] M. J. Piotrowicz, M. Lichtman, K. Maller, G. Li, S. Zhang, L. Isenhower, and M. Saffman, arXiv:1305.6102 [physics.atom-ph].

[91] M. J. Morrison and A. Derevianko, *Possibility of magic trapping of a three-level system for Rydberg blockade implementation*, Phys. Rev. A **85**, 033414 (2012).

[92] M. Mayle, I. Lesanovsky, and P. Schmelcher, *Dressing of ultracold atoms by their Rydberg states in a Ioffe-Pritchard trap*, J. Phys. B **43**, 155003 (2010).

[93] T. Topcu and A. Derevianko, arXiv:1305.6570 [physics.atom-ph].

[94] T. Topcu and A. Derevianko, arXiv:1308.6258 [physics.atom-ph].

[95] D. Barredo, H. Kübler, R. Daschner, R. Löw, and T. Pfau, *Electrical Readout for Coherent Phenomena Involving Rydberg Atoms in Thermal Vapor Cells*, Phys. Rev. Lett. **110**, 123002 (2013).

[96] J. A. Sedlacek, A. Schwettmann, H. Kb̈ler, R. Löw, T. Pfau, and J. P. Shaffer, *Microwave electrometry with Rydberg atoms in a vapour cell using bright atomic resonances*, Nature Phys. **8**, 819 (2012).

[97] C. Ates, T. Pohl, T. Pattard, and J. M. Rost, *Strong interaction effects on the atom counting statistics of ultracold Rydberg gases*, J. Phys. B **39**, L233 (2006).

[98] C. Ates, T. Pohl, T. Pattard, and J. M. Rost, *Many-body theory of excitation dynamics in an ultracold Rydberg gas*, Phys. Rev. A **76**, 013413 (2007).

[99] C. Ates, T. Pohl, T. Pattard, and J. M. Rost, *Antiblockade in Rydberg Excitation of an Ultracold Lattice Gas*, Phys. Rev. Lett. **98**, 023002 (2007).

[100] C. Ates, S. Sevinçli, and T. Pohl, *Electromagnetically induced transparency in strongly interacting Rydberg gases*, Phys. Rev. A **83**, 041802 (2011).

[101] T. Pohl and P. R. Berman, *Breaking the Dipole Blockade: Nearly Resonant Dipole Interactions in Few-Atom Systems*, Phys. Rev. Lett. **102**, 013004 (2009).

[102] S. Wüster, J. Stanojevic, C. Ates, T. Pohl, P. Deuar, J. F. Corney, and J. M. Rost, *Correlations of Rydberg excitations in an ultracold gas after an echo sequence*, Phys. Rev. A **81**, 023406 (2010).

[103] K. C. Younge, A. Reinhard, T. Pohl, P. R. Berman, and G. Raithel, *Mesoscopic Rydberg ensembles: Beyond the pairwise-interaction approximation*, Phys. Rev. A **79**, 043420 (2009).

[104] B. Olmos, R. González-Férez, and I. Lesanovsky, *Collective Rydberg excitations of an atomic gas confined in a ring lattice*, Phys. Rev. A **79**, 043419 (2009).

[105] B. Olmos, R. González-Férez, and I. Lesanovsky, *Fermionic Collective Excitations in a Lattice Gas of Rydberg Atoms*, Phys. Rev. Lett. **103**, 185302 (2009).

[106] B. Olmos, M. Müller, and I. Lesanovsky, *Thermalization of a strongly interacting 1D Rydberg lattice gas*, New J. Phys. **12**, 013024 (2010).

[107] B. Olmos, R. González-Férez, I. Lesanovsky, and L. Velázquez, *Universal time evolution of a Rydberg lattice gas with perfect blockade*, J. Phys. A **45**, 325301 (2012).

[108] I. Lesanovsky and H. Katsura, *Interacting Fibonacci anyons in a Rydberg gas*, Phys. Rev. A **86**, 041601 (2012).

[109] C. Ates, J. P. Garrahan, and I. Lesanovsky, *Thermalization of a Strongly Interacting Closed Spin System: From Coherent Many-Body Dynamics to a Fokker-Planck Equation*, Phys. Rev. Lett. **108**, 110603 (2012).

[110] J. V. Hernández and F. Robicheaux, *Simulation of a strong van der Waals blockade in a dense ultracold gas*, J. Phys. B **41**, 045301 (2008).

[111] F. Robicheaux, J. V. Hernández, T. Topçu, and L. D. Noordam, *Simulation of coherent interactions between Rydberg atoms*, Phys. Rev. A **70**, 042703 (2004).

[112] F. Robicheaux and J. V. Hernández, *Many-body wave function in a dipole blockade configuration*, Phys. Rev. A **72**, 063403 (2005).

[113] B. Sun and F. Robicheaux, *Numerical study of two-body correlation in a 1D lattice with perfect blockade*, New J. Phys. **10**, 045032 (2008).

[114] H. Weimer, R. Löw, T. Pfau, and H. P. Büchler, *Quantum Critical Behavior in Strongly Interacting Rydberg Gases*, Phys. Rev. Lett. **101**, 250601 (2008).

[115] R. Löw, H. Weimer, U. Krohn, R. Heidemann, V. Bendkowsky, B. Butscher, H. P. Büchler, and T. Pfau, *Universal scaling in a strongly interacting Rydberg gas*, Phys. Rev. A **80**, 033422 (2009).

[116] T. J. Carroll, S. Sunder, and M. W. Noel, *Many-body interactions in a sample of ultracold Rydberg atoms with varying dimensions and densities*, Phys. Rev. A **73**, 032725 (2006).

[117] T. J. Carroll, C. Daniel, L. Hoover, T. Sidie, and M. W. Noel, *Simulations of the dipole-dipole interaction between two spatially separated groups of Rydberg atoms*, Phys. Rev. A **80**, 052712 (2009).

[118] M. Gärttner, K. P. Heeg, T. Gasenzer, and J. Evers, *Finite-size effects in strongly interacting Rydberg gases*, Phys. Rev. A **86**, 033422 (2012).

[119] K. P. Heeg, M. Gärttner, and J. Evers, *Hybrid model for Rydberg gases including exact two-body correlations*, Phys. Rev. A **86**, 063421 (2012).

[120] C. S. E. van Ditzhuijzen, A. F. Koenderink, J. V. Hernández, F. Robicheaux, L. D. Noordam, and H. B. v. L. van den Heuvell, *Spatially Resolved Observation of Dipole-Dipole Interaction between Rydberg Atoms*, Phys. Rev. Lett. **100**, 243201 (2008).

[121] J. Qian, G. Dong, L. Zhou, and W. Zhang, *Phase diagram of Rydberg atoms in a nonequilibrium optical lattice*, Phys. Rev. A **85**, 065401 (2012).

[122] J. Qian, X.-D. Zhao, L. Zhou, and W. Zhang, arXiv:1309.0331 [physics.atom-ph].

[123] J. Qian, G. Dong, L. Zhou, and W. Zhang, arXiv:1206.6155 [cond-mat.quant-gas].

[124] I. Mourachko, W. Li, and T. F. Gallagher, *Controlled many-body interactions in a frozen Rydberg gas*, Phys. Rev. A **70**, 031401 (2004).

[125] J. Stanojevic and R. Côté, *Many-body Rabi oscillations of Rydberg excitation in small mesoscopic samples*, Phys. Rev. A **80**, 033418 (2009).

[126] J. Stanojevic and R. Côté, *Many-body dynamics of Rydberg excitation using the* Ω *expansion*, Phys. Rev. A **81**, 053406 (2010).

[127] T. A. Johnson, E. Urban, T. Henage, L. Isenhower, D. D. Yavuz, T. G. Walker, and M. Saffman, *Rabi Oscillations between Ground and Rydberg States with Dipole-Dipole Atomic Interactions*, Phys. Rev. Lett. **100**, 113003 (2008).

[128] D. Petrosyan, M. Höning, and M. Fleischhauer, *Spatial correlations of Rydberg excitations in optically driven atomic ensembles*, Phys. Rev. A **87**, 053414 (2013).

[129] D. Petrosyan, arXiv:1305.2341 [quant-ph].

[130] F. Bariani, Y. O. Dudin, T. A. B. Kennedy, and A. Kuzmich, *Dephasing of Multiparticle Rydberg Excitations for Fast Entanglement Generation*, Phys. Rev. Lett. **108**, 030501 (2012).

[131] F. Bariani, P. M. Goldbart, and T. A. B. Kennedy, *Dephasing dynamics of Rydberg atom spin waves*, Phys. Rev. A **86**, 041802 (2012).

[132] A. Chotia, M. Viteau, V. Vogt, D. Comparat, and P. Pillet, *Kinetic Monte Carlo modeling of dipole blockade in Rydberg excitation experiment*, New J. Phys. **10**, 045031 (2008).

[133] D. Yan, C.-L. Cui, M. Zhang, and J.-H. Wu, *Coherent population transfer and quantum entanglement generation involving a Rydberg state by stimulated Raman adiabatic passage*, Phys. Rev. A **84**, 043405 (2011).

[134] D. Petrosyan, Dynamics and equilibration of Rydberg excitations in dissipative atomic ensembles, 2013.

[135] D. Petrosyan and K. Mølmer, *Stimulated adiabatic passage in a dissipative ensemble of atoms with strong Rydberg-state interactions*, Phys. Rev. A **87**, 033416 (2013).

[136] M. Höning, D. Muth, D. Petrosyan, and M. Fleischhauer, *Steady-state crystallization of Rydberg excitations in an optically driven lattice gas*, Phys. Rev. A **87**, 023401 (2013).

[137] S. Bettelli, D. Maxwell, T. Fernholz, C. S. Adams, I. Lesanovsky, and C. Ates, arXiv:1306.0869 [physics.atom-ph].

[138] C. Ates and I. Lesanovsky, *Entropic enhancement of spatial correlations in a laser-driven Rydberg gas*, Phys. Rev. A **86**, 013408 (2012).

[139] D. Breyel, T. L. Schmidt, and A. Komnik, *Rydberg crystallization detection by statistical means*, Phys. Rev. A **86**, 023405 (2012).

[140] M. Gärttner, K. P. Heeg, T. Gasenzer, and J. Evers, *Dynamic formation of Rydberg aggregates at off-resonant excitation*, Phys. Rev. A **88**, 043410 (2013).

[141] M. Reetz-Lamour, T. Amthor, S. Westermann, J. Denskat, A. L. de Oliveira, and M. Weidemüller, *Modeling few-body phenomena in an ultracold Rydberg gas*, Nucl. Phys. A **790**, 728 (2007).

[142] J. Schachenmayer, I. Lesanovsky, A. Micheli, and A. J. Daley, *Dynamical crystal creation with polar molecules or Rydberg atoms in optical lattices*, New J. Phys. **491**, 103044 (2010).

[143] M. Mayle, W. Zeller, N. Tezak, and P. Schmelcher, *Rydberg-Rydberg interaction profile from the excitation dynamics of ultracold atoms in lattices*, Phys. Rev. A **84**, 010701 (2011).

[144] N. Tezak, M. Mayle, and P. Schmelcher, *Spectral properties of finite laser-driven lattices of ultracold Rydberg atoms*, J. Phys. B **44**, 184009 (2011).

[145] W. Zeller, M. Mayle, T. Bonato, G. Reinelt, and P. Schmelcher, *Spectra and ground states of one- and two-dimensional laser-driven lattices of ultracold Rydberg atoms*, Phys. Rev. A **85**, 063603 (2012).

[146] T. Pohl, E. Demler, and M. D. Lukin, *Dynamical Crystallization in the Dipole Blockade of Ultracold Atoms*, Phys. Rev. Lett. **104**, 043002 (2010).

[147] J. Otterbach and M. Lemeshko, arXiv:1308.5905 [cond-mat.quant-gas].

[148] R. M. W. van Bijnen, S. Smit, K. A. H. van Leeuwen, E. J. D. Vredenbregt, and S. J. J. M. F. Kokkelmans, *Adiabatic formation of Rydberg crystals with chirped laser pulses*, J. Phys. B **44**, 184008 (2011).

[149] M. Robert-de Saint-Vincent, C. S. Hofmann, H. Schempp, G. Günter, S. Whitlock, and M. Weidemüller, *Spontaneous Avalanche Ionization of a Strongly Blockaded Rydberg Gas*, Phys. Rev. Lett. **110**, 045004 (2013).

[150] G. Bannasch, T. C. Killian, and T. Pohl, *Strongly Coupled Plasmas via Rydberg Blockade of Cold Atoms*, Phys. Rev. Lett. **110**, 253003 (2013).

[151] T. Pohl, C. S. Adams, and H. R. Sadephpour, *Cold Rydberg gases and ultra-cold plasmas*, J. Phys. B **44**, 180201 (2011).

[152] P. McQuillen, X. Zhang, T. Strickler, F. B. Dunning, and T. C. Killian, *Imaging the evolution of an ultracold strontium Rydberg gas*, Phys. Rev. A **87**, 013407 (2013).

[153] C. Ates, I. Lesanovsky, C. S. Adams, and K. J. Weatherill, *Fast and Quasideterministic Single Ion Source from a Dipole-Blockaded Atomic Ensemble*, Phys. Rev. Lett. **110**, 213003 (2013).

[154] J. Honer, H. Weimer, T. Pfau, and H. P. Büchler, *Collective Many-Body Interaction in Rydberg Dressed Atoms*, Phys. Rev. Lett. **105**, 160404 (2010).

[155] N. Henkel, R. Nath, and T. Pohl, *Three-Dimensional Roton Excitations and Supersolid Formation in Rydberg-Excited Bose-Einstein Condensates*, Phys. Rev. Lett. **104**, 195302 (2010).

[156] N. Henkel, F. Cinti, P. Jain, G. Pupillo, and T. Pohl, *Supersolid Vortex Crystals in Rydberg-Dressed Bose-Einstein Condensates*, Phys. Rev. Lett. **108**, 265301 (2012).

[157] T. Macri and T. Pohl, arXiv:1308.5562 [cond-mat.quant-gas].

[158] F. Maucher, N. Henkel, M. Saffman, W. Królikowski, S. Skupin, and T. Pohl, *Rydberg-Induced Solitons: Three-Dimensional Self-Trapping of Matter Waves*, Phys. Rev. Lett. **106**, 170401 (2011).

[159] G. Pupillo, A. Micheli, M. Boninsegni, I. Lesanovsky, and P. Zoller, arXiv:0904.2735 [cond-mat.quant-gas].

[160] G. Pupillo, A. Micheli, M. Boninsegni, I. Lesanovsky, and P. Zoller, *Strongly Correlated Gases of Rydberg-Dressed Atoms: Quantum and Classical Dynamics*, Phys. Rev. Lett. **104**, 223002 (2010).

[161] A. W. Glaetzle, R. Nath, B. Zhao, G. Pupillo, and P. Zoller, *Driven-dissipative dynamics of a strongly interacting Rydberg gas*, Phys. Rev. A **86**, 043403 (2012).

[162] F. Cinti, P. Jain, M. Boninsegni, A. Micheli, P. Zoller, and G. Pupillo, *Supersolid Droplet Crystal in a Dipole-Blockaded Gas*, Phys. Rev. Lett. **105**, 135301 (2010).

[163] C.-H. Hsueh, T.-C. Lin, T.-L. Horng, and W. C. Wu, *Quantum crystals in a trapped Rydberg-dressed Bose-Einstein condensate*, Phys. Rev. A **86**, 013619 (2012).

[164] C.-H. Hsueh, Y.-C. Tsai, K.-S. Wu, M.-S. Chang, and W. C. Wu, arXiv:1305.5456 [cond-mat.quant-gas].

[165] J. E. Johnson and S. L. Rolston, *Interactions between Rydberg-dressed atoms*, Phys. Rev. A **82**, 033412 (2010).

[166] F. Grusdt and M. Fleischhauer, *Fractional quantum Hall physics with ultracold Rydberg gases in artificial gauge fields*, Phys. Rev. A **87**, 043628 (2013).

[167] A. Lauer, D. Muth, and M. Fleischhauer, *Transport-induced melting of crystals of Rydberg dressed atoms in a one-dimensional lattice*, New J. Phys. **14**, 095009 (2012).

[168] W. Li, L. Hamadeh, and I. Lesanovsky, *Probing the interaction between Rydberg-dressed atoms through interference*, Phys. Rev. A **85**, 053615 (2012).

[169] H. Weimer and H. P. Büchler, *Two-Stage Melting in Systems of Strongly Interacting Rydberg Atoms*, Phys. Rev. Lett. **105**, 230403 (2010).

[170] E. Sela, M. Punk, and M. Garst, *Dislocation-mediated melting of one-dimensional Rydberg crystals*, Phys. Rev. B **84**, 085434 (2011).

[171] S. Ji, C. Ates, and I. Lesanovsky, *Two-dimensional Rydberg Gases and the Quantum Hard-Squares Model*, Phys. Rev. Lett. **107**, 060406 (2011).

[172] S. Ji, C. Ates, J. P. Garrahan, and I. Lesanovsky, *Equilibration of quantum hard rods in one dimension*, J. Stat. Mech. Theor. Exp. **2013**, P02005 (2013).

[173] I. Lesanovsky, B. Olmos, and J. P. Garrahan, *Thermalization in a Coherently Driven Ensemble of Two-Level Systems*, Phys. Rev. Lett. **105**, 100603 (2010).

[174] I. Lesanovsky, *Many-Body Spin Interactions and the Ground State of a Dense Rydberg Lattice Gas*, Phys. Rev. Lett. **106**, 025301 (2011).

[175] I. Lesanovsky, *Liquid Ground State, Gap, and Excited States of a Strongly Correlated Spin Chain*, Phys. Rev. Lett. **108**, 105301 (2012).

[176] B. Olmos and I. Lesanovsky, *Rydberg rings*, Phys. Chem. Chem. Phys. **13**, 4208 (2011).

[177] T. Opatrný and K. Mølmer, *Spin squeezing and Schrödinger-cat-state generation in atomic samples with Rydberg blockade*, Phys. Rev. A **86**, 023845 (2012).

[178] H. Weimer, arXiv:1309.0514 [cond-mat.quant-gas].

[179] K. Saha, S. Sinha, and K. Sengupta, arXiv:1307.8126 [cond-mat.str-el].

[180] B. Olmos, I. Lesanovsky, and J. P. Garrahan, *Facilitated Spin Models of Dissipative Quantum Glasses*, Phys. Rev. Lett. **109**, 020403 (2012).

[181] A. Hu, T. E. Lee, and C. W. Clark, arXiv:1305.2208 [cond-mat.quant-gas].

[182] T. E. Lee, H. Häffner, and M. C. Cross, *Antiferromagnetic phase transition in a nonequilibrium lattice of Rydberg atoms*, Phys. Rev. A **84**, 031402 (2011).

[183] T. E. Lee and M. C. Cross, *Spatiotemporal dynamics of quantum jumps with Rydberg atoms*, Phys. Rev. A **85**, 063822 (2012).

[184] T. Pohl, *Rydberg Atoms Jump in Bunches*, Physics **5**, 5 (2012).

[185] T. E. Lee, H. Häffner, and M. C. Cross, *Collective Quantum Jumps of Rydberg Atoms*, Phys. Rev. Lett. **108**, 023602 (2012).

[186] C. Ates, B. Olmos, J. P. Garrahan, and I. Lesanovsky, *Dynamical phases and intermittency of the dissipative quantum Ising model*, Phys. Rev. A **85**, 043620 (2012).

[187] I. Lesanovsky, *Excited atoms spin out of equilibrium*, Physics **4**, 71 (2011).

[188] I. Lesanovsky and J. P. Garrahan, arXiv:1307.8078 [physics.atom-ph].

[189] T. Amthor, M. Reetz-Lamour, S. Westermann, J. Denskat, and M. Weidemüller, *Mechanical Effect of van der Waals Interactions Observed in Real Time in an Ultracold Rydberg Gas*, Phys. Rev. Lett. **98**, 023004 (2007).

[190] T. Amthor, M. Reetz-Lamour, C. Giese, and M. Weidemüller, *Modeling many-particle mechanical effects of an interacting Rydberg gas*, Phys. Rev. A **76**, 054702 (2007).

[191] S. Westermann, T. Amthor, A. L. de Oliveira, J. Deiglmayr, R. M. Lamour, and M. Weidemüller, *Dynamics of resonant energy transfer in a cold Rydberg gas*, EPJ D **40**, 37 (2006).

[192] W. Li, C. Ates, and I. Lesanovsky, *Nonadiabatic Motional Effects and Dissipative Blockade for Rydberg Atoms Excited from Optical Lattices or Microtraps*, Phys. Rev. Lett. **110**, 213005 (2013).

[193] M. Müller, L. Liang, I. Lesanovsky, and P. Zoller, *Trapped Rydberg ions: from spin chains to fast quantum gates*, New J. Phys. **10**, 093009 (2008).

[194] M. L. Wall, F. Robicheaux, and R. R. Jones, *Controlling atom motion through the dipole-dipole force*, J. Phys. B **40**, 3693 (2007).

[195] W. Li and I. Lesanovsky, *Electronically Excited Cold Ion Crystals*, Phys. Rev. Lett. **108**, 023003 (2012).

[196] C. Ates, A. Eisfeld, and J. M. Rost, *Motion of Rydberg atoms induced by resonant dipole-dipole interactions*, New J. Phys. **10**, 045030 (2008).

[197] S. Möbius, S. Wüster, C. Ates, A. Eisfeld, and J. M. Rost, *Adiabatic entanglement transport in Rydberg aggregates*, J. Phys. B **44**, 184011 (2011).

[198] S. Möbius, M. Genkin, S. Wüster, A. Eisfeld, and J. M. Rost, *Breakup of Rydberg-blockaded atom clouds via dipole-dipole interactions*, Phys. Rev. A **88**, 012716 (2013).

[199] S. Möbius, M. Genkin, A. Eisfeld, S. Wüster, and J. M. Rost, *Entangling distant atom clouds through Rydberg dressing*, Phys. Rev. A **87**, 051602 (2013).

[200] S. Wüster, A. Eisfeld, and J. M. Rost, *Conical Intersections in an Ultracold Gas*, Phys. Rev. Lett. **106**, 153002 (2011).

[201] S. Wüster, C. Ates, A. Eisfeld, and J. M. Rost, *Excitation transport through Rydberg dressing*, New J. Phys. **13**, 073044 (2011).

[202] M. Genkin, S. Wüster, S. Möbius, A. Eisfeld, and J. Rost, arXiv:1308.5864 [physics.atom-ph].

[203] V. Vuletic, *Quantum networks: When superatoms talk photons*, Nature Phys. **2**, 801 (2006).

[204] J. V. Hernández and F. Robicheaux, *Coherence conditions for groups of Rydberg atoms*, J. Phys. B **39**, 4883 (2006).

[205] H. Weimer, M. Müller, I. Lesanovsky, P. Zoller, and H. P. Büchler, *A Rydberg quantum simulator*, Nature Phys. **6**, 382 (2010).

[206] I. E. Protsenko, G. Reymond, N. Schlosser, and P. Grangier, *Operation of a quantum phase gate using neutral atoms in microscopic dipole traps*, Phys. Rev. A **65**, 052301 (2002).

[207] V. Leung, A. Tauschinsky, N. van Druten, and R. Spreeuw, *Microtrap arrays on magnetic film atom chips for quantum information science*, Quantum Inf. Process. **10**, 955 (2011).

[208] M. Müller, I. Lesanovsky, H. Weimer, H. P. Büchler, and P. Zoller, *Mesoscopic Rydberg Gate Based on Electromagnetically Induced Transparency*, Phys. Rev. Lett. **102**, 170502 (2009).

[209] L. H. Pedersen and K. Mølmer, *Few qubit atom-light interfaces with collective encoding*, Phys. Rev. A **79**, 012320 (2009).

[210] H. Weimer, N. Y. Yao, C. R. Laumann, and M. D. Lukin, *Long-Range Quantum Gates using Dipolar Crystals*, Phys. Rev. Lett. **108**, 100501 (2012).

[211] E. Brion, F. Carlier, V. M. Akulin, and K. Mølmer, *Quantum repeater with Rydberg-blocked atomic ensembles in fiber-coupled cavities*, Phys. Rev. A **85**, 042324 (2012).

[212] T. Keating, K. Goyal, Y.-Y. Jau, G. W. Biedermann, A. J. Landahl, and I. H. Deutsch, *Adiabatic quantum computation with Rydberg-dressed atoms*, Phys. Rev. A **87**, 052314 (2013).

[213] J. C. Garcia-Escartin and P. Chamorro-Posada, *Counterfactual Rydberg gate for photons*, Phys. Rev. A **85**, 032309 (2012).

[214] M. Saffman and T. G. Walker, *Analysis of a quantum logic device based on dipole-dipole interactions of optically trapped Rydberg atoms*, Phys. Rev. A **72**, 022347 (2005).

[215] X. L. Zhang, A. T. Gill, L. Isenhower, T. G. Walker, and M. Saffman, *Fidelity of a Rydberg-blockade quantum gate from simulated quantum process tomography*, Phys. Rev. A **85**, 042310 (2012).

[216] C. Carr, R. Ritter, C. G. Wade, C. S. Adams, and K. J. Weatherill, *Nonequilibrium Phase Transition in a Dilute Rydberg Ensemble*, Phys. Rev. Lett. **111**, 113901 (2013).

[217] L. Isenhower, E. Urban, X. L. Zhang, A. T. Gill, T. Henage, T. A. Johnson, T. G. Walker, and M. Saffman, *Demonstration of a Neutral Atom Controlled-NOT Quantum Gate*, Phys. Rev. Lett. **104**, 010503 (2010).

[218] E. Urban, T. A. Johnson, T. Henage, L. Isenhower, D. D. Yavuz, T. G. Walker, and M. Saffmanu, *Observation of Rydberg blockade between two atoms*, Nature Phys. **5**, 110 (2009).

[219] K. R. Patton and U. R. Fischer, arXiv:1307.0963 [quant-ph].

[220] E. Kuznetsova, T. Bragdon, R. Côté, and S. F. Yelin, *Cluster-state generation using van der Waals and dipole-dipole interactions in optical lattices*, Phys. Rev. A **85**, 012328 (2012).

[221] D. D. B. Rao and K. Mølmer, *Dark Entangled Steady States of Interacting Rydberg Atoms*, Phys. Rev. Lett. **111**, 033606 (2013).

[222] T. Baluktsian, B. Huber, R. Löw, and T. Pfau, *Evidence for Strong van der Waals Type Rydberg-Rydberg Interaction in a Thermal Vapor*, Phys. Rev. Lett. **110**, 123001 (2013).

[223] B. Huber, T. Baluktsian, M. Schlagmüller, A. Kölle, H. Kübler, R. Löw, and T. Pfau, *GHz Rabi Flopping to Rydberg States in Hot Atomic Vapor Cells*, Phys. Rev. Lett. **107**, 243001 (2011).

[224] A. Kölle, G. Epple, H. Kübler, R. Löw, and T. Pfau, *Four-wave mixing involving Rydberg states in thermal vapor*, Phys. Rev. A **85**, 063821 (2012).

[225] H. Kübler, J. P. Shaffer, T. Baluktsian, R. Löw, and T. Pfau, *Coherent excitation of Rydberg atoms in micrometre-sized atomic vapour cells*, Nature Photon. **4**, 112 (2010).

[226] M. Saffman and T. G. Walker, *Creating single-atom and single-photon sources from entangled atomic ensembles*, Phys. Rev. A **66**, 065403 (2002).

[227] P. Grangier, *Room for Just One Photon*, Science **336**, 812 (2012).

[228] V. Parigi, E. Bimbard, J. Stanojevic, A. J. Hilliard, F. Nogrette, R. Tualle-Brouri, A. Ourjoumtsev, and P. Grangier, *Observation and Measurement of Interaction-Induced Dispersive Optical Nonlinearities in an Ensemble of Cold Rydberg Atoms*, Phys. Rev. Lett. **109**, 233602 (2012).

[229] J. Stanojevic, V. Parigi, E. Bimbard, A. Ourjoumtsev, P. Pillet, and P. Grangier, *Generating non-Gaussian states using collisions between Rydberg polaritons*, Phys. Rev. A **86**, 021403 (2012).

[230] J. Stanojevic, V. Parigi, E. Bimbard, A. Ourjoumtsev, and P. Grangier, arXiv:1303.4927 [quant-ph].

[231] H. H. Jen, B. Xiong, I. A. Yu, and D.-W. Wang, arXiv:1305.2351 [quant-ph].

[232] H. H. Jen and D.-W. Wang, *Theory of electromagnetically induced transparency in strongly correlated quantum gases*, Phys. Rev. A **87**, 061802 (2013).

[233] J. Reslen, *Many-body effects in a model of electromagnetically induced transparency*, J. Phys. B **44**, 195505 (2011).

[234] H. Wu, Z.-B. Yang, and S.-B. Zheng, arXiv:1305.2351 [quant-ph].

[235] G. W. Lin, J. Yang, X. M. Lin, Y. P. Niu, and S. Q. Gong, arXiv:1308.2782 [quant-ph].

[236] T. Laycock, B. Olmos, and I. Lesanovsky, *Creation of collective many-body states and single photons from two-dimensional Rydberg lattice gases*, J. Phys. B **44**, 184017 (2011).

[237] B. Olmos and I. Lesanovsky, *Collective photon emission from symmetric states created with Rydberg atoms on a ring lattice*, Phys. Rev. A **82**, 063404 (2010).

[238] J. Honer, R. Löw, H. Weimer, T. Pfau, and H. P. Büchler, *Artificial Atoms Can Do More Than Atoms: Deterministic Single Photon Subtraction from Arbitrary Light Fields*, Phys. Rev. Lett. **107**, 093601 (2011).

[239] M. M. Müller, A. Kölle, R. Löw, T. Pfau, T. Calarco, and S. Montangero, arXiv:1308.1425 [physics.atom-ph].

[240] A. E. B. Nielsen and K. Mølmer, *Deterministic multimode photonic device for quantum-information processing*, Phys. Rev. A **81**, 043822 (2010).

[241] D. Petrosyan and M. Fleischhauer, *Electromagnetically induced transparency and photon-photon interactions with Rydberg atoms*, JPCS **350**, 012001 (2012).

[242] D. Petrosyan, J. Otterbach, and M. Fleischhauer, *Electromagnetically Induced Transparency with Rydberg Atoms*, Phys. Rev. Lett. **107**, 213601 (2011).

[243] Y. O. Dudin, F. Bariani, and A. Kuzmich, *Emergence of Spatial Spin-Wave Correlations in a Cold Atomic Gas*, Phys. Rev. Lett. **109**, 133602 (2012).

[244] G. Nikoghosyan, F. E. Zimmer, and M. B. Plenio, *Dipolar Bose-Einstein condensate of dark-state polaritons*, Phys. Rev. A **86**, 023854 (2012).

[245] J. Keaveney, A. Sargsyan, U. Krohn, I. G. Hughes, D. Sarkisyan, and C. S. Adams, *Cooperative Lamb Shift in an Atomic Vapor Layer of Nanometer Thickness*, Phys. Rev. Lett. **108**, 173601 (2012).

[246] C. Carr, M. Tanasittikosol, A. Sargsyan, D. Sarkisyan, C. S. Adams, and K. J. Weatherill, *Three-photon electromagnetically induced transparency using Rydberg states*, Opt. Lett. **37**, 3858 (2012).

[247] D. Maxwell, D. J. Szwer, D. Paredes-Barato, H. Busche, J. D. Pritchard, A. Gauguet, K. J. Weatherill, M. P. A. Jones, and C. S. Adams, *Storage and Control of Optical Photons Using Rydberg Polaritons*, Phys. Rev. Lett. **110**, 103001 (2013).

[248] J. D. Pritchard, D. Maxwell, A. Gauguet, K. J. Weatherill, M. P. A. Jones, and C. S. Adams, *Cooperative Atom-Light Interaction in a Blockaded Rydberg Ensemble*, Phys. Rev. Lett. **105**, 193603 (2010).

[249] J. D. Pritchard, A. Gauguet, K. J. Weatherill, and C. S. Adams, *Optical non-linearity in a dynamical Rydberg gas*, J. Phys. B **44**, 184019 (2011).

[250] J. D. Pritchard, C. S. Adams, and K. Mølmer, *Correlated Photon Emission from Multiatom Rydberg Dark States*, Phys. Rev. Lett. **108**, 043601 (2012).

[251] M. Tanasittikosol, J. D. Pritchard, D. Maxwell, A. Gauguet, K. J. Weatherill, R. M. Potvliege, and C. S. Adams, *Microwave dressing of Rydberg dark states*, J. Phys. B **44**, 184020 (2011).

[252] K. J. Weatherill, J. D. Pritchard, R. P. Abel, M. G. Bason, A. K. Mohapatra, and C. S. Adams, *Electromagnetically induced transparency of an interacting cold Rydberg ensemble*, J. Phys. B **41**, 201002 (2008).

[253] M. Gärttner and J. Evers, *Nonlinear absorption and density-dependent dephasing in Rydberg electromagnetically-induced-transparency media*, Phys. Rev. A **88**, 033417 (2013).

[254] M. Lukin, Quantum nonlinear optics with single photons enabled by strongly interacting atoms, in *Frontiers in Optics 2012/Laser Science XXVIII*, page LTu1J.5, Optical Society of America, 2012.

[255] D. Yan, J.-W. Gao, Q.-Q. Bao, H. Yang, H. Wang, and J.-H. Wu, *Electromagnetically induced transparency in a five-level* Λ *system dominated by two-photon resonant transitions*, Phys. Rev. A **83**, 033830 (2011).

[256] D. Yan, Y.-M. Liu, Q.-Q. Bao, C.-B. Fu, and J.-H. Wu, *Electromagnetically induced transparency in an inverted-*Υ *system of interacting cold atoms*, Phys. Rev. A **86**, 023828 (2012).

[257] A. V. Gorshkov, J. Otterbach, M. Fleischhauer, T. Pohl, and M. D. Lukin, *Photon-Photon Interactions via Rydberg Blockade*, Phys. Rev. Lett. **107**, 133602 (2011).

[258] A. V. Gorshkov, R. Nath, and T. Pohl, *Dissipative Many-Body Quantum Optics in Rydberg Media*, Phys. Rev. Lett. **110**, 153601 (2013).

[259] J.-F. Huang, J.-Q. Liao, and C. P. Sun, *Photon blockade induced by atoms with Rydberg coupling*, Phys. Rev. A **87**, 023822 (2013).

[260] D. Maxwell, D. J. Szwer, D. P. Barato, H. Busche, J. D. Pritchard, A. Gauguet, M. P. A. Jones, and C. S. Adams, arXiv:1308.1425 [physics.atom-ph].

[261] T. Peyronel, O. Firstenberg, Q.-Y. Liang, S. Hofferberth, A. V. Gorshkov, T. Pohl, M. D. Lukin, and V. Vuletic, *Quantum nonlinear optics with single photons enabled by strongly interacting atoms*, Nature **488**, 57 (2012).

[262] S. Baur, D. Tiarks, G. Rempe, and S. Dürr, arXiv:1307.3509 [quant-ph].

[263] J. Otterbach, M. Moos, D. Muth, and M. Fleischhauer, *Wigner Crystallization of Single Photons in Cold Rydberg Ensembles*, Phys. Rev. Lett. **111**, 113001 (2013).

[264] M. Mayle, *Ultracold Rydberg Atoms in a Ioffe-Pritchard Trap; Creating One-Dimensional Rydberg Gases and Exploiting their Composite Character*, PhD thesis, University of Heidelberg, 2009.

[265] T. Vogt, *Blocage dipolaire de l'excitation d'atomes froids vers des états de Rydberg: Contrôle par champ électrique et résonance de Förster*, PhD thesis, University of Paris - Orsay Campus, 2006.

[266] C. S. Hofmann, *Emergence of correlations in strongly interacting ultracold Rydberg gases*, PhD thesis, Ruperto-Carola University of Heidelberg, 2013.

[267] T. Amthor, *Interaction-Induced Dynamics in Ultracold Rydberg Gases - Mechanical Effects and Coherent Processes*, PhD thesis, Albert-Ludwigs-Universität Freiburg, 2008.

[268] H. Weimer, *Quantum many-body physics with strongly interacting Rydberg atoms*, PhD thesis, Universität Stuttgart, 2010.

[269] K. P. Heeg, *Models for correlated Rydberg gases*, Diploma thesis, University of Heidelberg, 2012.

[270] C. Ates, *Anregungsdynamik ultrakalter Rydberggase*, PhD thesis, Technische Universität Dresden, 2009.

[271] M. Scully and S. Zubairy, *Quantum Optics*, Cambridge University Press, 1997.

[272] N. Tezak, *Spectra and Excitation Dynamics of Laser-driven Lattices of Ultracold Rydberg Atoms*, Diploma thesis, University of Heidelberg, 2010.

[273] S. Hopkins, *Laser cooling of rubidium atoms in a magneto-optical trap*, PhD thesis, The Open University, 1996.

[274] R. G. Hulet and D. Kleppner, *Rydberg Atoms in "Circular" States*, Phys. Rev. Lett. **51**, 1430 (1983).

[275] C. J. Lorenzen and K. Niemax, *Quantum Defects of the $n^2P_{1/2,3/2}$ Levels in ^{39}K I and ^{85}Rb I*, Phys. Scr. **27**, 300 (1983).

[276] Y. Ralchenko, A. E. Kramida, J. Reader, and NIST ASD Team, NIST Atomic Spectra Database (version 3.1.5), http://physics.nist.gov/asd3 [2009, August 19]. National Institute of Standards and Technology, Gaithersburg, MD.

[277] V. A. Nascimento, L. L. Caliri, A. Schwettmann, J. P. Shaffer, and L. G. Marcassa, *Electric Field Effects in the Excitation of Cold Rydberg-Atom Pairs*, Phys. Rev. Lett. **102**, 213201 (2009).

[278] E. Brekke, J. O. Day, and T. G. Walker, *Excitation suppression due to interactions between microwave-dressed Rydberg atoms*, Phys. Rev. A **86**, 033406 (2012).

[279] I. Shavitt and L. T. Redmon, *Quasidegenerate perturbation theories. A canonical van Vleck formalism and its relationship to other approaches*, J. Chem. Phys. **73**, 5711 (1980).

[280] V. Paulisch, R. Han, H. K. Ng, and B.-G. Englert, arXiv:1209.6568 [quant-ph].

[281] B. T. Torosov and N. V. Vitanov, *Adiabatic elimination of a nearly resonant quantum state*, J. Phys. B **45**, 135502 (2012).

[282] H. Breuer and F. Petruccione, *The Theory of Open Quantum Systems*, Oxford University Press, 2002.

[283] G. Lindblad, *On the generators of quantum dynamical semigroups*, Comm. Math. Phys. **48**, 119 (1976).

[284] H. Wiseman and G. Milburn, *Quantum Measurement and Control*, Cambridge University Press, 2010.

[285] J. D. Pritchard, *Cooperative Optical Non-Linearity in a Blockaded Rydberg Ensemble*, PhD thesis, Durham University, 2012.

[286] C. S. Hofmann, G. Günter, H. Schempp, N. L. M. Müller, A. Faber, H. Busche, M. R. de Saint-Vincent, S. Whitlock, and M. Weidemüller, arXiv:1307.1074 [physics.atom-ph].

[287] H. Schempp, G. Günter, C. S. Hofmann, C. Giese, S. D. Saliba, B. D. DePaola, T. Amthor, M. Weidemüller, S. Sevinçli, and T. Pohl, *Coherent Population Trapping with Controlled Interparticle Interactions*, Phys. Rev. Lett. **104**, 173602 (2010).

[288] J. B. Balewski, A. T. Krupp, A. Gaj, D. Peter, H. P. Büchler, R. Löw, S. Hofferberth, and T. Pfau, arXiv:1306.5181 [physics.atom-ph].

[289] M. Kiffner, M. Macovei, J. Evers, and C. Keitel, Vacuum-induced processes in multilevel atoms, in *Progress in Optics*, volume 55, pages 85–197, Elsevier Science, Burlington, 2010.

[290] M. Gross and S. Haroche, *Superradiance: An essay on the theory of collective spontaneous emission*, Phys. Rep. **93**, 301 (1982).

[291] D. Breyel, T. L. Schmidt, and A. Komnik, *Rydberg crystallization detection by statistical means*, Phys. Rev. A **86**, 023405 (2012).

[292] M. Galassi, J. Davies, J. Theiler, B. Gough, G. Jungman, M. Booth, and F. Rossi, *Gnu Scientific Library: Reference Manual*, Network Theory Ltd., 2003.

[293] J. K. Cullum and R. A. Willoughby, *Lanczos Algorithms for Large Symmetric Eigenvalue Computations, Vol. 1*, Society for Industrial and Applied Mathematics, Philadelphia, PA, USA, 2002.

[294] W. L. Dunn and J. K. Shultis, *Exploring Monte Carlo Methods*, Elsevier, 2011.

[295] L. Mandel, *Sub-Poissonian photon statistics in resonance fluorescence*, Opt. Lett. **4**, 205 (1979).

[296] M. Le Bellac, F. Mortessagne, and G. G. Batrouni, *Equilibrium and Non-Equilibrium Statistical Thermodynamics*, Cambridge University Press, 2004.

[297] M. Lemeshko, R. V. Krems, and H. Weimer, *Nonadiabatic Preparation of Spin Crystals with Ultracold Polar Molecules*, Phys. Rev. Lett. **109**, 035301 (2012).

[298] J. Schachenmayer, B. P. Lanyon, C. F. Roos, , and A. J. Daley, arXiv:1305.6880 [cond-mat.quant-gas].

[299] D. W. Schönleber, *Dissipative dynamics in many-body Rydberg systems*, Master's thesis, University of Heidelberg, 2013.

[300] H. J. Carmichael, *An open systems approach to quantum optics*, Université Libre de Bruxelles, 1991.

[301] J. Dalibard, Y. Castin, and K. Mølmer, *Wave-function approach to dissipative processes in quantum optics*, Phys. Rev. Lett. **68**, 580 (1992).

[302] R. Dum, P. Zoller, and H. Ritsch, *Monte Carlo simulation of the atomic master equation for spontaneous emission*, Phys. Rev. A **45**, 4879 (1992).

[303] K. Mølmer, Y. Castin, and J. Dalibard, *Monte Carlo wave-function method in quantum optics*, J. Opt. Soc. Am. B **10**, 524 (1993).

[304] D. Schönleber, M. Gärttner, and J. Evers, in preperation.

[305] A. Jansen, *An Introduction to Kinetic Monte Carlo Simulations of Surface Reactions*, Lecture Notes in Physics, Springer, 2012.

[306] B. Efron, *Bootstrap Methods: Another Look at the Jackknife*, Ann. Stat. **7**, 1 (1979).

[307] T. C. Killian, *Ultracold Neutral Plasmas*, Science **316**, 705 (2007).

[308] M. Fleischhauer, A. Imamoglu, and J. P. Marangos, *Electromagnetically induced transparency: Optics in coherent media*, Rev. Mod. Phys. **77**, 633 (2005).

[309] S. Sevinçli, N. Henkel, C. Ates, and T. Pohl, *Nonlocal Nonlinear Optics in Cold Rydberg Gases*, Phys. Rev. Lett. **107**, 153001 (2011).

[310] S. Sevinçli, C. Ates, T. Pohl, H. Schempp, C. S. Hofmann, G. Günter, T. Amthor, M. Weidemüller, J. D. Pritchard, D. Maxwell, A. Gauguet, K. J. Weatherill, M. P. A. Jones, and C. S. Adams, *Quantum interference in interacting three-level Rydberg gases: coherent population trapping and electromagnetically induced transparency*, J. Phys. B **55**, 184018 (2011).

[311] Y. O. Dudin and A. Kuzmich, *Strongly Interacting Rydberg Excitations of a Cold Atomic Gas*, Science **336**, 887 (2012).

[312] M. Gärttner, D. Schönleber, S. Whitlock, and J. Evers, in preperation, 2013.

[313] J. Gea-Banacloche, Y.-q. Li, S.-z. Jin, and M. Xiao, *Electromagnetically induced transparency in ladder-type inhomogeneously broadened media: Theory and experiment*, Phys. Rev. A **51**, 576 (1995).

[314] B. J. Dalton, R. McDuff, and P. L. Knight, *Coherent Population Trapping*, Optica Acta: International Journal of Optics **32**, 61 (1985).

[315] J. Oreg, F. T. Hioe, and J. H. Eberly, *Adiabatic following in multilevel systems*, Phys. Rev. A **29**, 690 (1984).

[316] K. Bergmann, H. Theuer, and B. W. Shore, *Coherent population transfer among quantum states of atoms and molecules*, Rev. Mod. Phys. **70**, 1003 (1998).

[317] M. Fleischhauer and M. D. Lukin, *Dark-State Polaritons in Electromagnetically Induced Transparency*, Phys. Rev. Lett. **84**, 5094 (2000).

[318] M. D. Lukin, S. F. Yelin, and M. Fleischhauer, *Entanglement of Atomic Ensembles by Trapping Correlated Photon States*, Phys. Rev. Lett. **84**, 4232 (2000).

[319] C. Liu, Z. Dutton, C. H. Behroozi, and L. V. Hau, *Observation of coherent optical information storage in an atomic medium using halted light pulses*, Nature **409**, 490 (2001).

[320] D. F. Phillips, A. Fleischhauer, A. Mair, R. L. Walsworth, and M. D. Lukin, *Storage of Light in Atomic Vapor*, Phys. Rev. Lett. **86**, 783 (2001).

[321] L. Jin, M. Macovei, and J. Evers, arXiv:1202.0699 [quant-ph].

[322] H.-D. Meyer, U. Manthe, and L. Cederbaum, *The multi-configurational time-dependent Hartree approach*, Chem. Phys. Lett. **165**, 73 (1990).

[323] M. Beck, A. Jäckle, G. Worth, and H.-D. Meyer, *The multiconfiguration time-dependent Hartree (MCTDH) method: a highly efficient algorithm for propagating wavepackets*, Phys. Rep. **324**, 1 (2000).

Danksagung

Der erste Dank gilt meinem Betreuer und Ideengeber **Jörg Evers**. Bei dir habe ich nicht nur gelernt wie man gute Forschung macht, sondern vor allen Dingen wie man sie gut präsentiert. Außerdem danke ich sehr herzlich meinen mitunter ebenso konstruktiven Zweitbetreuern **Thomas Gasenzer** und auf der experimentellen Seite der stets interessierte **Matthias Weidemüller**.

Im Lauf der drei Jahre, die ich als Dokorand erleben durfte, hatte ich durch sehr viele Treffen immer wieder die Gelegenheit interessante Einblicke in die Sichtweise eines Experimetators zu bekommen. Dafür danke ich **Shannon Whitlock** und allen anderen aus der Weidemüllergruppe.

Auch geht mein Dank an **Kilian Heeg** und **David Schönleber**. Sie haben zum Gelingen dieses Projekts an vielen Stellen entscheidend beigetragen. Ich danke auch meinen Kollegen **Lida**, **Andreas** und dem echten **Andi**, durch die es nie langweilig wurde im Büro.

Ausdrücklicher Dank gilt meinen "externen Betreuern" **Michael**, der oft hilfreiche Tipps gegeben hat, und **Igor Lesoanovsky**, der zahlreiche E-Mails stets geduldig beantwortete.

Ganz besonders danke ich hier auch meiner **Familie**, **Eltern** und **Freunden**. Insbesondere danke ich der, ohne die alles nichts wäre, meinem über alles geliebten Schatz, der jeden noch so regengrauen Tag sonnig erscheinen lässt, **Vanessa**.